DISS. ETH No. 11940

# A PARAMETRIZED THREE-DIMENSIONAL ALPINE CRUSTAL MODEL AND ITS APPLICATION TO TELESEISMIC WAVEFRONT SCATTERING

A dissertation submitted to the

SWISS FEDERAL INSTITUTE OF TECHNOLOGY ZURICH

for the degree of
Doctor of Natural Sciences

presented by

FELIX WALDHAUSER
Dipl. Natw. ETH
born August 31, 1966
in Basel-Stadt

accepted on the recommendation of

Prof. Dr. St. Mueller, examiner
Prof. Dr. E. Kissling, co-examiner
Prof. Dr. J. Ansorge, co-examiner
Dr. W. L. Ellsworth, co-examiner

1996

# CONTENTS

# ABSTRACT

Different seismic methods do not necessarily show the same characteristics in the data they produce, nor do they necessarily image the same structure at the same location with the same resolution. The comparative use of seismic data and information derived by different seismic methods to construct quantitative 3D seismic models is, however, of great significance. Such models, by depicting the lateral continuity of differently imaged structures, are needed to cross-check results from different seismic investigations and to use them as ‘a priori’ information in inversion methods.

The aim of this thesis was to develop a method for construction of 3D seismic models using data and information from different seismic methods and to apply and test the method on dominant structural features in the Alpine region. A concept for a 3D seismic lithospheric model construction is established, that incorporates the strength of controlled-source seismic and earthquake tomographic methods. It entails a 3D parametrization scheme that accounts for seismic structures to which all methods are most sensitive. The parametrization scheme is flexibly designed in order to allow revising and updating model parameters, and refining established models by including new structural elements. The model consists of discretely distributed model parameters on an even 3D grid. Model parameters on grid nodes are P-velocities, location of refractors and reflectors, confidence values and resolution information. The concept uses controlled-source seismic information to derive 3D crustal structures in such a way that teleseismic wavefront scattering can be studied. It can also be used for integration of local earthquake tomographic results.

A procedure is developed to model seismic information in three dimensions obtained from two-dimensional (2D) controlled-source seismic (CSS) investigations. The procedure involves relocation of 2D derived structural elements in 3D space (3D migration) and interpolation processes to obtain continuity of model parameters. Quantification of data uncertainties allows calculation of the simplest models satisfying the data. The procedure is applied to the crust-mantle boundary in the Alpine region using the seismic information from a dense network of CSS-profiles. A laterally continuous crust-mantle interface showing least surface roughness and highest continuity is modeled, featuring interface offsets where required (principle of simplicity). P-velocities associated with the crust-mantle boundary such as lower-crustal, uppermost-mantle and average crustal velocities are volumetrically represented within their volume of influence.

This well established structural and velocity information, near-surface structures such as low-velocity sedimentary basins, as well as reference velocities for information gaps are parametrized and a 3D seismic model of the central and western Alps and

northern Apennines is derived. The 3D crustal model depicts three crustal blocks, separated from the upper mantle by a European, Adriatic and Ligurian Moho.

The established 3D Alpine velocity model is subsequently used to calculate teleseismic first arrival travel times, using an existing finite-difference approach to the 3D eikonal equation accounting for strong velocity heterogeneities. Absolute and relative teleseismic travel times have been calculated through the 3D model accounting for spherical travel time fields of incoming wavefronts at the base of the 3D model at a depth of 70 km. Azimuthal dependence of teleseismic travel time delays due to wavefront scattering at the dominant Alpine crustal structures is investigated and residuals between -0.6 s and +1.8 s with respect to a 1D reference model down to a depth of 70 km are obtained. Migration of travel time anomalies at the surface due to deep Alpine crustal structures depend on the azimuth of the incoming teleseismic waves. Teleseismic travel time residuals along 2D profiles have been calculated and compared with earlier studies. Compared with these studies, the method followed in this present work has some significant advantages. It uses a quantified velocity model, consistently parametrized and with a reliability estimation for the model parameters. This allows to determine the confidence of the calculated teleseismic travel times, and to improve the velocity model according to new findings. Furthermore, an accurate calculation of teleseismic travel times through strong heterogeneous 3D velocity structures is possible, considering spherical time fields of incoming wavefronts from any azimuth at the base of the model. 2D teleseismic data modeling can account for effects from strong heterogeneous structures outside the profile only approximately by projecting these structures onto the profile. Heterogeneous velocity structures in 3D models influence seismic waves at the proper location in space.

# ZUSAMMENFASSUNG

Aufgrund ihrer unterschiedlichen Abbildungsmechanismen produzieren verschiedene seismische Methoden in den seltensten Fällen äquivalente Daten mit gleichen Eigenschaften, auch bilden sie gleiche seismische Strukturen nicht in gleicher räumlicher Lage mit der gleichen Auflösung ab. Trotzdem ist eine kombinierte Verwendung von Daten aus verschiedenen seismischen Methoden zur Erstellung von drei-dimensionalen (3D) Modellen von grosser Bedeutung. Solche Modelle sind, da sie die wahrscheinliche räumliche Dimension von verschiedenartig abgebildeten Strukturen aufzeigen, eine wertvolle Hilfe zur Verifikation von seismischen Interpretationen und eignen sich deshalb besonders zur Verwendung als ‘a priori’ Information bei der Verwendung tomographischer Methoden.

Die vorliegende Arbeit hatte zum Ziel, die Methodik zur Erstellung von seismischen 3D Modellen unter Verwendung von unterschiedlichen seismischen Daten zu entwickeln und auf die wichtigsten Strukturen im Alpenraum anzuwenden und dadurch zu testen. Ein Konzept zur Konstruktion von 3D Lithosphären-Modellen wurde ausgearbeitet, das die sich ergänzenden Stärken von aktiven und passiven seismischen Methoden in Bezug auf ihre Auflösung seismischer Strukturen betont. Eine 3D Modell-Parametrisierung wurde definiert, welche die wichtigsten strukturellen Elemente erfasst und das Überprüfen von bestehenden und das Einfügen von neuen strukturellen Elementen ermöglicht. Das Geschwindigkeitsmodell besteht aus einem gleichmässigen 3D-Gitter mit Modellparametern wie P-Wellen-Geschwindigkeiten, räumliche Lage von Reflektoren und Refraktoren, Gewichtungen und Informationen über das Auflösungsvermögen. Das Konzept benutzt Modellinformationen von aktiven seismischen Untersuchungen (Refraktions- und Reflexionsseismik) zur Erstellung eines 3D Geschwindigkeitmodells, das es erlaubt Streueffekte von teleseismischen Wellenfronten an den parametrisierten Strukturen zu quantifizieren.

Zwei-dimensional (2D) erfasste strukturelle Informationen von aktiven seismischen Untersuchungen wurden - unter Berücksichtigung von Messungenauigkeiten und Fresnel-Volumen - drei-dimensional modelliert. Die dazu entworfene Prozedur beinhaltet eine Relokalisierung der 2D-Strukturen im Raum (3D-Migration) und einen Interpolationsprozess mit dem Ziel, eine räumliche Kontinuität der Modellparameter anzustreben. Die Quantifizierung der Datenungenauigkeit erlaubt die Berechnung von einfachsten 3D Modellen, welche alle Daten befriedigen.

Die Prozedur wurde auf die alpine Krusten-Mantel-Grenze (Moho) angewendet, unter Verwendung publizierter Interpretationen aus dem dichten aber unregelmässigen Netzwerk von aktiv-seismischen Profilen. Eine lateral möglichst kontinuierliche Moho-

Grenzfläche wurde modelliert, welche die geringste Topographie in ihrer Oberfläche aufweist und mit minimaler lateraler Ausdehnung von vertikalen Versätzen auskommt. Mit der Krusten-Mantel-Grenze assozierte Geschwindigkeiten, wie diejenigen aus der Unterkruste, dem obersten Mantel und Durchschnittsgeschwindigkeiten für die Kruste wurden im Volumen ihres Einflussbereichs dargestellt.

Diese gut dokumentierten Struktur- und Geschwindigkeits-Informationen zusammen mit oberflächennahen Strukturen wie Sedimentbecken sowie Referenz-Werten für Informationslücken ergaben ein 3D P-Wellen Geschwindigkeitsmodell der Zentral- und West-Alpen und des nördlichen Apennins bis zu einer Tiefe von 70 km. Das 3D Modell bildet drei Krustenblöcke ab, welche durch die Europäische, die Adriatische und die Ligurische Moho vom oberen Mantel darunter abgesetzt sind.

In einem nächsten Schritt wurde das 3D Geschwindigkeitsmodell für die Berechnung teleseismischer Laufzeiten verwendet. Dafür wurde ein existierender Algorithmus verwendet, der die 3D Eikonal-Gleichung für lateral stark variierende Geschwindigkeitsfelder mit der Methode der finiten Differenzen löst. Algorithmus und Modell-Parametrisierung wurden für das teleseismische Vorwärtsproblem getestet. Unter Berücksichtigung von sphärischen teleseismischen Wellenfronten an der Basis des 3D Modells in 70 km Tiefe, berechnet mit dem Standard-Erdmodell IASP91, wurden absolute und relative Laufzeiten für verschiedene Einfallsrichtungen und Epizentraldistanzen an der Oberfläche des 3D Modells berechnet. Laufzeitresiduen in der Grösse von -0.6 s bis +1.8 s, verglichen mit einem 1D Referenz- Modell bis in 70 km Tiefe, wurden dabei festgestellt. Die Lage der Laufzeit-Anomalien an der Oberfläche verschiebt sich für tiefliegende Krustenstrukturen in Abhängigkeit vom Azimuth der einfallenden teleseismischen Wellenfronten. Laufzeitresiduen entlang Profil-Linien wurden berechnet und im Vergleich zu Resultaten früherer Untersuchungen diskutiert. Aus der in dieser Arbeit entwickelten Methode und deren Anwendung auf den Alpenraum ergaben sich folgende Vorteile. Für Laufzeitberechnungen steht ein konsistent parametrisiertes und quantifiziertes 3D Geschwindigkeitsmodell zur Verfügung, das es erlaubt, die Zuverlässigkeit der berechneten teleseismischen Laufzeiten an der Oberfläche abzuschätzen. Das 3D Modell kann überprüft, verbessert und verfeinert werden. Im weiteren ist das Vorwärtsrechnen von teleseismischen Laufzeiten auch in stark variierenden Geschwindigkeitsstrukturen, wie in derjenigen des 3D Alpen-Modells, möglich. Azimuth- und epizentraldistanzabhängige, gekrümmte Wellenfelder an der Basis des Modells werden berücksichtigt. Während bei 2D Untersuchungen prägnante, ausserhalb des Profils liegende Inhomogenitäten auf das Profil projiziert werden müssen, beeinflussen Inhomogenitäten im 3D Modell die teleseismische Wellenfront an der richtigen Stelle im Raum.

# CHAPTER 1

# INTRODUCTION

Any hypothesis on present tectonic style and evolution of the lithosphere requires information about its structure and physical parameters.

After being a target of geophysical investigations for almost a century, the insight into deep structure of the Alpine lithosphere contribute to a better understanding of the late Alpine orogeny described by the concept of continent-continent collision. Previous images of Alpine lithospheric structure have served as a basis to derive tectonic models (e.g. Fleitout and Froidevaux, 1982; Butler, 1986; Lemoine and Trümpy, 1987; Laubscher, 1988; Ménard, 1988; Stampfli, 1993) and geodynamic models (e.g. Mueller, 1989; Bott, 1990; Werner and Gudmundsson, 1992). After all these efforts, still pending problems exist, such as quantification of crustal shortening and/or subduction by material balancing (Laubscher, 1988; Ménard et al., 1991) or the exact definition of subduction related dynamical processes (Lyon-Caen and Molnar, 1989). Answers to these and other unsettled problems can only be provided by more detailed and, most important, quantified images of deep structure of the present Alpine lithosphere-asthenosphere system which will lead to improved tectonic and geodynamic models.

The three-dimensional (3D) distribution of seismic velocities (seismic structure) is the most important parameter from which lithospheric structure and composition can be determined. The velocity structure of the Alpine lithosphere has been investigated by means of refraction and reflection seismology (e.g. Mueller et al., 1980; Frei et al., 1990; Blundell et al., 1992), the analysis of surface waves (e.g. Panza et al., 1980; Snieder, 1988b), teleseismic travel time residual studies (e.g. Baer, 1980, Babuska et al., 1990; Guyoton, 1991), and seismic tomography (e.g. Kradolfer, 1989; Spakman, 1991; Kissling and Spakman, 1996).

Refraction and reflection (both controlled-source) seismology are complementary high-resolution imaging techniques (Banda and Mooney, 1982) that have provided most of the information presently available on the Alpine crustal structure. Because of the complex three-dimensional structure of the Alpine lithosphere, only in a few cases (see Kissling, 1993) these studies have been able to image lower lithospheric structure. Knowledge of lower lithospheric structure, however, is important to understand interaction and dynamic processes in the crust-mantle system.

Group and phase velocities calculated from dispersion analysis of surface waves are good indicators of the average shear velocity of the volume penetrated. Due to the low-frequency content of surface waves and the complex tectonic situation in the Alps

the resolving power remains poor and detailed lithospheric structure can therefore not be imaged (Snieder, 1988a).

Teleseismic travel time residuals can be used to map lithospheric thickness with respect to the underlying asthenosphere. This requires detailed ‘a priori’ knowledge of crustal velocity structure beneath the seismic array. Without such information, depth resolution of this method is poor. Since 3D effects such as wavefront deformation at strong discontinuities (e.g. crust-mantle boundary) are neglected by this method, no reliable information of internal lithospheric structure can be obtained.

The inversion of earthquake travel time data developed into seismic tomography (Aki et al., 1977), the method with highest potential to resolve 3D velocity structure at lithospheric (local earthquake tomography) and global (teleseismic tomography) scales. The quality of tomographic results is strongly influenced by the resolution capability of the data, by the errors in determination of source location and origin time, and by the approximations in the method to derive 3D velocity structure from seismic travel times (i.e. approximative solutions to the forward problem, linearizing the relation between travel time and velocity field).

Despite the sometimes large uncertainties in tomographic models, seismic tomography is a powerful method for investigating the 3D velocity structure and teleseismic tomography is presently the only method for better imaging deeper parts of the earth’s mantle. Studies using teleseismic data shed some light onto the general 3D structure of the Alpine lithosphere-asthenosphere system (Babuska et al., 1990; Cattaneo and Eva, 1990; Guyoton, 1991; Spakman et al., 1993). The results, however, still fail in revealing the detailed geometry of the collision zone between the European and the African plate such as the exact thickness of the lithosphere, or as the dip and length of the subducting slabs. The problems lie in the applied methods not considering the crustal structures and in the quality and quantity of the earthquake data used.

Due to the low-frequency contents of waves from distant earthquakes, teleseismic tomography is not capable to clearly image crustal scale structures, though velocity contrasts such as across the crust-mantle boundary influence teleseismic travel times (Guyoton, 1991). Baer (1980) interpreted the observed regional variation of teleseismic ray parameters in the Alpine region as an effect of the deepening structure of the Alpine crust-mantle boundary. Spakman et al. (1993) performed travel time tomography of the European-Mediterranean mantle on the basis of a 1D initial reference velocity model (PM2) that is determined from delay times obtained by the International Seismological Centre (ISC). Ray paths through the velocity models are found by approximative forward solutions which are accurate for smooth velocity variations only. The complex 3D Alpine crustal structure is not accounted for. The facts that results of tomographic studies strongly depend on the initial velocity model (Kissling et al., 1994) and that complex crustal structures critically influence ray geometry may be the explanation for the limited resolution of teleseismic models. Furthermore, decreased resolution is also caused by relatively large errors (Spakman, 1991) in the ISC earthquake travel time data.

An increasing quantity of high-quality earthquake data is available today for the Alpine region. Since they are recorded by different seismic networks and, unfortunately, stored in different formats, efforts have to be made to merge that data to obtain a

homogeneous data set (Solarino et al., 1997). Having such a homogeneous data set at hand, effects of the neglected upper lithospheric 3D structure on teleseismic travel times remain the main source for unreliable and/or speculative tomographic results about the lithosphere-asthenosphere system in the Alps. To better image upper-mantle structure by teleseismic tomography, 3D crustal structure must be taken into account. This can be achieved by incorporating 'a priori' known 3D crustal velocity structures in the initial model for the inversion process. It is obvious, that, in addition to be able to account for scattering effects on travel times, proper integration of 'a priori' information in the initial velocity model for seismic tomography decreases the number of unknown and poorly resolvable model parameters and thus may increase the overall resolution of tomographic models.

'A priori' velocity information for initial models in the inversion process may be obtained from results of other seismic methods applied to the same region of interest. It must be considered, however, that different seismic methods not necessarily show the same characteristics in their data, and that they do not necessarily image the same structure at the same location with the same resolution. Thus, the strength of each method must be considered and their characteristics uniformly parametrized. Erroneous 'a priori' information in initial models for seismic tomography may produce artifacts in the velocity structure to invert for. Errors in 'a priori' information are based on uncertainty of the data used to derive such information, the uncertainty of the spatial location of this information within the initial model, improper model parametrization, or, most likely, a combination of all this sources of errors. Hence, adequate methods must be developed and tested for modeling 'a priori' information to integrate as fixed parameters - i.e. no updating during inversion - in initial velocity models for seismic inversion processes. In order to handle strongly heterogeneous velocity structures, such as the velocity contrast across the crust-mantle boundary, the forward calculation of seismic travel times must be adequately performed. Wavefront scattering by the parametrized structures in a 3D velocity model may then be simulated and its effect on teleseismic travel times investigated.

*Outline of work performed*

Guided by above considerations, the scope of this work is to establish a 3D Alpine velocity model with emphasis on the main crustal structures which is subsequently used to quantify its effect on teleseismic wavefront scattering.

A concept is outlined for 3D lithospheric model construction using different seismic data and information from different seismic methods such as controlled-source and tomographic investigations. A combined use of controlled-source and earthquake data requires a review of their characteristic properties (e.g. frequency content) and resolution capabilities and the determination of seismic structures influencing these seismic data. According to this, a 3D physical parametrization is designed (Fig. 1.1) that allows construction of 3D seismic velocity models by integration of relevant seismic structures such as the crust-mantle boundary and low-velocity sedimentary basins (not indicated in Fig. 1.1). The subsequent modeling of earthquake data such as teleseismic travel

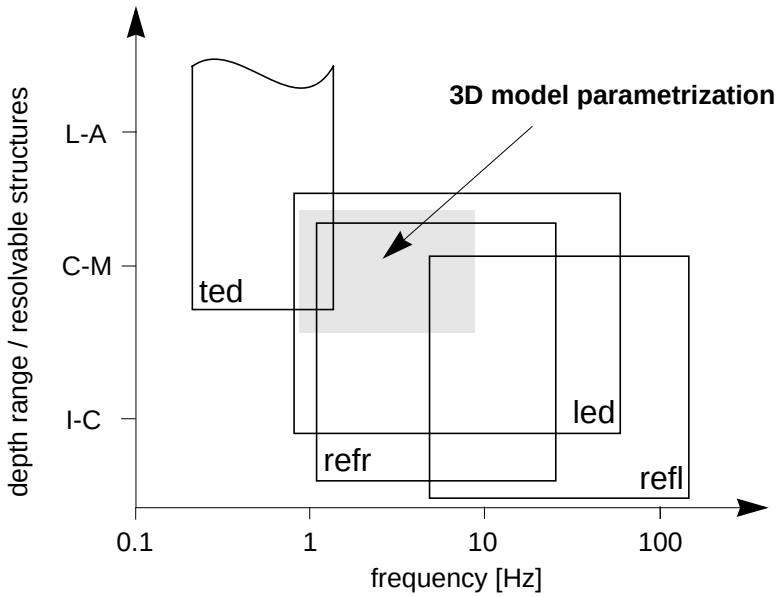


**Figure 1.1** Frequency range and resolvable seismic structures (intra-crustal (I-C), crust-mantle (C-M) and lithosphere-asthenosphere (L-A) velocity discontinuities) for different seismic data and methods such as controlled-source near-vertical (refl) and wide-angle reflection / refraction (refr) data, local earthquake data (led) and teleseismic data (ted). The 3D model parametrization in the present case is designed for the shaded area. It accounts for a wide frequency range of the 'refr' and 'led' data, for the high frequencies of the 'ted' data and for the low frequencies of the 'refl' data.

times requires spatial parameter continuity, i.e. no information gaps are allowed within the model.

A 3D model of crustal and upper mantle P-wave velocity structure is developed using the dense network of controlled-source seismic (CSS) profiles in the Alpine region (for an overview see Giese et al, 1976; Blundell et al. 1992; Heitzmann et al., 1996). The CSS investigations lead to detailed crustal velocity models along 2D profiles, in many cases showing the fine structure of the Alpine crust (see e.g. Fig. 1.2). For construction of a 3D crustal model, however, only the dominant structural features, imaged by and correlated between a great number of profiles, can be used to model reliable, laterally continuous 3D structures. Such a structural feature is the crust-mantle boundary, imaged by both near-vertical and wide-angle reflection data along most profiles (Fig. 1.3). Following the 3D parametrization scheme, the reflecting structural elements from the crust-mantle boundary and, when available, its associated velocities (velocity contrast across the boundary and average crustal velocity) are used to establish the 3D crustal model.

The derivation of 3D seismic models from a network of 2D seismic model information as provided by CSS techniques poses two main problems. The first results from the fact that CSS techniques are 2D methods applied to 3D structures. In predominantly 3D structures, CSS-derived reflecting structural elements must be 3D-migrated in order to account for the structural 3D effects on the 2D seismic data (e.g. Holliger, 1991; Kissling et al., 1996). The second problem is caused by the sometimes large information

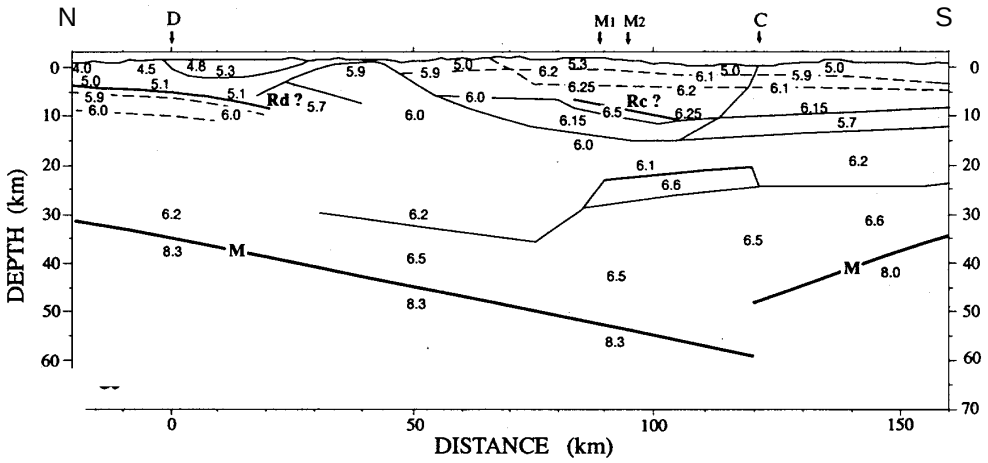


**Figure 1.2** 2D velocity-depth model through the Central Alps derived from EGT seismic refraction data (Ye et al., 1995).

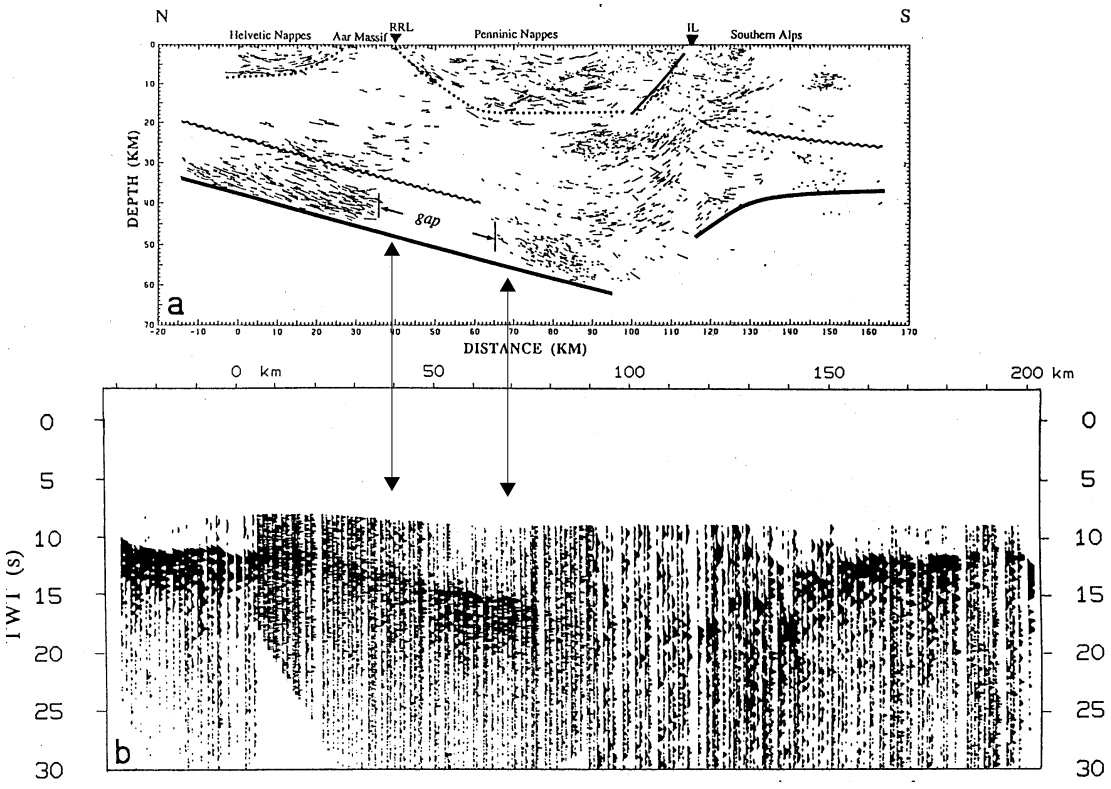


**Figure 1.3** Summary of seismically determined 2D main crustal structure and Moho depth along the NFP20 eastern transect (reproduced from Schmid et al., 1996). Horizontal and vertical scale are the same in both panels. (a) Migrated near-vertical reflections along the eastern traverse and generalized seismic crustal structure derived from orogen-parallel refraction profiles (Holliger and Kissling, 1992). Solid lines indicate the position of Moho, derived from orogen-parallel refraction profiles. (b) Normal-incidence representation of the wide-angle Moho reflections along the EGT (European Geotraverse = eastern traverse across the Swiss Alps) refraction profile perpendicular to the orogen (Valasek et al., 1991). Note, that the gap in the reflectivity signal from the lower crust between 35 and 65 km profile distance in (a) is clearly covered by wide-angle reflection data.

gaps that may appear also in dense CSS-profile networks. These information gaps can be partly overcome by interpolation and extrapolation based on the uncertainty of the data, and on the physical characteristics of the structure to be modeled. Such structural characteristics are, for example, roughness and continuity of seismic interfaces, and Fresnel volumes associated to sampled parameters.

A procedure is developed that performs 3D modeling of 2D controlled-source seismic information considering data quality and Fresnel volumes. It involves 3D seismic interface modeling of CSS-derived structural data, and volumetric modeling of CSS-velocities. A special effort has been undertaken in this study to quantify errors of structural information, such as Moho depths, provided by CSS profiling. These errors define the 'noise level' below which 3D model adjustments become insignificant (Fig. 1.4). Thus, during the modeling process the smoothest 3D model is seeked that best fits the data with the residual data variance equal to the 'noise level'.

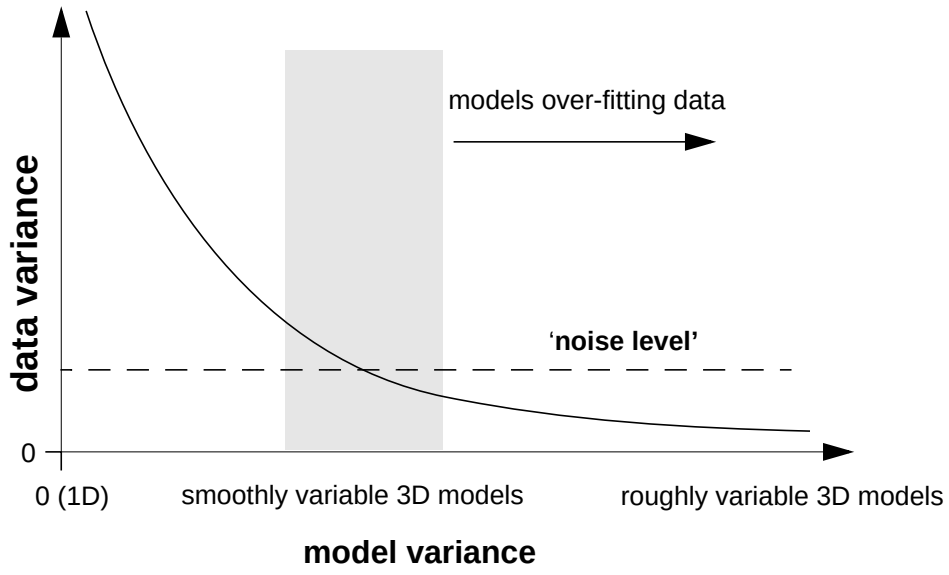


**Figure 1.4** Model variance as a function of data variance. Increasing model variance lead to an increased 3D heterogeneous distribution of model parameters causing a decrease of data variance. The shaded area indicates an appropriate model variance with respect to the 'noise level' of the data.

Although available near-surface and CSS information has been correctly modeled in a 3D context and its proper assemblage was secured by the 3D model parametrization, resulting 3D models may still reveal gaps of measured seismic information. However, required spatial continuity of parameters in resulting 3D models must be assured by relying on a continuous 1D reference velocity model for the region of interest. On the basis of such a reference model for the Alpine upper lithosphere, seismic information is assembled with respect to the 3D model parametrization and a continuous 3D seismic model of the Alpine crust is derived. The resulting 3D model extends from 4° to 12° East longitude and from 43.5° to 49.5° North latitude and reaches to a depth of 70 km.

The teleseismic forward problem consists of a description of the ray path between a teleseismic source location and the surface of the derived local 3D model (Fig. 1.5). In order to meet the aim of a more accurate calculation of teleseismic travel times, incoming teleseismic wavefronts at the base of the local 3D model must be described by spherical travel time fields by relying on the IASP91 model (Kennett and Engdahl, 1991), accounting for varying slowness across the model base. With the correct slowness as starting values, teleseismic first arrival times are computed through the local 3D model from the base to the surface. The forward problem to calculate seismic travel times in the local, strongly heterogeneous 3D velocity model is solved adequately by a finite difference approach to the 3D eikonal equation (Vidale, 1990; Hole and Zelt, 1995).

The computation of teleseismic travel times for the derived 3D model allows to test the model by independent data. This procedure significantly increases the reliability of the derived 3D model. By simulating teleseismic wavefronts for a number of selected azimuths, azimuthal dependence of scattering effects by the 3D Alpine crustal structure is revealed and the effect on teleseismic travel times can be investigated. Teleseismic travel time residuals at the Earth's surface are calculated and compared along 2D profiles with results from recent two-dimensional studies. For future tomographic studies, the crust can be stripped off from the mantle lithosphere and the corrected teleseismic travel time residuals inverted for sub-crustal structure.

The thesis is structured as follows:

Chapter 2 is dedicated to the method developed to construct 3D seismic lithospheric models. It treats the characteristics of different seismic data and methods used to construct the models and describes the 3D model parametrization with respect to these characteristics. The procedure for 3D modeling of 2D seismic data is outlined and the

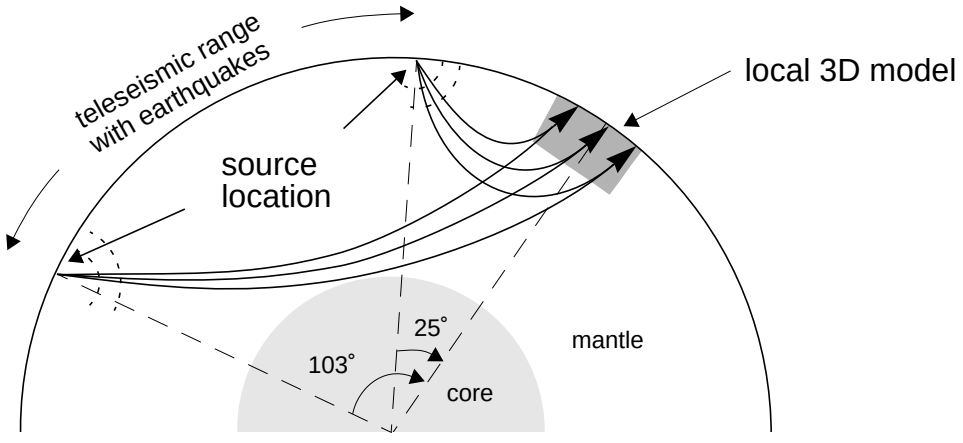


**Figure 1.5** The teleseismic forward problem when using a local 3D velocity model. It requires the description of the complete ray paths between the teleseismic source location and the Earth's surface above the local 3D model derived from controlled source seismic data. An adequate solution to this problem must account for the varying slowness across the base of the local 3D model and for accurate calculation of teleseismic travel times in the local, strongly heterogeneous 3D velocity model.

assemblage of the different seismic information needed for a continuous 3D seismic model is described.

In Chapter 3, the method derived in Chapter 2 is applied to the Alpine region. It starts with a description of the compiled structural and velocity information from the network of Alpine CSS profiles. Using this data base, a horizontally continuous Alpine crust-mantle boundary is established. A simplified 3D Alpine crustal P-velocity model is then assembled by integration of reference data, near-surface information and CSS information with respect to the crust-mantle boundary.

Chapter 4 addresses the teleseismic forward problem and its application to the 3D Alpine model. It first describes a 3D wavefront tracer which is used to forward calculate teleseismic travel times through strongly heterogeneous 3D velocity models. Methods to describe incoming teleseismic wavefronts are treated and teleseismic travel times are computed through the Alpine 3D model designed in Chapter 3 using selected azimuths.

In Chapter 5, a discussion with recommendations for future work is given.

# CHAPTER 2

# 3D SEISMIC LITHOSPHERIC MODEL CONSTRUCTION

The derivation of seismic model parameters ($m^*$) from seismic data such as P-wave travel times ($t$-$t_o$, where $t_o$ is the origin or zero time of the source) is mostly described by an inversion process (Fig. 2.1). The weight attributed to seismic model parameter information (seismic model information or short: seismic information), therefore, depends on the strengths and weaknesses of the seismic investigation method, the quality of measured seismic data, and the strengths and weaknesses of the applied inverse method.

Seismic investigation methods (or short: seismic methods) to derive seismic model parameters are one-dimensional (1D) (e.g. bore-hole measurements), two-dimensional (2D) (e.g. controlled-source seismic methods) and sometimes three-dimensional (3D) (a few tomographic methods). These methods differ in the way seismic waves sample seismic parameters within the volume of investigation. Different seismic methods also sample different seismic parameters like impedance contrasts (e.g. near-vertical reflection methods) or seismic velocity averaged for some volume (e.g. refraction or tomographic methods). In other cases, different seismic methods image the same seismic parameters with waves of different physical characteristics (i.e. frequency content) and origin (e.g. teleseismic and local earthquake methods).

Seismic data are interpreted with the aim to derive values for seismic model parameters in order to describe the natural system (inversion process). Various methods for inversion processes have been developed with respect to the nature of seismic data and methods. Among them are for instance trial-and-error forward methods (e.g. 2D ray-tracing, see e.g. Luetgert, 1988; Ye et al., 1995), Monte Carlo method, or mathematical inversion of large matrices (seismic tomography, e.g. Aki et al., 1977; Nolet, 1987). Forward methods presume model parameters in order to predict data, whereas inverse theory inverts the data to determine model parameters.

Different seismic investigation and interpretation methods lead to systematically unequal seismic models. The reliability and the degree of ambiguity of each seismic model depends on the advantages or disadvantages of the applied method in respect to specific structures. For example, the degree of ambiguity of seismic models derived by controlled-source seismic methods is small, when it is applied to one-dimensional structures. But it is large when the same method is applied to complex three-dimensional structures.

Joint interpretation is mostly performed by combining different seismic data and

methods, and joint inversion of data from different seismic methods is in a few cases possible. However, 3D seismic velocity model construction, by means of combining different seismic data *and* model information, can not be performed by simply merging seismic models that have been individually derived by different seismic methods.

Thus, a 3D seismic velocity model must be constructed by integration of available seismic data and model information that are itself sensitive to and/or imaged by each 2D and 3D seismic method. The model must depict the strength of the included individual seismic information. To achieve these requirements, the methodological considerations, which are described in the following four sections, are:

- Analyzing of strengths and weaknesses of each seismic method and the derived seismic models with respect to the construction of an integrated 3D Alpine seismic lithospheric model (Section 2.1).
- Definition of a 3D seismic model parametrization that accounts for the strengths of the different seismic methods and models and combines the relevant seismic parameter information (Section 2.2).
- Definition of a procedure for 3D modeling of 2D controlled-source seismic model information including re-evaluation and weighting of the seismic information, 3D migration, interpolation, and extrapolation (Section 2.3).
- Assemblage of seismic data and model information with respect to the 3D model parametrization to a 3D, spatially continuous model (Section 2.4).

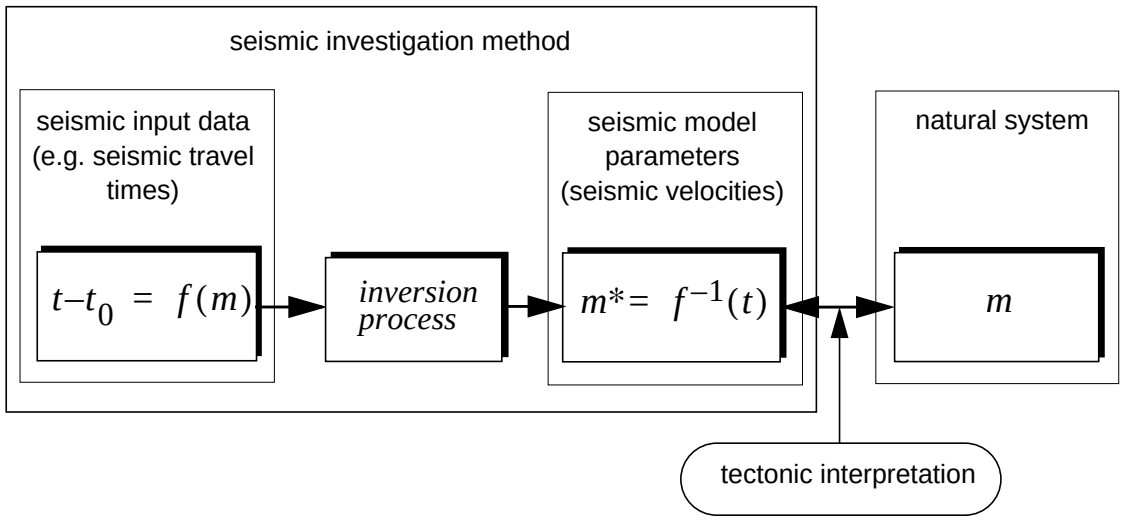


**Figure 2.1** General procedure of seismic investigation methods. Seismic model parameters ( $m^*$ ), as e.g. seismic P-velocities, are derived from seismic P-wave travel times ($t$-$t_0$) by an inversion process. $m^*$ is a description of the natural system $m$ which is the basis for a tectonic interpretation (see text).

# 2.1 Characteristics of Seismic Methods and Seismic Data

Since about the 1950's earthquake seismology, as a method of investigating the thickness and internal structure of the crust, has been largely superseded by seismic refraction and reflection studies using artificial explosions and vibrators (controlled-source seismology or CSS). In the past few years, however, quantity and quality of local and teleseismic earthquake data for the use of structural studies are increasing rapidly. The use of modern receiver techniques and sophisticated computing techniques together with fast computers and large memory access enable us to reveal mantle and crustal structure by teleseismic and local earthquake tomography. Surface-wave analysis allows to image long-period velocity anomalies with a lateral resolution of about 300 km (Snieder, 1988b). Because of their insufficient resolution for Alpine lithospheric structure surface-wave studies are not included in this work. It is beyond the scope of this section to give a detailed overview on the characteristics and capabilities of seismic data and interpretation methods to derive lithospheric structures. This is, however, extensively done by, e.g., Mooney (1989) and Braile et al. (1995). A review of the various seismic methods applied to reveal Alpine lithospheric structure is given by Kissling (1993). In the following, only a short outline of characteristics of these seismic methods (i.e. refraction / wide-angle reflection and near-vertical reflection seismology, teleseismic and local earthquake tomography) is given in terms of source location, spatial sampling, resolution, interpretation methods and derived seismic model information (see Figs. 1.1 and 2.2). An approach to a combined usage of this data and model information is outlined at the end of this section.

## 2.1.1 Controlled-Source Seismic (CSS) Methods and Data

Seismic refraction, wide-angle reflection, and near-vertical reflection techniques using artificial sources are powerful methods to illuminate the subsurface structure. The high resolution and high reliability generally attributed to 2D structural models derived with these seismic techniques (e.g. Banda and Mooney, 1982) are based on the knowledge of source coordinates, origin time, and, in principle, source function. Mostly, CSS data are collected along profiles and subsequently interpreted by 2D methods within the source-receiver plane (Kissling et al., 1996). Thus, no information about the off-line (out-of-plane) structure can be obtained from a single profile unless the profile is part of a profile network. The problem of 3D migration accounting for 3D effects by in-line and off-line migration of reflecting structural elements is discussed in more detail in Section 2.3.

*Refraction and wide-angle reflection method*

Travel paths in long-range refraction experiments are predominantly sub-horizontal due to the large distance between source and receivers relative to the depths of the interface being mapped. Beyond the critical distance, refracted head waves travel within a seismic layer and tend to smooth the velocity structure of that layer along their ray paths.

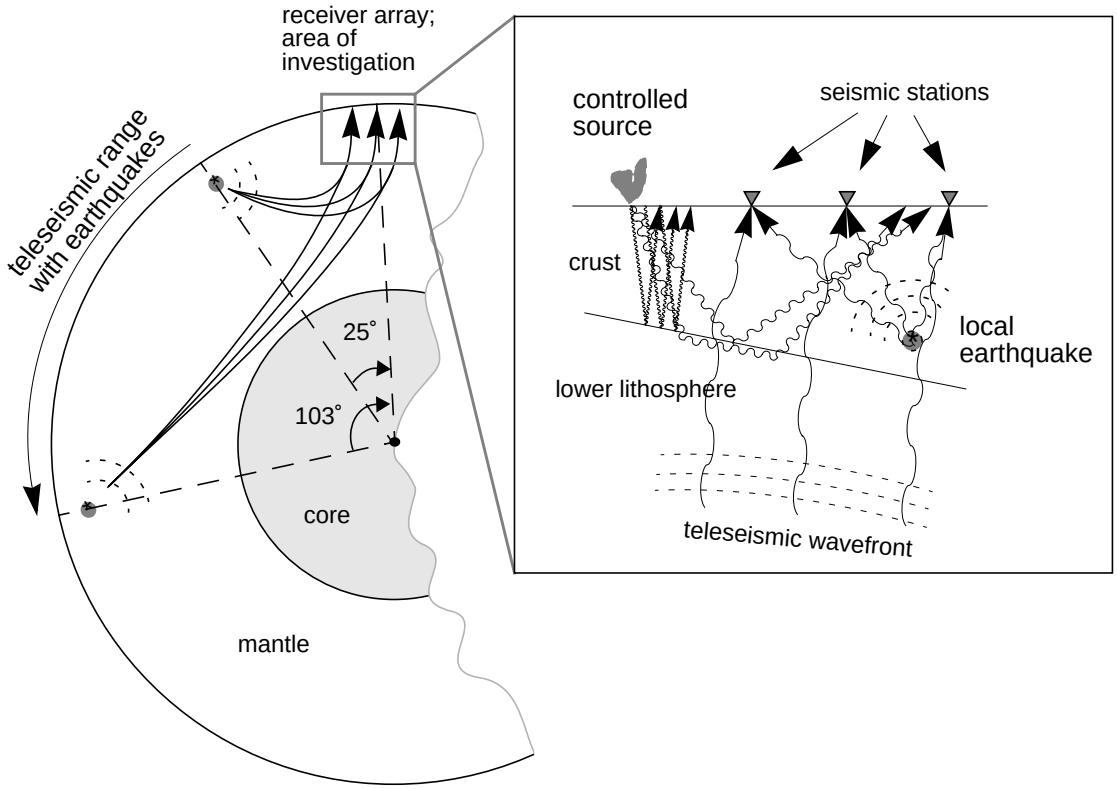


**Figure 2.2** Teleseismic, local earthquake and controlled-source seismic data and their source locations. Differing wavelengths are indicated on wave paths.

Wide-angle reflection and refraction ray paths are both sensitive to horizontal and vertical seismic velocity gradients. The frequency of refraction and wide-angle reflections covers the range between 1 and 20 Hz. Lower crustal reflections have a typical frequency of about 5 Hz.

1D and 2D interpretation methods are used to model seismic wide-angle and refraction travel time data. The Herglotz-Wiechert 1D-method (Herglotz, 1907; Wiechert, 1910) inverts continuous travel time curves originating from diving waves into a one-dimensional velocity-depth structure. Although several authors (e.g. Meissner, 1973; Hinz et al., 1976) have shown that the Herglotz-Wiechert inversion can be adapted to interpret entire crustal wide-angle profiles, in a strict sense the method is applicable for diving waves only and is as such always limited by the possible existence of low-velocity zones. However, constraints can be placed on the existence of low-velocity zones.

The $x^2$- $t^2$ method (see e.g. Sheriff and Geldart, 1995) is an excellent 1D-method to analyze wide-angle reflected waves in general. $x^2$- $t^2$ analysis of PmP travel time branches allows a fair estimate of the average crustal velocity and thickness.

All 1D interpretation methods assume a homogenous velocity distribution along the profile. Early interpretations of seismic wide-angle data used these 1D methods to derive final velocity models by interpolating between the derived 1D velocity structures below the shotpoints (e.g. Egloff, 1979). Since no control on the ray paths can be ob-

tained, 1D interpreted wide-angle data do not depict reflecting structural elements at the location where they are actually covered by seismic rays. Nevertheless, 1D interpretations are still valid approximations in regions of an 'a priori' known or accepted homogeneous (1D) velocity structure. The Herglotz-Wiechert inversion and the $x^2$- $t^2$ method are often used to construct initial 1D velocity models for subsequent ray-tracing in 2D.

Modern 2D ray-tracing techniques (e.g. Cerveny et al., 1977; Luetgert, 1988) compute seismic rays and travel times through a predefined 2D velocity structure. In a trial-and-error forward modeling procedure a velocity model is obtained for which the calculated and observed travel times fit best. 2D ray-tracing of wide-angle data implicitly in-line migrates the reflecting structural elements and allows to depict their ray-covered part on a seismic interface below the profile. However, 3D effects from off-line structure can not be accounted for unless the profile is part of a profile network.

One of the most important approximations of the ray-tracing methods involves the replacement of wave theory by ray theory. This so-called high-frequency approximation causes the unrealistically high theoretical resolution of the ray-traced final velocity models. For uncertainty estimations of the modeled structural elements Fresnel volume consideration (Lindsey, 1989; Cerveny & Soares, 1992) must be carried out by replacing the infinitely thin ray by a ray tube with small diameter that is inversely proportional to the wave frequency (Woodward, 1989, Baumann, 1994).

Interpretation techniques based on inversion theory have recently been developed for controlled-source seismic travel time data to invert for 2D crustal velocity structure (Zelt and Smith, 1992; Hole and Zelt, 1995). Parsons et al. (1996) inverted first-arrival times for upper crustal structures which then have been used to forward calculate secondary reflected arrivals. The non-linear characteristic of travel time inversions require a starting model that is 'close' to the true model.

Although this interpretation methods can be used for both, P-wave and S-wave velocity modeling, only few studies (e.g. Waldhauser, 1992) on S-wave travel times have been carried out. Because of the limited amount of available S-velocity models in the Alpine region, this work concentrates on 2D P-velocity models for 3D model construction.

*Near-vertical reflection seismic method*

The principle difference between refraction and reflection methods is that for near-vertical reflections, the distance between source and geophones is smaller relative to the depths of the interface to be mapped, whereas it is larger or comparable to the depths for refraction. Consequently, travel paths in reflection experiments are predominantly near-vertical, whereas for refraction experiments, they are predominantly horizontal. Such vertical incident reflections are pronounced where the impedance contrast is sharp across the discontinuity. They illuminate the structure in terms of its reflectivity pattern with a resolution which is determined by the dominant wavelength of the incident signal, i.e. a few hundred meters (15-25 Hz) for deep crustal reflection profiling. Reflectivity patterns reveal structural information such as geometry, sharpness of discontinuities, internal heterogeneity within layers and in rare cases the polarity of ve-

locity changes.

The data are usually processed to filter out or attenuate noise relative to the reflected energy based on characteristics that distinguish them from each other, and the data are displayed in a form suitable for interpretation. 2D in-line migration of the original time-sections (Holliger and Kissling, 1991) and approximate 3D migration (Valasek, 1992) can only be performed by using the independently derived refraction velocities.

*Combined CSS methods*

Refraction and reflection seismic methods differ in their imaged seismic parameters. The refraction seismic method images the subsurface in terms of velocity whereas the reflection seismic method is most sensitive to impedance contrasts. Holliger and Kissling (1991) used the along-strike average refraction velocity information as input to migrate the line drawings along reflection traverses, which run transverse to the Alpine structure. Valasek (1992) used the velocity information from three longitudinal and one perpendicular Alpine refraction profiles to establish a simplified three-layer 3D crustal model for the Central Alps. With this refraction-based velocity model he depth-migrated the reflection data of individual near-vertical reflection profiles which were transversely oriented to the Alpine structure.

The complementary nature of reflection and refraction seismic methods allows a combined usage of the two techniques (Mooney and Brocher, 1987). A unified 2D acoustic image along the EGT (Holliger and Kissling, 1992) was obtained by an appropriate projection of the unmigrated reflection images onto the refraction seismic profiles of the EGT (see Fig. 3.1 for location) and subsequent depth migration.

For a reliable combined use of information from controlled-source seismic data, both refraction and reflection, uncertainty estimations are necessary because of the broad range of data quality and interpretation methods (see Section 3.1).

### 2.1.2 Teleseismic Earthquake Data

Teleseismic data, by definition, are obtained from earthquakes at greater distances ($\Delta > 25^{\circ}$) from the receiver array (Fig. 2.2). Source coordinates, origin time and source function are, compared to controlled-source data, difficult to obtain exactly and are normally derived by solving the coupled hypocenter-model parameter problem in the focal area of the event. However, for relative teleseismic travel time studies the absolute event parameters are mainly used for phase correlation. Due to the long distance of travel of teleseismic signals and the generally positive velocity gradient within the mantle (except for the asthenosphere), wavefronts entering the lithosphere are assumed to be plane with ray incident angles of about $\pm 20^{\circ}$. Regional or local earthquakes, occurring outside the area of investigation up to a distance of $25^{\circ}$, generate signals that are strongly influenced by the source parameters and by 3D effects of the upper-mantle velocity structure. Therefore, the plane-wave assumption is not valid for regional earthquakes.

Teleseismic rays sample the seismic parameters of the upper-lithosphere three-dimensionally and the parameter values (i.e. velocity), therefore, are derived at the spa-

tially correct location. Due to relatively long wave-lengths of about 10 km (Fig. 1.1) and the small angle of incident of rays entering the lithosphere, teleseismic travel time data, in general, have a resolving power limited to relatively large crustal structures compared to controlled-source seismic data. While the horizontal resolution of teleseismic data can be improved by a dense station network, the vertical resolution of near-surface structures will remain poor.

In regions with complex lithospheric structure the incident angles between teleseismic rays and major discontinuities (e.g. lithosphere-asthenosphere boundary, crust-mantle boundary) are in the range of ±50° which causes deflection of incoming rays. Therefore, non-horizontal interfaces with sharp velocity gradients strongly influence teleseismic travel times (as shown e.g. by Guyoton, 1991) although teleseismic data are not able to resolve these velocity discontinuities over the appropriate distance of velocity change (i.e. thickness of discontinuity).

Assuming, that teleseismic travel time residuals are primary an effect of velocity anomalies below the recording site, available 'a priori' information of crustal thickness can be used to map the lithospheric thickness (e.g. Baer, 1980). Quantitative 3D velocity structure (although with variable reliability) can be obtained by inversion of the teleseismic travel time residuals (e.g. Aki et al., 1977, Ellsworth, 1977). Iterative forward-/inverse-problem solving procedures approach a possible solution (seismic tomography, e.g. Nolet, 1987). The resulting models show velocity differences (relative to a predefined reference or start model) that average the velocity structure within blocks of a dimension equal to the resolving power. First studies on teleseismic tomography used the ACH method (Aki et al., 1977) that involves the inversion of large matrices. The forward problem is solved approximatively within the volume of investigation. The ACH method assumes a homogeneous velocity distribution which is a valid approximation only for very few regions (with pre-dominantly 1D lithospheric structure). Tests with modern 3D ray-tracers for heterogeneous velocity media (e.g. Steck and Prothero, 1991) reveal the necessity for the use of such forward algorithms (Weiland et al., 1995), although they are much more time consuming. Iteratively updating travel paths based on the updated velocity model lead to a better resolved final model in the tomographic procedure.

### 2.1.3 Local Earthquake Data

Ray paths from local earthquakes can show a broad range of azimuths and incident angles that depend on event depths and geometry of the receiver array (Fig. 2.2). For direct arrivals, the seismic velocities are three-dimensionally sampled. In the case, where the structural target is below the event, the method becomes two-dimensional (reflected rays) and the problem of migration is posed. Local earthquake wave-lengths are about 2 km for the lower crust and therefore similar to that of controlled-source refraction seismic methods (Fig. 1.1). Wave-lengths in the mantle may exceed 10 km. With a sensitivity to velocity inhomogeneities larger than 2 km for the crust and larger than 10 km for the mantle, local earthquake data (LED) are used to image upper lithospheric structure. The advantages of LED over teleseismic data to investigate upper lithospheric

structures lies in the higher frequency content and the great variation of the angle of incidence compared to the narrow angle for teleseismic data.

Local earthquake tomography (Aki, 1977; Thurber, 1981) is a 3D interpretation method used to resolve the 3D velocity structure below the recording site. Since local earthquake sources are situated within the volume of study (Fig. 2.2), deriving the event parameters (event location and origin time) becomes a crucial part in the modeling procedure. Unlike the inversion of teleseismic travel times, the inversion of local earthquake data for three-dimensional velocity structure requires the simultaneous solution of the coupled hypocenter-model-parameter problem. This leads to absolute model velocities whereas teleseismic tomography can only determine relative velocity variations across horizontal layers.

### 2.1.4 Combination of CSS Methods and Earthquake Tomographic Methods

The CSS data base, described later in this work, is derived from a large network of Alpine CSS profiles with available interpreted seismic profiles and 1D and 2D seismic models. For this case, therefore and for the above-mentioned problems with CSS travel time inversions, a simultaneous inversion (joint inversion) of controlled-source and earthquake seismic data for 3D velocity structure is not an adequate procedure. However, joint inversions of geophysical data require compatible structural sensitivity for both methods, which is not always existent. Instead of jointly-inverting controlled-source and earthquake data, the CSS model information must be used to construct a 3D seismic model for subsequent modeling of earthquake data. Thus, the problem of combination lies not in raw data merging, but in merging seismic data and seismic model information by analyzing the characteristics of each method (as done previously) and outlining their common sensitivity to the imaged seismic parameters.

The major disadvantage of CSS data over earthquake data recorded on a network is the fact that CSS profiling is a 2D method applied to 3D structures. Whereas earthquake signals travel from the hypocenter directly to the recording stations through the volume of investigation, controlled-source signals are generated at the surface and most of their energy is reflected and refracted before it is recorded. The exact spatial reflector position can not be determined by seismic profiling since effects of nearby structures on the ray path cannot be quantified unless the 3D structure close to the profile is ‘a priori’ known. Therefore, when combining 2D and 3D data and methods, the 2D seismic information must be re-modeled in a 3D context. In regions with a dense CSS profile network, 3D effects can be accounted for by 3D migration of the 2D seismic information (see Section 2.3).

The broad range of seismic wavelengths to deal with requires to define the structural features such that all methods are sensitive to or can be imaged by them.

The major structural feature (i.e. seismic discontinuity) within the upper lithosphere of most parts on Earth is the crust-mantle boundary. Although not in the same

way, this seismic interface is imaged by all methods, depending on the source-receiver configuration. With the use of large controlled sources, wide-angle reflections (PmP) and refractions (Pn) on long-range refraction profiles and near-vertical reflections on reflection profiles from the crust-mantle boundary can be observed. Teleseismic wavefronts are scattered due to the large velocity contrast at that interface. Reflections and/or deflections of local earthquake energy are generated at the crust-mantle boundary, depending whether the earthquake occurs in the crust or in the upper mantle. For first-arrival studies of intra-crustal earthquakes, the crust-mantle boundary does not affect the data. Intra-crustal structures, such as the upper/lower crust discontinuity, have velocity contrasts much smaller compared to that of the crust-mantle boundary. Because of the difficulty in imaging and tracing them as lateral continuous interfaces over larger regions and their less significant influence on teleseismic wavefronts, intra-crustal structures are not parametrized in this study.

Average crustal velocities are obtained by CSS data as well as by earthquake data. As outlined previously, refraction seismic studies tend to smooth the velocity structure along their ray path in the sub-vertical and sub-horizontal direction. Thus, average crustal velocities can be derived from PmP phase observations or calculated from ray-traced seismic models (see Section 2.2 and 3.1). Due to the resolution capabilities of teleseismic earthquake data, tomographic results average crustal velocities within rather large model blocks in sub-vertical direction, with a theoretical horizontal resolution of about 20 km (depending on array configuration), which in some studies is in the range crustal thickness. Tomography with local earthquake data averages crustal velocities within model blocks which represent the 3D crustal velocity field with a resolution depending on the available amount of data and their frequency content. Rays from controlled sources, local and teleseismic earthquakes all sample seismic velocity, but, due to different wavelengths, not necessarily the same parameters. Teleseismic rays and refracted rays from long-range refraction profiles even tend to travel perpendicular to each other (Fig. 2.2). Thus, the combination of crustal travel time data and teleseismic travel time data involves the mixing of predominantly horizontal and vertical raypaths through the crust. Combining these two ray paths permit to identify possible effects due to spatial anisotropy within the crust. Their joint interpretation in a isotropic model, however, may cause a significant source of errors when anisotropic crustal structure is present. For a seismic layer with rays travelling faster in horizontal direction than in vertical direction, teleseismic arrival times calculated on the base of an isotropically CSS-derived velocity structure are consistently early.

Sedimentary basins, with thicknesses of several kilometers, exhibit strikingly lower velocities compared to that of the crystalline basement. These near-surface velocity inhomogeneities are visible on refraction profile data as variations of travel times from diving waves (Pg) and reflections from the basement. Earthquake arrival times show delays for seismic stations situated on sedimentary basins. In addition, rays from local near-surface earthquakes are deflected at the sediment-basement transition.

The integration of these variable seismic parameters (i.e. surface velocity, lower-crustal, upper-mantle, and average crustal velocity and their depth distribution) in a 3D lithospheric velocity model must be realized by designing an appropriate 3D lithospheric

model parametrization, which will be discussed in the following section. Model parametrization includes also the proper definition of grid parameters, which result from the resolution of seismic travel time data discussed that are used either for 3D model construction or for subsequent modeling through the established model.

## 2.2 3D Lithospheric Model Parametrization

The main problem of model parametrization is to design the 3D model such that it serves the purpose of combined studies with different seismic methods. The parametrization must allow the construction of a 3D seismic model by integration of seismic information from controlled-source and earthquake tomographic methods. Subsequent modeling of earthquake travel times through that model must be possible. Seismic parameters involved in this work are P-velocities, location of reflecting structural elements and confidence attributes. Additional seismic parameters such as S-velocities, densities, or Q-values can be added for other purposes than travel time calculations (e.g. geodynamic modeling or visco-elastic calculations).

Experimental seismic data that are used for 3D model construction are mostly derived in a spherical coordinate system. The spherical coordinates are transformed to cartesian coordinates by applying a short-distance conversion (SDC) with respect to a fixed geographical point in the center of the study area. The spherical character of the real Earth model is taken into account using the Earth flattening approximation (Müller, 1973) for depth, velocity and travel time transformation.

Solutions to the forward problem of earthquake travel time calculations for a 3D velocity field are provided by a finite-difference approach (Vidale, 1990; see Chap. 4). For reasons of accuracy, wavefront tracing by finite-difference methods requires an evenly gridded input model ($hx = hy = hz$). A 3D velocity grid represents velocity structures by velocity values assigned to each grid node. Gaps of velocity information within the 3D model are not allowed. The 3D grid simulates spatial continuity by linear interpolation between the grid nodes and provides an efficient medium to computation and visualization. A 3D grid parametrization is a more realistic representation of the Earth than that of block or refraction layer models, although the Earth shows evidence for discrete layers and relatively abrupt velocity discontinuities. If present, velocity discontinuities (seismic interfaces) are represented as velocity gradients with a sharpness depending on the vertical and/or horizontal grid spacing.

In general, spatial resolution for a 3D velocity field is directly proportional to the seismic wavelengths travelling through that medium. Grid dimension must, therefore, be chosen fine enough to allow for structural details resolvable by seismic methods such as controlled-source seismic refraction and reflection profiling. Seismic discontinuities need to be adequately represented by velocity contrasts over the required vertical distance (i.e. thickness of transition zones). Thus, definition of grid parameters strongly depends on the lateral velocity variation in the study area and the interfaces (i.e. first or second order) to be resolved.

Based on the discussion in Section 2.1.4, the corresponding seismic model parameters

are (see Fig. 2.3a):

- Crustal thickness, resp. depth of the crust-mantle boundary ($z_{cr}$)
- Surface layer thickness ($z_{srf}$) accounts for low-velocity sediments
- Surface P-velocity ($vp_{srf}$)
- Average crustal P-velocity ($vp_{acr}$)
- Lower-crustal P-velocity ($vp_{lcr}$)
- Upper-mantle P-velocity ($vp_{uma}$)
- Mantle P-velocity ($vp_{ma}$)

The location of structural elements or the thickness of seismic layers are called structural parameters, the associated velocities velocity parameters.

These seismic parameters are used to parametrize the vertical lithospheric velocity distribution at each vertical grid line. A three-layer model is constructed that consists of a near-surface layer (A), middle and lower crust (B) and uppermost mantle (C)

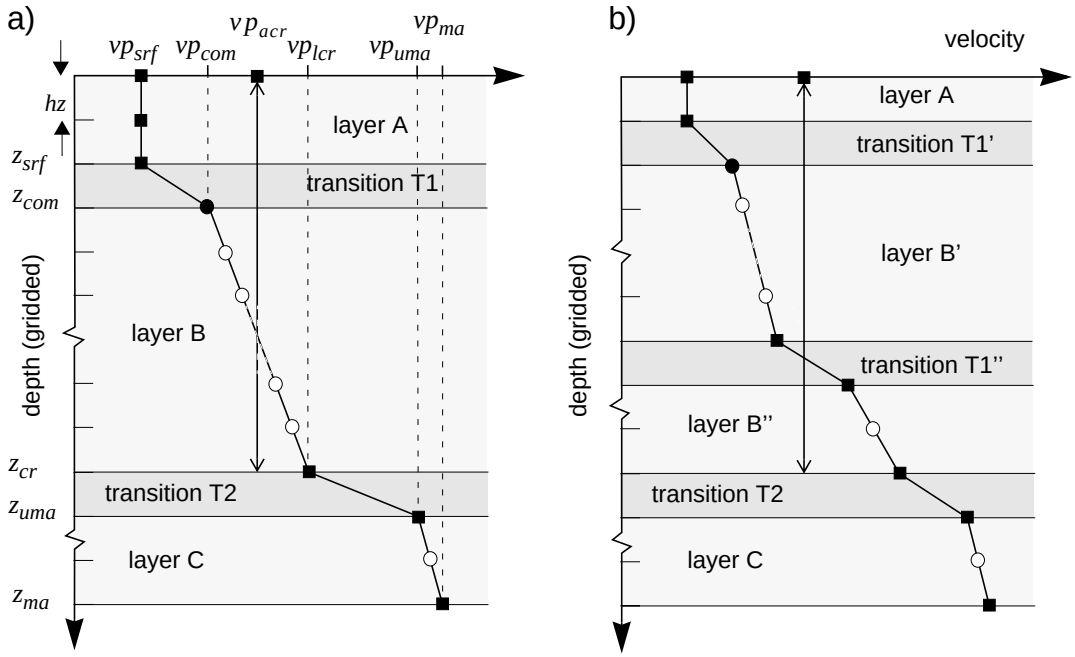


**Figure 2.3** a) Parametrization of the velocity-depth function by a three-layer model A-T1-B-T2-C as used in this work. Layer A: near-surface layer. Transition T1: transition zone. Layer B: middle and lower crust. Transition T2: transition zone simulating the crust-mantle boundary zone. Layer C: upper mantle. ■ Seismic parameters defined by the parametrization scheme which must be derived from seismic data. Structural parameters: $z_{srf}$ = near-surface layer thickness; $z_{cr}$ = crustal thickness; $z_{ma}$ = depth limit of model. Velocity parameters: $vp_{srf}$ = surface velocity; $vp_{acr}$ = average crustal velocity; $vp_{lcr}$ = lower crustal velocity; $vp_{uma}$ = upper mantle velocity; $vp_{ma}$ = mantle velocity. ● Computed compensation velocity $vp_{com}$ (see text). **o** Linearly interpolated values.
b) Possible refinement of the parametrization scheme shown in (a) by integration of an intra-crustal interface T1'', such as the transition from upper to lower crust. Thus a four-layer model results.

(Fig. 2.3a). The seismic interface between layer B and C (i.e. the crust-mantle boundary) is modeled with a velocity transition zone (T2). $z_{cr}$ corresponds to the top of the transition zone T2. The thickness of T2 is by default the distance between two neighboring z-grid nodes (*hz*) in order to approximate best the characteristics of first-order discontinuities. Linear interpolation between surface velocity and lower-crustal velocity not necessarily fits the average crustal velocity. A transition zone T1 between the near-surface layer A and the crustal layer B is introduced, with the top at $z_{srf}$ and a default thickness corresponding to the vertical grid dimension *hz*. A new, artificial, velocity parameter, called compensation velocity ($vp_{com}$), at the bottom of T1 at depth $z_{com}$, is used to retain the average crustal velocity without violating the velocity parameters $vp_{srf}$ and $vp_{lcr}$. Linear interpolation is performed between $vp_{com}$ and $vp_{lcr}$.

Average velocities of layered media (e.g. controlled-source seismic 2D models) can be derived by averaging over the velocities of the individual layers, or by averaging over the travel times a ray uses in each layer or transition zone (see e.g. Sheriff and Geldart, 1995). Assuming straight ray paths and crustal structure consisting of *n* parallel, horizontal layers of velocity $v_i$ and thickness $\Delta z_i$, the average velocity derived by a first alternative results in:

$$vp_{acr1} = \frac{\sum_{i=1}^{n} (v_i \cdot \Delta z_i)}{\sum_{i=1}^{n} \Delta z_i}, \qquad (2\text{-}1)$$

or by a second alternative:

$$vp_{acr2} = \frac{\sum_{i=1}^{n} \Delta z_i}{\sum_{i=1}^{n} (\Delta z_i / v_i)} . \qquad (2\text{-}2)$$

Although both types of average seismic velocities are calculated later in this work from controlled-source seismic 2D models (see Section 3.1), only the second alternative (travel-time based) is used to parametrize the seismic model. The use of the 3D seismic model for teleseismic travel time calculations requires average crustal velocities that are most appropriate with respect to travel times of teleseismic rays travelling nearly vertical through the sub-horizontal crustal structure.

The compensation velocity must be derived from the given seismic parameters. Relating average crustal travel time *t* to the average travel times in each of the three layers *A*, *T1* and *B* yields (see Fig. 2.3):

$$t(A + T1 + B) = t(A) + t(T1) + t(B) \qquad (2\text{-}3)$$

or (see Equation 2-2)

$$\frac{(z_A + z_{T1} + z_B)}{vp_{acr}} = \frac{z_A}{v_A} + \frac{z_{T1}}{v_{T1}} + \frac{z_B}{v_B} \qquad (2\text{-}4)$$

with $z_A = z_{srf}$ ,

$z_{T1} = z_{com} - z_{srf} = hz$ ,

$z_B = (z_{cr} - z_{com})$,

$v_A = vp_{srf}$ ,

$v_{T1} = (vp_{srf} + \boldsymbol{vp_{com}})/2$ ,

$v_B = (\boldsymbol{vp_{com}} + vp_{locr})/2$ .

Solving Equation 2-4 for $\boldsymbol{vp_{com}}$, the quadratic equation

$$a \cdot vp_{com}^2 + b \cdot vp_{com} + c = 0 \qquad (2\text{-}5)$$

with $a = \frac{z_{cr}}{vp_{acr}} - \frac{z_{srf}}{vp_{srf}}$,

$b = a \cdot (vp_{srf} + vp_{locr}) - 2 \cdot (hz + z_{cr} - z_{com})$,

$c = (vp_{srf} \cdot vp_{locr} \cdot a) - 2 \cdot (hz \cdot vp_{locr} + z_{cr} \cdot vp_{srf} - z_{com} \cdot vp_{srf})$,

is obtained from which compensation velocities are calculated.

Adjusting the values of individual seismic parameters (e.g. replacing reference by experimental values) will affect the compensation velocity. This is shown in Figure 2.4 where each seismic parameter value is varied and the effect on the compensation velocity is shown.

It must be noted that the velocity gradient of the first transition zone T1 is not related to the real structure but is needed to adjust the individual layer travel times of the model to the average crustal travel time. It is possible, that crustal structures with pronounced low velocities in the middle crust will even produce negative T1 gradients in order to compensate a comparable normal lower crustal velocity. This can produce artificial deflections of local earthquake and teleseismic waves when hitting the bottom of T1. However, considering that teleseismic rays hit the sub-horizontal T1 nearly vertical and that the surface layer is relatively thin (thickness of sedimentary basins), the effect on travel times due to geometrical deflection at the T1 transition is negligible.

The described 3D model parametrization allows to store velocity and structural information in a 3D grid model. It shows great flexibility in updating existing (already parametrized) interfaces and in integrating new interfaces (e.g. the Conrad discontinuity,

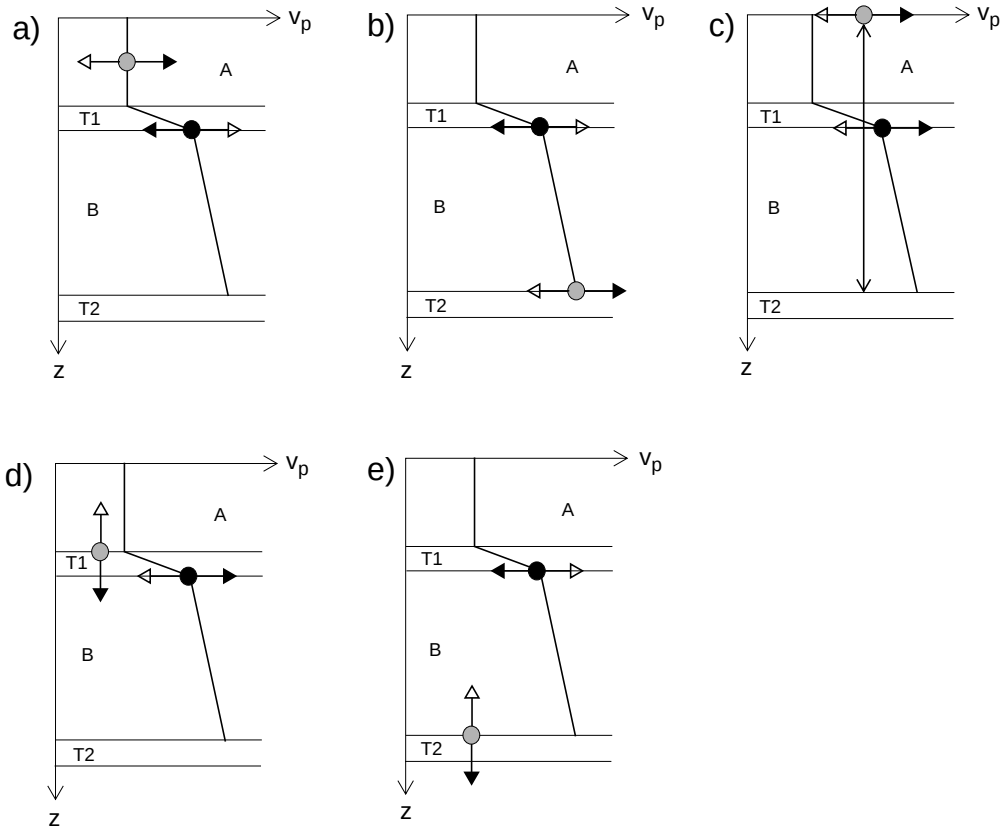


**Figure 2.4** Variation of individual velocity (a-c) and structural (d, e) parameters (gray) for the crust and its effect on the compensation velocity $vp_{com}$ (black). Other seismic parameters were held fixed. Variations of $vp_{srf}$ (a), $vp_{lcr}$ (b), $vp_{acr}$ (c), $z_{srf}$ (d), and $z_{cr}$ (e).

and/or the lithosphere-asthenosphere boundary) by using the same parametrization scheme. Integration of new intra-crustal interfaces is possible with extension of the A-T1-B layer model to a A-T1'-B'-T1''-B'' layer model (see Fig. 2.3b) and an update of Equation 2-4 with average velocity terms for the additional transition zone and layer. Thus, stepwise refinement of the established average crustal velocity model or extension to lithospheric scales is possible.

The parametrization scheme used in this work (Fig. 2.3a), averages velocities over crustal-scale structures which makes it compatible with the characteristics of controlled-source, local and teleseismic earthquake data (see Section 2.1). Before applying this parametrization scheme to available seismic information in order to construct 3D seismic models, i.e. assigning velocity values to a given grid, it must be assured that the seismic information is derived from seismic data at their proper location in the 3D space. This being so for most results of earthquake tomographic studies, this is not the case for controlled-source seismic data which are derived by 2D techniques and interpreted by 2D, or even 1D, methods. The 2D seismic model information from controlled-source seismic investigations must, therefore, be carefully located in the 3D surveyed area or space.

## 2.3 3D Modeling of 2D Controlled-Source Seismic Data: Migration and Interpolation

The previous section treated the 3D model parametrization that outlined the purposes and definition of a 3D seismic model for a combined use of different seismic methods. In this section, it is shown, how controlled-source seismic (CSS) profiling, as one of this methods, is used to derive 3D seismic P-velocity models (3D models).

CSS investigations imply for each profile a 2D interpretation (see Section 2.1). 2D interpretations are usually presented as 2D seismic models $m=f(d,z)$, with $m$ as varying P-velocity in the vertical plane beneath the profile $d$ (see e.g. Ye et al., 1995). For a network of CSS profiles, approximations can be made to derive 3D models by interpolation between the 2D seismic models.

Classical fence diagrams of networked CSS profiles are a convenient approach to give a 3D view of the available 2D structures (e.g. Giese, 1976). Missing structural and velocity information along transects are determined by projection and interpolation (fences). Between the fences, no connection is made which yields a simple perspective view. Different from this, Valasek (1992) and Hitz (1995) derived 3D models by mathematical interpolation between and extrapolation from migrated reflectors of near-vertical reflection profiles. Their method is adequate only for dense networks of high-quality near-vertical reflection profiles with independently derived migration velocities from crossing refraction profiles. This is, however, rarely the case even in areas such as the Alpine region with dense CSS profile networks.

In the following, a method is outlined to construct digital 3D seismic models on the base of 2D seismic information of various reliability that is derived from an arbitrary network of CSS refraction and reflection profiles. The 3D model parametrization, as outlined in the previous section, implies two key postulates with respect to which the modeling procedure must be developed:

- 3D models must characterize the crustal velocity distribution by their average P-velocities for larger or smaller volumes as resolved by CSS methods at proper locations.
- 3D models require continuous seismic information without information gaps (spatial parameter continuity).

The first postulate requires a simplification of the CSS-derived 2D models by extracting the required parameters for 3D model construction. These parameters are structural information such as the depth locations of reflecting structural elements of, e.g., the crust-mantle interface, the respective velocity information (i.e. velocity gradient across the interface and average crustal velocity), and a related parameter uncertainty. The derivation of these parameters from CSS models is outlined in Sections 2.3.1 and 2.3.2. A consistent data base of CSS information and quantification of the spatial uncertainty associated with this data base is a key requirement for 3D modeling procedures since the search for model simplicity strongly depends on the range of uncertainty at each discrete point. For description of a complete data base of CSS data in the Alpine region see Section 3.1 and Appendix A.

The second requirement (i.e. spatial parameter continuity) must be fulfilled *after* integration of all parametrized seismic information in a 3D seismic grid model. 2D CSS information must be presented in 3D by trying to minimize information gaps. This involves two main problems: Migration and interpolation. Migration is the process to restore 3D structures from 2D CSS-derived reflecting structural elements (or reflectivity patterns). Effects from nearby structural variations significantly influence the geometry of 2D models, i.e. spatial locations of reflecting structural elements. Velocity values, however, do not change significantly. The problem of 3D depth migration of structural elements considering in-line and off-line migration is broadly discussed by e.g. Holliger and Kissling (1991), Sénéchal and Thouvenot (1991), Kissling et al. (1996). In this work, a method is outlined that performs 3D migration of CSS-derived reflectors following the geometrical trend of that interface (migration surface) in the vicinity of the structural element. The migration surface is obtained by interpolation of the CSS-derived reflectors.

The need for maximizing spatial parameter continuity and the 3D migration procedure requires interpolation between the discretely observed CSS data. As mentioned in Section 2.1, CSS methods - in contrast to tomographic methods for earthquake data - are sensitive to first-order velocity discontinuities which produce the location of reflectors defined by the velocity gradient at that interface and to the average velocity along the reflected ray path. Interpolation processes for reflectors differ from those for velocity data. Reflectors are modeled to obtain the topography of a reflecting interface (surface interpolation) whereas velocity data must be spatially modeled based on the averaging character of CSS velocities in model space (volume interpolation):

$$z^{obs}(x, y) \rightarrow \text{Surface Interpolation} \rightarrow z^{cal}(i, j)$$

$$v^{obs}(x, y, z) \rightarrow \text{Volume Interpolation} \rightarrow v^{cal}(i, j, k)$$

where ($i$,$j$,$k$) represents the gridded model space. 3D modeling of CSS model information, therefore, includes interface modeling and velocity modeling (with respect to the corresponding interface) which are separately treated in Section 2.3.1 and 2.3.2. Figure 2.5 shows the general structure of the 3D modeling procedure for CSS model information.

Section 2.3.1 describes the 3D interface modeling concept and procedure to derive seismic interfaces from unevenly sampled, imperfect structural information derived from CSS models. Two interpolation processes are needed. The first (initial) interpolation process produces a migration surface with respect to which 3D migration of the CSS-derived reflectors is performed. Subsequently, the 3D migrated reflectors are interpolated in order to obtain the simplest interface satisfying the structural data within the spatial uncertainty. In our case, the modeling concept is designed for structural data belonging to the crust-mantle boundary in order to obtain a smooth, locally weighted interface that shows no information gaps (horizontal continuity) and includes vertical offsets when required according to certain criteria.

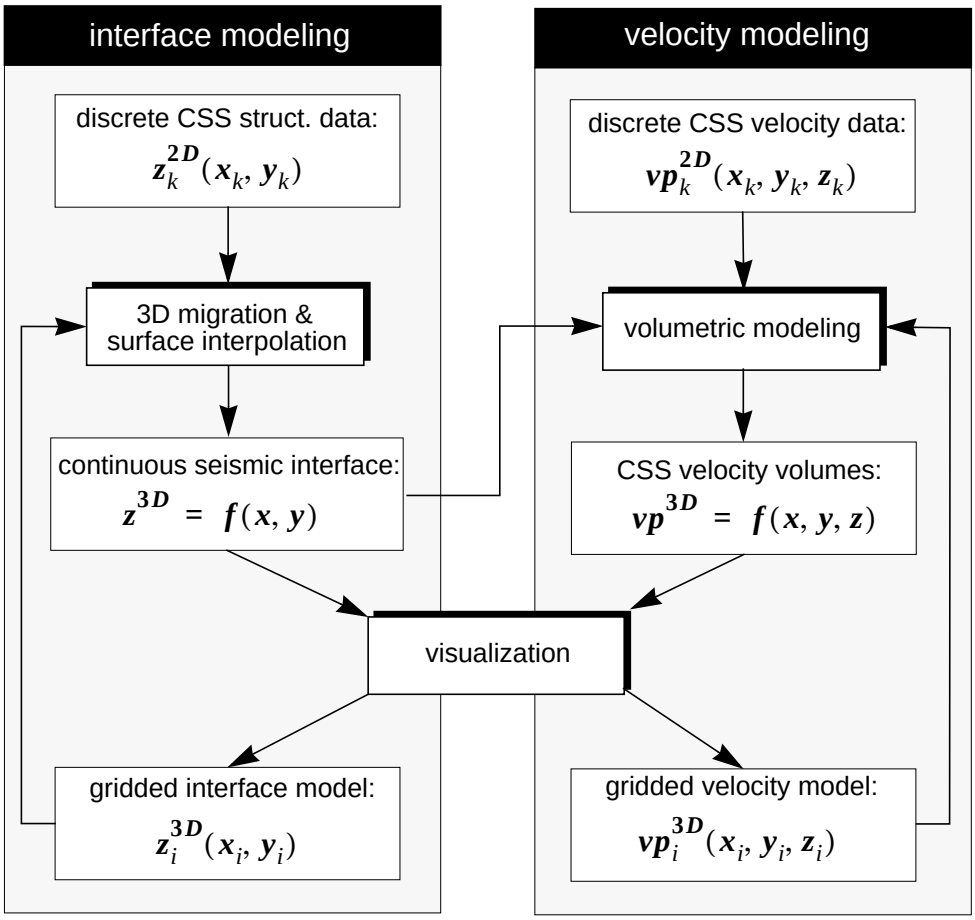


**Figure 2.5** General structure of the procedure developed for 3D modeling of CSS 2D model data as described in Section 2.3. See text.

Section 2.3.2 describes volumetric modeling by CSS velocity information. Seismic velocities within the crust generally vary strongly and behave often discontinuously in any direction (intra-crustal thrusting). In case of loosely networked profiles, real 3D interpolation would not properly fill the sometimes large information gaps. Therefore, instead of 3D interpolation of the observed velocity values, the individual velocity parameters are in a first approach assigned to their physical volume of influence with respect to the interface they belong to. The problem of CSS velocity information gaps is helped by integrating the volumetric CSS velocity information in a pre-defined lithospheric reference model, which is discussed later in Section 2.4.

### 2.3.1 Seismic Interface Modeling from Unevenly Sampled, Imperfect Data

*Concept and procedure*

Seismic interfaces, such as the crust-mantle interface, have a range of complexity from

smooth planes to intensely folded and broken structures. These characteristics of seismic interfaces must be accounted for when designing the modeling concept in general and the interpolation routine in particular. In the following the concept is presented to model structural data describing the crust-mantle interface. The crust-mantle interface is not only the most important structural feature for 3D model construction, but it is the best resolvable velocity discontinuity for CSS methods in most regions of the world. The 3D interface modeling procedure as described below, however, can be applied to other interfaces as well, after minor adaptations to the specific interface characteristics.

The aim of any modeling process is to obtain the simplest model that satisfies the observed data. Hence, seismic interface modeling is performed with the aim to obtain the smoothest interface that fits observed structural data within the spatial uncertainty. The most striking characteristic of the crust-mantle interface expressed by the strong velocity gradient from about 7 to 8 km/s - compared to intra-crustal interfaces - is its existence as seismic horizon and base of the continental crust (Braile and Chiang, 1986) almost everywhere. This leads to modeling of a crust-mantle interface that features no gaps between the observed structural data (horizontal continuity), but, if required, may show vertical offsets. Tectonic and geodynamic implications of this conceptual considerations are discussed in Chapter 3 in connection with the Alpine crust-mantle interface.

Observed structural data are small parts of a seismic interface (reflectors) at spatial locations that are obtained from correlation and modeling of continuously observed reflected and refracted phases on CSS reflection and refraction profiles. A reflector is built-up by linear segments (reflector segments) along that reflector. Reflector segments (see Fig. 2.6) are defined by two segment endpoints ($x_1$,$y_1$,$z_1$) and ($x_2$,$y_2$,$z_2$) (structural depth points, black spheres in Fig. 2.6) in model space with linear interpolation between them and discretized for computational purposes by structural depth points along these segments (white spheres in Fig. 2.6). Excluding the end members along a reflector, two adjoining reflector segments always have a structural depth point in common. Because of their straight line representation, reflector segments can be described by simple linear equations (see Fig. 2.6):

$$z = z_1 + d \cdot s + \Delta z, \qquad (2\text{-}6)$$

where $d$ is the inclination (or dip) of the segment and $s = (x_2 - x_1) + (y_2 - y_1)$. The first derivative of Equation 2-6 yields the dip of the reflector segment:

$$d = \frac{\delta(z_1 + d \cdot s \pm \Delta z)}{\delta s} + \Delta d. \qquad (2\text{-}7)$$

Reflectors may consist of several adjoining reflector segments. In the following, the term reflector is used when describing the continuously imaged part of an interface and reflector segments when referring to the linear pieces with constant dip along that part.

In order to obtain a consistent data base of structural information from a network of CSS profiles, their quality is quantified by application of a weighting scheme which

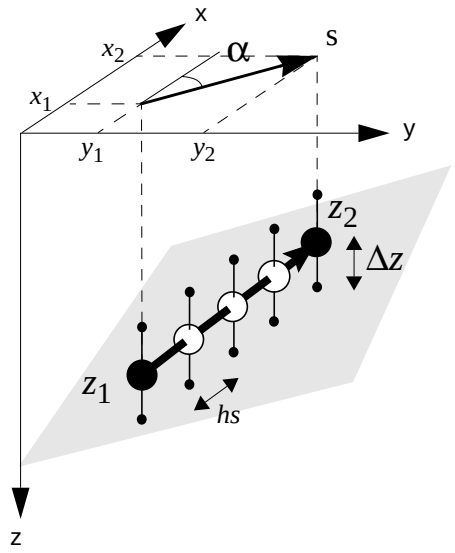


**Figure 2.6** Description of a reflector segment (bold vector) defined by the two endpoints of the element (large black spheres $x_1$,$y_1$,$z_1$ and $x_2$,$y_2$,$z_2$ and structural depth points). The reflector segment is discretized for interpolation by structural depth points (white) along the reflector segment between the two element endpoints, with *hs* as the sampling distance. Depth error limits are indicated. The interface, to which the reflector segment belongs, is represented by the gray area. α= azimuth of reflector segment. Reflectors may consist of several such reflector segments representing dip variation along that reflector.

attributes a weighting factor to each derived reflector segment that summarizes the quality of specific properties for each profile (Baumann, 1994; see Section 3.1 in this work). Weighting factors are transformed to depth error estimations ($\Delta z_i$) considering Fresnel volumes.

Reflectors from CSS models need to be 3D-migrated in order to account for 3D effects of nearby structures on these reflectors. As mentioned previously, the 3D migration process uses an initial interpolation of the CSS-derived reflectors in order to obtain the general trend (migration surface) of the seismic interface. Thus, the interpolation procedure is first described and the 3D migration taken up later.

Horizontal interface continuity (i.e. no interface data gaps are allowed), as demanded by the modeling concept for the crust-mantle interface, is achieved by interpolation between the reflectors. Any interpolation process of imperfect data is ambiguous in a way that more than one solution exists fitting all data within their uncertainties. In order to find the simplest (smoothest) interface, surface properties must be defined that allow to differentiate between possible interfaces.

**Roughness** and **continuity** are the two surface properties to characterize interfaces and to quantify simplicity with respect to observed data. **Roughness** quantifies interface depth variations with respect to a reference interface and is a direct measure for the complexity (or curvature) of a continuous interface (see below and Fig. 2.8). **Continuity** describes an interface in terms of its vertical offsets. Continuity *along* reflectors is given by correlation of continuously observed phases reflected from a specific seismic interface. Phase correlation between profiles leads to the identification of reflectors which belong to the same interface. Continuity *between* the reflectors, however, can not be presumed in general. A vertical **discontinuity** (offsets) occurs when seismic interfaces are interrupted by, in case of the crust-mantle interface, crustal-scale thrusting or block faulting. In some cases, a vertical offset between reflectors is revealed by discon-

tinuously observed phases reflected from the same interface. Interface offsets can then be assumed, when ray-traced reflectors or reflectivity patterns show an abrupt (relative to the general roughness) change in depth relative to their depth error. Interface continuity can be quantified by the length of interface edges along the offsets (i.e. shortest is most continuous).

Reflectors do not allow interface depths to be predicted outside their imaged position. This leads to a broad range of possible interfaces which differ in complexity in terms of roughness and/or continuity (see Fig. 2.7). Assume a series of possible interfaces that fit all reflectors within their uncertainties. One end of the spectrum is marked by an interface that is simplest in its continuity, but, as a consequence, most complex in its roughness (line A in Fig. 2.7). The high roughness value results from the attempt to interpolate between large vertical offsets of possibly thrusted reflectors in order to obtain a spatially continuous interface. The other end of the spectrum marks an interface that is simplest in its roughness and, as consequence, features vertical offsets (line B in Fig. 2.7). This interface shows several plane (smooth) sub-interfaces that are discontinuous at those locations where the corresponding interpolated interface would lie outside the depth uncertainty. The task is now to find an interpolated interface with the highest continuity and least roughness (equally weighting continuity and roughness) with respect to the structural data and their errors (line C in Fig. 2.7).

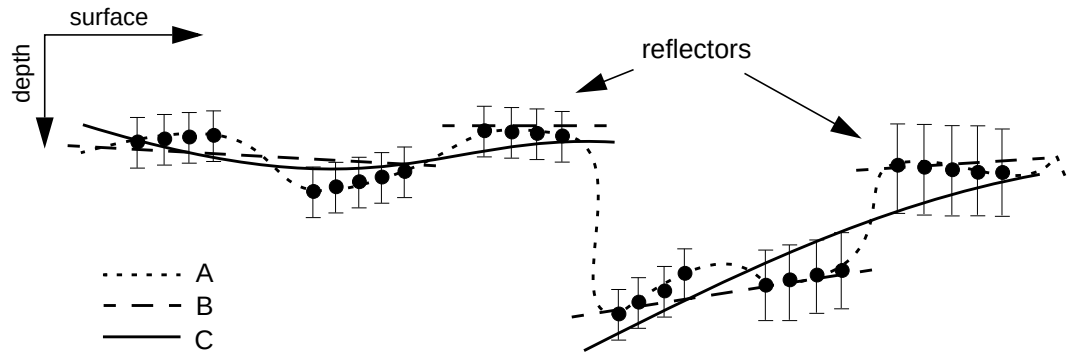


**Figure 2.7** Range of possible interpolated interfaces (with varying roughness/continuity) to correlate reflectors (in this case consisting of one reflector segment, see Fig. 2.6) within their uncertainty. A: Rough interface with exact data point fit. B: Straight-line interface that exhibits several vertical offsets (roughness zero for the individual sub-interfaces). C: Smooth interface that accounts for data uncertainty and shows vertical offsets when required.

The following sub-sections discuss interface roughness, the applied interpolation algorithm and the 3D migration process in more detail. Finally, the procedure for 3D interface interpolation is outlined.

*Interface roughness*

Roughness of a scattering surface depends on the incident scattered wave (Ogilvy, 1991). Thus, roughness may only be used as the property of a seismic interface in relation to a given wavelength. The dominant wavelength that is used to resolve a seismic interface defines the sampling rate of that interface (e.g. grid size for numeric interface representations). The term roughness of a curve (2D) or a surface (3D) is a value for 'simplicity' (see Fig. 2.8). It can be mathematically described as an areal average of second derivatives of an analytically defined surface or a weighted sum of local depth variations with respect to a reference surface.

CSS refraction methods have a resolution that leads to structures with (locally) smooth interfaces (represented by smooth lines in 2D structural models) over longer distances. Roughness along observed reflectors is expressed by the variation of depths and dips of their reflector segments (Eqs. 2-6 and 2-7). Interpolation of these reflectors may lead to interfaces that on average represent the roughness observed along the reflectors. In case of locally concentrated high roughness values on the interpolated interface, interface offsets must be expected.

Local roughness for numerically represented surfaces is in the following quantified by applying the 2D finite-difference Laplacian operator $\Delta$ (see Lees and Crosson, 1989) over the interface. Let $z_{i,\,j}$ be discrete depth values attached to the nodes of an even grid describing a horizontally continuous interface. The grid consists of *imax* grid nodes in *i*-direction and *jmax* grid nodes in *j*-direction. Roughness can then be described as local depth variations by

$$RGH = \sum_{i=2}^{imax-1} \sum_{j=2}^{jmax-1} \left(4z_{i,\,j} - z_{(i-1),\,j} - z_{i,\,(j+1)} - z_{(i+1),\,j} - z_{i,\,(j-1)}\right)^2 . \qquad (2\text{-}8)$$

Equation 2-8, however, allows to compare roughness values *RGH* for interfaces of equal size only (see Fig. 2.8).

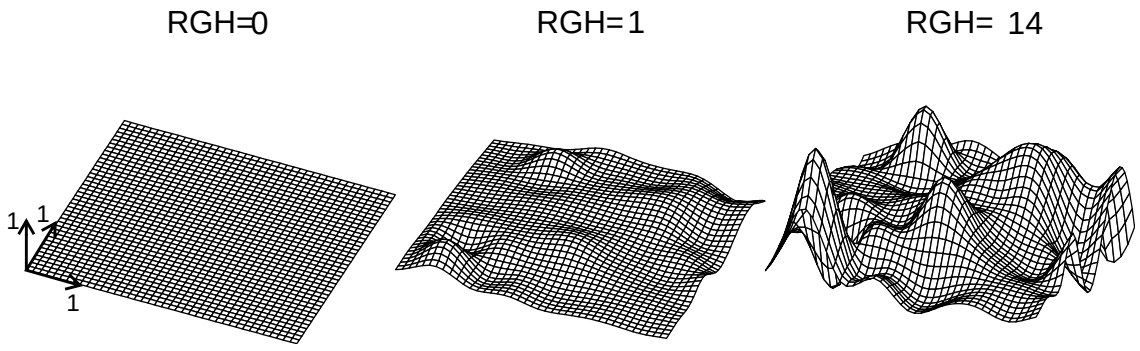


**Figure 2.8** Values for local (short-wavelength) surface roughness (*RGH*) derived for increasing rough surfaces by applying the 2D finite-difference Laplacian operator $\Delta$ over the grid points. See text.

In the following, an interpolation algorithm is described that allows to control surface roughness when interpolating discretely observed structural depth points.

*Interpolation algorithm*

In general, the technique for interpolation should depend on the nature of the data, the nature of the phenomena to be treated and the characteristics of that technique (Lancaster and Salkauskas, 1990). CSS profiling produces non-uniform and inhomogeneous data distribution (see Section 3.1). Any interpolation procedure should exclude numeric instabilities in these cases. Since the shape of seismic interfaces is not of an analytical form a numeric approach to interpolation of structural depth points must be chosen. Finally, the interpolation algorithm must be able to handle interface roughness through an appropriate interpolation parameter. The interpolation algorithm described here mainly follows Klingelé (1972) (see also e.g. Lancaster and Salkauskas, 1990).

The numerical solution to interpolation of unevenly distributed experimental data points is carried out in two stages. The first stage computes local parabolas with their apices lying on a coarse, two-dimensional grid with even grid spacing. For each grid point ($x_p$,$y_p$) to be interpolated, data points ($x_i$,$y_i$) within a predefined area of influence (circle with radius $R$) are used (Fig. 2.9).

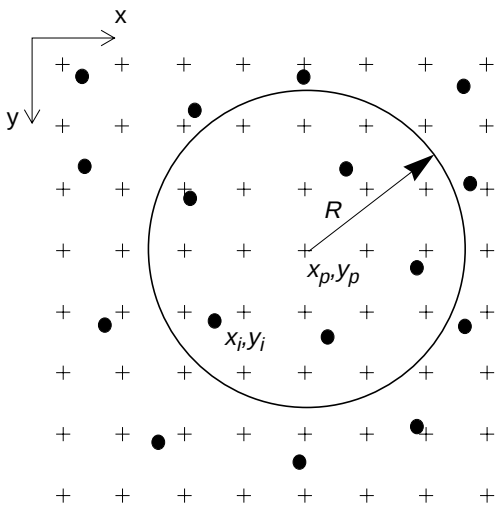


**Figure 2.9** Sketch depicting parameters for interpolation of one grid point ($x_p$,$y_p$). R: radius of circle of influence; ($x_i$,$y_i$): experimental point; + grid points; • experimental points. (After Klingelé, 1972).

The data points are weighted depending on the distance to the center of the circle (i.e. the grid point to be interpolated) by

$$W_i = \left( \frac{R^2 - d_i^2}{d_i^2 + \eta^2} \right)^N , \qquad (2\text{-}9)$$

with $d_i^2 = (x_p - x_i)^2 + (y_p - y_i)^2$ . $\eta$ is used to prevent numerical instabilities for data points very close to the grid point to be interpolated.

The initial parabola is described by a second-order polynomial:

$$F(x_p, y_p) = ax_r^2 + bx_r y_r + cy_r^2 + dx_r + ey_r + f \qquad (2\text{-}10)$$

with $x_r = x_i - x_p$ and $y_r = y_i - y_p$.

*F(0,0)* is the apex of the parabola and corresponds to the interpolated value at ($x_p$,$y_p$). The polynomial order is not changed during the interpolation procedure.

If $\varepsilon_i$ is the difference between the experimental value $g_i$ and the interpolated value we can write

$$\varepsilon_i = g_i - F(x_i, y_i) \; . \qquad (2\text{-}11)$$

Since we are interested in a surface fitting the experimental data best with respect to the distance from the center of the interpolation circle we can write:

$$\sum_i (W_i \cdot \varepsilon_i^2) = min \qquad (2\text{-}12)$$

Solving Equation 2-12 produces a system of linear equations from which the unknown parameter in Equation 2-10 (the apex of the parabola) is determined. The interpolated surface is the location of the apices of all local parabolas.

The second stage of the interpolation process allows the refining of the derived squared grid. It is performed by a line by line interpolation followed by an interpolation column by column on the previously obtained grid. This twofold uni-dimensional interpolation uses a spline under tension whose variations of the stress factor allows an interpolation ranging from broken line to a classical bi-cubic spline (Cline, 1974). The fine grid has a size of *NI (K-1)* by *NJ (K-1)*, where *NI* and *NJ* are the dimension of the large scale grid, and *K* is the refinement factor.

The advantage of this interpolation algorithm is in having control of the shape of the interpolated surface through to the two parameters *R* and *N* (see Equation 2-9), which define the local parabolas. *R* describes the circle of influence of the neighboring data points and *N* the weighting of distant data values. *N* is also known as the roughness (or smoothing) factor. Both parameters together describe the shape of the local parabola and with its apices the shape of the final interpolated surface. It is obvious that a higher weight of the more distant data values (large *N*) will affect the interpolated value in the apices of the local parabola more than a lower weight (small *N*). *N* therefore controls the curvature of the local parabola and with it the curvature (or roughness) of the final interpolated surface. *N* is related to the roughness parameter *RGH* (see Equation 2-8). Using *RGH* instead of *N* allows roughness quantification that is independent from the

interpolation algorithm and therefore better reproducible.

Attention has to be paid to the distribution and density of the available interface data (i.e. reflectors) when choosing grid and interpolation parameters. Depending on the chosen grid spacing (*hg*) and the weighting factor of the reflector (see Section 3.1), sampling distance (*hs*) of structural depth points along the reflector segments (see Fig. 2.6) is determined by

$$hs = \frac{hg}{C \cdot wght}, \qquad (2\text{-}13)$$

*wght* weight of reflector segment (between 0.1 and 1)
*C* constant factor

In Section 3.2 (modeling the Alpine crust-mantle interface), *C* is determined to be around 3 which lead - for an arbitrary chosen grid spacing of 6 km - to a sampling distance of 2 km for structural depth points along a highly weighted reflector segment. The search radius must be chosen with respect to the tectonic setting and the density of available data. Interface roughness is determined by the interface modeling process as described below.

It is of great interest to interpolate interfaces to the edge of available data (e.g. in case of interface thrusting). Because the interpolation algorithm requires a homogenous distribution of values within the search radius, numeric instabilities occur when interpolating grid points at interface edges. Thus, artificial supporting points are placed beyond the interface boundaries to prevent numeric instabilities (Fig. 2.10). Supporting point values are chosen to linearly extrapolate the geometry of the area near the interface edge.

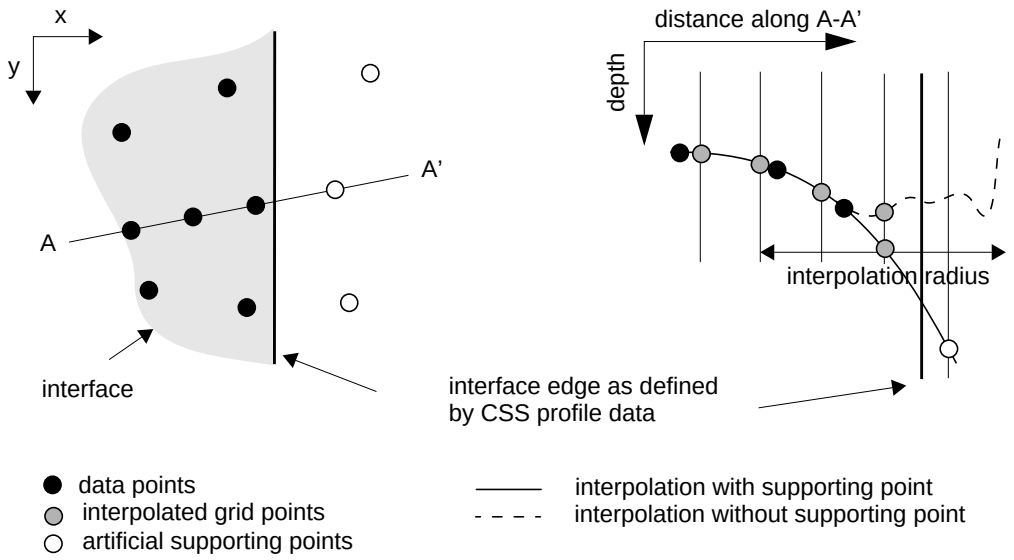


**Figure 2.10** Introduction of supporting points to prevent numeric instabilities at interface edges (see text for explanation).

*3D migration*

CSS are basically 2D techniques applied to 3D structure. 2D interpretations of CSS data imply in-line migration of reflectors. Off-line location of these reflectors, however, remains ambiguous. In case of networked profiles ambiguity can be overcome by using additional structural information from nearby profiles.

For the case of a homogeneous 2D cylindrical structure, reflectors from transverse CSS profiles in-line migrate along the profile in direction of the up-dipping interface (in-line migration) (Fig. 2.11). For longitudinal profiles, reflectors lie outside the vertical plane beneath the profile and migrate perpendicular to the profile (off-line migration).

1D interpretation methods generally project reflector depths to locations below the shot point. In this work, reflectors derived by 1D interpretations have been re-located at half the distance of phase observation below the profile (assuming lateral homogeneous structure) and, therefore, have been approximately in-line migrated. Using 2D interpretation methods, in-line migration of reflectors along the profile can be properly carried out by migration algorithms applied to near-vertical reflection data (e.g. Mayrand et al., 1987; Holliger and Kissling, 1991) or 2D ray-tracing methods applied to wide-angle reflection data (e.g. Ye et al., 1995). None of the methods reveal off-line migration by individual profiles on their own.

Off-line migration of reflectors from longitudinal profiles can be revealed by in-line migrated reflectors from transverse crossing profiles (Fig. 2.12, Ye et al. 1995). Off-line migration of reflectors from oblique crossing profiles can not exactly be determined, since the migration vector can not be correctly separated into an in-line and off-line component.

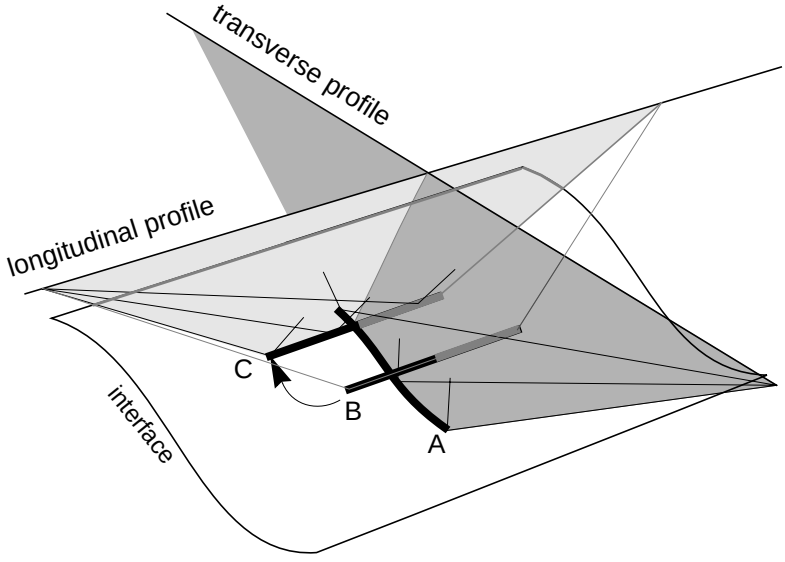


**Figure 2.11** Two perpendicularly crossing refraction profiles, running transverse and parallel to a cylindrical (2D) structure. A, B and C are reflectors belonging to the interface (white area). A: In-line migrated (2D interpreted) reflector derived from the transverse profile. B: In-line migrated reflector derived from the longitudinal profile. This reflector is not correctly located in its off-line position. C: Off-line migration of the in-line migrated reflector B to the correct location outside the profile plane.

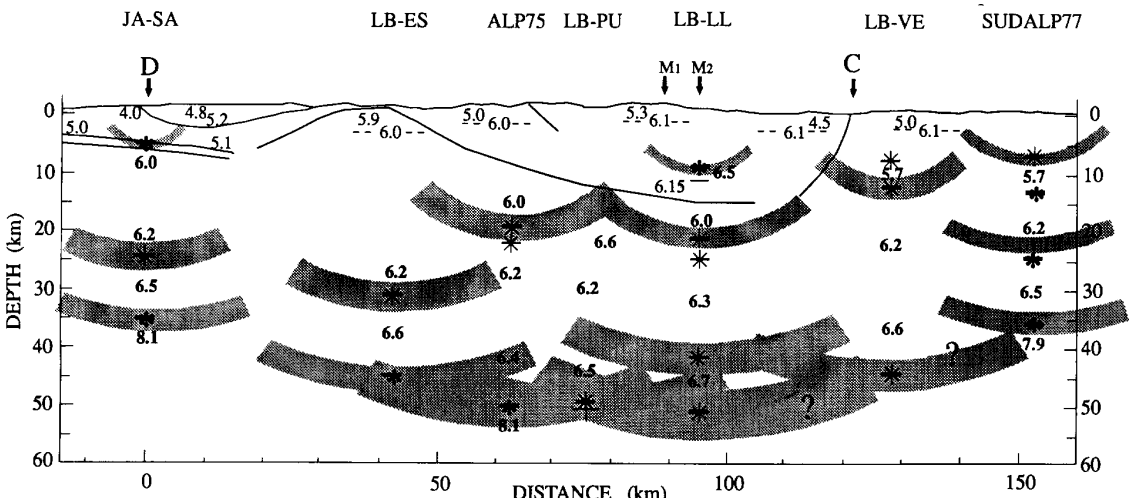


**Figure 2.12** Off-line migration (shaded area) of reflectors from longitudinal profiles in the Alpine region constrained by in-line migrated reflectors from transverse profiles (After Ye, 1992; modified by Kissling, 1993).

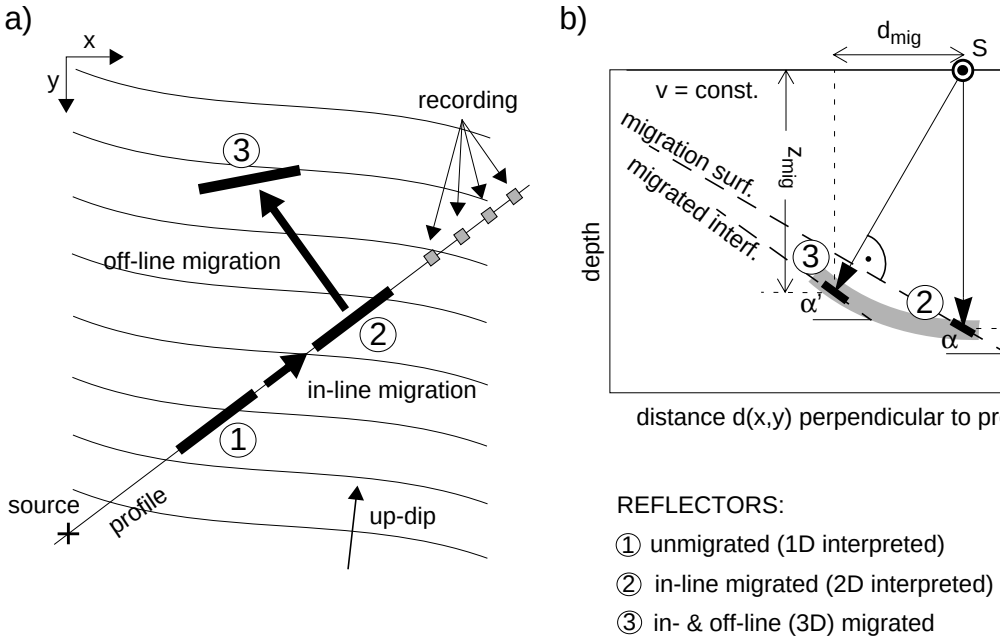


**Figure 2.13** a) 3D migration procedure. Separation of 3D migration vector into an in-line and off-line component. In-line migrated (2D interpreted) reflectors (2) are off-line migrated perpendicular to the profile in the direction of the up-dipping interface. Interface geometry in the vicinity of the element to be migrated is revealed by initial interpolation of reflectors belonging to the same interface (migration surface).
b) Schematic illustration of the off-line migration process in two dimensions (see text). Profile direction (S) perpendicular to drawing plane.

The 3D migration process, that is applied to the reflectors in the interface modeling procedure, separates the 3D migration vector for all reflectors into an in-line and off-line component (see Fig. 2.13a). In the case of reflectors derived from oblique profiles, the so derived 3D migration is an approximation to the real 3D migration. Due to the smaller weight given to oblique profiles (see Section 3.1), the migration error for these profiles will, therefore, be in the range of the depth uncertainty of corresponding reflectors. Separation of the 3D migration vector into an in-line and off-line component is a good approximation only for smooth interfaces, such as most parts of the crust-mantle interface. In the vicinity of each reflector, the interface can then be considered as plane and the separation of the migration path is reasonable.

The case of a CSS network with perpendicular crossing along-strike and transverse profiles to accurately determine off-line migration of in-line migrated along-strike structures is rare. More often loosely networked CSS profiles exist. In this case, information about the approximate 3D geometry of the interface in the vicinity of the reflector to be migrated must be taken from surrounding reflectors. This 3D geometry is derived by an initial interpolation between the in-line migrated reflectors (migration surface, Fig. 2.13b). 3D migration is performed with respect to the migration surface.

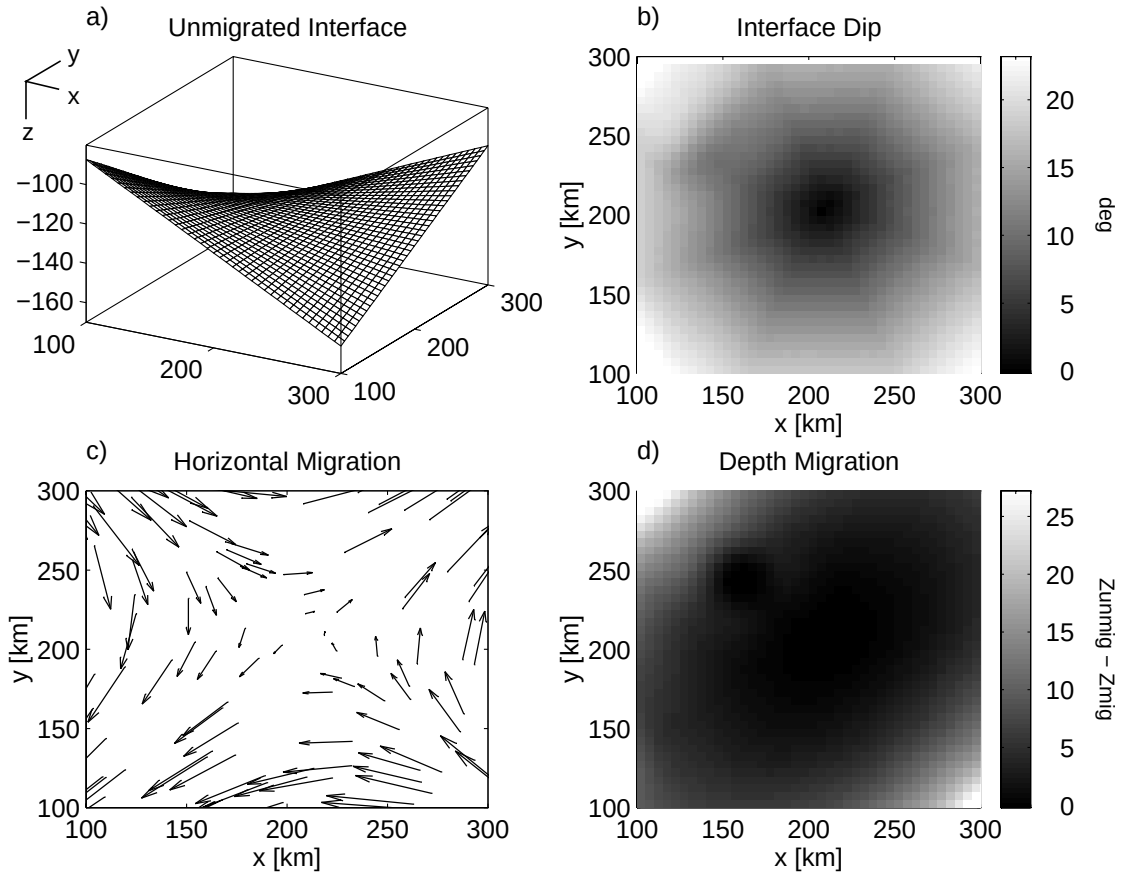


**Figure 2.14** Numeric results for the 3D migration algorithm. a) Unmigrated saddle-like interface. b) Variation of interface dip. c) Horizontal migration paths of structural depth points in direction of largest interface dip. d) Depth migration of structural depth points.

2D-interpreted, and therefore properly in-line migrated, reflectors are off-line migrated perpendicular to the profile in up-dipping direction (see Fig. 2.13a). 1D-interpreted and approximately in-line migrated reflectors are migrated in direction of the up-dipping migration surface directly. The location of the 3D-migrated reflector is found by searching for vertical incidence of the ray on the migration surface (Fig. 2.13b). The velocity in the model is assumed to be constant (ray-theoretical migration) and, therefore, effects from intra-crustal velocity inhomogeneities on the migration path are neglected. Results of the numeric solution to the 3D migration process are shown for 1D-interpreted structural depth points on a saddle-shaped interface (Fig. 2.14).

Migration surfaces, derived by interpolation of in-line migrated reflectors, differ from the corresponding migrated interfaces mainly in terms of their depth location. However, more important for the migration process than the exact depth location of the migration surface is the surface geometry (roughness) that controls the migration path of the ray. Rough surfaces lead to 3D migration path scattering that could not be resolved by the applied method (see Fig. 2.15).

The next section addresses the problem of finding an appropriate roughness for migration surfaces and outlines the procedure for interface interpolation.

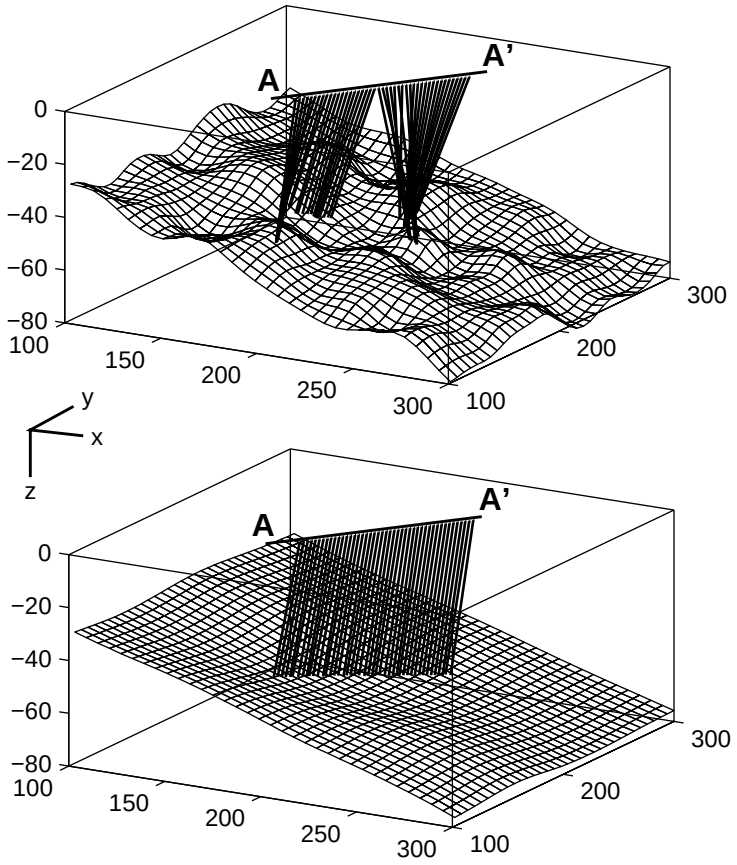


**Figure 2.15** Effect of interface roughness on 3D migration paths. Upper half: rough interface and 3D-migrated rays from a near-vertical reflection profile A-A' are shown. Scattering of migration paths below resolution capabilities is observed. Lower half: smooth interface and resulting consistent 3D migration paths along the profile A-A'.

*Procedure for interface interpolation: roughness versus continuity*

The discrete information provided by each reflector segment are (see Figs. 2.6 and 2.16):

- structural depth points and related depth uncertainties: $z_i^{obs} + \Delta z$ (see Eq. 2-6).
- first derivative of reflector segments (dip) and related uncertainties: $d^{obs} + \Delta d$ (see Eq. 2-7).

For any interpolated interface, residuals (or misfits) for depths ($z^{obs}$-$z^{cal}$) and dips ($d^{obs}$-$d^{cal}$) for each reflector segment can be computed as follows (see Fig. 2.16):

- Calculated structural depth points $z_i^{cal}(x, y)$ along reflector segments are derived by projection of the location (x,y) of the observed structural depth points $z_i^{obs}(x, y)$ onto the interpolated interface (line B in Fig. 2.16). Depth residual of the *k*-th reflector segment is derived by averaging the depth residuals of the structural depth points along that reflector segment:

$$z_k^{res} = \frac{\sum_{i=1}^{imax} z_i^{obs} - z_i^{cal}}{imax}, \qquad (2\text{-}14)$$

  where *imax* is the number of structural depth points along the *k*-th reflector segment.
- Comparison between observed and calculated first derivatives (dips) of reflector segments must be done within units that can be resolved. Dip residual $d^{res}$ of the *k*-th reflector segment is therefore obtained by averaging the residuals $d_i^{res}$ obtained along that reflector segment (see $d_1^{cal}$-$d_4^{cal}$ in Fig. 2.16):

$$d_k^{res} = \frac{\sum_{i=1}^{imax-1} d^{obs} - d_i^{cal}}{imax - 1}, \qquad (2\text{-}15)$$

  where again *imax* is the number of structural depth points along the *k*-th reflector segment. Note that $d^{obs}$ is constant along reflector segments.

The objective now is to find an interface that shows maximum continuity and minimum roughness with respect to the observed data and their errors. The procedure to derive such an interface requires to determine first migration surfaces and then interfaces from the 3D migrated reflectors (see Fig. 2.17).

**STEP 1** (Migration surface): Since no ‘a priori’ information about interface offsets can be derived from the 2D-migrated observed reflectors, a series of *n* spatially continuous surfaces $f_n(x,y)$ is interpolated using all reflectors within the model area. These surfaces are all characterized by equally high continuity and differ only in terms of their rough-

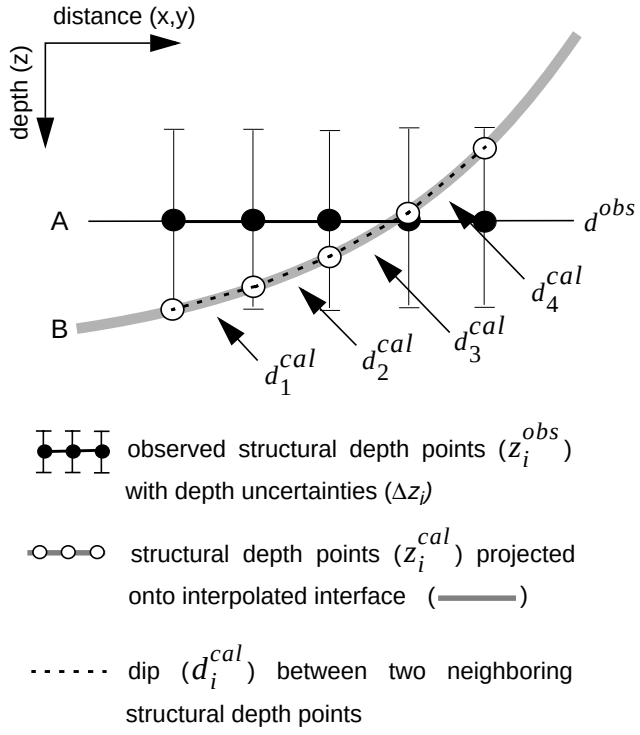


**Figure 2.16** Derivation of calculated depth ($z^{cal}$) and dip ($d^{cal}$) of corresponding observed reflector segments on interpolated interface. See text.

ness. The roughness spectrum ranges from very smooth to extremely rough. A criterion must be found that evaluates the quality of each interpolation with respect to the variance of the observed data and their errors, and to the physical principle of interface continuity.

In order to satisfy these criteria it is necessary to compute for each of the *n* surfaces residual vectors for depth ($z^{res}$) and dip ($d^{res}$) belonging to each reflector segment and to derive their rms-value (root-mean-square):

$$z_{rms}^{res} = \sqrt{\frac{\sum_{k=1}^{kmax} (z_k^{res})^2}{kmax}}, \qquad (2\text{-}16)$$

$$d_{rms}^{res} = \sqrt{\frac{\sum_{k=1}^{kmax} (d_k^{res})^2}{kmax}}. \qquad (2\text{-}17)$$

Rms-residuals for depth and dip are plotted against interface roughness and compared with the smallest reasonable error determined from the resolution capability of CSS methods for the specific interface (expected rms-error). Interfaces with rms-residuals larger than this expected error are too smooth to fit all data in average within their error limits. Interfaces with rms-residuals smaller than the optimal error tend to over-fit the

data. A best interface *f*(x,y)* is determined with rms-residuals for depth and dip in the range of the expected error values.

**STEP 2** (3D migration): This surface *f*(x,y)*, now called migration surface (see above), is the correct surface which has to be used for 3D migration. After 3D migration of the reflectors with respect to this migration surface, step 1 is performed again for one interface using now the 3D-migrated reflectors for interpolation and the previously defined roughness value. In case that the resulting 3D-migrated interface fits all data within the observed error bars, no offsets must be considered and one can proceed to step 4. If misfits between interpolated and observed data exceed the observed errors (significant misfits), offsets between the corresponding reflectors are too large and can, therefore, not be interpolated with respect to the general roughness trend. In this case, one has to consider interface offsets and proceed to step 3.

It must be noted that in some cases significant misfits may appear on the migration surface but vanish on the 3D migrated interface. This can occur because 3D migration has a smoothing effect on opposingly dipping structures that are imaged by transverse profiles. In general, however, significant misfits occurring on the migration surface indicate the necessity to proceed to step 3. Furthermore, 3D migration path scattering along reflectors indicate areas of inappropriate interpolation.

**Step 3** (Interface offsets): Misfits in depths and dips larger than the observed errors (i.e. $z^{res} > \Delta z^{obs}$ and $d^{res} > \Delta d^{obs}$) must be located on the interpolated interface. At these locations, the interface is too smooth in order to follow the observed local depth variations within their errors. The corresponding reflector segments lie partly, or even totally, outside the interpolated interface with respect to their depth errors and are assumed to indicate interface offsets. To model such interface offsets, the unmigrated (original) reflectors are separated and the interface is sub-divided into two 'sub-interfaces', *g(x,y)* and *h(x,y)*. By doing so, the shortest length of the interface edge along the offset is seeked (principle of interface simplicity). Modeling of interface offsets by connecting clusters of significant misfits must be done with respect to the tectonic setting of the area of investigation. After creating all necessary sub-interfaces, the 3D interface interpolation procedure is restarted with step 1, now for each sub-interface individually (i.e. interpolation of $g_n(x,y)$ and $h_n(x,y)$). Interpolation to the edge of sub-interfaces is helped by using supporting depth points outside the sub-interfaces (see interpolation algorithm).

The assumption behind this step is that a generally smooth interface will not show locally concentrated spots of rough interface behavior. It is more likely that two smooth interfaces define a general trend and are disjointed over short distances.

**STEP 4** (Final interface): Since a 3D-migrated interface is now found with highest possible continuity (least number of sub-interfaces, i.e. least length of offsets) it remains to find the smoothest solution of that interface. Such a final interface is obtained by selecting the smoothest surface that still fits all data within the observed error bars.

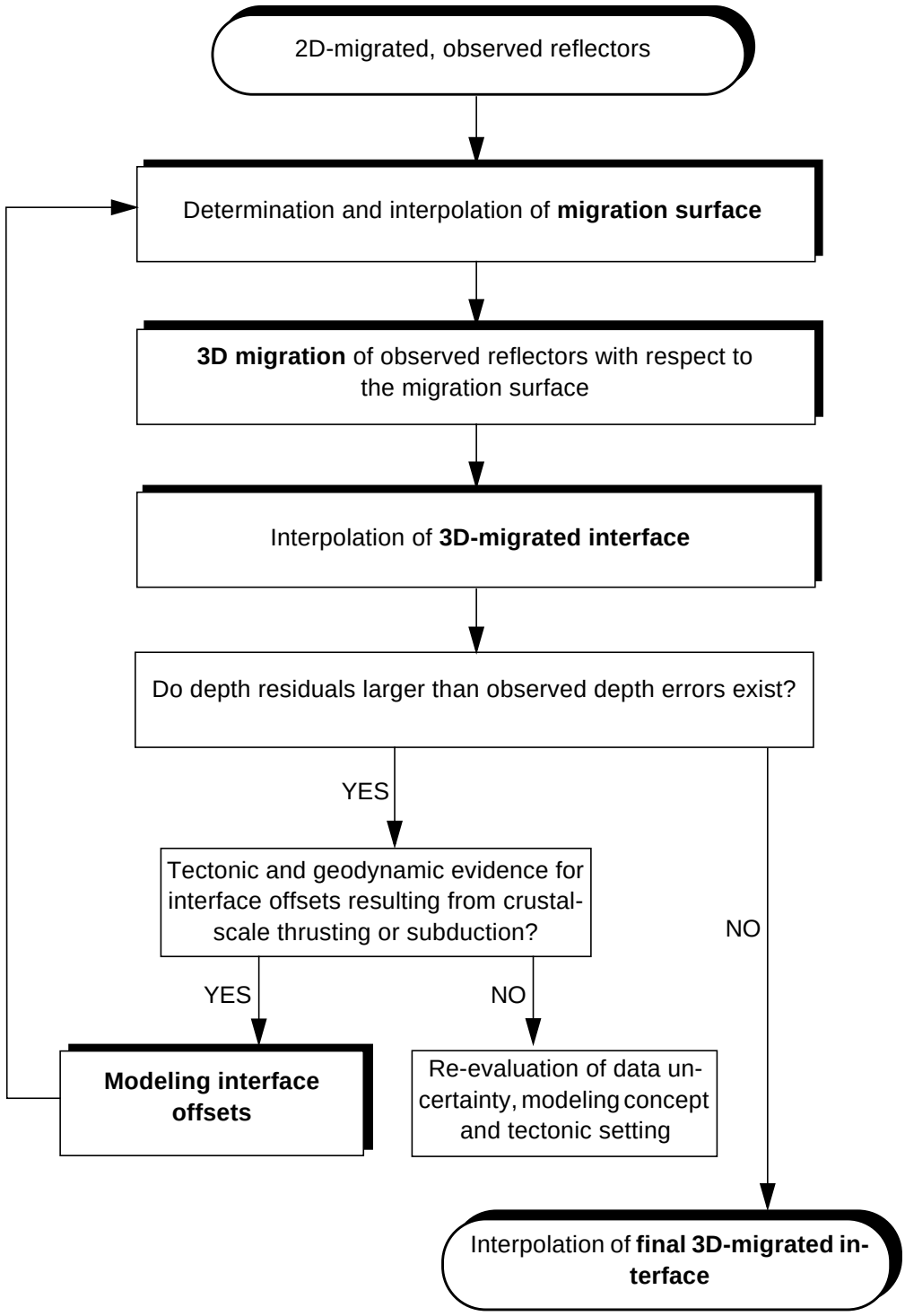


**Figure 2.17** General flow of the 3D interface modeling procedure.

### 2.3.2 Volumetric CSS Velocity Modeling

CSS methods reveal the detailed velocity structure of the Earth's crust and uppermost mantle. Nonetheless, simplification of this information is required for a 3D crustal model that contains all the velocity information in a simplified average P-velocity. Therefore, corresponding to the previously obtained crust-mantle interface (Section 2.3.1), the following information must be extracted from the 2D CSS models for the crust: average crustal velocity, lower-crustal velocity, and upper-mantle velocity. These discretely observed CSS velocity data, for which spatial locations are 3D migrated as outlined in the previous section, are used for the volumetric velocity modeling process.

Any seismic interface depth is directly related to the average velocity along the corresponding reflected ray; i.e. for any reflector belonging to the crust-mantle interface an estimation of average crustal velocity is made. Average velocities are actually measured along down- and up-going ray tubes of reflecting PmP phases (see Fig. 2.18a). In order to simplify the derivation of average velocities from ray-traced refraction and wide-angle reflection models, intra-crustal velocity information, horizontally sampled by refracted rays, is used. Travel times within these individual layers at distances of imaged reflectors are summed using Equation 2-2 and the average crustal velocity over these horizontal layer-velocities derived. This procedure is an approximation that projects average velocities, actually measured also to large recording distances, to distances where reflectors are imaged (Fig. 2.18a). 1D interpretations (Herglotz-Wiechert inversion, $x^2 - t^2$ method) directly provide average velocities and interface depths. Near-vertical reflection interpretations use independently estimated average velocities for migration of the reflecting structures.

Physical volumes of the velocity field that have strong influence on the rays are accounted for in a simplified way by assigning average velocities to rectangular 'boxes' along observed reflectors (Fig. 2.19a). The boxes are bounded by the surface and crust-mantle interface. The horizontal box dimension corresponds to the Fresnel zone radii for the specific interface depth (Sheriff and Geldart, 1995):

$$R_{Frsn} = \sqrt{\frac{vpa \cdot z}{2 \cdot \upsilon}}, \qquad (2\text{-}18)$$

| | |
|---|---|
| *vpa* | average crustal velocity, |
| *z* | depth of the crust-mantle interface, |
| $\upsilon$ | frequency of the PmP phase. |

Crossing (or interlocked) boxes (see Fig. 2.19a) allows to control the consistency of the measured average velocity.

Seismic interfaces are characterized by strong velocity gradients (velocity discontinuities); i.e. the crust-mantle interface by the gradient between lower-crust and upper-mantle velocity. On wide-angle reflection profiles lower-crustal velocity is measured by PmP phases that are observed to long recording distances (see Fig. 2.18b). In addition the intra-crustal velocity structure must be properly revealed. Measured lower-crustal

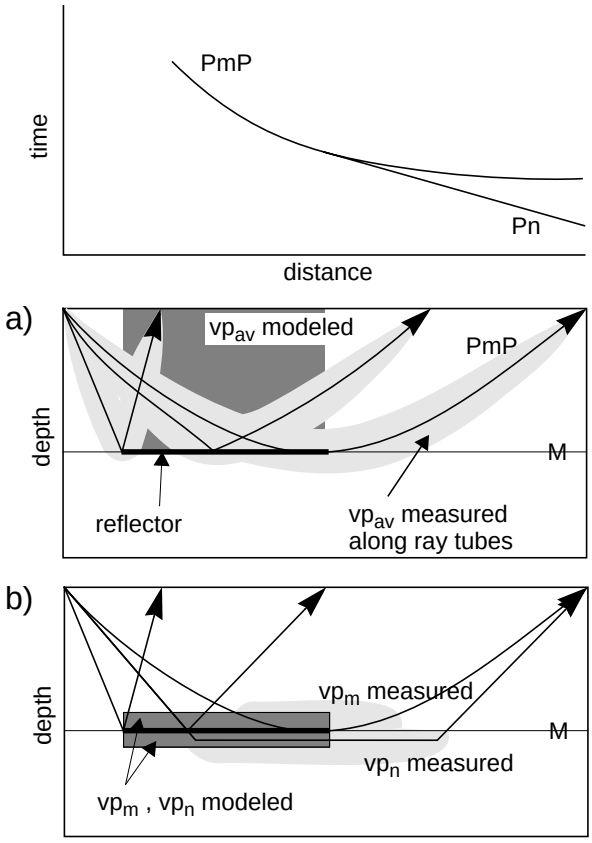


**Figure 2.18** Schematic travel time curves with derivation of (a) average vp$_{av}$, and (b) lower-crust vp$_m$ and upper-mantle vp$_n$ velocities from refraction and wide-angle reflection data and models. Projection of measured velocity to distances of imaged reflectors.

velocities are projected to distances where reflectors are imaged. Upper-mantle velocities are sampled by rays refracted at the crust-mantle interface (see Fig. 2.18b). They are mostly visible as Pn phases on seismogram sections of refraction profiles. Fan observations and near-vertical reflection profiles reveal no quantitative information about lower-crust and upper-mantle velocities.

Lower-crustal and upper-mantle velocities derived from wide-angle and refraction profiles average the velocity distribution along ray paths. Interpolation and extrapolation of these velocity parameters along the crust-mantle interface is therefore performed over these distances, over which the velocity distribution is sampled (see Fig. 2.19b). As these distances depend on the profile lengths, the radii of influence for interpolation must be determined according to the CSS network. Interpolation is only performed within regions of tectonic units, i.e. within the dimension of crustal blocks or, in other words, along the individual Moho surfaces. A weighting factor is applied to each value within the area of influence ($R$) that accounts for the distance ($d$) of that value to the grid point to interpolate and the quality with which the velocity value is known (*wght*, see Eqs. 3-1 and 3-2). The weighting factor for velocity interpolation, therefore, yields:

$$w_{vpm,\,vpn} = \left(\frac{R-d}{d+\eta}\right)^2 \cdot wght\,, \qquad (2\text{-}19)$$

where $\eta$ prevents division by 0 for data values very close to the grid point to interpolate.

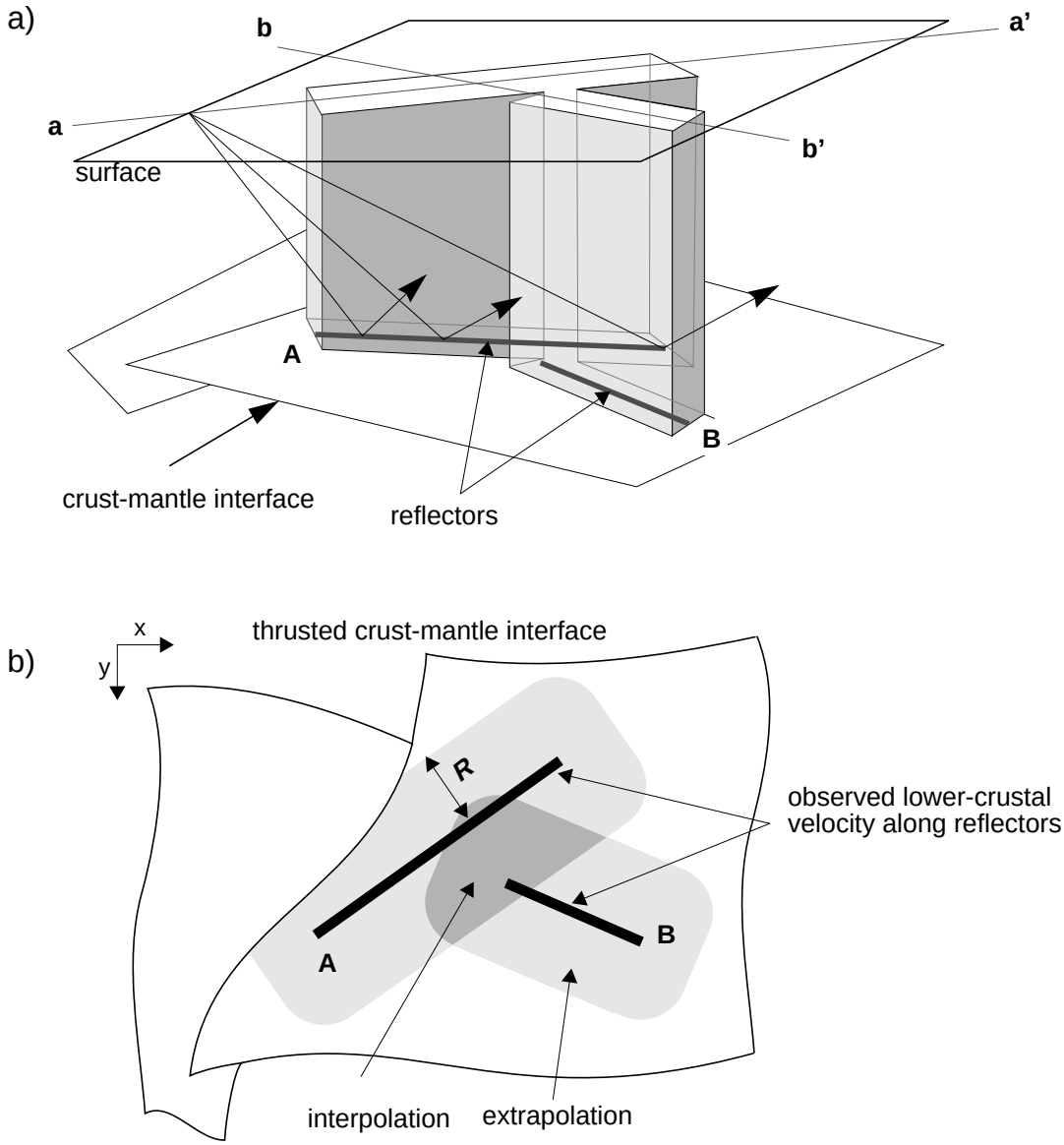


**Figure 2.19** a) Volumetric ('box') representation of average velocities between surface and crust-mantle interface by approximated Fresnel volumes (see text). a-a' and b-b' are the wide-angle profiles along which the reflectors (A and B) of the crust-mantle interface are observed.
b) Horizontal lower-crustal velocity interpolation and extrapolation along the crust-mantle interface within an area of influence defined by *R*. A and B are observed reflectors of the crust-mantle interface with attached lower-crustal velocity parameter. The same procedure is applied to upper-mantle velocities.

No smoothing of the original data is performed. Grid nodes that have no data within the area of influence are not filled, i.e. are later filled with reference values.

In the case of very dense CSS profile networks, volumetric modeling of velocities as described above may lead to spatial continuity of velocity parameters within the 3D model (no velocity data gaps). For loosely connected profile networks, however, volumetric CSS velocity modeling will leave information gaps between the CSS data volumes. The problem of CSS velocity information gaps is helped by integrating the

volumetric CSS velocity information in a pre-defined lithospheric reference model that is discussed in the next section.

## 2.4 Assemblage of Seismic Data to Continuous 3D Models

Ideally, a continuous measure of the velocity variation throughout the region of interest is required in order to derive continuous 3D seismic models. In the real world, however, only a limited amount of isolated, discrete measurements of velocities is available. These velocities are measured within smaller or larger volumes (see Section 2.1), between which, in some cases, interpolation is possible (see previous section). Putting together seismic information from various seismic methods may decrease the volume of information gaps. Gaps in controlled-source seismic (CSS) velocity information, for example, may be filled with tomographic results from local earthquake data. The crustal-scale compatibility between the two data sets is secured by the model parametrization (see Section 2.2). However, an assemblage of all available seismic data and inclusion of 'a priori' information not necessarily leads to continuous 3D models. Therefore, the assemblage of seismic data from different methods and of variable density is performed stepwise by integration of these data in a pre-defined continuous lithospheric reference velocity model.

In the following section, the method for stepwise assemblage of seismic model information is described. It starts with the definition of a reference model, integration of 'a priori' information such as sedimentary basins, and updating the model with CSS model information as obtained in the previous section. The realization of the 3D model construction and the visualization of the steps in procedure steps and of the final models is described in Section 2.4.2.

### 2.4.1 Method for Seismic Data Assemblage

*Lithospheric reference velocity model*

The Earth's velocity field is, to a first-order approximation, a function of depth only. Effects of increasing pressure and temperature make this an excellent approximation for depths below about 100 km, where strong lateral inhomogeneities in the Earth's physical properties (velocity, density) are unstable over long time period. Near the Earth's surface (i.e. lithosphere), effects of chemical differentiation dominate over pressure and temperature effects on P- and S-velocities. There are, however, typical (continental) lithologies (Mueller, 1977) with their associated velocity structures. These velocity-depth functions show certain characteristics that may be interpreted as a) the characteristics of the illumination methods that are used to derive the velocity information or, b) the characteristics of the state of the crust and the processes at work (e.g. orogeny, subduction, etc.). Within tectonically stable regions, similar velocity-depth functions can be observed.

Such velocity-depth functions are used as reference models to secure parameter continuity of 3D models in areas where no seismic information is available and interpolation would lead to ambiguous results. Reference models provide reference values

for the required velocity and structural parameters defined by the 3D model parametrization (see Figs. 2.3 and 2.20). The vertical velocity distribution between the given parameters is derived according to the model parametrization scheme by computing the reference compensation velocity below the near-surface layer (see Eq. 2-5; Fig. 2.21a).

To allow a direct comparison of reference data with model data, reference structures should advantageously be part of the model or adjoining the model region. For model areas with complex structures (e.g. collision zones, such as the Alpine region), reference models are derived from the 'undisturbed' crust-mantle system nearest to the target area (e.g. foreland, hinterland). 1D reference models are the base on which the subsequent adaptation to the real velocity distribution of the target area is performed by incorporation of measured data.

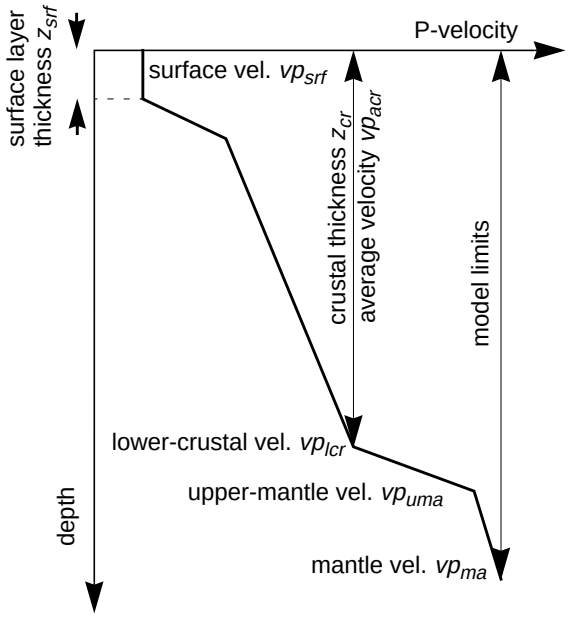


**Figure 2.20** 1D lithospheric reference model: structural and velocity parameters.

*Adapted reference models: integration of 'a priori' information.*

Reference models are in a first step adapted to the region of investigation by integration of 'a priori' known strong velocity inhomogeneities (adapted reference models). 'A priori' knowledge of strong velocity inhomogeneities in the area of investigation is generally restricted to surface observations, such as the low-velocity sedimentary basins. The necessary information for horizontal extension of sedimentary basins, basin depth (i.e. $z_{srf}$) and sediment velocities ($vp_{srf}$) are derived from tectonic maps, borehole, and/or CSS investigations. Their integration in reference models is carried out by adjusting the reference surface layer thickness by the sedimentary thickness and updating the reference surface velocity with the sedimentary velocity (see left model in Fig. 2.22). The compensation velocity and the vertical velocity distribution are re-computed solving Equation 2-5. Compensation velocities for adapted reference models in areas of integrated sedimentary basins must be calculated using the reference surface velocity in-

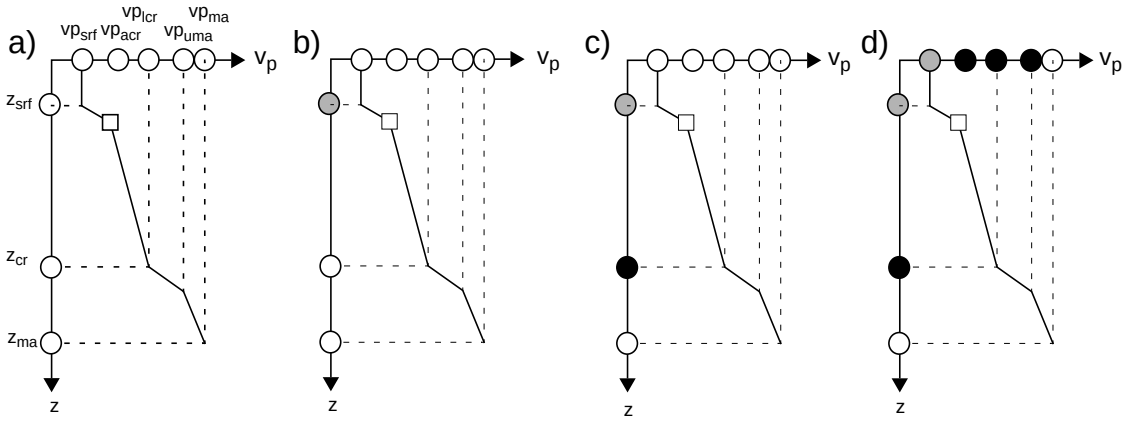


**Figure 2.21** Parametrized velocity-depth functions to illustrate the values used for the computation of compensation velocities (squares) when assembling reference velocities (white circles), near-surface velocity information (gray circles) and CSS-derived information (black circles). $vp_{srf}$ = surface velocity; $vp_{acr}$ = average crustal velocity; $vp_{lcr}$ = lower-crustal velocity; $vp_{uma}$ = upper-mantle velocity; $vp_{ma}$ = mantle velocity; $z_{srf}$ = surface layer thickness; $z_{cr}$ = crustal thickness; $z_{ma}$ = vertical model limit. a) Reference model. b) Adapted reference model: integration of depth in sedimentary basins as 'a priori' information. c) Integration of CSS-derived crust-mantle interface. d) Integration of a complete data set of CSS velocity information together with 'a priori' known sediment velocity as surface velocity. See text.

stead of the lower sediment velocity (see Fig. 2.21b). This is because reference average velocities are given with respect to reference structures and the use of low sedimentary velocities at the surface of adapted reference models would shift the compensation velocity to unrealistically high values (see Fig. 2.4a).

*Integration of CSS data*

Adapted reference models are subsequently updated with structural and velocity information obtained from CSS methods as described in the previous section. Seismic interfaces such as the crust-mantle interface (see Section 2.3.1) are integrated in adapted reference models by adjusting the interface depth (e.g. crustal thickness). Because interfaces have to lie at a grid node in depth, a dipping interface is replaced by a piecewise-horizontal interface with discrete steps. The size of errors produced by this discretization depends on the grid sampling. The compensation velocity and the vertical depth distribution with reference velocity values are recomputed (see right model in Fig. 2.22). It must be noted again, that, since reference average crustal velocities are used, the compensation velocity is calculated using the reference surface velocity for areas with integrated sedimentary basins (see Fig. 2.21c). The resulting structural 3D model depicts CSS-derived crustal thickness and an average crustal velocity distribution that corresponds to the given reference value at every horizontal position.

Volumetrically modeled CSS velocities (see Section 2.3.2) are used to subsequently replace reference velocity values in the 3D model (see Fig. 2.23). The compensation velocity and the vertical velocity distribution is re-computed using the updated velocity parameters (see Fig. 2.21d). Within the 'average velocity boxes', velocities are calculated at each grid point according to the linear interpolation between the compensation

velocity and the lower-crustal velocity. The sediment velocity to compute the compensation velocity is only used when average velocities are determined by CSS methods.

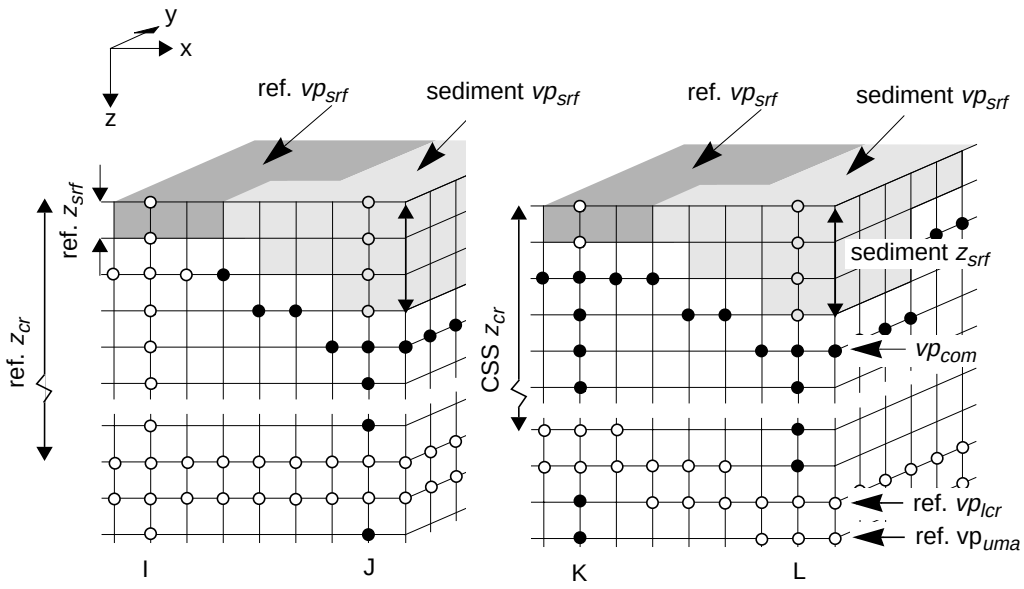


**Figure 2.22** Left: Adapted reference model; integration of sedimentary basins as 'a priori' information in reference model. Right: Integration of crust-mantle interface as structural CSS information in adapted reference model. Grid points (white = reference values; gray = 'a priori' values; black = recomputed and adjusted reference values) are represented by circles for compensation depth (with $vp_{com}$), crust-mantle interface depth (with $vp_{lcr}$ /$vp_{uma}$), and along four vertical grid lines (I, J, K, L). I: in reference model. J: in adapted reference model. K: in reference model with CSS structure integrated. L: in adapted reference model with CSS structure integrated. For calculation of reference and adjusted compensation velocity $vp_{com}$ see text.

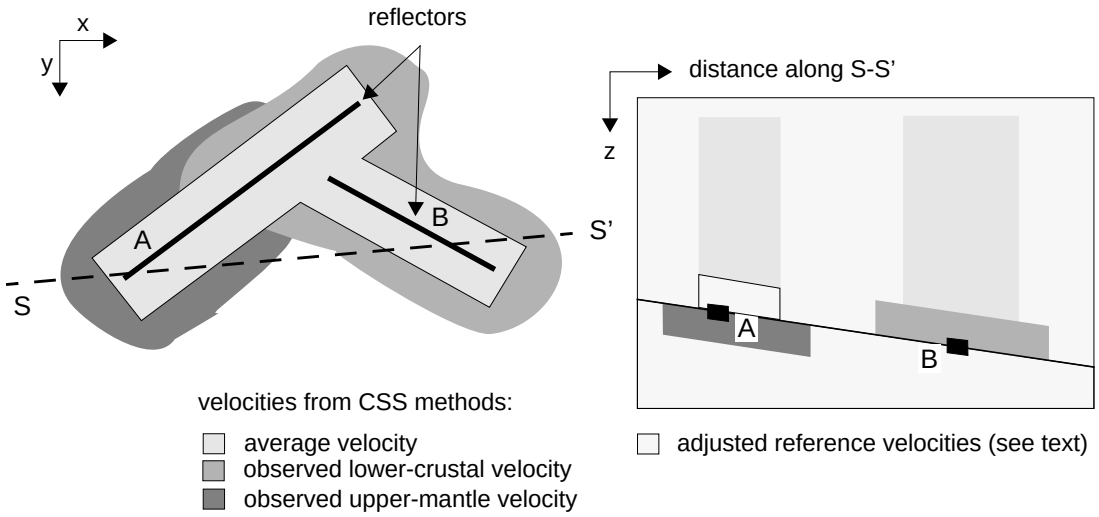


**Figure 2.23** Integration of CSS velocity information in the adapted reference velocity model with integrated crust-mantle interface derived from CSS methods. Left: reflectors (A, B), average, lower-crustal, and upper-mantle velocities as obtained from CSS methods. Right: Integration of the CSS velocity information in 3D model. A 2D cross-section along S-S' (horizontal dashed line) is shown.

### 2.4.2 Realization of 3D Model Construction

The seismic investigation of the Earth's physical properties is an ongoing process and not yet completed. CSS profiling to derive 2D sub-surface structure can be continued at any time in almost every region and its results added to an existing network of CSS 2D model information. An increasing amount of local earthquake data and their enhanced quality lead to better resolved and more reliable models of 3D velocity distributions in the regions where these earthquakes occurred. Teleseismic tomography allows to image the deeper structure of the lithosphere-asthenosphere system. Considering these aspects, seismic model information should be assembled and stored in a way that allows to change, update and extend 3D models according to new or revised interpretations and findings. Model recomputing has to be easy and reproducible. Tracing back of each step in the modeling procedure not only allows to understand the results, it also allows to judge the influence of individual steps on the final 3D model.

Since a manual approach to 3D model construction would not satisfy these requirements (see also previous sections), program *SeisMod3D* (see Appendix B) has been developed that performs 3D seismic model construction (see Fig. 2.24). *SeisMod3D* has basically two main stages. The first is dedicated to the 3D interface modeling process using 2D CSS model data as described in Section 2.3.1. It includes 3D migration and interpolation of CSS-derived reflectors. Input to this first program block is a data base with structural information derived from CSS data (see Appendix A.1 for the Alpine data base). The CSS data base can be displayed and analyzed using program *SeisMap* (see Appendix A.2).

The second stage of *SeisMod3D* contains the velocity modeling part. It performs volumetric modeling of CSS-derived velocity data and incorporates seismic information derived from different sources to a continuous 3D seismic model. It mainly follows the steps outlined in the previous section. *SeisMod3D* provides also reliability and resolution information for structural and velocity parameters throughout the 3D model. A flexible parameterization scheme also allows to adopt the 3D model design to other purposes, not only for teleseismic wavefront tracing as it is used for in Chapter 4.

*Visualization*

The evaluation of resulting 3D seismic velocity models typically involves spatial analysis of the variation of one or more variables (e.g. velocity, structural location, reliability). Geometric models can be classified in two main groups, namely surface and volume models. Volume models store the physical parameters explicitly in three-dimensional space (e.g. $vp = f(x,y,z)$). Surface models represent discrete interfaces with respect to a specific model parameter (e.g. velocity contrast $vp^*$, $z = f(x,y,vp^*)$). The information of surface models is part of the volume model since they represent only a specific physical parameter of the volume model. Because of the difficulty of volume visualization (four-parameter visualization), surface models are often used to represent specific parameters of the volume model. In seismic models, for example, surface models depict seismic horizons (i.e. topography of a specific seismic velocity gradient)

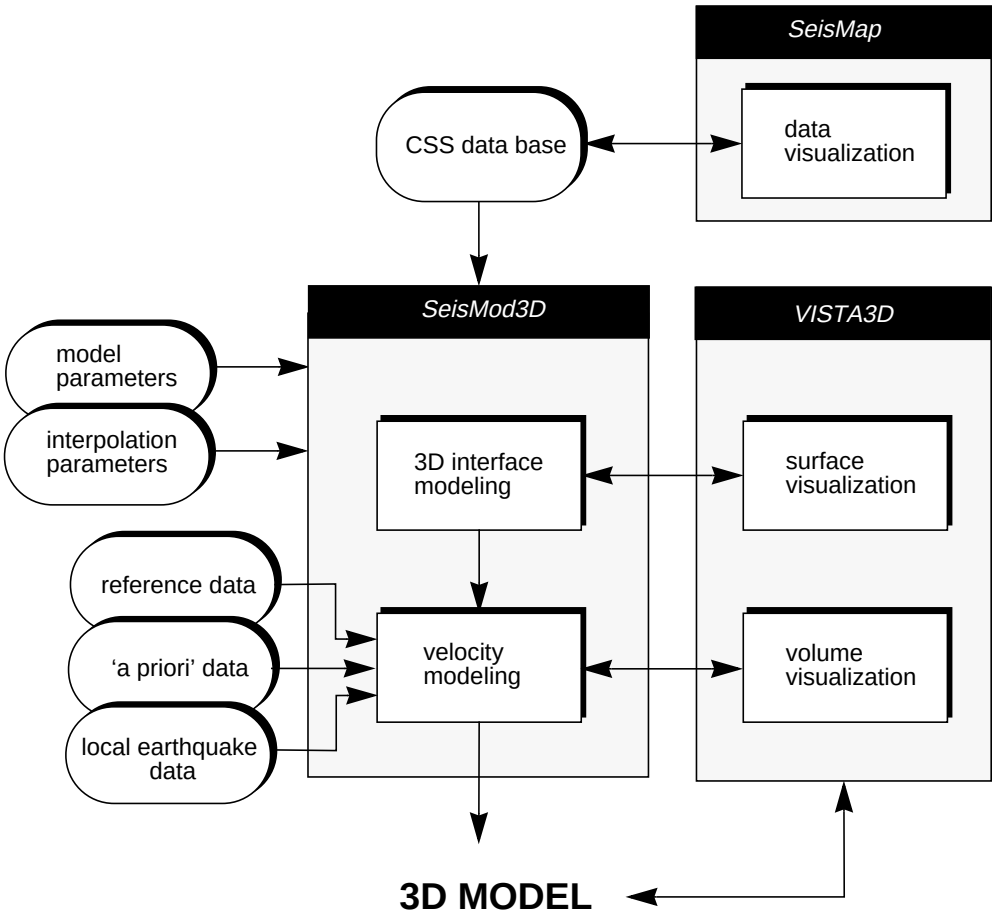


**Figure 2.24** Realization of the procedure for 3D seismic model construction. *SeisMod3D* is a Fortran77 program for 3D model construction. *SeisMap* and *VISTA3D* are programs based on Matlab modules for visualization of 1D, 2D, and 3D data. A description of the CSS data base is given in Section 3.1 and Appendix A. The programs are documented in Appendix B and D.

whereas the spatial variation of the velocity information is represented by volume models.

Visual analysis and control of 3D model parameter values and their spatial variation require an adequate way of visualization. *VISTA3D,* a program package based on MATLAB modules (see Appendix D), efficiently displays 3D surface and volume models as produced by *SeisMod3D* by:

- vertical sections (x-slices, y-slices, crossline)
- horizontal sections (z-slices)
- tracked sections (surface models)
- 1D velocity-depth functions
- parameter analysis

*VISTA3D* also provides control on all major modeling steps involved in both parts of the program *SeisMod3D* such as 3D migration, interpolation, extrapolation, volumetric modeling or data assemblage. Thus, *VISTA3D* is an important tool throughout the mod-

eling procedure since it uncovers artifacts and numeric instabilities arising during the modeling process.

Finally, for clarity's sake, it must be noted, that, although represented by an infinitely thin surface in the following chapters, seismic interfaces such as the crust-mantle boundary are in the real world rather thin, laminated layers characterized by strong velocity gradients across these layers (transition zones) (see e.g. Deichmann and Ansorge, 1983).

# CHAPTER 3

# 3D P-VELOCITY MODEL OF THE ALPINE CRUST

In this chapter, the previously outlined concept and method for 3D seismic model construction (see Chap. 2) is applied to and tested against the controlled-source seismic (CSS) data in the Alpine region. The goal of this chapter is to obtain a 3D P-velocity model of the central and western Alpine crust and uppermost mantle.

*Alpine tectonic setting: the broad 3D structure*

The mountain chain of the Alps and the northern Apennines define a collision zone resulting from the convergence of the Adriatic promontory of the African plate (Channell et al., 1979) and the European lithospheric plate (e.g. Mueller, 1989; Pfiffner, 1992; Giese et al., 1992; Mueller, 1996). The nearly 1000 km long Alpine orogen, associated with the collision zone, stretches from the Ligurian Sea to eastern Austria and is subdivided into three main zones; the western, the central and the eastern Alps. The central Alps extend across Switzerland in a ENE-WSW direction. Towards the west, the central Alps merge into the arc of the western Alps in France and Italy. Adjacent to the southern rim of the Alps, the northern Apennines mark the collision-generated structure SW of the Adriatic promontory (Giese et al., 1992). They form a WNW to ESE striking orogen that borders at its western end the western Alps and merges to the east with the more NW-SE striking central Apennines.

With the western and the central Alps semi-encircling the Po-plain, the Alpine collision zone is a 3D structure in large scale. The large-scale structure of the upper lithosphere in the Alpine region is dominated by the interaction of three crustal blocks; the European, Adriatic and Ligurian crust. The interaction of the three crustal blocks in the Alpine region is seismically reflected by the topography of the European, Adriatic and Ligurian Moho (Kissling, 1993), that represent the boundary between crust and upper mantle. The N-compressional and WNW-rotational motion of the African plate against the European plate (Schmid et al., 1996) lead to a thickening of the European crust from about 30 km in the Alpine foreland to over 55 km below the Insubric line, where it underthrusts the Adriatic crust (Valasek & Mueller, 1994; Ye et al., 1995). The Adriatic crust, warped under the subduction load and the thrust loads of the Alps and the Apennines (Giese et al., 1992), thickens towards the south to about 60 km below the southern rim of the Po-plain where it is overthrusted by the thin Ligurian crust (Buness, 1992; Ye et al., 1995). This structure can be followed in WNW direction with a thinning Adriatic crust toward the arc of the western Alps (Buness, 1992). To the east the trend re-

mains unclear.

Erosion of the rising Alpine chain caused the fill of the northern and southern foredeeps of the Alps, the Molasse basin (Pfiffner, 1986) and the Po-basin (Pieri & Cropi, 1981; Pieri, 1983; Cassano et al., 1986). The low velocities of the Molasse sediments (Staeuble & Pfiffner, 1991a; Ye, 1992) and Po sediments (Ye, 1992; Buness, 1992) compared to the surrounding basement values make these basins to strong near-surface velocity inhomogenities in the Alpine region.

Strong intra-crustal velocity inhomogenities are observed in the Ivrea zone (Berckhemer, 1968) where lower-crust material near the surface causes high average-crustal velocities (Cattaneo & Eva, 1990; Solarino et al., 1997).

*Previous work*

In the last decade, national and international programs have stimulated and funded a series of studies, in particular deep seismic reflection profiling (see Fig. 3.1), that have enormously increased our knowledge of the deep structure of the western and central Alps (Frei et al., 1990; Roure et al., 1990; Blundell et al., 1992). This has allowed two- and even three-dimensional seismic models to be established (Mueller et al., 1980; Ménard and Thouvenot, 1987; Tardy et al., 1990; Buness, 1992; Holliger and Kissling, 1992; Valasek and Mueller, 1994).

The importance of 2D and 3D images for tectonic and dynamic evolutionary models of Alpine orogeny (Ménard et al., 1991; Pfiffner, 1992; Schmid, 1992) demands the critical assessment of their reliability. With respect to their theoretical resolving power, however, modern imaging techniques are of poorly known reliability and error assessment. As a consequence, most models of the deep structure have been presented without quantitative or even qualitative error estimates, and ambiguity is rarely adressed. Furthermore, 2D and 3D seismic images, by their nature, generally mask the fact that they are based on information of sometimes extremely variable reliability. For the sake of completeness and consistency of a 3D image, interpolation is performed either for smoothing or to fill gaps and for a non-specialist in the particular geophysical method, this process, which results in apparently uniformly-defined final images, remains irreversible. On a qualitative basis, Kissling (1993) reviewed resolution and reliability of the various modern interpretation methods that have been applied to the Alps and derived, with respect to the reliability information, a qualitative model of three crustal blocks. Baumann (1994) established a scheme to weight CSS data according to the quality with which they are known.

*3D Alpine seismic model*

Therefore, for the first time, quantified reliability assessment of CSS derived data has been integrated in a modeling method (Chap. 2) developed to derive 3D seismic models from 2D seismic data. In this Chapter, the method is used to establish a 3D digital seismic model of the central and western Alpine crust and uppermost mantle while accounting for quantified reliability of the included structural features. Accounting for data

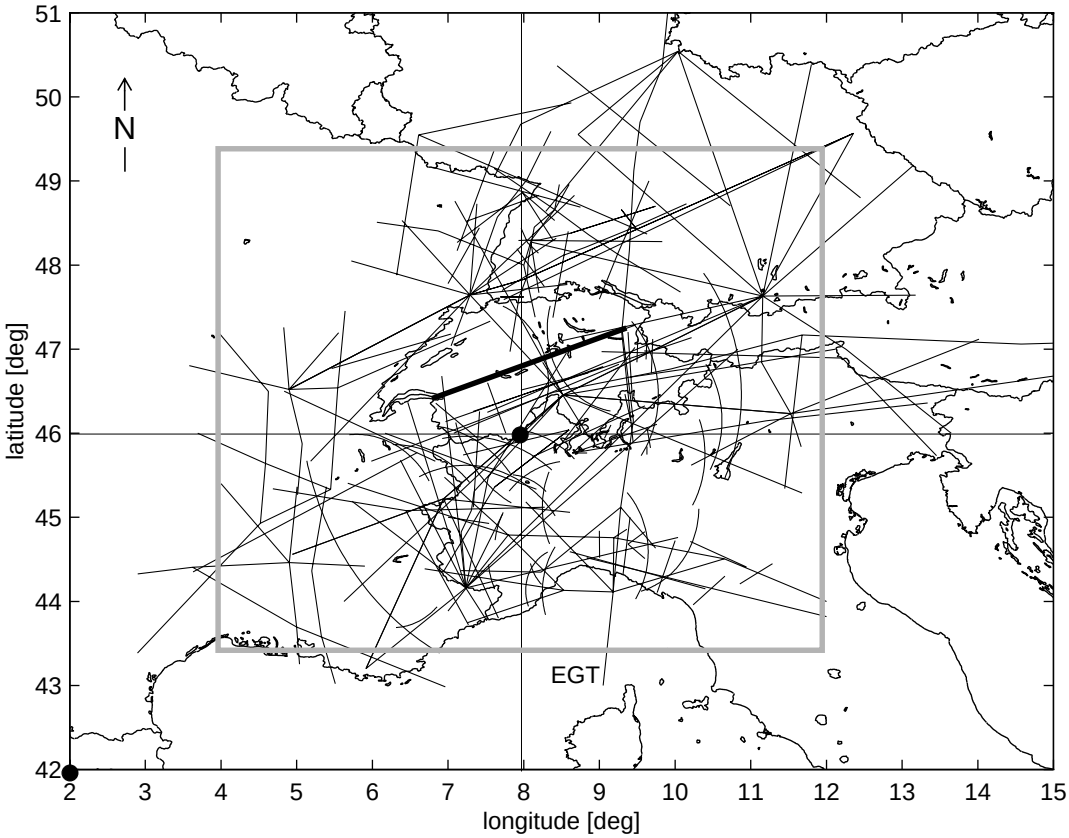


**Figure 3.1** Seismic refraction / wide-angle reflection and near-vertical reflection profiles carried out over the last decades in the Alpine region. Bold line: location of the ALP87 profile (Maurer and Ansorge, 1992) (see text). ● at 46°/8°: Origin of short distance conversion. ● at 42°/2°: Origin of cartesian coordinate system for 3D model. Box: Horizontal extension of 3D model. EGT = European Geotraverse.

uncertainty during modeling processes allows to better seek for the simplest model fitting the data within their errors. Thus, compared to previous interpretations, the derived 3D Alpine model depicts simpler structural features.

The consistency in modeling method and data compilation allows recomputing, revising and updating the established 3D model and provides a system to store, represent and update the present seismic model. The 3D Alpine model, or specific structural components of it, may serve as tools for further studies and numerical computations - such as the calculation of earthquake traveltimes to study effects on wavefront scattering by 3D Alpine crustal structure (Chap. 4).

The 3D model ranges from 4° to 12° east-longitude and from 43.5° to 49.5° north-latitude (Fig. 3.1). It includes the central and western part of the Alps, the Rhine-Rhone Graben area, the southernmost part of Germany and the northern part of the Ligurian region. The spherical coordinates (longitude, latitude) are transformed to cartesian coordinates (x, y) using short distance conversion with transformation origin at 8° east longitude and 46° north latitude (see Fig. 3.1) near the center of the model region. The origin of the cartesian coordinate system (positive x-axis toward E, y-axis toward N) is

located at 2° east longitude and 42° north latitude. The cartesian model ranges from 200 km to 800 km model distance in both horizontal directions and reaches 70 km in depth in order to include the entire Alpine crust with the information of uppermost mantle velocities from Pn phases.

As outlined in Section 2.2, grid parameters (number of grid nodes *nx, ny, nz* and grid spacing *hx, hy, hz*) of 3D models are determined with respect to the available amount and density of data, to the resolving power of the involved seismic methods to construct 3D models, to the resolving power of seismic methods subsequently applied to the 3D model, and to available dynamic computer memory. For teleseismic waves ($\phi$ ~ 0.5 Hz; $\lambda$ ~ 10-20 km) computed in a 3D model based basically on CSS data ($\phi$ ~ 1-10 Hz; $\lambda$ ~ 0.5-6 km), grid spacing must be, with respect to resolution considerations (see Section 2.1), in the range between 2 and 10 km. Strong local variations in the velocity field, such as across the Moho, must be properly resolved. Braile and Chiang (1986) determined a general thickness of the Moho transition zone between 0-5 km. Deichmann et al. (1986) determined the Moho to be about 1 km thick in the southern Alps. Therefore, in order to best approximate this most important velocity inhomogeneity in the lithosphere with respect to available computer memory, the 3D model for further teleseismic wavefront tracing (Chap. 4) is parametrized by an even grid consisting of 301x301x36 grid nodes with grid spacing of 2 km in each direction. Horizontal grid spacing of the Moho interface, however, is, in accordance with the CSS resolution capability, 6km which then is refined to 2 km before integrating in the 3D model.

As the first step toward a 3D seismic model of the Alpine belt, an internally consistent data base of CSS model information from the Alpine network of CSS profiles is established (Section 3.1).

CSS-derived structural data is well suited to model the Moho in the Alpine region. In order to account for the importance of this interface, careful modeling of the compiled structural CSS data using the method outlined in Section 2.3.1 is performed (Section 3.2).

With respect to this interface, CSS velocities are volumetrically modeled and, together with the low velocity sedimentary basins as a priori velocity information, are integrated in a pre-defined Alpine reference velocity model (Section 3.3).

## 3.1 CSS Data Compilation for 3D Model Construction

The controlled-source seismic (CSS) profile network in the central and western Alpine region consists of more than 200 reversed or unreversed refraction / wide-angle reflection profiles (short: refraction profiles), 25 fan observations, and 30 near-vertical reflection profiles (see Fig. 3.1). Overviews of seismic experimental activity in the Alpine region are given by, e.g., Giese et al. (1976), Roure et al. (1990), Meissner and Bortfeld (1990), Meissner et al. (1991), Freeman and Mueller (1992), Buness (1992) and references therein, Montrasio and Sciesa (1994), Prodehl et al. (1995), Ansorge and Baumann (1996).

These seismic data and their interpretations have now been compiled to obtain a

CSS data base that is used for 3D seismic model construction as described in Chapter 2. Experimental data such as shot points, profile direction and profile type are separately compiled for refraction and near-vertical reflection experiments and stored in the files *RFRprof.dat* and *RFLprof.dat* (see Appendix A.1). Published structural CSS models were evaluated with respect to the required seismic parameters for 3D model construction as outlined in Section 2.2. The methodological considerations to derive these seismic parameters from published CSS models is outlined in Section 2.3. The parameters are compiled in a data base containing structural and velocity information from the Alpine Moho interface (*moho.dat*). A detailed description of file formats is given in Appendix A. CSS experimental and model data can be displayed and controlled graphically with the program *SeisMap* (see Appendix A.2). *RFRprof.dat*, *RFLprof.dat*, and *moho.dat* are input files to the 3D model construction process (Sections 3.2 and 3.3, and Appendix B).

File *moho.dat* stores seismic parameters for each profile. Within profiles, seismic parameters are grouped to structural parameters, weighting parameters, velocity parameters, and profile parameters with experimental and interpretational characteristics of the profile. Table 3.1 depicts an example of one profile as it is stored in *moho.dat* for the refraction profile ALP87 in Figure 3.2, interpreted by Maurer and Ansorge (1982).

Section 3.1.1 outlines the scheme to convert structural Moho data from CSS models to data base format (see structure parameters in *moho.dat*, Tab. 3.1), explains weighting of structural data (weighting parameters) and displays compiled structural CSS model information from the Moho in the Alpine region. Section 3.1.2 describes and displays the velocities associated to the Alpine Moho (see velocity parameters in *moho.dat*, Tab. 3.1).

### 3.1.1 Structural Moho Data

The most striking feature on the Alpine CSS record sections are the reflecting phases from the Moho interface (PmP), that can be observed on almost every wide-angle and some near-vertical reflection profiles. PmP phases have been interpreted in order to estimate crustal thickness, i.e. depth of the Moho interface, below the profiles.

Alpine Moho depths have been compiled before by, e.g., Ansorge et al. (1987), Kissling (1993), and an extended version of this preliminary compilations can be found in Baumann (1994). The compilation by Baumann (1994) mainly includes weighted Moho depth points from the central Alps with some of them being off-line (3D) migrated by hand. A new attempt for a consistent compilation of structural data from the central and western Alpine Moho has been undertaken within the scope of this work. Different from previous compilations, structural data has been compiled by mapping the actually imaged reflecting segments on the interface. They are stored as unmigrated (some 1D interpretations) or 2D-migrated (2D ray-traced interpretations) reflecting elements in the Moho data base *moho.dat*. 3D- and off-line migration is performed during the interface modeling procedure.

**Table 3.1** Format and parameter description of seismic parameters stored in the Moho data base (*moho.dat*). The shaded area is an extract from the file *moho.dat*. Parameter values are derived from the wide-angle reflection profile ALP87 interpreted by Maurer and Ansorge (1992). RFR: reflectors derived from refraction and wide-angle reflection profiles; FAN: fan observations; RFL: near-vertical reflection profiles. M1-M4: structural depth points. For detailed parameter description and format specification see Appendix A.

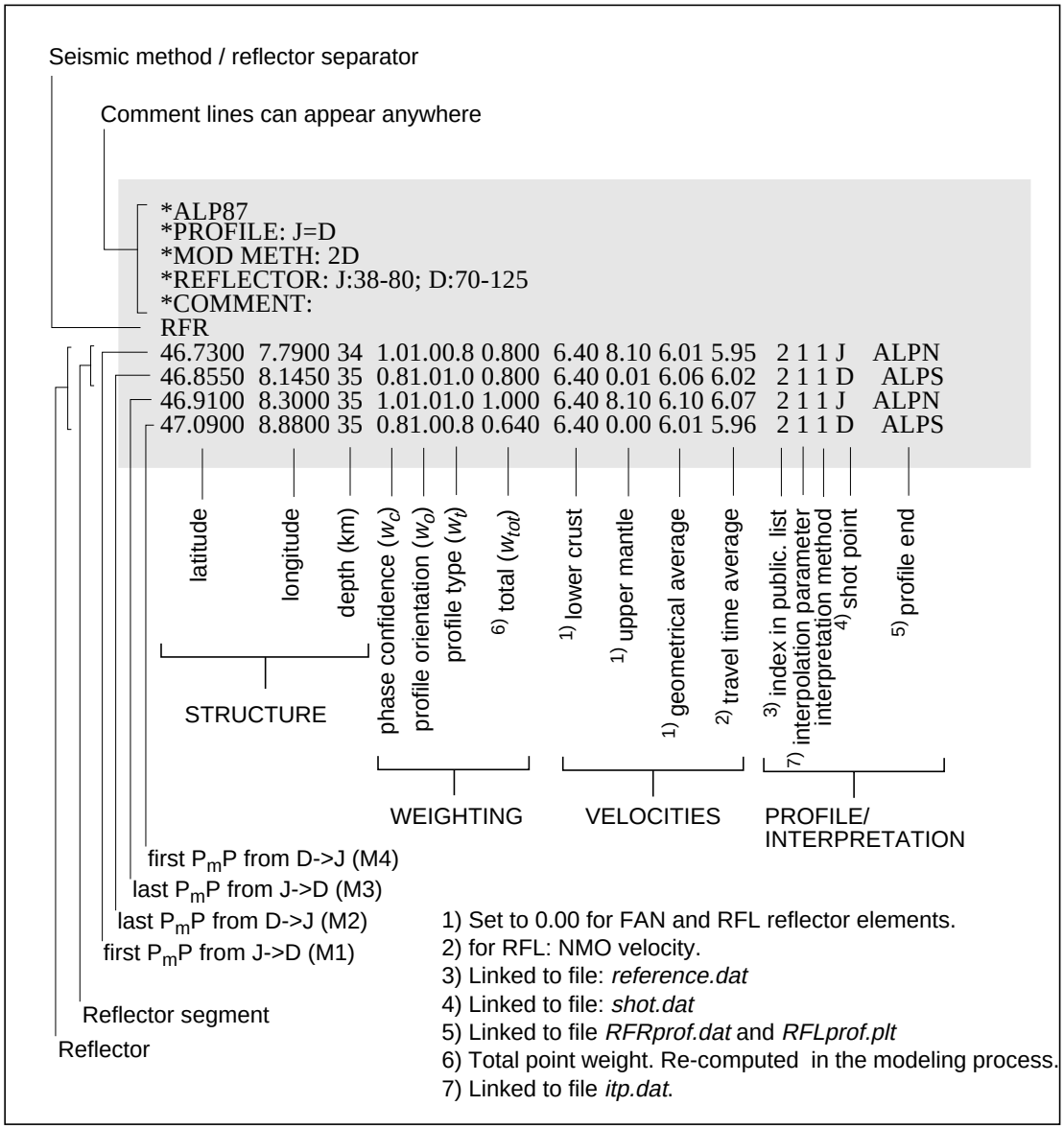


## *Parametrization of structural data*

2D ray-traced seismic models provide continuously ray covered parts on Moho interfaces which are referred to in the following as reflectors. Reflectors may be imaged by phases reflecting from different shotpoints (bold interface line in Fig. 3.2a and b). Such reflector elements are defined by start and end points (structural depth points, see M1-M4 in Fig. 3.2 and Fig. 3.3a) from first and last observed $P_mP$ phases in the seismogram

sections. Juxtaposed and/or overlapping reflector elements build up reflectors (see Fig. 3.3). Reflectors are stored in *moho.dat* using the properties of the structural depth points (see Tab. 3.1). In case of relative depth variation along reflector elements they are splitted up in juxtaposed, linear parts, each one defined by two structural depth points.

Reflectivity patterns identified as interface from near-vertical reflection profiles normally show increased relative depth variations due to the higher resolution capability of this method compared to refraction methods. Such reflectors are, therefore, represented by juxtaposed linear parts in the same way as done for ray-traced reflector elements.

The linear parts along reflectors, each defined by neighboring structural depth points, are termed reflector segments (see rs1, rs2, rs3 in Fig. 3.3a). Reflector segments are the modeling units for seismic interface modeling as explained in Section 2.3.1 and applied to the Alpine data in Section 3.2.

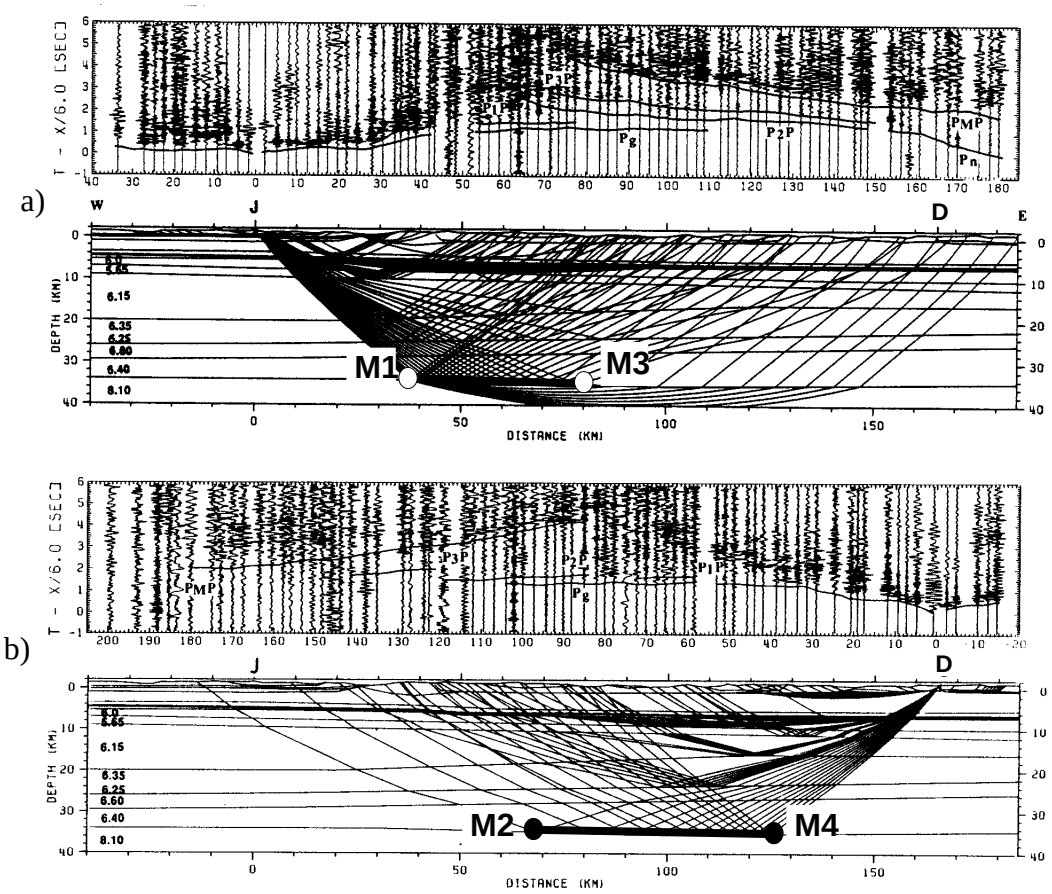


**Figure 3.2** Interpretations of the ALP87 refraction and wide-angle reflection profile after Maurer and Ansorge (1992). P-velocity models are derived by 2D ray-tracing from shot point J to the east (a) and from shot point D to the west (b). Two reflector elements from the Moho (bold line) and four structural depth points (points labeled M1-M4) are shown (see text). For profile location see Fig. 3.1.

a)

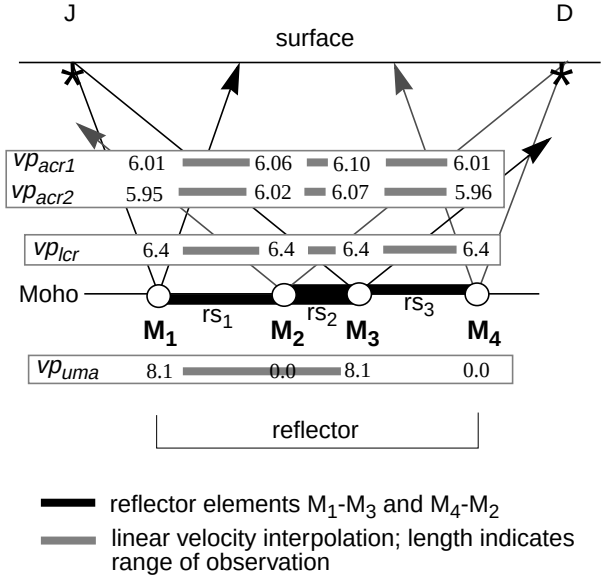


b)

| | $w_c$ | $w_o$ | $w_t$ | $w_{tot}$ |
|---|---|---|---|---|
| **$M_1$** | 1.0 | 1.0 | 0.8 | 0.8 |
| **$M_2$** | 0.8 | 1.0 | 1.0 | 0.8 |
| **$M_3$** | 1.0 | 1.0 | 1.0 | 1.0 |
| **$M_4$** | 0.8 | 1.0 | 0.8 | 0.64 |
| rs1 | 1.0 | 1.0 | 0.8 | **0.8** |
| rs2 | 1.0 | 1.0 | 1.0 | **1.0** |
| rs3 | 0.8 | 1.0 | 0.8 | **0.64** |

**Figure 3.3** a) Schematic ALP87 model with compiled structural and velocity parameters shown (see Figs. 3.2 and 3.3). M1-M4 are structural depth points. $M_1$ and $M_4$ define the beginning, $M_2$ and $M_3$ the end of individually observed reflector elements (according to continuously observed $P_MP$ phases). The continuously ray covered part of a seismic interface is termed reflector. $rs_1$ - $rs_3$ are the linear reflector segments, defined by two neighboring structural depth points and are used to assign different weighting factors along the reflector. $vp_{acr1}$ = geometry based average crustal velocity. $vp_{acr2}$ = traveltime based average crustal velocity. $vp_{lcr}$ = lower-crust velocity. $vp_{uma}$ = upper-mantle velocity. See text for explanation.
b) Table of weighting factors (see text and Tab. 3.2) for phase confidence ($w_c$), profile orientation ($w_o$) and profile type ($w_t$) applied to the reflector elements (resp. their structural depth points) of the ALP87 refraction profile. $w_c$, $w_o$, $w_t$ , and the total reflector segment weight $w_{tot}$ (shaded boxes) for reflector segments are derived. $w_{tot}$ is used to calculate depth error estimations.

### *Weighting of reflectors*

The compiled structural model information shows a large range of uncertainty with age of the data, mainly because of improved acquisition and interpretation techniques over the last years. Data quality is increased by the trend towards still smaller shot and receiver spacing and data interpretation is becoming more reliable using modern ray-tracing techniques. Furthermore, complex tectonic settings with pronounced lateral variations in the area of investigation may strongly influence the reliability of the interpreted data. In order to account for the varying confidence in the structural Moho data, reliability for each reflector is quantified.

Reflectors are weighted using the weighting scheme introduced by Baumann (1994). The scheme combines separate weighting criteria for wide angle and near vertical reflection surveys (see Tab. 3.2). Reflector elements derived from wide angle profiles are weighted considering data confidence ($w_c$) (phase correlation, interpretation method), profile orientation in respect to the three-dimensional tectonic setting ($w_o$) and profile type (reversed, unreversed profiles, fans) ($w_t$). Reflector elements from near-vertical reflection profiling are attributed with weights for signature quality ($w_{cr}$), migration ($w_{mig}$) and projection types ($w_{proj}$) (Tab. 3.2).

**Table 3.2** Weighting scheme for reflector elements (after Baumann, 1994). *) Extension made in this work: Accounting for strong Pn phases (sub-Moho refracted energy).

Wide-angle reflection and refraction profiles:

*Data quality, phase confidence ($w_c$)*:
1.0 = Very confident.
0.8 = Confident
0.6 = Likely
0.4 = Poorly constrained.
0.2 = Speculative

*Profile orientation ($w_o$):*
1.0 = Along strike profiles; 0 <= alpha <= 10.
0.8 = Oblique profiles; alpha > 10.

*Profile type, ray coverage ($w_t$):*
1.0 = Reversed refraction profile.
0.8 = Unreversed refraction profile.
1.0 = Fan connected with reversed profile.
0.6 = Fan connected with unreversed profile.
0.4 = Unconnected fan.
0.4 = Interface covered by refracted rays. *)

Near-vertical reflection profiles:

*Reflectivity signature ($w_{cr}$):*
1.0 - 0.2 = Confidence rate of the reflectivity signature.

*Migration criteria ($w_{mig}$):*
1.0 = Migration with independent velocities from refraction surveys.
0.9 = Migration with stacking velocity from reflection profiles. Migration velocity model from refraction data projected over distances with no considerable structural changes.
0.8 = Else

*Projection criteria ($w_{proj}$):*
1.0 = Projection distance < 4 km.
0.9 = Projection distance > 4 km and < 10 km.
0.8 = Projection distance > 10 km.

Along reflectors, weighting may vary due to different phase quality, reversed and/ or overlying reflector elements from different explosive locations. In order to account for changing weights along the reflectors, each reflector segment is weighted using the weighting factors attached to the nearby structural depth points. In case of overlapping reflector elements with different confidence weights ($w_c$), the higher $w_c$-value is assigned to the corresponding reflector segment. Total weighting factors ($w_{tot}$) were build for each reflector segment by multiplying the individual weights:

$$w_{tot} = w_c \cdot w_o \cdot w_t \qquad (3\text{-}1)$$

for wide-angle reflection data and

$$w_{tot} = w_{cr} \cdot w_{mig} \cdot w_{proj}. \qquad (3\text{-}2)$$

for near-vertical reflection data. The derivation of reflector segment weights from reflector element weights is shown in Figure 3.3b using values derived from of the ALP87 profile (see Tab. 3.1 and Fig. 3.2).

Depth error ranges ($z_{err}$) are calculated during the interface modeling procedure (Section 3.2) by transforming the total weighting factor ($w_{tot}$) to depth scale considering data resolution which is influenced by investigation method and depth. Baumann (1994) considered an average frequency content of 6 hz for Moho reflections from ac-

tive sources and an average Alpine Moho depth of 40 km to derive, assuming perfect profile design and data, a value of 3 km for the vertical component of the fresnel volume ($frsn_{err}$). The weight dependent depth uncertainty is considered to be:

$$z_{err} = frsn_{err} / w_{tot} \qquad (3\text{-}3)$$

with $frsn_{err}$ = +/- 3 km and $w_{tot}$ according to Equations 3-1 or 3-2.

About 120 reflectors from wide-angle reflection surveys, 25 reflectors from fan registrations and 15 reflectors (reflectivity signatures) from near-vertical reflection profiling were compiled (Appendix A) from the available published CSS data and models in the Alpine region. Figure 3.4a displays the depth values along the imaged, unmigrated or in-line migrated reflectors. Although all profiles are shown in Figure 3.4a, not all pro-

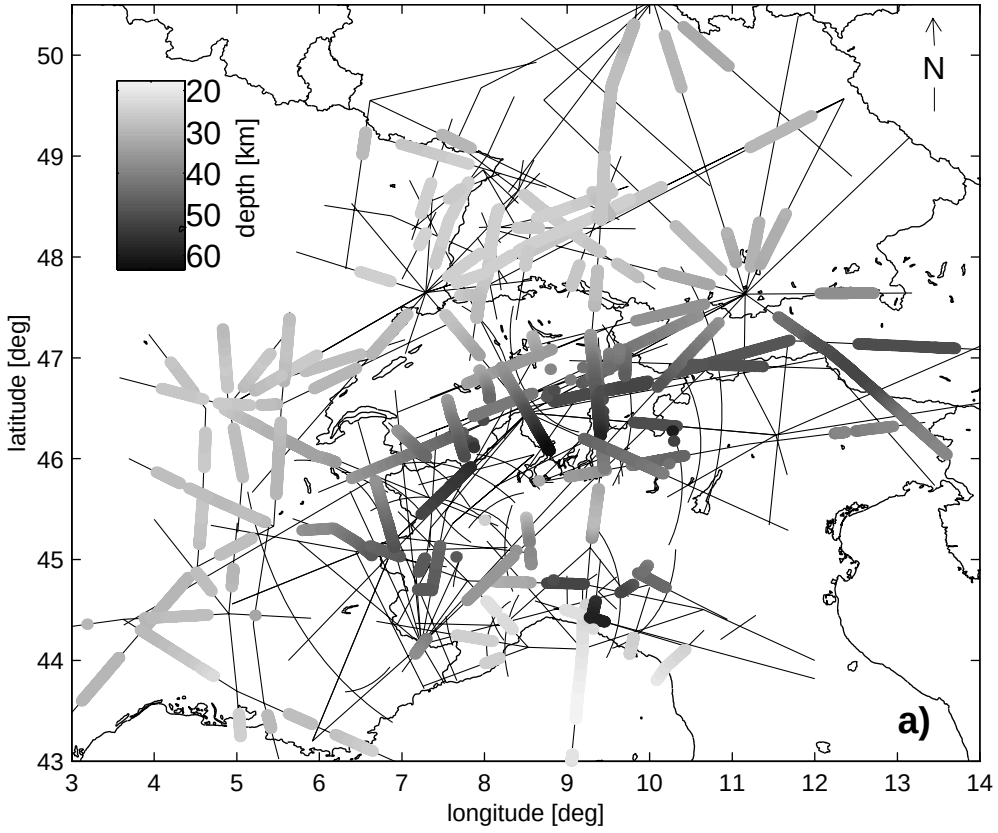


**Figure 3.4** a) Spatial location (depth in km) of unmigrated (some 1D interpretations) and in-line migrated (2D interpretations) reflectors of the Moho interface obtained by wide-angle and near-vertical reflections obtained by controlled-source seismic experiments in the Alpine region. Gray scale represents reflector depths. The entire CSS profile network is shown (thin lines) that contains also profiles which do not provide information about the Moho. Geographical coordinates are indicated.
b) Weighting index along reflectors obtained by wide-angle and near-vertical reflections from the Moho interface. Color on reflectors shows total reflector segment weights ($w_{tot}$). See text.
c) Depth error estimation along the reflectors (represented by colors). Depth error values are derived using $z_{err} = frsn_{err} / w_{tot}$ , where $frsn_{err}$ is the vertical Fresnel volume axis (set to +/- 3 km for Moho reflections) and $w_{tot}$ the total weighting factor.

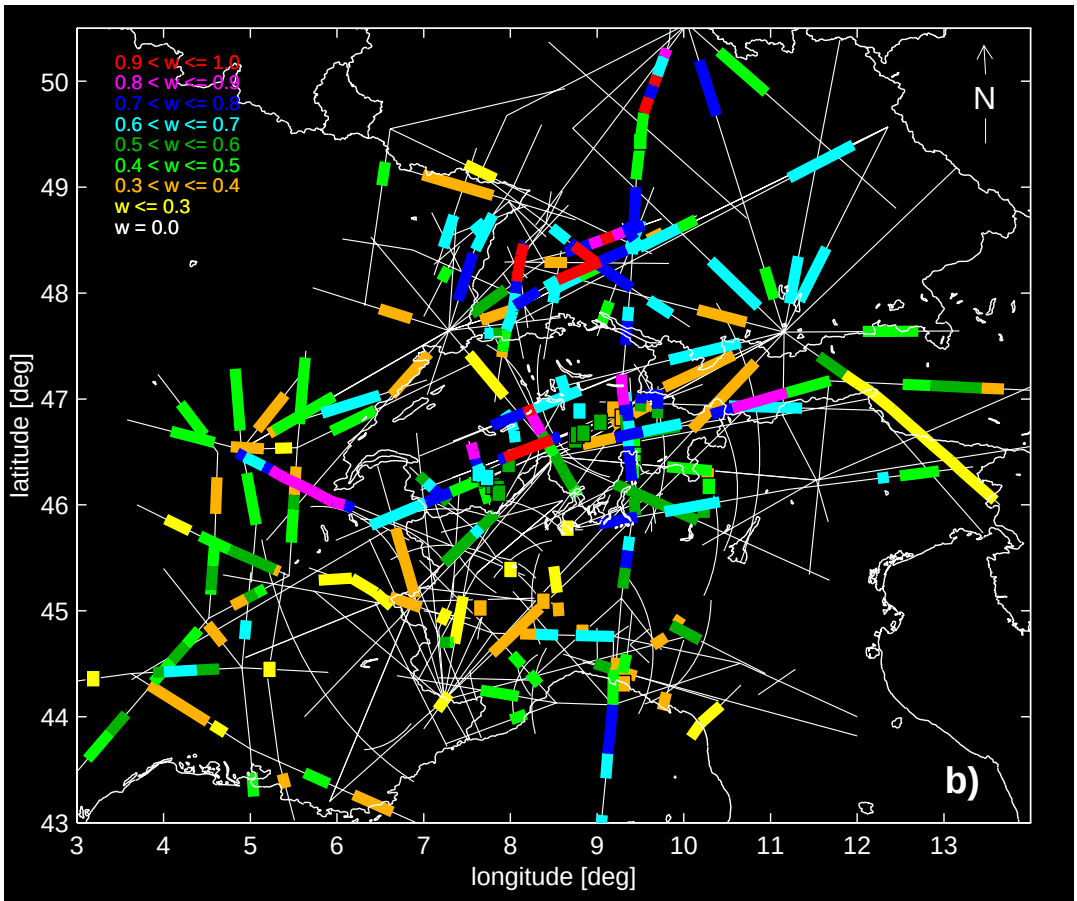
0.9 < w <= 1.0
0.8 < w <= 0.9
0.7 < w <= 0.8
0.6 < w <= 0.7
0.5 < w <= 0.6
0.4 < w <= 0.5
0.3 < w <= 0.4
w <= 0.3
w = 0.0
N
b)
latitude [deg]
longitude [deg]
50
49
48
47
46
45
44
43
3
4
5
6
7
8
9
10
11
12
13

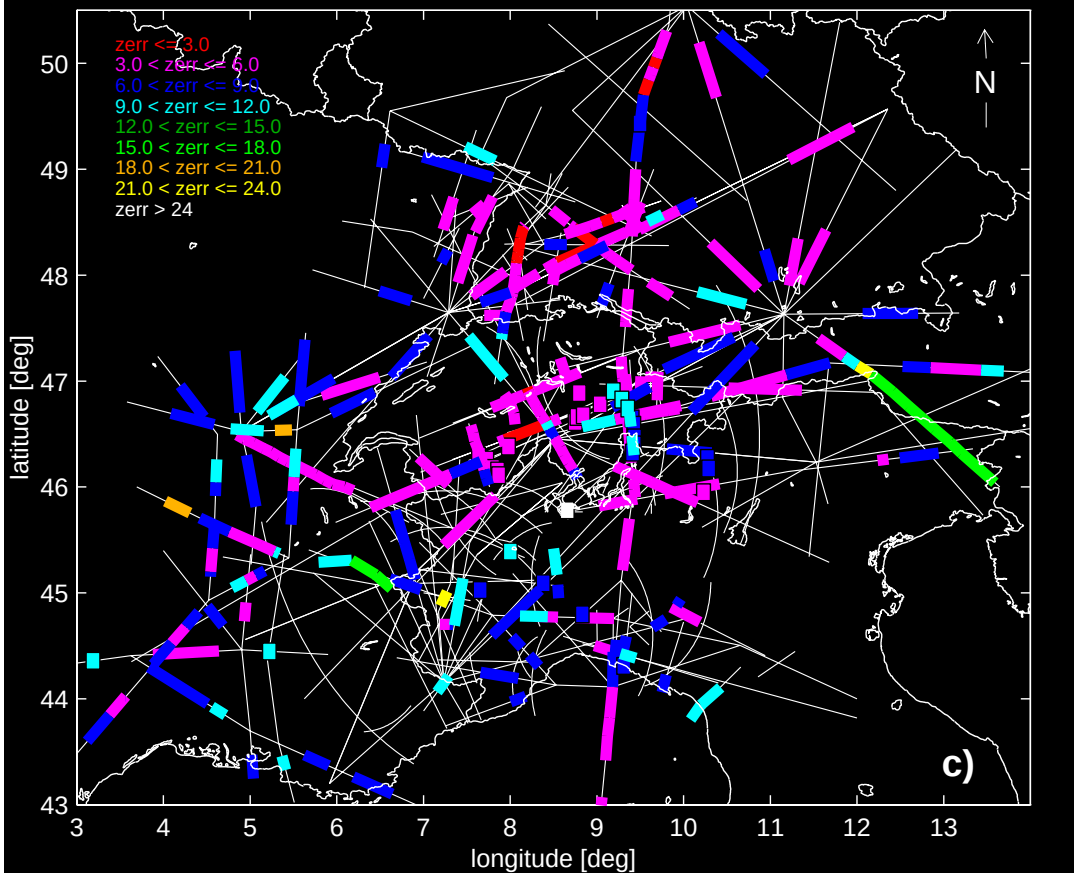
zerr <= 3.0
3.0 < zerr <= 6.0
6.0 < zerr <= 9.0
9.0 < zerr <= 12.0
12.0 < zerr <= 15.0
15.0 < zerr <= 18.0
18.0 < zerr <= 21.0
21.0 < zerr <= 24.0
zerr > 24
N
c)
latitude [deg]
longitude [deg]
50
49
48
47
46
45
44
43
3
4
5
6
7
8
9
10
11
12
13

files provide structural information about the Moho interface. In general, refraction profiles with lengths greater than about 150 km - depending on crustal thickness and velocity - continuously display a wide-angle reflection from the Moho. For details on interpretational characteristics of individual profiles, the reader is referred to the Moho data base file and the indicated references therein. Figure 3.4b shows total weighting factors ($w_{tot}$) assigned to reflector segments. Highly rated structural Moho information is obtained along the EGT profile (partly reversed profiles with reliable phase quality and correlation), from the Alpine longitudinal profiles ALP75, ALP77, ALP87 and AAR88 (partly reversed along-strike profiles), from the ECORS-CROP reflection studies in the Western Alps (migrated sections with reliable reflectivity signature) and from profiles in southern Germany (partly reversed along-strike profiles with reliable phase quality and correlation). The distribution of total weighting factors ($w_{tot}$) for the individual seismic methods (wide-angle, fan and near-vertical reflections) is shown in Figure 3.5. Finally, depth uncertainties, obtained from weighting factor and reflector segment depths using Equation 3-3, are displayed in Figure 3.4c.

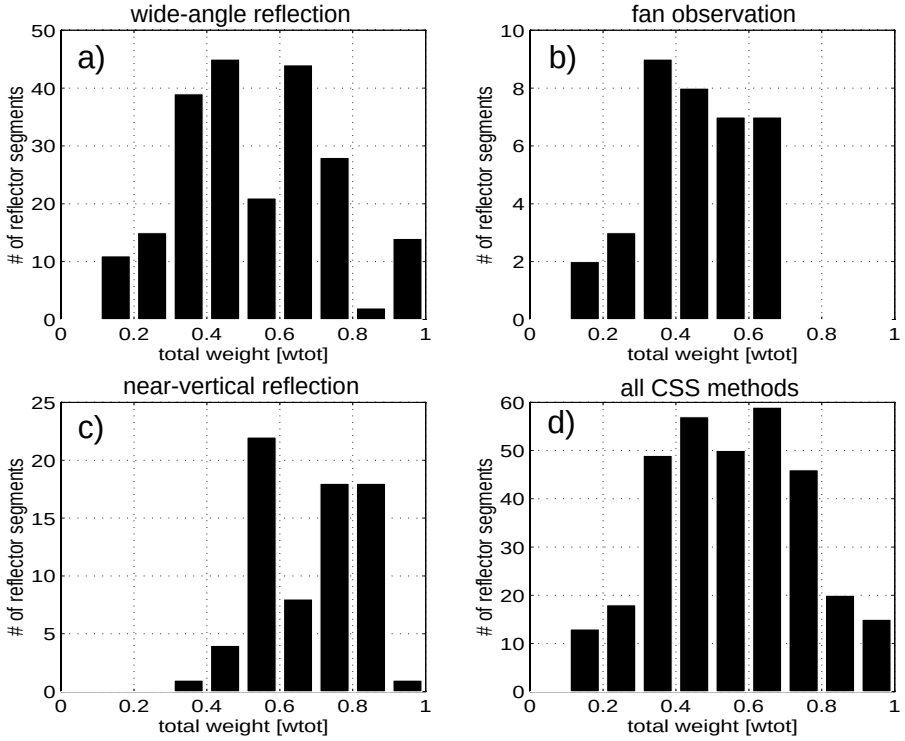


**Figure 3.5** Distribution of the total weighting factor ($w_{tot}$) for reflector segments (see Fig. 3.4b) derived from wide-angle reflection (a), fan observation (b) and near-vertical reflection data (c). d) Distribution of weighting factors summed up for all CSS methods.

### 3.1.2 Crustal Velocity Information

The methodological procedure to derive average crustal velocity, lower-crustal and upper-mantle velocities from CSS refraction and wide-angle reflection models is dis-

cussed in Section 2.3.2. In Figure 3.6a velocity values, derived from the ALP87 profile (see Fig. 3.2) and stored in *moho.dat* (see Tab. 3.1), are displayed. Both profiles show well constraint lower-crustal velocities ($vp_{lcr}$= 6.4 km/s). Upper-mantle velocity is measured by Pn phases only from shotpoint J ($vp_{uma}$= 8.1 km/s). Average velocities are computed according to Equations 2-1 and 2-2 (see Section 2.2). The velocity parameters are 'attached' to the structural depth points (M1-M4) and their unmigrated or in-line migrated vertical positions in the 3D model defined by the 3D model parameterization (see Fig. 2.3 in Chap. 2). Average velocities are later (during the velocity modeling process) averaged over the distance of reflector segment lengths. Measured lower-crustal and upper-mantle velocities are linearly interpolated between the structural depth points (M1-M4) along the reflector segments. Near-vertical reflections and fan observations reveal no information about lower-crust and upper-mantle velocity. Figure 3.6a-c display lower-crustal velocity and upper-mantle velocity that are sampled by CSS methods along the unmigrated reflectors from the Alpine Moho interface and the associated average crustal velocity.

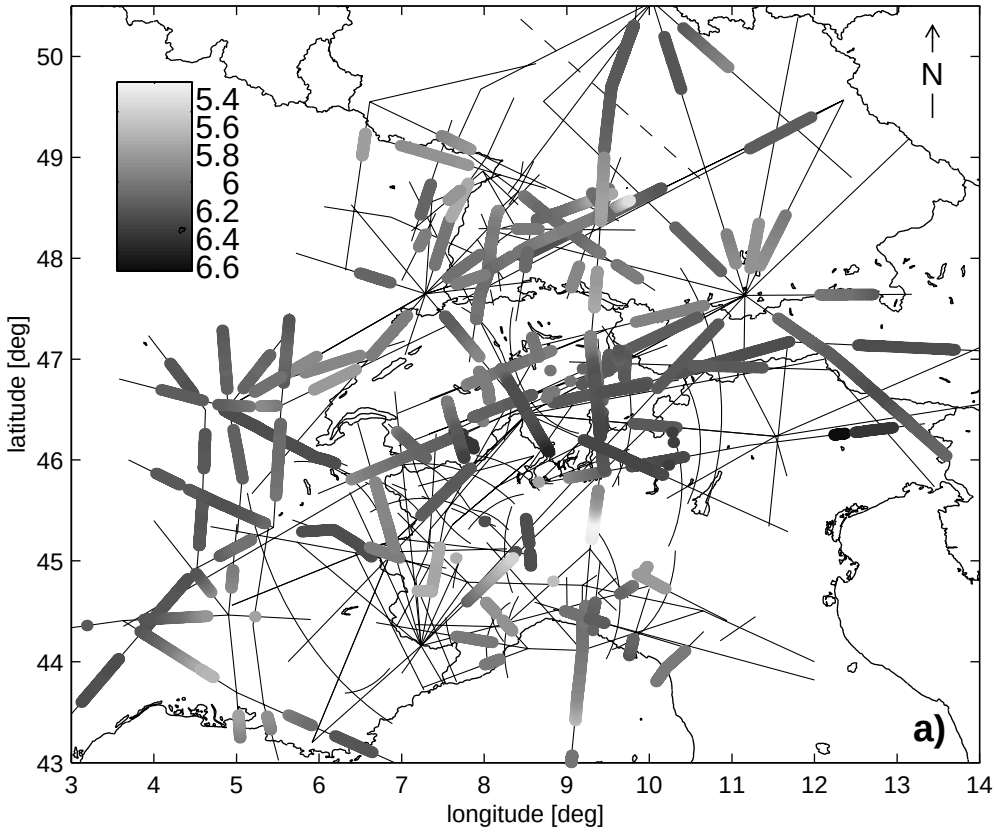


**Figure 3.6** P-velocities (km/s) derived from CSS profiling. a) Average crustal velocity obtained from wide-angle reflection and refraction models (Eq. 2-2) and used for depth migration of near-vertical reflections. b) Lower-crust velocity derived from CSS wide-angle reflection and refraction profile data. c) Upper-mantle velocity derived from the Pn-phase on refraction profiles.

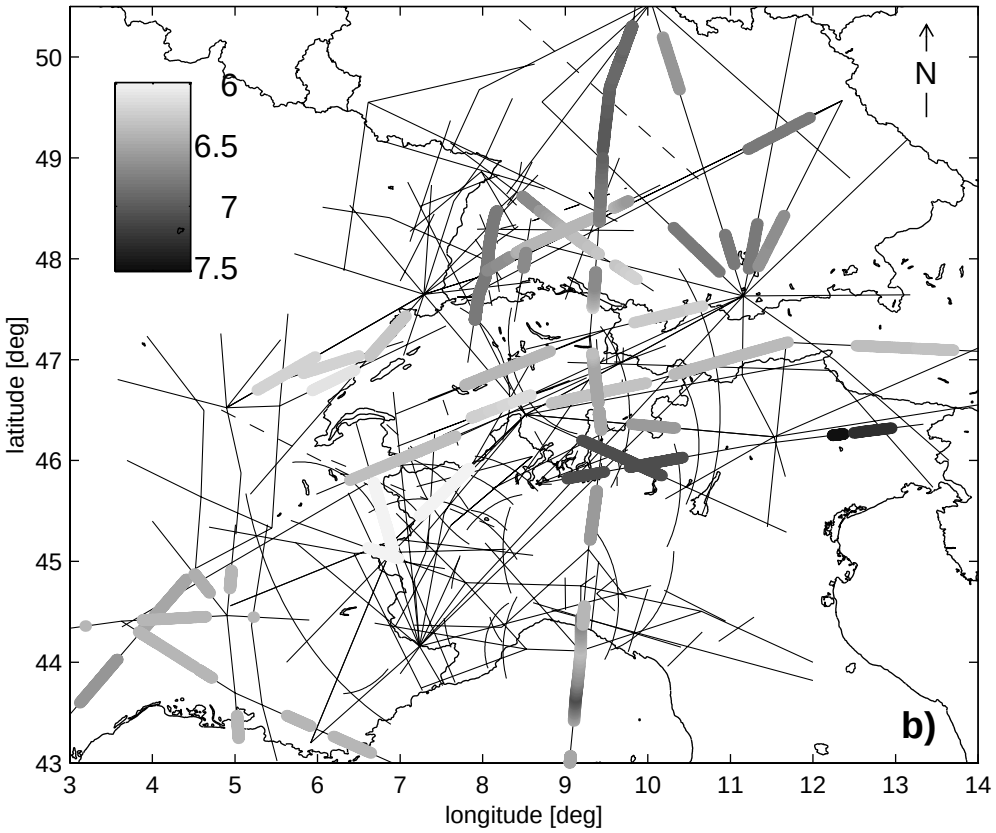
6
6.5
7
7.5
N
b)
latitude [deg]
longitude [deg]
50
49
48
47
46
45
44
43
3
4
5
6
7
8
9
10
11
12
13
14

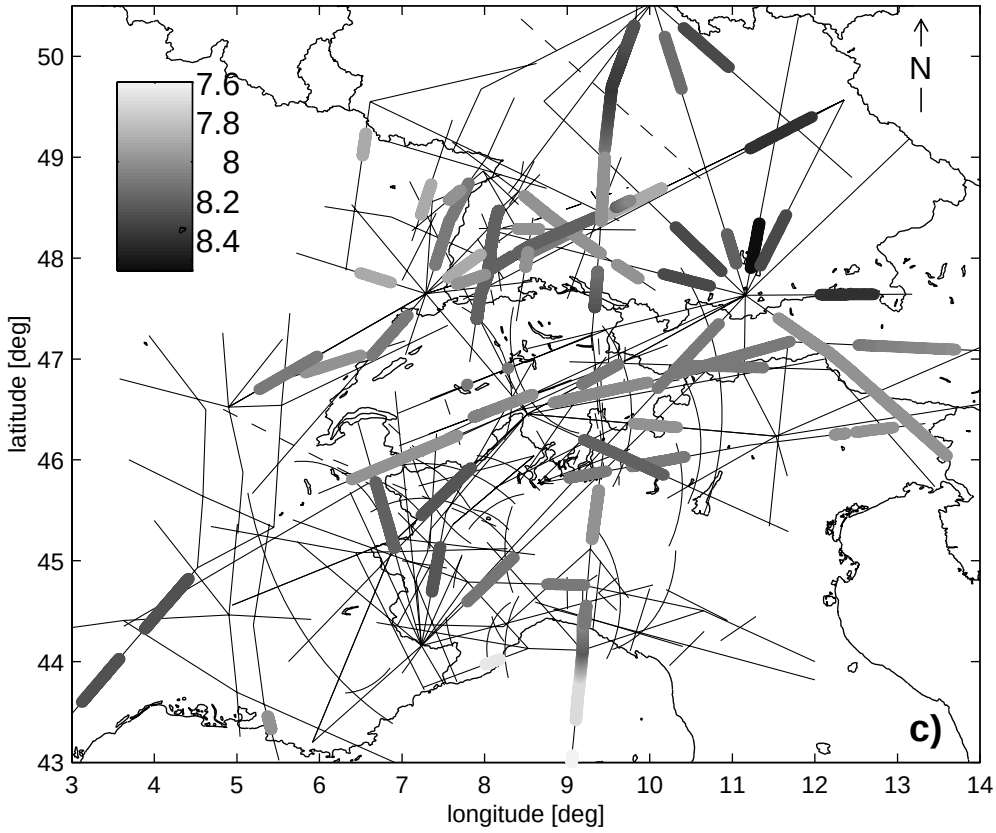
7.6
7.8
8
8.2
8.4
N
c)
latitude [deg]
longitude [deg]
50
49
48
47
46
45
44
43
3
4
5
6
7
8
9
10
11
12
13
14

## 3.2 3D Modeling of the Crust-Mantle Boundary

*Characteristics of the Moho*

The primary geophysical information concerning the nature of the crust-mantle boundary (or Moho; Mohorovicic, 1909) comes from controlled-source seismic (CSS) experiments. The Moho is best visible using CSS techniques due to its relatively shallow depth of 25-60 km below continents and the strong velocity contrast being close to a first-order discontinuity (Giese et al., 1976; Braile and Chiang, 1986; Mooney and Brocher, 1987). It is a key horizon guiding the identification and interpretation of crustal and upper-mantle phases in controlled-source seismic sections. Data from refraction profiles are generally interpreted using layered 1D or 2D models that approximate the Moho as a first-order discontinuity in velocity where the P-velocity increases from 6.8-7.2 km/s in the lower crust to the range of 7.8 - 8.4 km/s in the upper mantle (e.g. Egloff, 1979; Ye et al., 1995). Deep seismic reflection profiling infers a rather laminated transition zone of several kilometers thickness for the crust-mantle boundary (Braile and Chiang, 1986; Deichmann et al., 1986).

The observation of Pn and PmP arrivals on most Alpine refraction profiles, as well as the general continuity of these phases, indicate that the Moho exists virtually everywhere throughout the Alpine sub-surface and is generally a continuous feature (see Section 3.2.1). However, the resolution of the method may not be sufficient to determine the fine structure of the Moho such as it is provided, for example, by near-vertical reflection profiling (Holliger, 1991).

Careful attention has been paid to the derivation of the 3D Alpine Moho interface. Beside the role of a seismic key horizon, the relief of the Moho interface, i.e. its lateral continuity, is of primary interest for models of tectonic evolution and for crustal balanced cross-section techniques (Butler, 1986; Laubscher, 1988; Schmid, 1992; Hubbard & Mancktelow, 1992). Furthermore, it is used as density horizon for gravity modeling (Kissling, 1980; Schwendener, 1984; Holliger and Kissling, 1992). This work concentrates on estimating effects of seismic data scattering caused by the 3D structure and the high velocity contrast of the Alpine Moho (Chap. 4).

*Previous Moho maps*

The complex shape of the Alpine Moho, which is a result of the complex tectonic history of Alpine mountain building (e.g. Mueller, 1989; Pfiffner, 1992), was the topic of many geophysical studies, mainly using seismic and gravimetric data (for an overview see Baumann, 1994 and references therein). The most recent Moho maps available for the area relevant for this work (see Fig. 3.1) are those by Giese & Buness (1992), Kissling (1993), and Baumann (1994). They have been derived by hand-interpolation (Giese & Buness, 1992; Kissling, 1993) or mathematical interpolation using isostatic compensation models (Baumann, 1994) of Moho depth points. Kissling (1993) and Baumann (1994) weighted the compiled CSS structural Moho information according to the quality with which it was derived (see Section 3.1) and manually off-line migrated

the in-line migrated structural depth points in areas of pronounced 3D structure. All Moho maps were derived in order to better determine tectonic and geodynamic aspects that are related to the relief of the Alpine Moho. They all feature information gaps in areas where questionable Moho depths exist due to missing or unreliable data.

*This work*

With respect to the requirements for the Moho depth as a structural parameter of the 3D model (see Section 2.3.1), a new attempt has been made to derive the 3D topography of the Moho interface in the Alpine region. The method for interface modeling is outlined in Section 2.3.1. The basic idea behind the method is the principle of simplicity that requires maximal continuity and minimal roughness for the interface to derive. The structural data base to which this method is applied in the following has been described in Section 3.1.1 (see Fig. 3.4a-c). It consists of observed in-line migrated reflecting and refracting elements from the Moho that are represented by structural depth points with an appropriate uncertainty range along this element.

A Moho interface is modeled that overcomes information gaps by interpolation and features highest possible continuity with respect to the general smoothness of that interface and the tectonic concept of the Alpine lithosphere. Thus the simplest Moho interface in terms of roughness and continuity is derived.

Section 3.2.1 concentrates on the results of the individual modeling steps whereas for details on the method one is referred to Section 2.3.1.

Section 3.2.2 discusses the derived Alpine Moho and compares the results with previous work.

### 3.2.1 Alpine Moho Modeling

According to the distribution and density of the observed Moho reflectors (Fig. 3.4), interpolation is performed on a grid with 6 km grid spacing in both horizontal directions. With respect to the chosen grid spacing, reflector segments are sampled by structural depth points every 2 to 4 km, depending on the factor with which the reflector segments are weighted (higher weights imply higher density of structural depth points, see Section 2.3.1, Eq. 2-13).

The procedure to derive the 3D Alpine Moho interface is structured as follows. Starting with an interface of highest continuity (principle of simplicity), single Moho surfaces have been derived by initial interpolation of all structural data (see Fig. 3.4a) with various roughness values (*RGH*, see Eq. 2-8). Based on residuals for depth and for dip of reflector segments, necessary Moho offsets with minimum length (principle of simplicity) are introduced. Accounting for these offsets, an initial interpolation for three separate surfaces is carried out. It is followed by the 3D migration process that migrates the in-line migrated reflecting elements on the base of these three Moho surfaces. The final Moho interface is derived by interpolation of the 3D-migrated structural data for each of the three Moho surfaces individually.

*Initial single-surface interpolation*

To start the Alpine Moho modeling procedure as outlined in Section 2.3.1, initial interpolation is performed for surfaces with highest continuity (i.e. single surfaces with no offsets) of various roughness (*RGH*). Such interfaces are derived by taking for interpolation all CSS data in the Alpine region (see Fig. 3.4) in order to derive spatially continuous surfaces. Series of 20 spatially continuous surfaces are derived within a roughness spectra between very smooth and extremely rough. Figure 3.7 gives a perspective view of four such surfaces, $RGH_{22}$ (very smooth), $RGH_{118}$, $RGH_{520}$, and $RGH_{2040}$ (extremely rough), representing end members and intermediate roughness values.

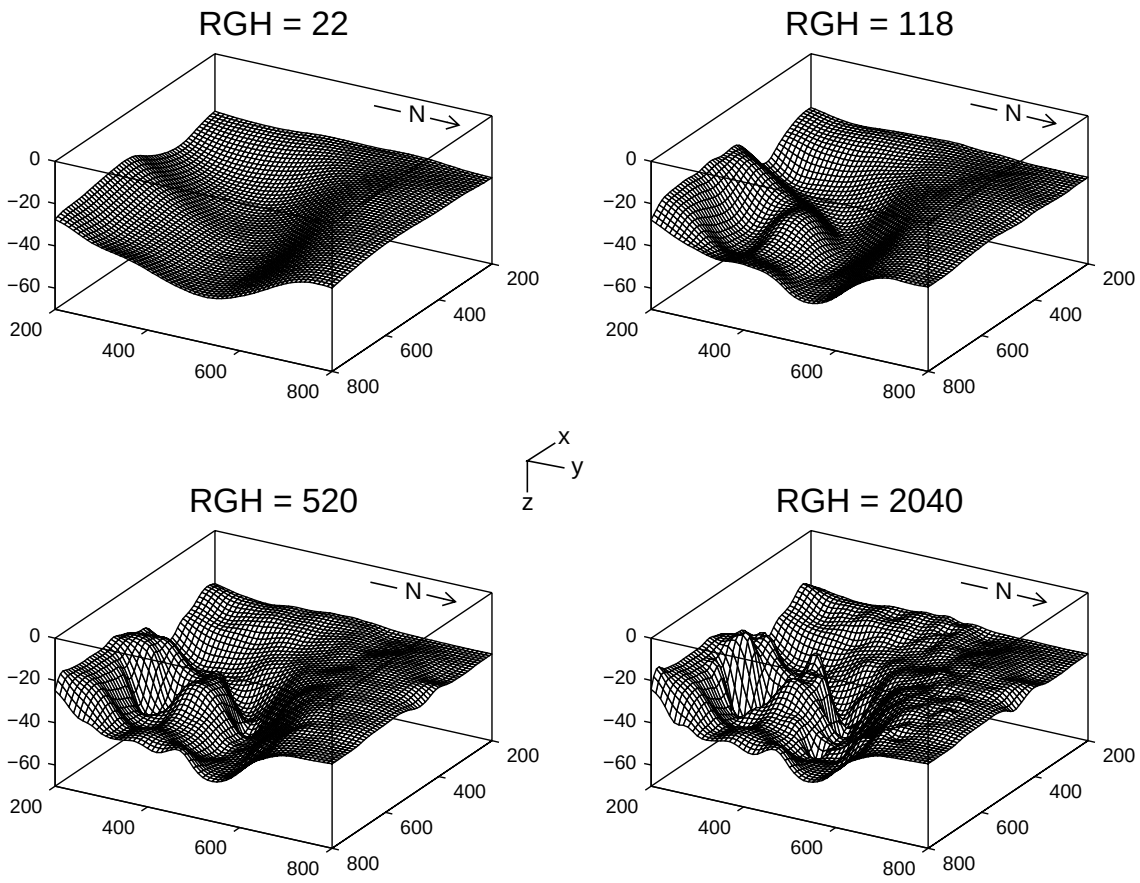


**Figure 3.7** Perspective view of four spatially continuous single surfaces of the Alpine Moho showing specific surface roughness within the roughness spectra used for the initial interpolation process: $RGH_{22}$ -, $RGH_{118}$ -, $RGH_{520}$ -, and $RGH_{2040}$ - surface.

For each of the 20 surfaces, absolute residuals for depth and dip of reflector segments are calculated by subtracting the observed from the calculated values (see Section 2.3.1 for derivation of observed and corresponding calculated value). The quality of each surface can be expressed by an average fit value that is derived by calculating the square root of the average of the squares of the residuals (root-mean-square, rms-residuals) for each surface individually. Figure 3.8 shows the rms-residuals for depth (Fig. 3.8a) and dip (Fig. 3.8b) for surfaces between a roughness of 0 (plane) and 600 (rough). Solid circles indicate surfaces depicted in Figure 3.7. A strong decrease in rms-residuals from 10 km to about 3 km for depth and a smaller decrease from 7.6° to about 5.7° for dip can be observed for increasingly rougher surfaces between roughness *RGH*=0 (plane) and about *RGH*=120 (Fig. 3.7). Beyond a surface roughness of 120, rms-residuals for depth continue to decrease slightly to about a value of 2 km near *RGH*=600 (Fig. 3.8a). For surfaces of higher roughness rms-residuals for dip slightly increase (Fig. 3.8b). This is caused by numeric oscillations by the interpolation process.

A ‘best fit’ surface from the calculated 20 surfaces must be obtained with respect to the observed depth error of about +/- 3km (see Section 3.1.1). Surfaces near *RGH*=120 (Fig. 3.8a) show rms-residuals for depth around 3 km, rapidly increasing for smoother surfaces with depth misfits that lie outside the observed optimal depth error. Surfaces with roughness higher than about 300 all fit the structural depth points within the depth error. These surfaces represent unnecessary rough Moho surfaces by trying to exactly fit the structural depth points (see f.e. $RGH_{2040}$ or $RGH_{520}$ in Fig. 3.7). Thus, based on depth residuals, a best roughness value is determined around *RGH*=120. A similar behavior is documented for rms-residuals for dip of reflector segments (Fig. 3.8b). For surfaces with roughness values around 120 dip rms-residuals show a minimum.

A best-fit surface is chosen that features a roughness *RGH*=118. Figure 3.9 depicts this $RGH_{118}$- surface by depth-isolines for the area of central and western Alps and northern Apennines. All structural depth points along the in-line migrated reflectors are used for this interpolation and are marked by small dots. In addition, structural depth points of a misfit larger than observed depth errors (significant depth misfits) are shown. Observed depth points significantly above the $RGH_{118}$-surface are represented by solid circles, those located below the $RGH_{118}$-surface by open circles. No significant depth misfits are observed outside the area shown in Figure 3.9 within the greater Alpine area. Four areas A, B, C, and D indicate regions with significant depth misfits: the south-central Alps (A), the northern part of western Alps (B), and the northern Apennines (C and D).

Before modeling Moho offsets in these areas, it must be shown, that the indicated areas of significant depth misfits (A-D in Figure 3.9) do not strongly depend on the chosen surface roughness (e.g. *RGH*=118). Figure 3.10 shows absolute depth residuals for the $RGH_{118}$-surface and for surfaces with roughness 326 (rougher) and 59 (smoother). Depth residuals in black in Figure 3.10 indicate significant depth misfits (i.e. calculated depths that lie outside the observed depth error). A-D label the areas where the depth misfits are located (compare with Fig. 3.9).

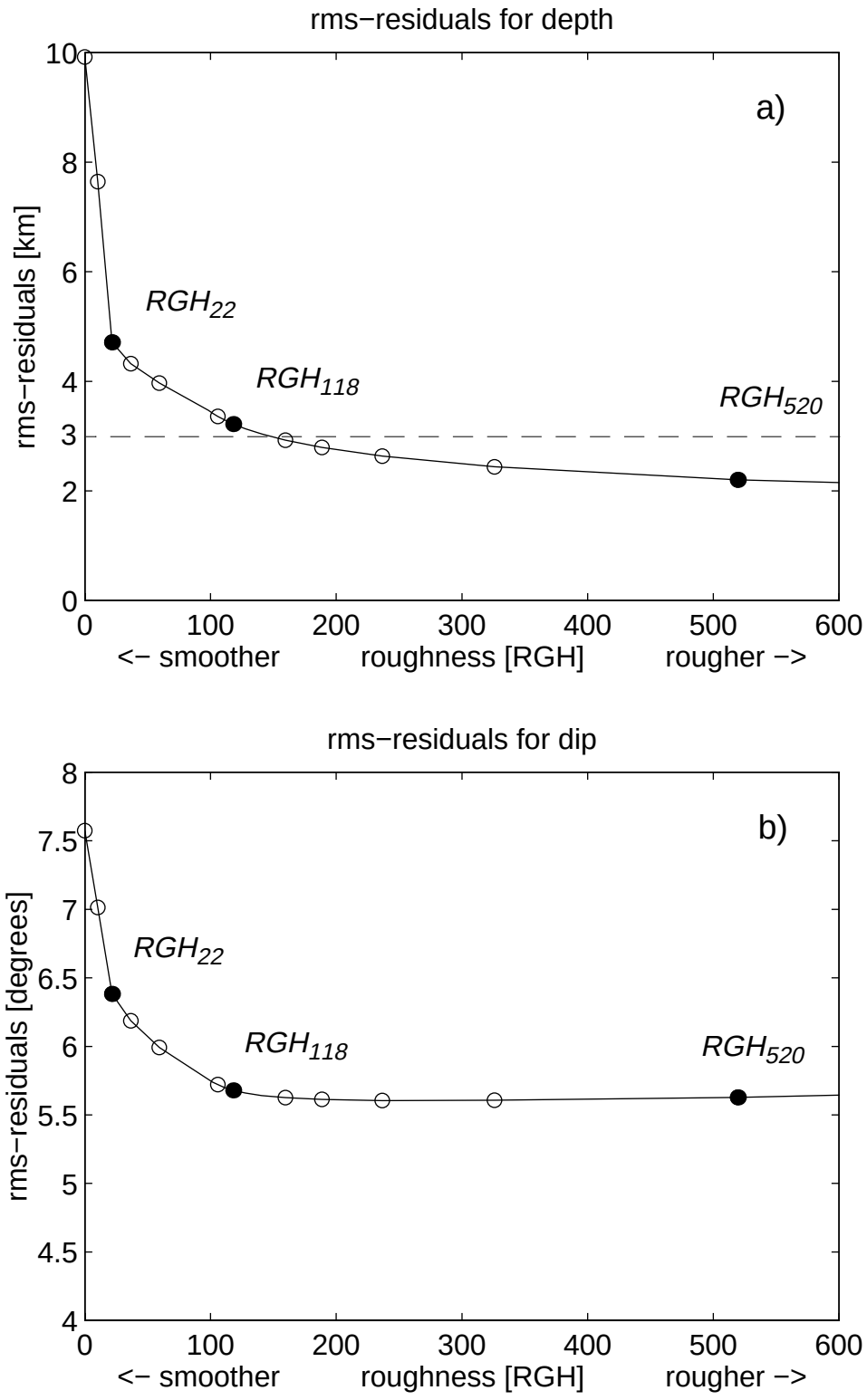


**Figure 3.8** Average fit for depth and dip of reflector segments. Rms-residuals for depth (a) and dip (b) for a series of single surfaces with roughness (RGH) between 0 (smooth) and 600 (very rough). Dashed line in (a) represents observed depth error. Solid circles indicate surfaces depicted in Figure 3.7. See text for explanation.

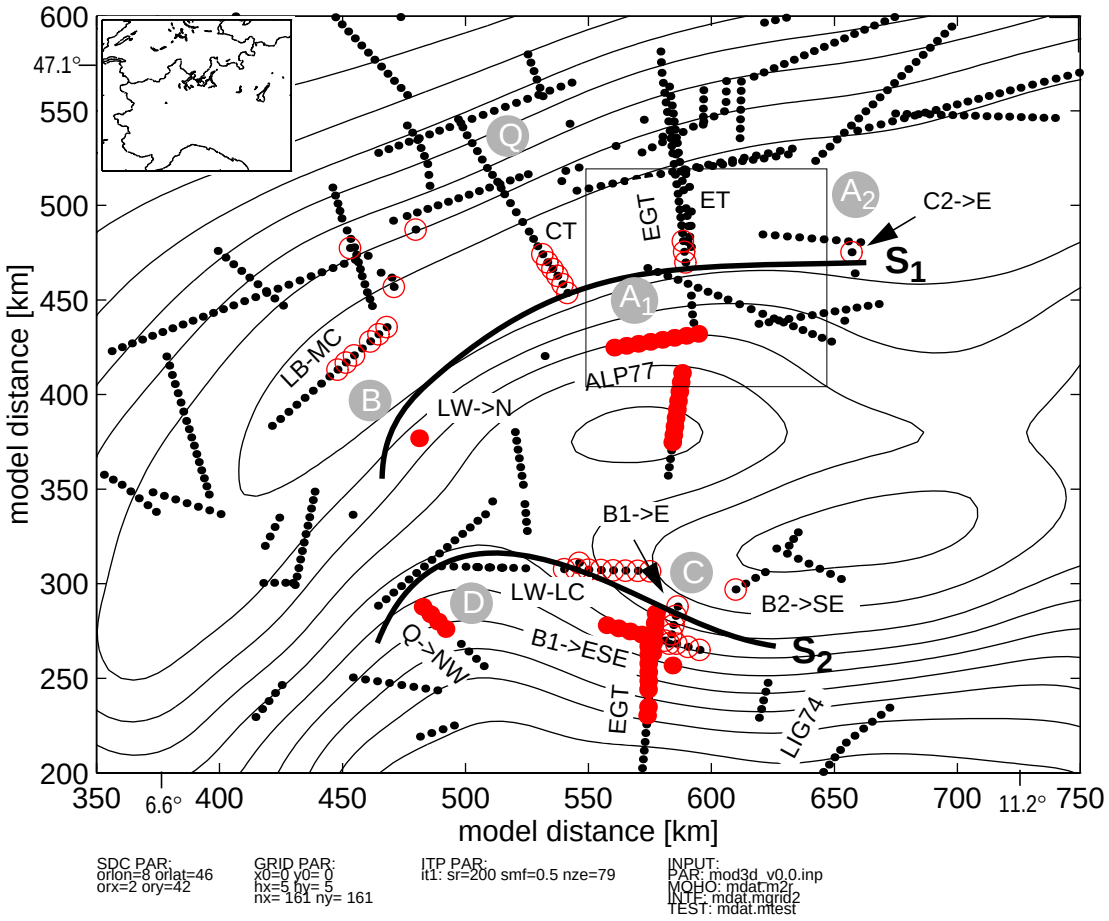


**Figure 3.9** Individual fit of structural depth points (small dots). The $RGH_{118}$-single-surface Moho (represented by depth isolines) is derived by interpolation of all in-line migrated structural depth points. Numbers label isoline depth values. Significant depth misfits lying above (filled circles) and below (open circles) the $RGH_{118}$-surface are shown. Proposed Moho offsets $S_1$ and $S_2$ are shown by bold lines. See inset in upper left corner for geographic location. Box indicates area shown in Figure 3.12. Cartesian coordinates in model distance, geographic coordinates indicated. See text for further explanations.

Figure 3.10b shows depth residuals for the $RGH_{118}$-surface as represented by isolines in Figure 3.9. The strong peaks of depth residual (in black) correspond to the significant depth misfits as indicated in Figure 3.9. Figure 3.10a depicts the depth residuals and significant depth misfits from the $RGH_{326}$-surface. It can be seen, that this rougher surface (Waldhauser et al., 1995) still shows considerable significant depth misfits in the south-central Alps (A) and the northern Apennine (C), where Moho offsets are directly imaged by seismic wide-angle data along the EGT. Smoothing the surface to a roughness of 59 (Fig. 3.10c) yields increased significant depth misfits at the same location as observed from the $RGH_{118}$-surface (Fig. 3.10b), and additional significant depth misfits that are located in area Q (see Fig. 3.9) along the strike of the central Alps. Significant depth misfits in area Q are a direct result from interpolation across the Moho offsets in area A and B by a smooth continuous surface.

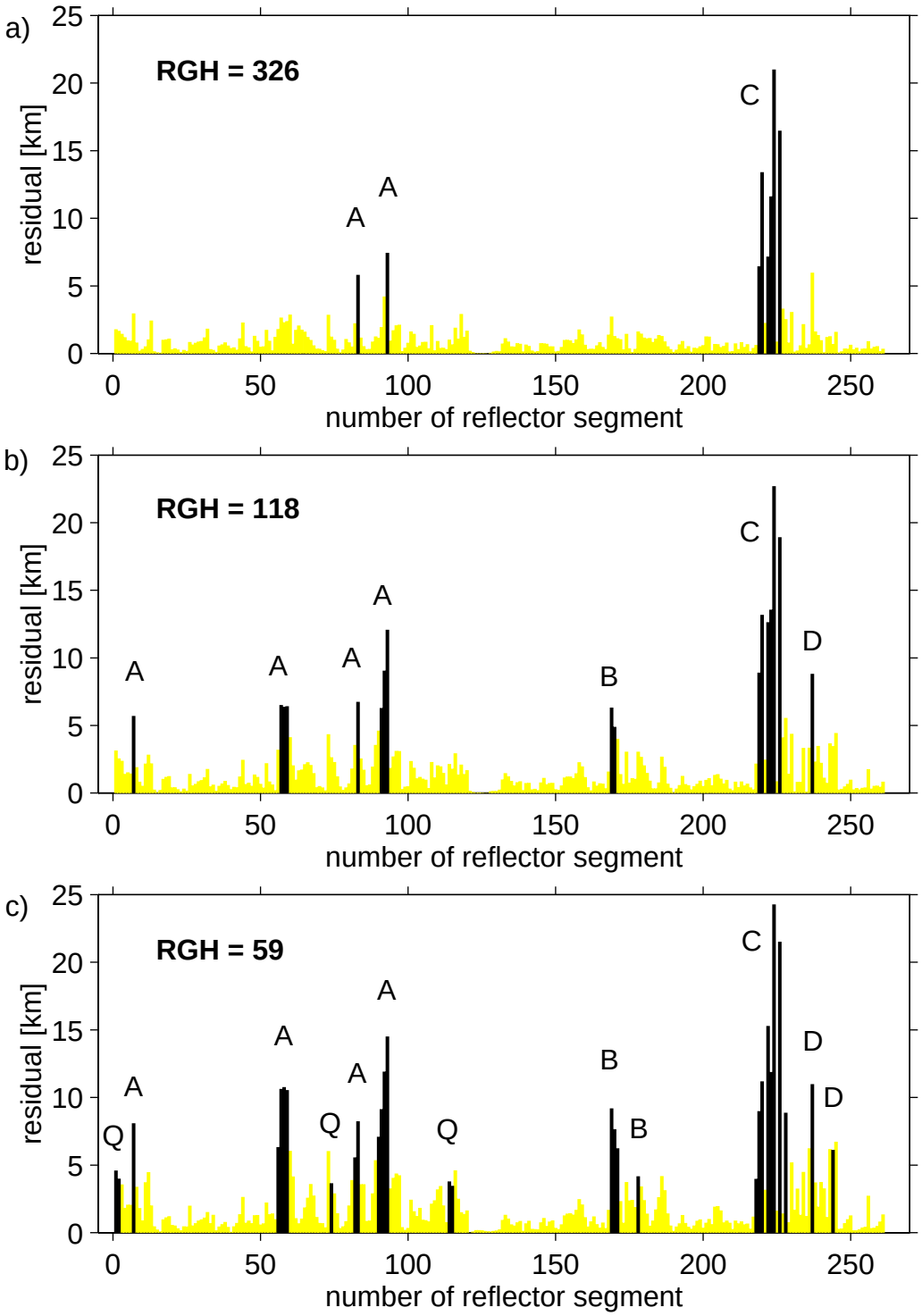


**Figure 3.10** Absolute depth residuals for single surfaces $RGH_{59}$ (a), $RGH_{118}$ (b),and $RGH_{326}$ (c). A, B, C, D and Q indicate areas where significant depth misfits (black) are observed (see Fig. 3.9).

These results show, that taking the $RGH_{118}$-surface to discuss the Alpine Moho offset modeling does not lead to considerable different offsets as for example by taking somewhat smoother or rougher surfaces. Modeling Moho offsets on the basis of observed significant depth misfits must be done with respect to obtain highest possible continuity (shortest length of offsets) for the resulting interface.

*Modeling Moho offsets: the European / Adriatic Moho transition*

The south-dipping character of the European Moho and the north-dipping Adriatic Moho are revealed by the transverse near-vertical reflection profiles CT and ET (Holliger, 1991; Holliger & Kissling, 1991; Valasek, 1992; Valasek & Mueller, 1994) and the refraction / wide-angle reflection profiles along the EGT (Ye, 92; Ye et al., 1995). On the basis of depth error estimates for the imaged reflectors, Baumann (1994) showed evidence for a seismic gap between the two oppositely down-dipping Moho's. Thus, an ESE-WNW striking Moho offset (bolt line $S_1$ in Fig. 3.9) is introduced for area $A_1$ that separates the European Moho (imaged to a depth 60 km) from the Adriatic Moho. The Adriatic Moho is imaged to a depth of 46 km by refracted rays from shotpoint A along the EGT to the north (see Ye, 1992). The reflector from the along-strike ALP77 profile (located in area $A_1$ in Fig. 3.9), that may not be accounted for by the $RGH_{120}$-surface, is assumed to belong to the Adr-Moho and will migrate to the south when accounting for the interface offset.

Offset $S_1$ (Fig. 3.9) between the European and the Adriatic Moho (Kissling, 1993) from location $A_1$ (Fig. 3.9) in WSW-direction forms an arc following the Insubric line along the strike of the east-south-east dipping western Alpine Moho (Thouvenot et al., 1990; Sénéchal & Thouvenot, 1991). This suture line is suggested by the significant depth misfits of structural depth points derived from the refraction profile LB↔MC and the fan profile LW→N (see area B in Fig. 3.9). Moho depths derived from the LB↔MC profile are about 55 km (Ansorge, 1968) and those obtained from the LW→N fan around 25 km (Thouvenot et al., 1990). In the west (area B) offset S1 separates the European Moho from the shallow, east dipping high-velocity Ivrea body (Berckhemer, 1968; Nadir, 1988; Thouvenot et al., 1990). No seismic data show direct evidence for continuity between the Adriatic Moho and the high-velocity contrast(s) related to the Ivrea body (Solarino et al., 1997).

The extend of the Moho offset $S_1$ from location $A_1$ (Fig. 3.9) to the east is unclear (Kissling, 1993). Only a fan profile (C2→E, see area $A_2$ in Fig. 3.9) indicates a south-dipping European Moho and a slightly shallower, north-dipping Adriatic Moho (Mussachio et al., 1993). The question whether the connection between the European and the Adriatic Moho builds a trough or one or several small offsets cannot be answered by the available data. The significant depth misfit in area $A_2$ is at least partly due to 3D-migrating effects. 3D migration would migrate the fan observations from the two 'different' Moho interfaces in opposite up-dipping directions and thus smooth the structure between the two Mohos. This would support the evidence for a continuous, trough-like structure further to the east (Sleiko et al., 1986).

*The Adriatic / Ligurian Moho transition*

The south-dipping Moho beneath the Apennine front and the adjoining shallow and slightly north-dipping Ligurian Moho (area C in Fig. 3.9) are well documented by refraction profiles along the EGT (Ye, 1992; Egger, 1992) and along the strike of the Apennines (LW↔LC, B1→ESE; Buness, 1992), and fan registration from shotpoint B1 and B2 to the east (B1→E, B2→SE; Buness, 1992). An WNW-ESE striking offset (bolt line $S_2$ in Fig. 3.9) of nearly 35 km is modeled between the Adriatic Moho (imaged to a depth of 60 km; Buness, 1992) and the Ligurian Moho (imaged to a depth of 25 km; Ye, 1992; Ye et al., 1995).

The Moho-offset $S_2$ at location C (Fig. 3.9) is traced to the west and merges into a south-turning arc including the shallow located reflectors from the refraction profiles LW↔LC, Q→NW and Q→W that are assumed to belong to the Ligurian Moho (Buness, 1992). A 3D interpretation of the LW↔LC profile (Waldhauser et al., 1994, Fig. 3.11), that migrates the reflector from the Ligurian Moho (L in Fig. 3.11) to the south and the one from the Adriatic Moho (A in Fig. 3.11) to the north, clearly indicates that the Moho offset modeled at location C extends to the west below the LW↔LC profile. The significant depth misfits along the Q→NW profile in area D require an offset modeling in the west as shown in Figure 3.9 by $S_2$. Such an offset will shallow the Ligurian Moho which provides a better fitting of the structural data within their error limits in this area.

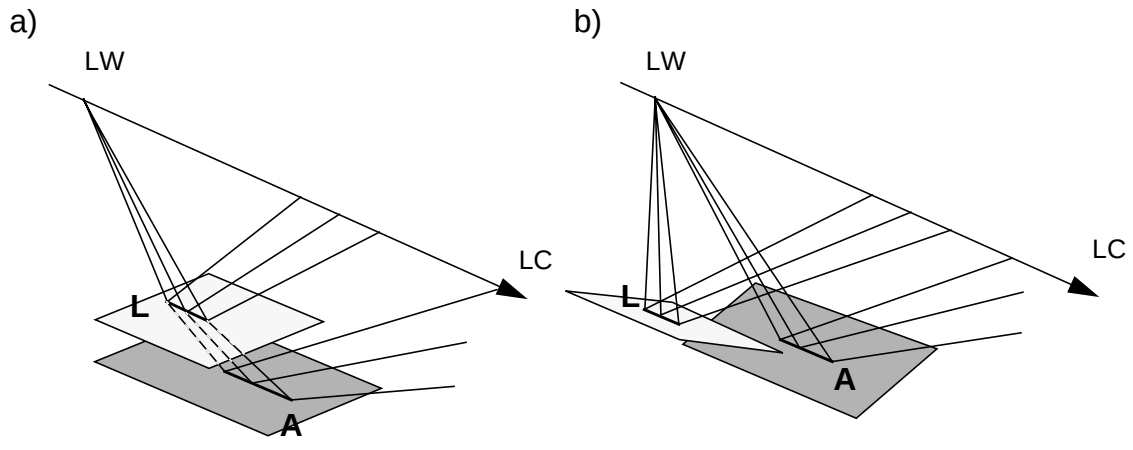


**Figure 3.11** Schematic depiction of the 2D- (a, Buness, 1992) and 3D- (b) interpretation of the Apennine longitudinal profile LW-LC. L and A are reflectors from the Ligurian and the Adriatic Moho. The 2D-interpretation derived by ray-tracing (Buness, 1992) shows a 'double Moho' with the Ligurian Moho (L) lying above the Adriatic Moho (A). Off-line migration with respect to the oppositely dipping Adriatic and Ligurian Moho migrates the structural elements in oppositely direction (b).

The extend of the Moho offset $S_2$ from area C (Fig. 3.9) to the east is unclear. Seismic data from the refraction profile B2→SE (Buness, 1992) and the fan observation B2→SW (Buness, 1992) indicate a still south-dipping Adriatic Moho to the east. The Ligurian Moho seems to continue in a general shallow fashion (LIG74 refraction profiles; Colombi et al., 1977; Buness, 1992).

According to this observations an offset between the Adriatic and the Ligurian Moho is modeled as shown by the bold line $S_2$ in Figure 3.9. This structure will also provide better results for 3D-migration of the reflectors in this area than using a continuous transition between the Adriatic and the Ligurian Moho (see below).

*Initial interpolation for three Moho surfaces*

Kissling (1993) interpreted on a qualitative basis the Alpine Moho interface as consisting of three surfaces; the European, Adriatic and Ligurian Moho. A similar system of three Moho surfaces is now quantitatively derived by modeling Alpine Moho offsets along $S_1$ and $S_2$ (Fig. 3.9). This is achieved by cutting open the single-surface along $S_1$ and $S_2$, i.e. separating the reflectors along these offsets and performing individual interpolation of the European-, Adriatic- and Ligurian Moho data. The effect of cutting open the single-surface with respect to observed significant depth misfits is shown in Figure 3.12 with the example of the Moho in the south-central Alps (see box in Fig. 3.9). Figure 3.12a shows in a ESE-oriented perspective view the single $RGH_{118}$-surface with structural depth points and their error bars along reflecting elements. Significant depth misfits are indicated on the surface below or above the corresponding structural depth points. Figure 3.12b shows, in a same view, European (left) and Adriatic (right) Moho after cutting open the single $RGH_{118}$-surface along $S_1$ (see Fig. 3.9). No significant depth misfits are observed in this region after the cut-open-process. Numeric instabilities during interpolation at the surface edges are prevented by using supporting depth points outside the surfaces that linearly extrapolate the geometry of the area near the interface edge (see Section 2.3.1).

Roughness values for European ($RGH^{eur}$), Adriatic ($RGH^{adr}$) and Ligurian ($RGH^{lig}$) Moho have now to be determined to obtain migration surfaces on which basis 3D-migration can be performed. As done at the beginning of the single-surface modeling process, series of 20 surfaces featuring a broad roughness spectra are calculated each for the three Moho's individually. The surfaces are derived by individual interpolation of the structural data grouped to the European-, Adriatic- and Ligurian Moho. Smoothest surfaces are seeked from the series that fit all data within observed depth errors. In Figure 3.13 numbers of significant depth misfits are plotted against surface roughness for each Moho. Roughness values are chosen for the European Moho ($RGH$=77; Fig. 3.13a), the Adriatic Moho ($RGH$=58; Fig. 3.13b), and the Ligurian Moho ($RGH$=4; Fig. 3.13c). Figure 3.14a-c display the $RGH_{77}^{eur}$ -, $RGH_{58}^{adr}$ -, and $RGH_{4}^{lig}$ -surfaces by depth isolines in km. Structural data (dots), depth values of isolines, and limits of the model area (gray lines) are indicated.

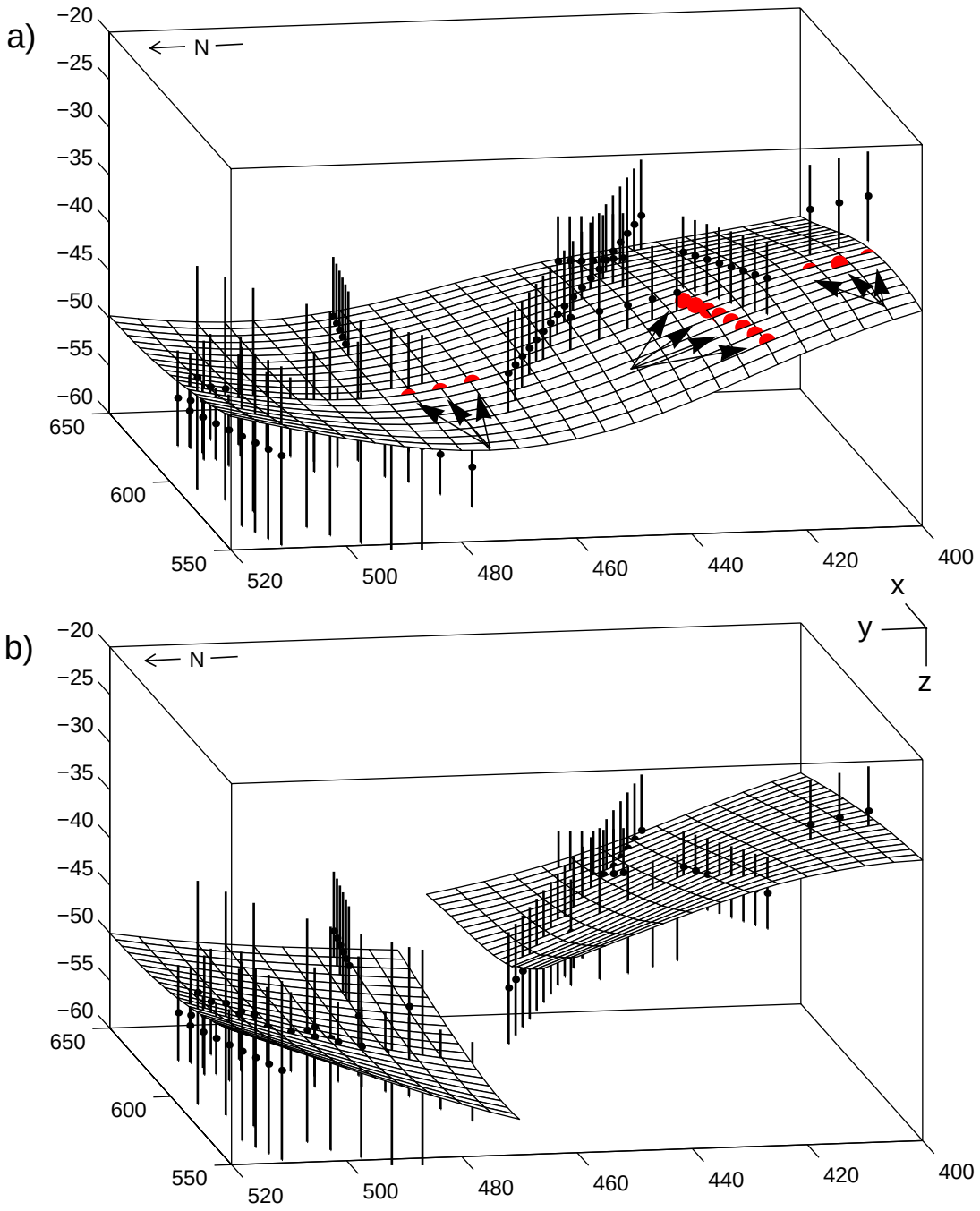


**Figure 3.12** a) Perspective, ESE-oriented view on continuously modeled $RGH_{118}$-surface of the Moho in the region of the south-central Alps below the Insubric line along the EGT (see box in Fig. 3.9). Structural depth points are shown with depth errors and significant depth misfits by arrows on the $RGH_{118}$-surface. b) Perspective view on the Moho offset between European Moho (left) and Adriatic Moho (right) after cutting open the $RGH_{118}$-surface.

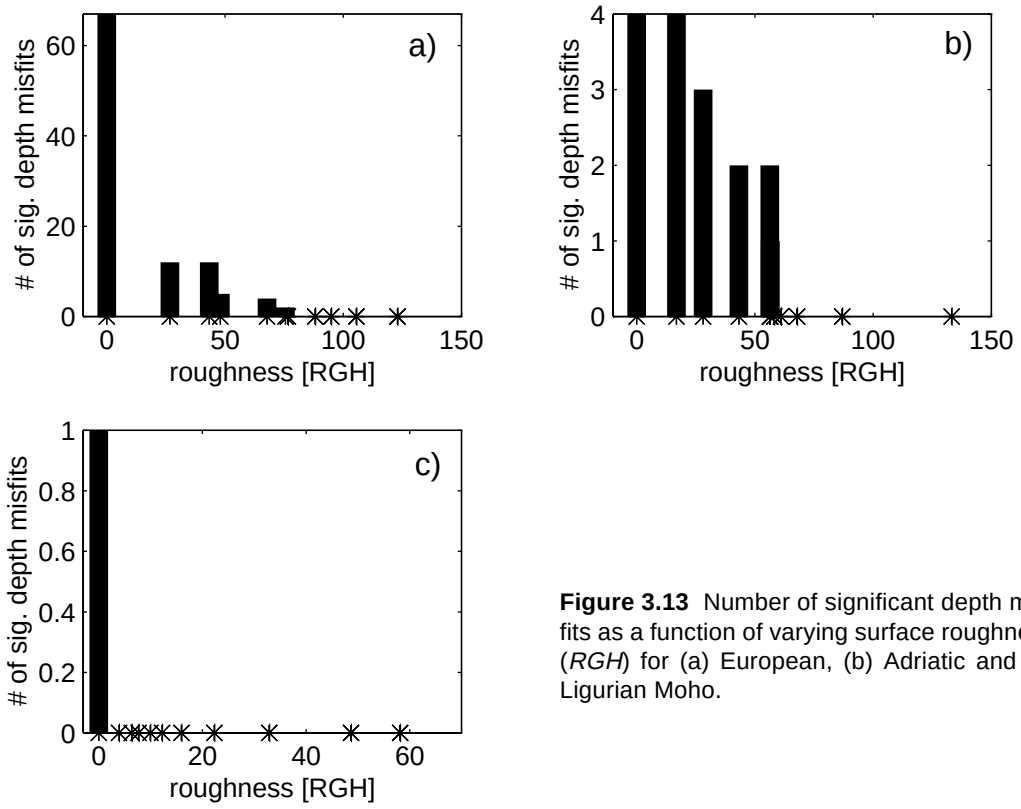


**Figure 3.13** Number of significant depth misfits as a function of varying surface roughness (*RGH*) for (a) European, (b) Adriatic and (c) Ligurian Moho.

*3D-migration*

Merging these three surfaces (Fig. 3.14), a horizontally continuous Alpine Moho surface (migration surface), including the required vertical offsets, is obtained (Fig. 3.15). On the basis of that migration surface, 3D-migration of the in-line migrated structural depth points is performed. The numeric results for the horizontal migration paths are shown by arrows for the whole model area (Fig. 3.15a) and for the region of the northern Apennines (Fig. 3.15b). Figure 3.15b shows how the qualitative 3D interpretation of the wide-angle reflection data in the northern Apennines (see Fig. 3.11) is quantified by the 3D migration process applied to the in-line migrated data (reflectors L and A, see Fig. 3.11) from the LW↔LC profile. Off-line migrations with respect to opposite dipping Adriatic and Ligurian migration surfaces migrate the reflectors in opposite direction - the reflector from the Adriatic Moho (A) by about 20 km to the north and the element from the Ligurian Moho (L) by about 7 km to the south.

The amount of vertical (depth) migration of the Alpine Moho by off-line migration of the in-line migrated reflectors from longitudinal profiles is shown in Figure 3.16. The effect of depth migration depends on the actual depth and dip of the interface, and whether a reflector is derived by along-strike or transverse profiles. A maximum depth migration of the Alpine Moho of more than 2 km is obtained in the northern Apennine, where the deep reaching and strongly dipping Adriatic Moho is imaged by the along-strike profile LW↔LC (Fig. 3.16). Vertical depth migration of the Alpine longitudinal profile data from the European Moho along the Alpine arc is in the range of 1 km.

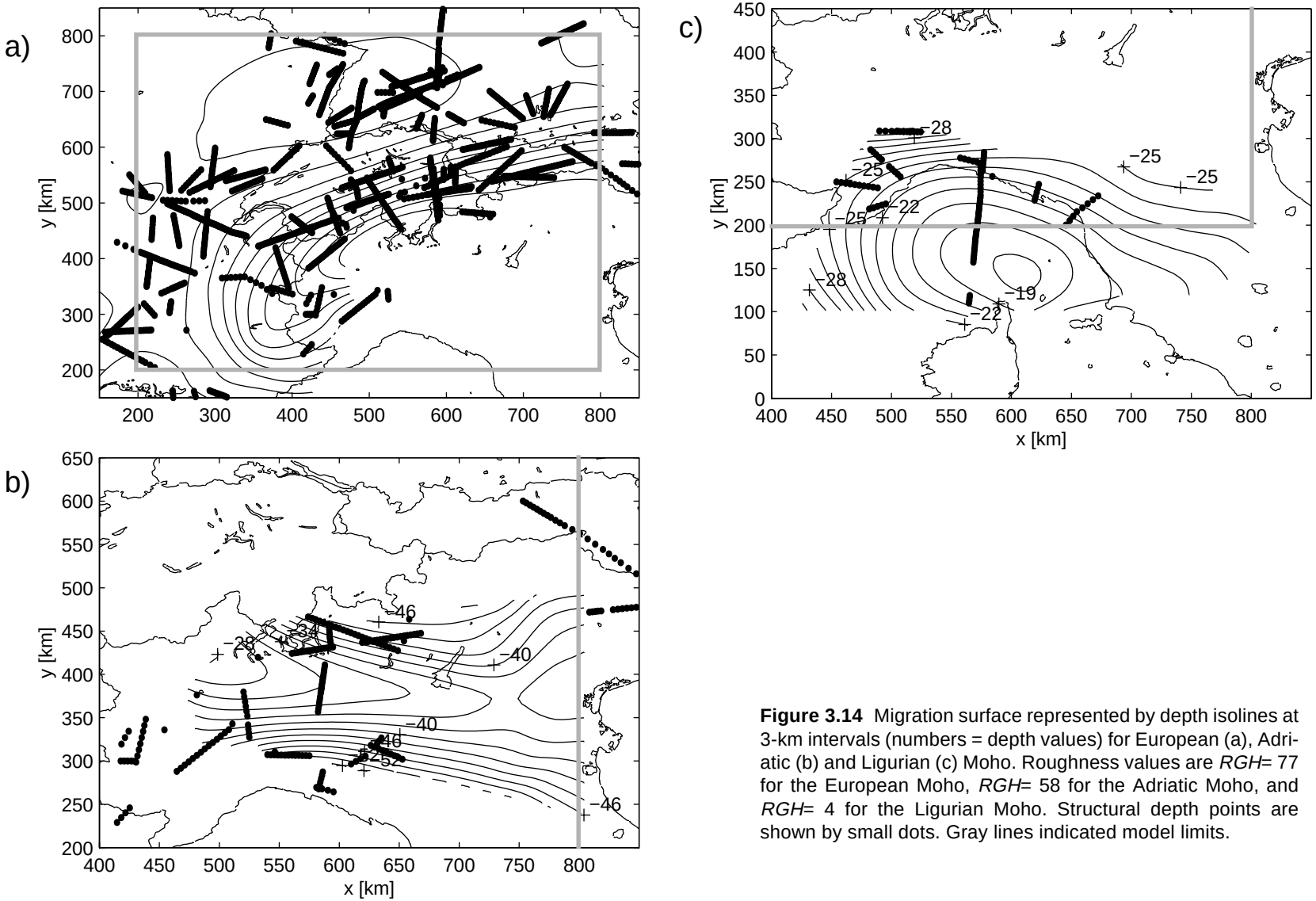


**Figure 3.14** Migration surface represented by depth isolines at 3-km intervals (numbers = depth values) for European (a), Adriatic (b) and Ligurian (c) Moho. Roughness values are *RGH*= 77 for the European Moho, *RGH*= 58 for the Adriatic Moho, and *RGH*= 4 for the Ligurian Moho. Structural depth points are shown by small dots. Gray lines indicated model limits.

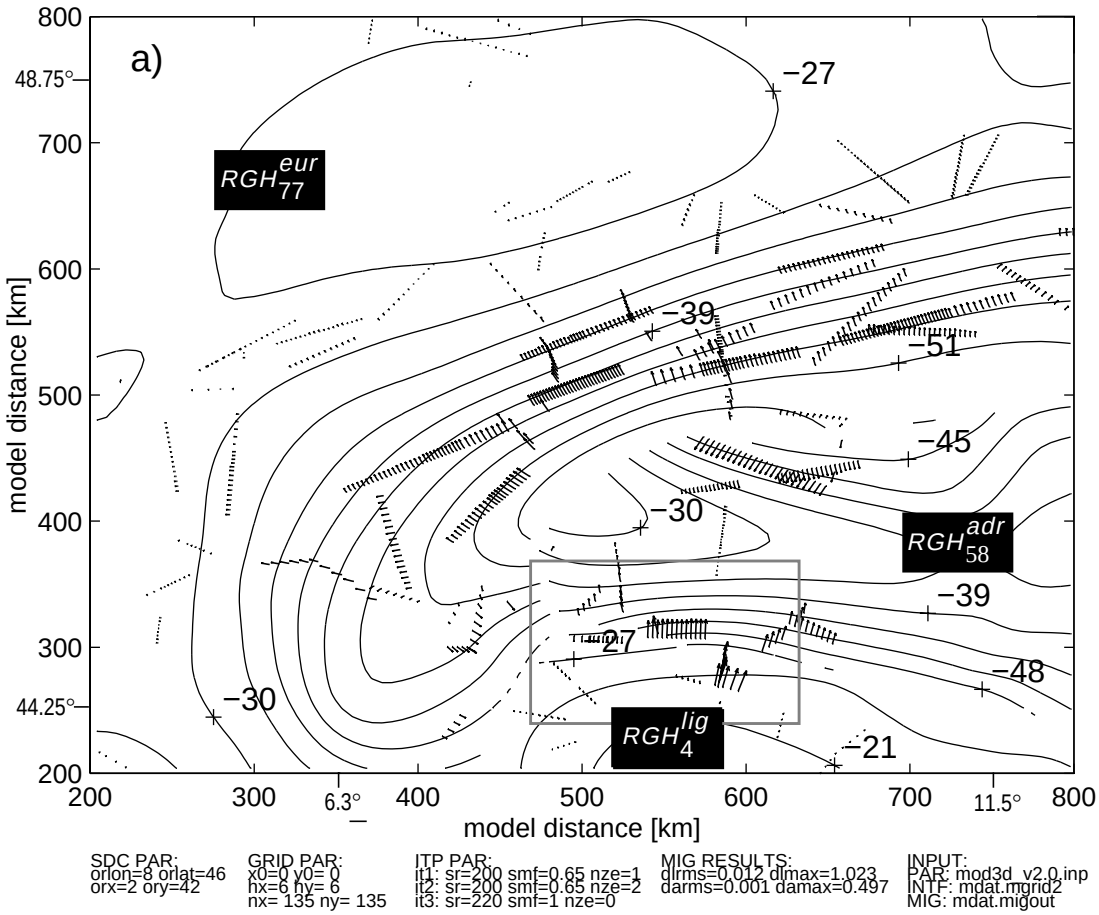


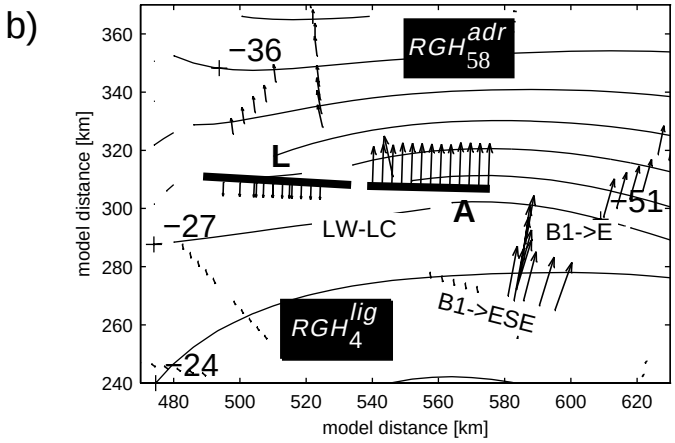


**Figure 3.15** a) Migration surfaces for the European Moho ($RGH^{eur}$=77), the Adriatic Moho ($RGH^{adr}$=58), and the Ligurian Moho ($RGH^{lig}$=4) represented by depth isolines at 3-km intervals. Isoline values are indicated by numbers. Horizontal migration paths are marked by arrows.
B) Horizontal migration paths (arrows) in the region of the northern Apennine (see box in a and Fig. 3.11). Off-line migration of the two reflectors (A and L) is performed on the basis of the $RGH^{adr}$- and $RGH^{lig}$ -migration-surface.

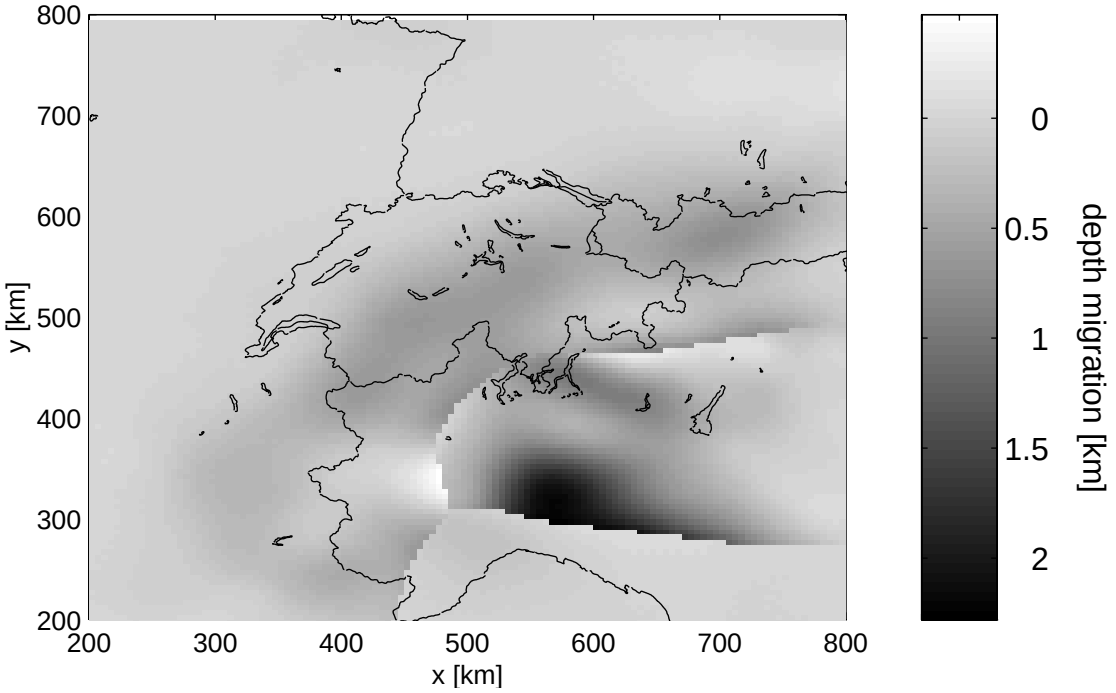


**Figure 3.16** Amount of vertical (depth) migration derived by 3D migration of reflectors from controlled-source seismic profiles in the Alpine region.

*Final interpolation of the 3-D migrated Moho reflectors*

The final 3D Moho of the Alpine region is derived by interpolation of the 3D-migrated structural data from European, Adriatic and Ligurian Moho. This interface is depicted in Figure 3.17a by depth isolines and in Figure 3.17b in a WSW-oriented perspective view. Both figures additionally display information about the local reliability of the derived interface. Structural weighting factors (i.e. the weighting factor as derived by eq. 3-1 and 3-2) are projected on the Fresnel zones of the reflectors on the 3D Moho interface. Interpolated area of the interface outside the Fresnel zones has a weighting factor zero.

The derived Alpine Moho (Figs. 3.17 and 3.18) fits all structural depth points within their observed depth error and features maximal continuity and minimal roughness, thus depicting the simplest possible interface.

## 3.2.2 Discussion of the Derived Moho Interface

The European Moho (Fig. 3.18) as derived by the above described process features below the central Alps a south-dipping interface, deepening from 25 km below the stable Alpine foreland to more than 55 km below the Insubric line. This structure is well constraint by combined wide-angle and near-vertical reflection data. Although most likely, a further south-ward deepening of the European Moho below the Adriatic Moho, as, f.e. proposed by Valasek (1992), has not be imaged by controlled-source seismic methods.

The European Moho in the central Alps changes to an east-dipping structure in the western Alps, building the arc of the western Alps. The shape of the European Moho below the southern end of the western Alps can not be termed reliable due to missing seismic data as can be seen from Figure 3.17. Also the proposed offset between the European and Ligurian Moho is of lesser reliability. A shallow Moho at a depth of about 25 km to 30 km is depicted under the Bresse-Graben and the southern Rhone valley. Below the Rhine-Graben, Moho depth of about 25 km can be observed.

The Adriatic Moho is best imaged along the EGT profile, where it is sandwiched between the European and the Ligurian Moho and up-doming below the Po-plain. At the northern rim at 45 km depth, the Adriatic Moho is underthrusted by the European Moho whereas at the southern rim it is overthrusted by the Ligurian Moho. There, the Adriatic Moho is lost at a depth of about 60 km and further deepening can not be revealed by 2D controlled-source seismic methods. To the west, near the western margin of the Po-plain, the Adriatic Moho merges into the structure of the Ivrea zone where the situation is unclear. Strong near-surface reflections, related to the Ivrea body, with phase characteristics similar to PmP-phases can be observed in this region. Since no evidence exists for a direct contact between these near-surface reflections related to the Ivrea body and the PmP-reflections from the Adriatic Moho, the Adriatic Moho is modeled as a slightly west-ward, to lesser than 30 km up-dipping interface that still keeps the saddle-like structure imaged along the EGT. The Ivrea body with its Moho-like velocity contrast is accounted as an intra-crustal high-velocity zone (see Section 3.3). A direct contact between the Adriatic and European Moho may possibly exist below the southwestern Po-plain, where the two Mohos show a common depth of about 36 km. To the east, no seismic data has been completed and the Adriatic Moho has been modeled by extrapolating the observed structure in the western and central part to east.

The Ligurian Moho along the EGT beneath the Apennines has been well located at a shallow depth of around 20 km. At its northern rim, below the front of the Apennines, the Ligurian Moho shows an offset of about 35 km to the deeper Adriatic Moho. West of the EGT profile, the Ligurian Moho shows a possible slight deepening, breaking off below the western Po-plain. There the Ligurian Moho lies above the European Moho, separated by an offset of about 13 km. To the east, the Ligurian Moho seems to continue in a shallow fashion, with a unrevealed contact to the European Moho.

The Alpine Moho interface model proposed in this Section depicts a smoother surface and shows fewer offsets compared to the interpretations by Buness (1992) and Giese & Buness (1992). The difference is a result of the interface modeling concept and method, that seeks for the simplest interface with respect to structural depth errors.

**Figure 3.17** (next page) Alpine Moho interface contoured at 2-km intervals (a) and in a perspective, WSW-oriented view (b) derived by interpolation of the 3D-migrated CSS data. The structural, 3D migrated data base is shown. Color on the interface indicate weighting factors between 0.2 (information poorly constraint by CSS methods) and 1 (highly reliable reflectors from CSS methods). The weighting factors are projected on the Fresnel zone of the corresponding structural data on the Moho. Wight grid lines in (b) indicate Moho depth derived by interpolation only.

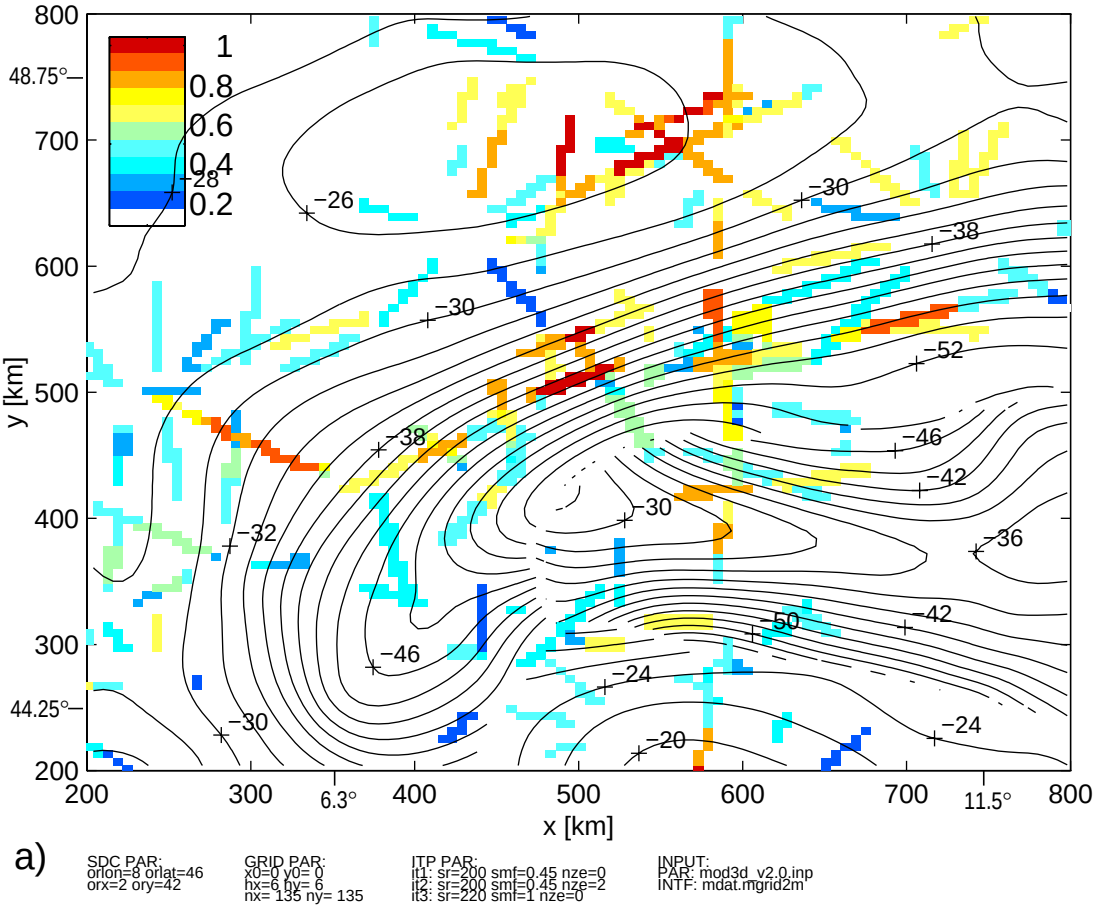
800
48.75°
700
600
500
400
300
44.25°
200
y [km]
200
300
6.3°
400
500
600
700
11.5°
800
x [km]
1
0.8
0.6
0.4
0.2
−26
−30
−38
−52
−46
−42
−36
−50
−24
−20
−32
−28
a)
SDC PAR:
orlon=8 orlat=46
orx=2 ory=42
GRID PAR:
x0=0 y0= 0
hx=6 hy= 6
nx= 135 ny= 135
ITP PAR:
it1: sr=200 smf=0.45 nze=0
it2: sr=200 smf=0.45 nze=2
it3: sr=220 smf=1 nze=0
INPUT:
PAR: mod3d_v2.0.inp
INTF: mdat.mgrid2m

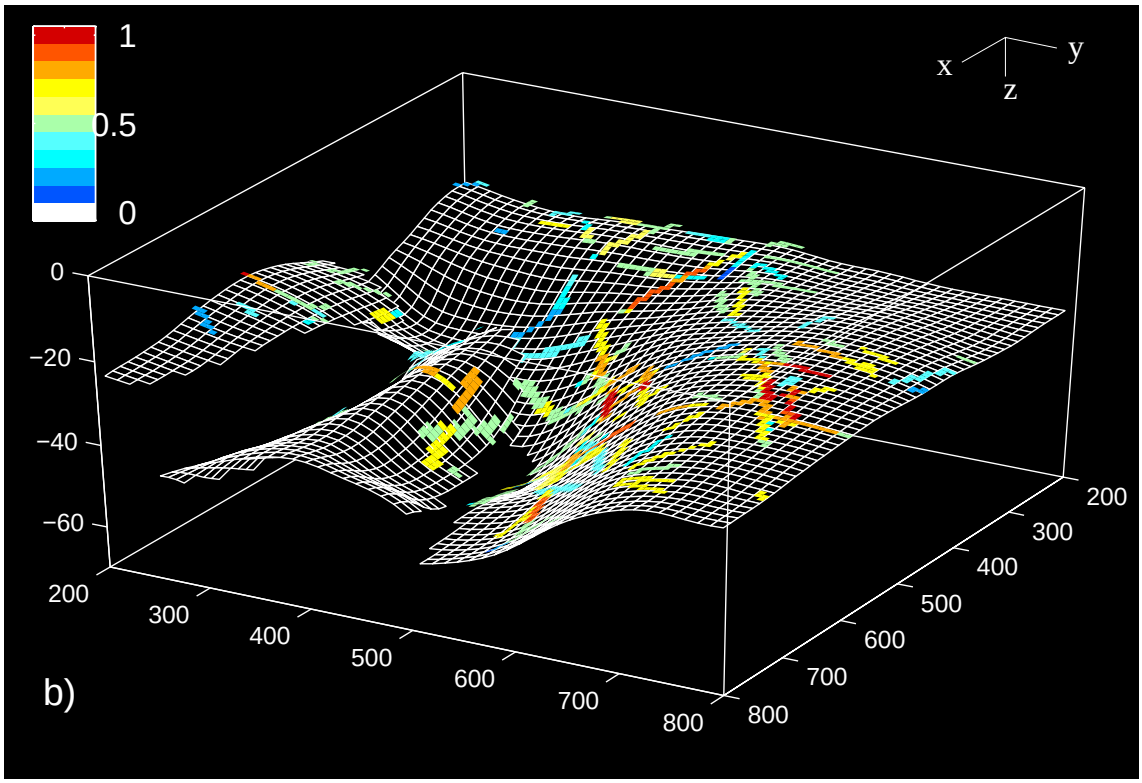
1
0.5
0
x
y
z
0
−20
−40
−60
200
300
400
500
600
700
800
b)

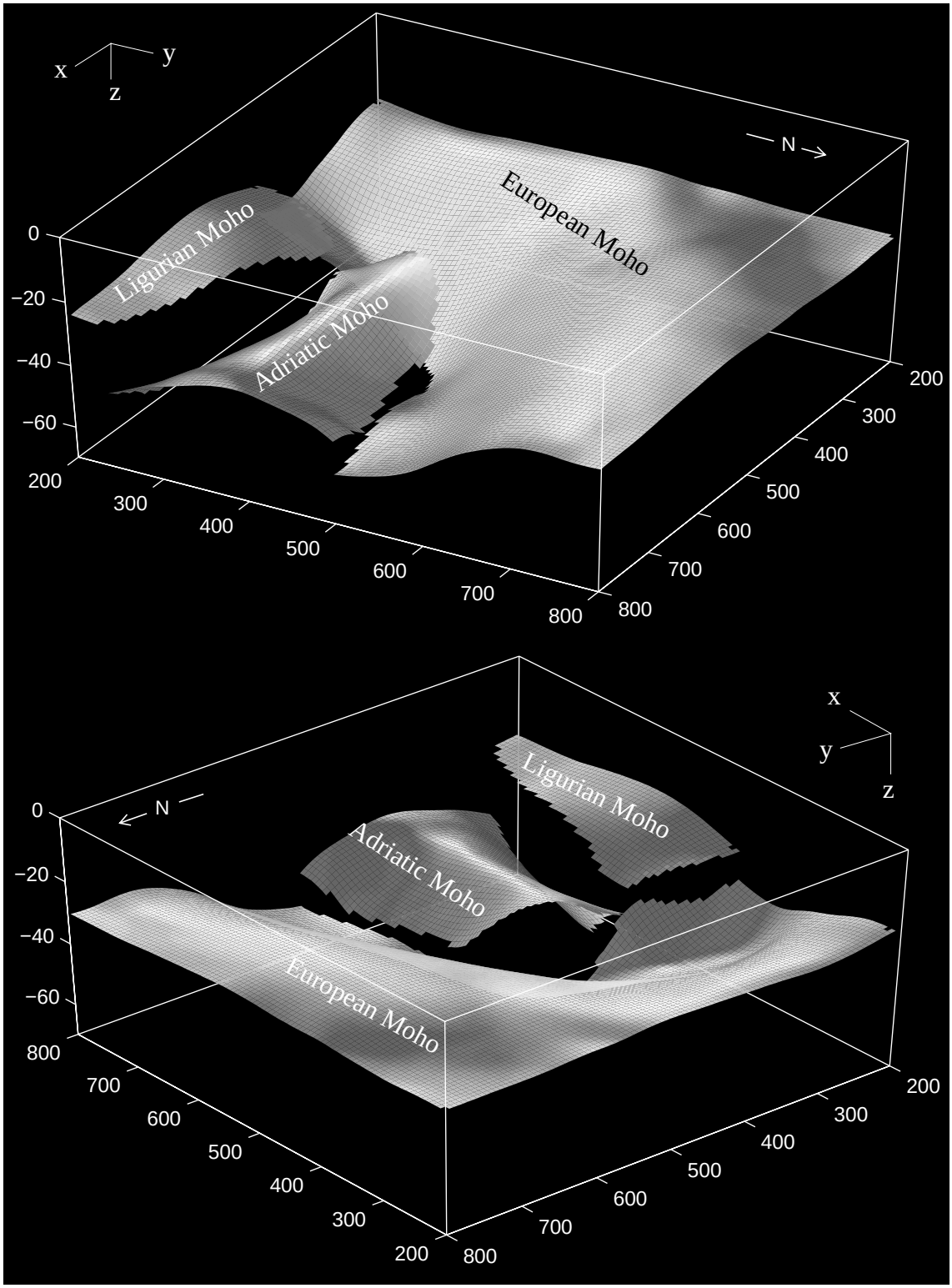


**Figure 3.18** Perspective SW-view (upper half) and SE-view (lower half) on the Moho below the Alpine region. The European, Adriatic and Ligurian Moho are depicted.

## 3.3 Construction of a 3D P-Velocity Model of the Alpine Crust and Uppermost Mantle

Most information about deep crustal velocity distribution in the Alpine region are obtained by 2D refraction studies completed over the last decades (see Section 3.1). The main scope of these experiments was to reveal in details velocity structure within the Alpine crust and uppermost mantle. In the last decade, increased data quality due to better instrumentations and the use of sophisticated interpretation methods such as 2D ray tracing resulted in detailed (i.e. n-layered) velocity models along the seismic profiles (see f.e. Fig. 3.2). Many of the derived models, although sometimes overestimated in terms of the resolution capability of the applied method (Kissling, 1993; Baumann, 1994), depict sharp intra-crustal velocity contrasts such as between upper and lower crust (Conrad discontinuity) and/or the layering and interaction of the Alpine nappe system. From these models of present seismic structure, petrophysical models are inferred that allow interpretations with respect to Alpine tectonics (e.g. Mueller, 1977; Laubscher, 1994).

*Simplification of n-layered CSS models to 3-layered lithospheric models for 3D model construction*

These detailed CSS models shall be used with respect to the concept and method for 3D seismic model construction as outlined in Chapter 2. According to this concept, a 3-layered lithospheric velocity model includes strong velocity inhomogenities such as the crust-mantle boundary and near-surface sedimentary basins. The crust is represented by a simple 2-layer model with a high-velocity gradient in the surface layer and a small to moderate velocity gradient from top basement to Moho. Superimposed on this uniform reference model are locally the sedimentary basins within the surface layer.

Thus, the n-layered 2D crustal models from CSS methods (an example is shown in Fig. 3.19a) need to be simplified to models featuring a near-surface layer, a main crustal layer and an uppermost mantle layer. The detailed parameterization of such 3-layered lithospheric models is described in Section 2.2. Figure 3.19d shows the result after simplification of the 2D CSS model (Fig. 3.19a) derived by Maurer & Ansorge (1992) from the ALP87 profile data. Along the profile, constant lower crustal and sub-Moho velocities of 6.4 km/s and 8.1 km/s, respectively, are observed (see Fig. 3.2 and Fig. 3.19a) which has been used to parametrize the velocity contrast across the Moho (Fig. 3.19d). Average crustal velocities ($vp_a$) along the CSS model are derived within the rectangle above all three reflector segments (Fig. 3.19b). Together with a reference surface velocity of 4.6 km/s (see below), observed average crustal and lower crustal velocities are used to compute the compensation velocity ($vp_{com}$) at 2 km depth above each reflector segment (Fig. 3.19b, c).

Such a simplification, which neglects much intra-crustal information that has been obtained during decades of painstaking work, is justified with respect to the prospected use of the 3D model that differs from the scopes behind earlier CSS data modeling.

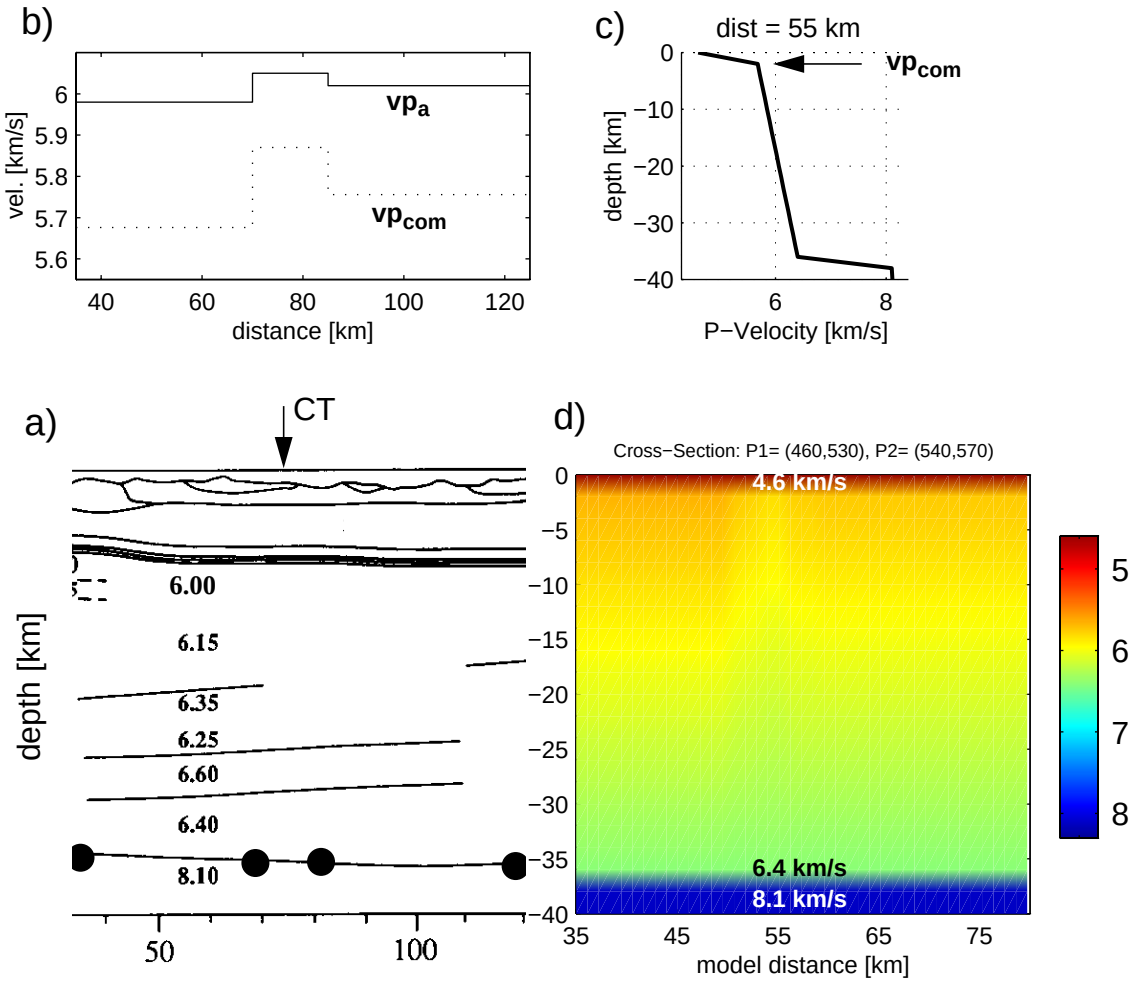


**Figure 3.19** Simplification of detailed 2D seismic models derived from CSS methods. a) Interpretation of seismic data obtained along the Alpine longitudinal seismic profile ALP87 (after Maurer and Ansorge, 1992). The part between 35 km and 120 km is shown where the Moho discontinuity is imaged as a continuous reflector. For travel time sections and raytraced model see Figure 3.2. At 80 km model distance, the northern end of the perpendicular to the ALP87 profile lying NFP20 Central Traverse (CT) borders to the ALP87 profile. Solid circles represent structural depth points (i.e., end points of reflector segments).
b) Average crustal velocity (solid line) over the reflector length averaged along the three reflector segments (limited by black points).
c) Velocity-depth function at 55 km model distance. A 2-layered crustal model is shown with a strong velocity gradient from 4.6 km/s (surface velocity) at the surface to 5.68 km/s (compensation velocity) at top basement (compensation depth) and with a small velocity gradient over the main crust from 5.68 km/s at top basement to 6.4 km/s at top Moho. A Moho contrast from 6.4 km/s to 8.1 km/s is used.
d) 2D Velocity distribution along the ALP87 reflector as used for 3D model construction (km/s). The variation of the velocity field is caused by the slightly different average crustal and compensation velocities for each reflector segment. Average velocity changes from 5.98 km/s to 6.05 km/s to 6.02 km/s (see b). At 75 km model distance the effect of the CT average velocity which amounts 6.07 km/s and averaged to 6.06 km/s is visible.

The main objective of CSS investigations is to obtain the distribution of actual physical parameters such as P-velocities with depth at every location along the profile. From these detailed 2D velocity models petrophysical models have been inferred (e.g. Mueller, 1977) that allowed to understand tectonic processes related to these structures.

Lateral extension of structures derived by CSS methods are restricted to the area directly below the seismic profile. Thus, CSS profiles, on their own, can not estimate the continuity of the imaged structure outside profile lines (see Section 2.3). Rarely quantified reliability of different parts of detailed models and neglected 3D effects on the data from structures outside the profile plane (3D migration) lead, in most cases, to overinterpreted models.

Different from the objectives of CSS data modeling, this work concentrates on modeling the three-dimensional extension of dominant seismic structures that appear on *all* CSS data within the 3D model area. Such a 3D model need to be consistently parametrized with the least possible parameters (least degree of freedom) in order to continuously represent these dominant structures and to compare them against reference models. Thus, the 3D models does not contain speculative structural elements, as in many CSS models. Such a model does not easily relate to petrophysical meaning, but rather will lead to simplified physical models that three-dimensionally represent specific seismic parameters associated throughout a certain volume (i.e. model volume). It does not necessarily represent actual velocity parameters a every spatial location within the crust and uppermost mantle.

Simplifying detailed crustal and uppermost mantle structures from CSS methods to a 3-layered lithospheric model is, therefore, a step forward in terms of consistent and quantitative modeling of the main seismic structures in a 3D context. It seems to represent a step backward in terms of petrophysical relevance of suchlike derived 3D models. This disadvantage, however, may be overcome by future refinement of these models by repeatingly applying this method to other intra-crustal seismic features as reliable CSS or tomographic data become available.

With respect to these conceptual considerations, all CSS models along the compiled seismic profiles (see Section 3.1; Fig. 3.19a) have been transformed into 3-layered lithospheric models by extracting the key parameters - average crustal velocity, lower-crustal and upper-mantle velocity - from the CSS models and building 3-layered velocity-depth functions along the reflectors (as shown in Fig. 3.19d). This process simplifies the available CSS models and, in the same time, retains the important seismic characteristics of these models that are demanded from the 3D model concept: the strong velocity contrast at the crust-mantle boundary and the average crustal velocity. Spatial location of the crust-mantle velocity contrast has been 3D migrated in order to account for the 3D structure of the Alpine Moho (Sections 2.3.1 and 3.2). Such a 3D model meets the requirements of the modeling concept.

*3D model construction*

The 3D model construction procedure (see Section 2.4) is straight forward, once having at hand information from surface observation, the lateral continuous topography of the crust-mantle boundary and the CSS velocity information associated to it in the form of 3-layered lithospheric models.

The CSS velocity parameters are volumetrically modeled according to approximated Fresnel volumes along the 3D migrated reflectors (see Section 2.3.2 and below). As

can be seen later (Fig. 3.22), volumetrically modeled CSS velocities together with surface information will not lead to a spatially continuous P-velocity model (continuum 3D model). Information gaps do exist between the measured velocity data. Thus, a 1D reference model for the Alpine crust and uppermost mantle is needed. This reference model is then subsequently updated with near-surface sedimentary basins, the previously derived crust-mantle boundary (Section 3.2) and its associated velocities from the seismic profiles.

In the following, a 1D reference model is established, information about near-surface sedimentary basins are compiled and CSS velocities volumetrically modeled. On the base of the reference model, the 3D model is constructed by integration of the sediment basins, the crust-mantle boundary and its associated velocities.

### 3.3.1 Reference Velocities and Alpine Sedimentary Basins

*1D reference data*

Even with a extraordinary dense CSS profiling network as in the Alps, only about 10% of the Alpine model volume is sampled. Interpolation between the sampled data in many parts is strongly ambiguous. In order to follow the principle of simplicity, a well established 1D reference model (see Chap. 2) is used as background. A reference European crust from outside the Alpine collision zone is used, i.e., in an area of - on lithospheric scale ‘undisturbed’ - continental crust-mantle system. To allow direct comparison of reference data with model data, such a reference structure should advantageously be part of the model or adjoining the model region.

A tectonically stable area near the Alpine collision zone is the European foreland outside the Rhine- and Bresse-Grabens. This area is crossed by the EGT central segment (Blundell et al., 1992) that imaged between shotpoint E and H, at the northern tip of the model region, a 30 km thick, lateral more or less homogeneous crust (Aichroth et al. (1992); see also Blundell et al., 1992).

According to this model, the 1D reference model (Fig. 3.20) is parametrized with a surface velocity of 4.6 km/s which gradually increases with depth to a compensation velocity of 5.85 km/s at the top of basement in 2 km depth. The compensation velocity (see Eq. 2-4) is calculated using an average crustal velocity of 6.1 km/s and a crustal thickness of 30 km (Aichroth et al., 1992). The reference velocity contrast at the Moho is defined by a lower-crustal velocity of 6.5 km/s and a uppermost mantle velocity of 8.1 km/s. The 6.5 km/s for the lower crust is slightly smaller than the value proposed by Aichroth et al. (1992) (6.7 km/s). This is necessary in order to obtain a compensation velocity near 5.9 km/s which is quite reasonable for the European crust. At the bottom of the model, at 70 km depth, velocity is set to 8.3 km/s in order to model a positive velocity gradient below the crust-mantle boundary. Although the established reference model does not represent petrophysical characteristics it is a physical reference that is applicable throughout the model region and which can be adapted to locally measured structures.

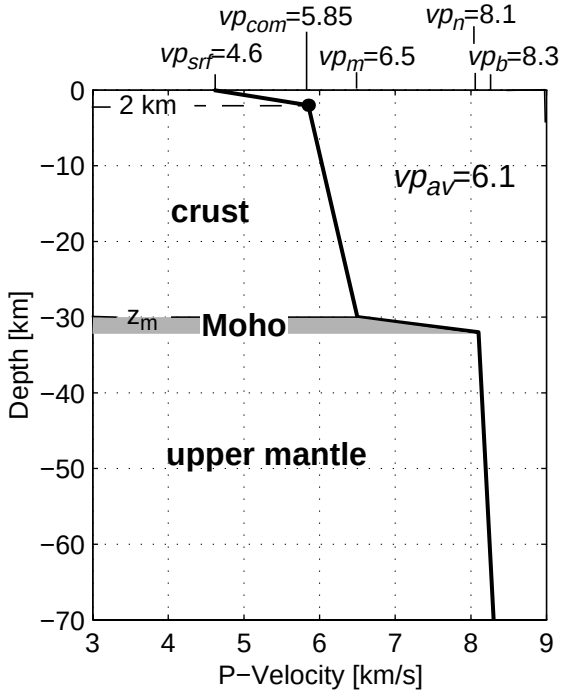


**Figure 3.20** 1D reference velocity-depth function for the Alpine crust and uppermost mantle. Compensation velocity ($^{\bullet}$) is calculated using reference values for surface ($vp_{srf}$), lower-crustal ($vp_m$) and average crustal ($vp_a$) velocity.

*Near-surface sedimentary basins*

The Alpine region is dominated by two large near-surface low-velocity sedimentary basins, the Molasse basin in the northern foredeep and the Po basin in the southern foredeep of the Alps. Their lateral extension is best visible on geologic maps (see Fig. 3.21) whereas basin depths are locally obtained by well logging or controlled source seismic investigations.

Horizontal extension and depths of the Tertiary sediments of the Molasse Basin are derived from Berthelsen et al. (1992) (Fig. 3.21a). This sedimentary basin, running parallel to the Alpine strike in the northern part of Switzerland, thickens towards the south from 0 km to about 5 km, where it is overthrusted by the Helvetic Nappes. The Molasse Basin is traversed by the EGT profile, with shotpoints D and E at the southern and norther margin of the basin. Sediment P-velocities for the top (3.5 - 4.0 km/s) and for the bottom (4.0 - 5.0 km/s) of the basin are derived by Ye (1992) from 2D ray-tracing of the Pg-phase. The average velocity within the sediment layer increases from about 4.2 km/s in the north to 4.75 km/s in the south. This values are in good agreement with refraction studies carried out by Zeis et al. (1990) in the eastern part of the Molasse Basin. Figure 3.21b shows the discretized depth and velocity information for the Basin.

The Quarternary and Pliocaen formations of the Po basin are sandwiched between the Alps and the northern Apennine and run as a east-west elongated trough along the strike

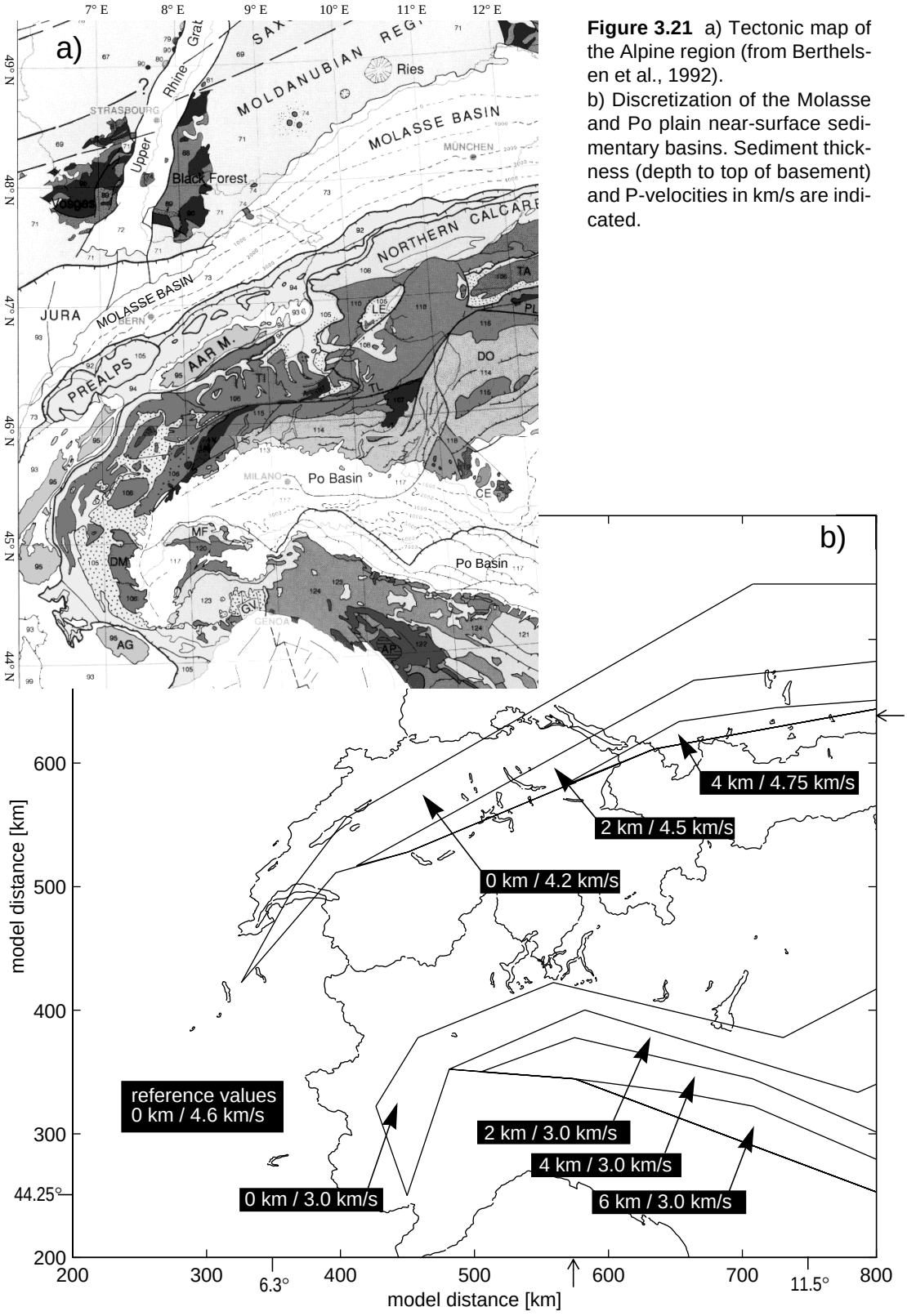


**Figure 3.21** a) Tectonic map of the Alpine region (from Berthelsen et al., 1992).
b) Discretization of the Molasse and Po plain near-surface sedimentary basins. Sediment thickness (depth to top of basement) and P-velocities in km/s are indicated.

of the northern Apennines (Berthelsen et al., 1992; see Fig. 3.21a). The EGT profile between shotpoint $B_2$ and $C_2$, and geologic depth sections by Cassano et al. (1986) in the northern Po Plain that obliquely cross the EGT profile in SW-NE direction, reveal a thickening of the sedimentary layer from 0 km at the northern margin to about 6 km in the south where it borders to the Apennine front.

Sediment velocities have been carried out by 2D ray-tracing of the Pg phase between shotpoint $B_2$ and $C_2$ along the EGT profile (Buness, 1992). For the topmost Quarternary layer a P-velocity of 2.6 km/s has been derived, for the upper Pliocaen 2.9 km/s and for the lower Pliocaen 3.5 km/s. The beneath lying upper Miocaen and the subsequently following Mesozoikum with P-velocities near the reference surface velocity (4.6 km/s and 5.4 km/s) are not included in the parametrized Po Basin since they are in the range of the reference surface velocity around 4.6 km/s.

Based on this information, a SSE deepening Po basin is modeled with increasing sediment thickness reaching 6 km at the southern rim (Fig. 3.21b). The sediment velocities derived along the EGT for the individual near surface formations (Buness, 1992) are averaged and a velocity of 3 km/s derived. Since the EGT is the only profile along which near surface layer velocities can be obtained, the average sediment velocity of 3 km/s is extrapolated to the entire Po Basin (see Fig. 3.21b).

### 3.3.2 Volumetric Modeling of Alpine CSS Velocity Information

In the following, velocities measured by CSS methods are modeled within the approximated physical volume of the velocity field that have strong influence on the rays (volumetric CSS velocity modeling, Section 2.3.2).

Average crustal velocities (*vpa*) obtained for each reflector segment (see Fig. 3.19b) are represented within ‘boxes’ along the reflector and between surface layer (*vpcom*) and crust-mantle boundary (*vpm*). Figure 3.22 displays the horizontal extension of the modeled boxes with the associated average velocities derived from the data base described in Section 3.1 (Fig. 3.6a). Fresnel zone radii at Moho depth vary between about 2.8 km and 5.7 km. Using a grid spacing of 2 km this will lead to a stair-like image of horizontal cross-section through the boxes (Fig. 3.22).

Lower-crustal (*vpm*) and uppermost mantle (*vpn*) velocities, measured by CSS methods, are interpolated and extrapolated along the European, Adriatic and Ligurian Moho interface individually, building its velocity contrast across one vertical grid unit (i.e. 2 km). Interpolation radii of influence of 20 km for lower-crustal velocities and of 30 km for upper mantle velocities are used. These interpolation parameters are obtained considering the distance and volume over which these velocities are sampled along the Alpine profiles. Figure 3.23 maps the results that are derived using the data base for lower-crustal and upper-mantle velocities as described in Section 3.1 (Fig. 3.6b, resp. Fig. 3.6c).

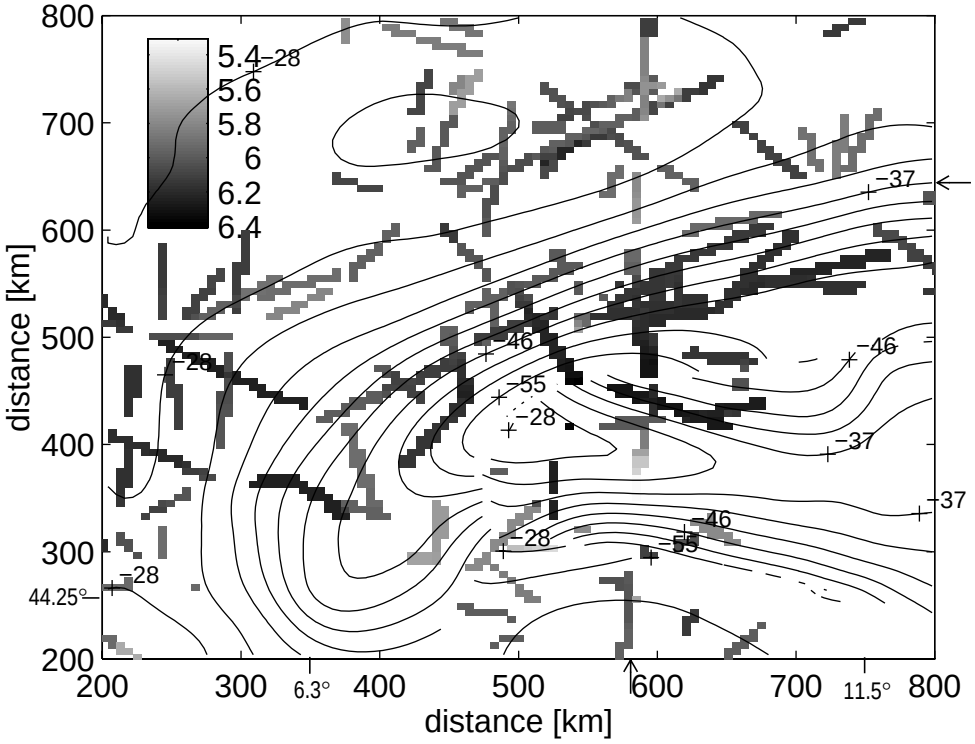


**Figure 3.22** Average velocity distribution in the Alpine region derived from CSS methods (km/s). The data is represented by the approximated Fresnel volumes (box representation). Larger boxes represent larger Fresnel volumes and, hence, data of less quality. The average velocity is represented on a even grid with 2 km grid spacing. Isolines illustrate depth of the Moho discontinuity (see Section 3.2) at 3-km intervals.

### 3.3.3 Construction of the Resulting 3D Model

As already discussed in the introduction to this chapter, the 3D seismic model is parameterized by 301x301x36 grid nodes, to which P-velocities are attached every 2 km in all three spatial directions. The 3D model construction procedure, that integrates the information from surface observation and CSS methods in the 1D reference model, is illustrated in Figure 3.24. The 3D velocity model is shown cut open along the EGT in S-N direction with the volume between x=580 to 800 km, y=650 to 800 km and z=0 to 70 km visually removed (for location see open arrows in Fig. 3.21 - Fig. 3.23). The numerical solution to the construction procedure has been discussed in the section on seismic data assemblage (Section 2.4).

Figure 3.24a shows the 3-layered lithospheric 1D reference model, built up with the structural and velocity reference values as discussed above (Fig. 3.20). It is adapted in a first step for the near-surface sedimentary basins such as the Po and the Molasse basin (Fig. 3.24b). The compensation velocity below the sediment basins (adjusted depth of top basement) is calculated by replacing the sediment velocities with reference surface velocities, because the reference average velocity accounts for a normal crust. Thus, including sedimentary basins cause a decrease of average crustal velocity with respect to areas outside sedimentary basins.

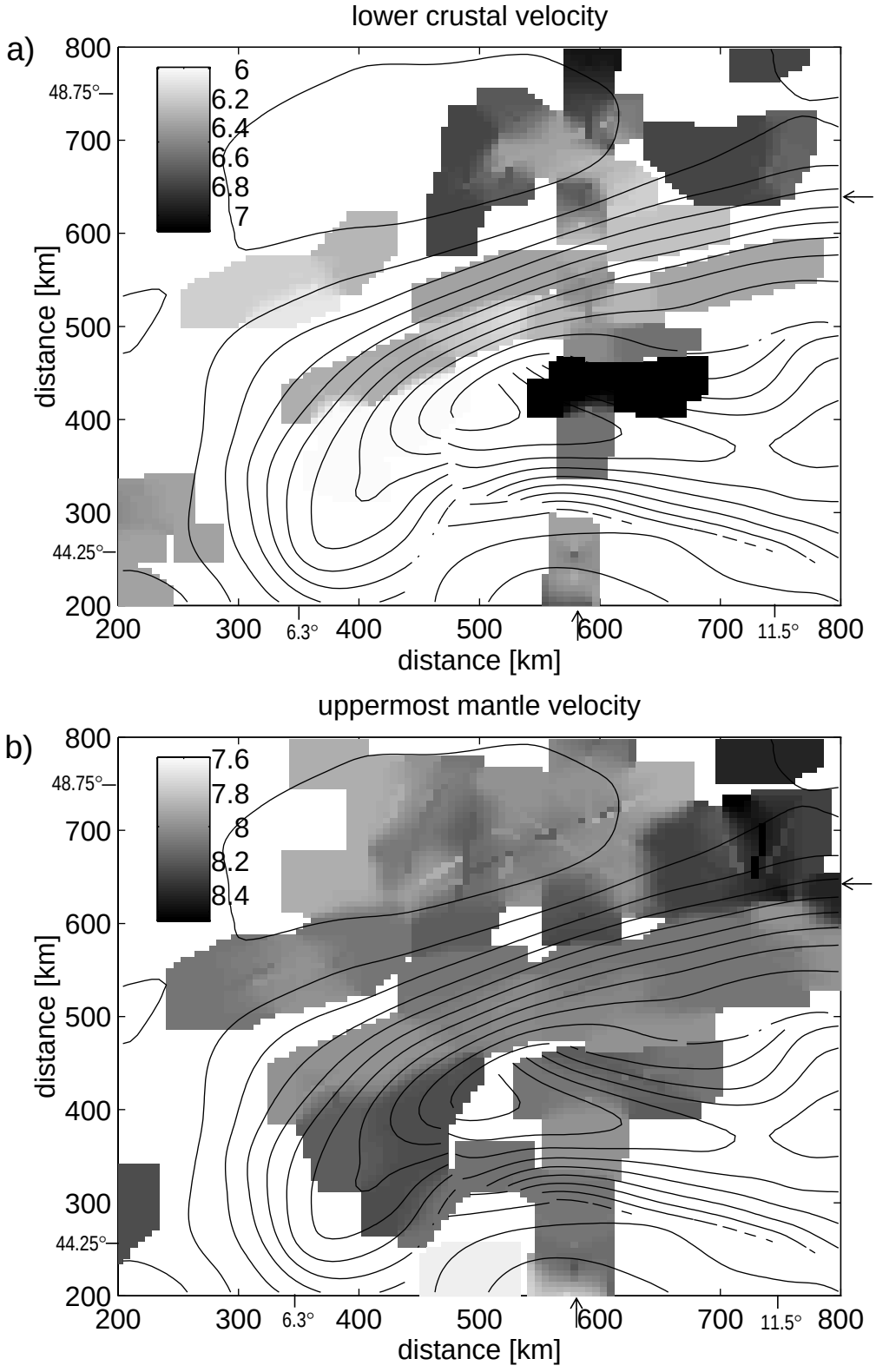


**Figure 3.23** Lower-crustal (a) and uppermost mantle (b) velocity (km/s) after interpolation and extrapolation along the Moho discontinuity. Interpolation is performed on a even grid with 2 km grid spacing. Interpolation radius is for lower-crustal velocity 20 km and for upper-mantle velocity 30 km (see text). Isolines illustrate depth of the Moho discontinuity (see Section 3.2) at 3-km intervals.

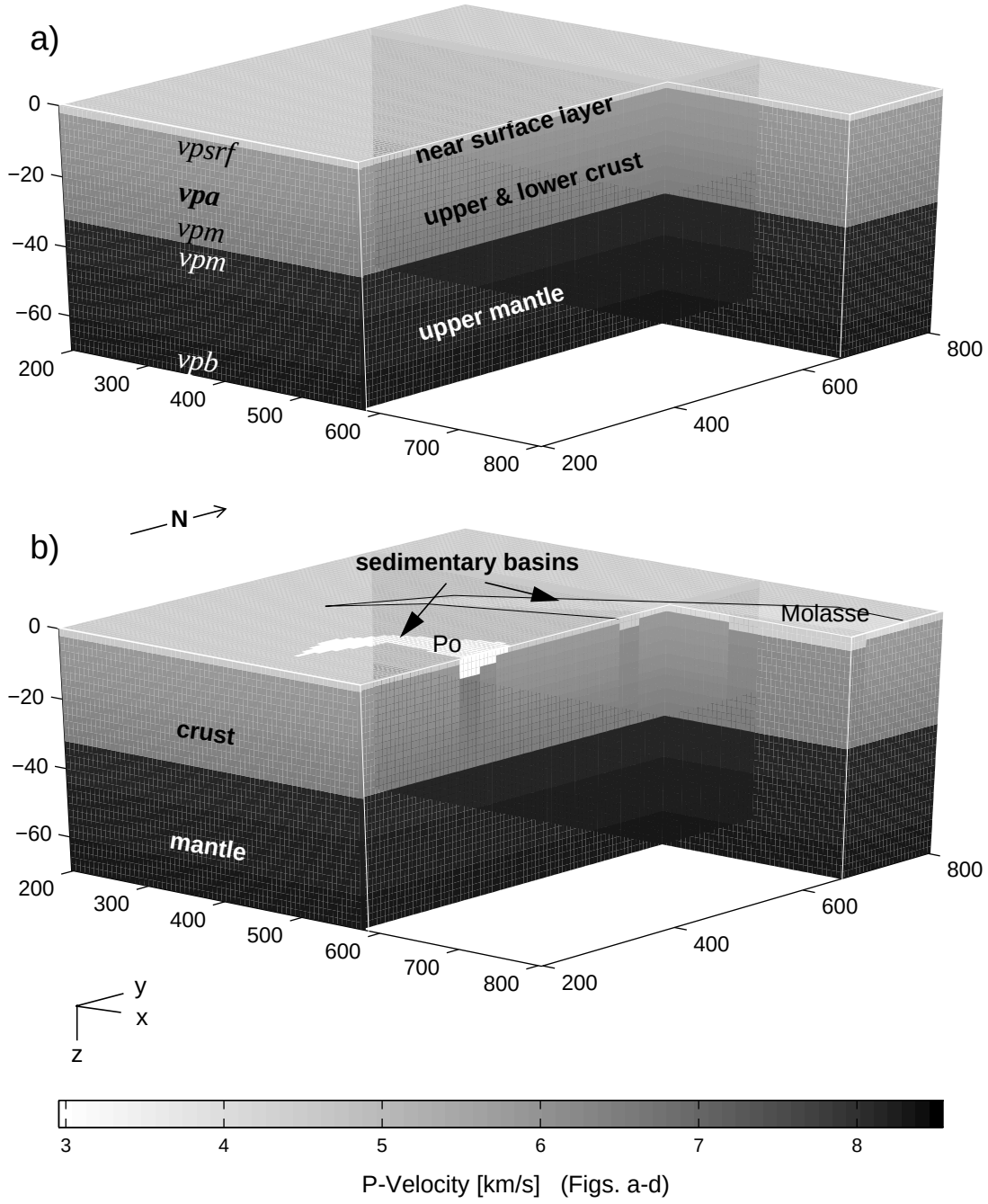


**Figure 3.24** (This and next page) Updating of the Alpine reference model for crust and uppermost mantle (a) with information derived from surface observations and CSS methods. A cut out of the 3D velocity model at x=580 km model distance (along the EGT) is shown. For model location see Fig. 3.1 or Fig. 3.21. b) Reference model adapted for the near-surface Po and Molasse sedimentary basins. c) Integration of the horizontal continuous crust-mantle boundary that is derived from CSS data (see Section 3.2). Crustal thickness is adjusted while reference values as indicated in b) are retained. d) Integration of velocities such as average crustal velocities, lower-crustal and upper mantle velocities which have been measured by CSS methods. e) Overview of data origin in final 3D model: reference velocities (light gray), velocities from surface observations (gray) and CSS velocities (black). All models are sampled on an even grid with 6 km grid spacing. Velocities for (a) to (d) in km/s.

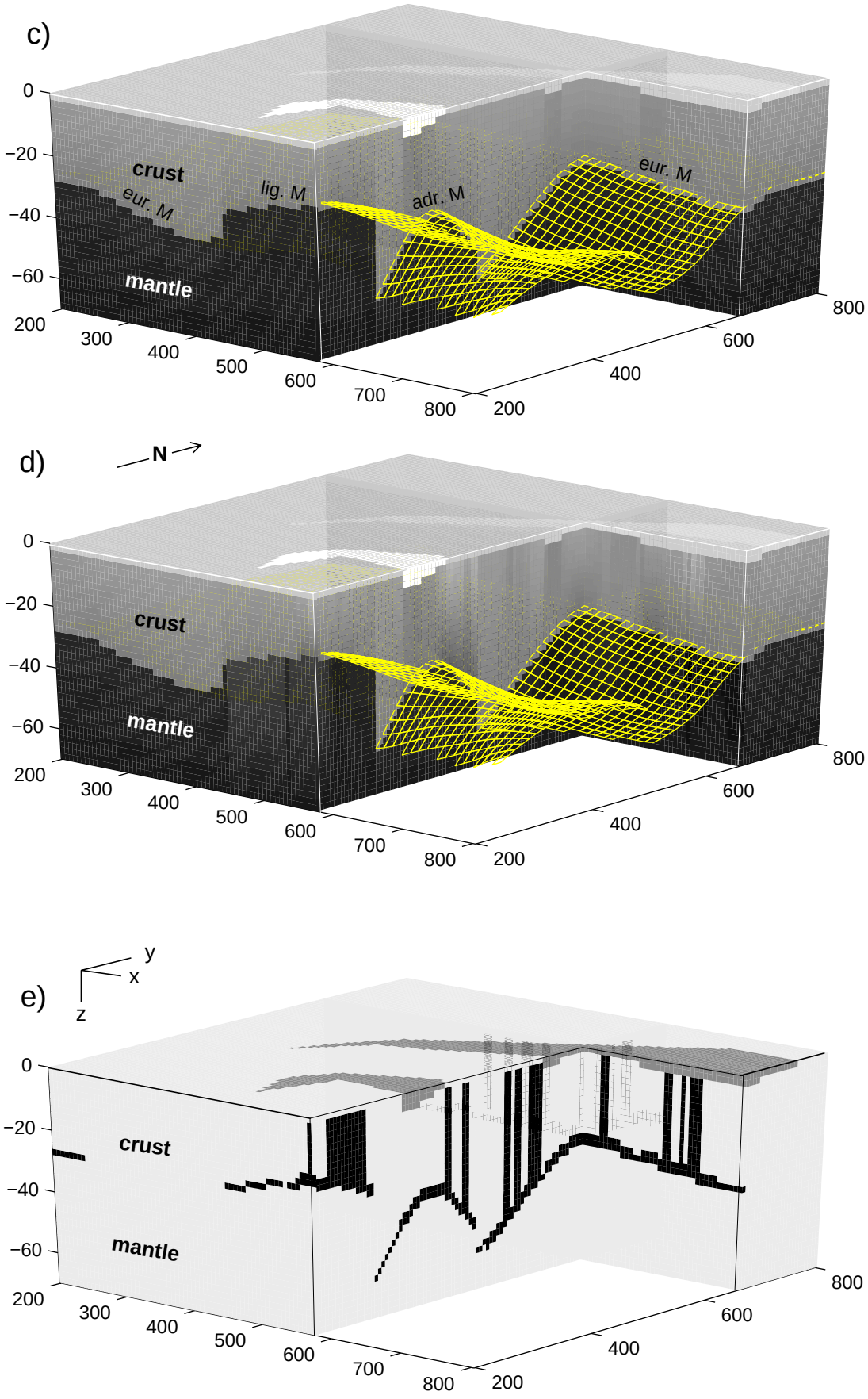
c)
0
−20
−40
−60
crust
eur. M
lig. M
adr. M
eur. M
mantle
200
300
400
500
600
700
800
200
400
600
800
d)
N
0
−20
−40
−60
crust
mantle
200
300
400
500
600
700
800
200
400
600
800
e)
y
x
z
0
−20
−40
−60
crust
mantle
200
300
400
500
600
700
800
200
400
600
800

The previously derived topography of the crust-mantle boundary (Section 3.2) needs to be resampled from a 6 x 6 km grid (representing structural resolution) to a 2 x 2 km grid to adjust interface grid spacing to 3D velocity grid spacing (Fig. 3.25). A spline technique has been used to perform the resampling of the original (coarser) grid. Grid nodes on the resulting finer grid that lie near interface edges are linearly interpolated between the grid nodes on the original grid defining edges of adjoining interfaces (Fig. 3.25). The likewise resampled Moho interface is then replaced by a piecewise-horizontal surface with discrete steps according to the vertical grid spacing and included in the 3D model by adjusting crustal thickness (Fig. 3.24c). In this process, reference velocities as displayed in Figure 3.24b are retained and compensation velocity and vertical depth distribution recomputed with respect to the updated Moho depth.

In a last step, reference velocities are subsequently replaced with lower-crustal, average crustal and upper mantle velocities derived from CSS methods. Compensation velocity and vertical velocity distribution is recomputed according to the updated velocities (for the method, see Section 2.4; Fig. 3.24d).

Overview of the origin of the integrated velocity data within the 3D model is given by Figure 3.24e. The model distinguishs between reference data, information from surface observation and that from CSS methods. Note that only the method with which velocity data is obtained, is visible. Structural information such as the Moho topography, although represented in the color of reference data, is derived as horizontal continuous feature from CSS data (see Section 3.2). It completely replaces the 30 km deep plane reference Moho (see Fig. 3.24a). The black rectangles between surface layer and Moho are the boxes which represent CSS derived average velocities within their volume of influence. Narrow rectangles are the fronts of boxes of profiles that run perpendicular to the cross-section (i.e. along the Alpine strike). Its widths correspond to the observed Fresnel zone at Moho depth. Wider rectangles in black belong to reflectors from the parallel to the cross-section running EGT profile. Its widths correspond to the length of the reflectors.

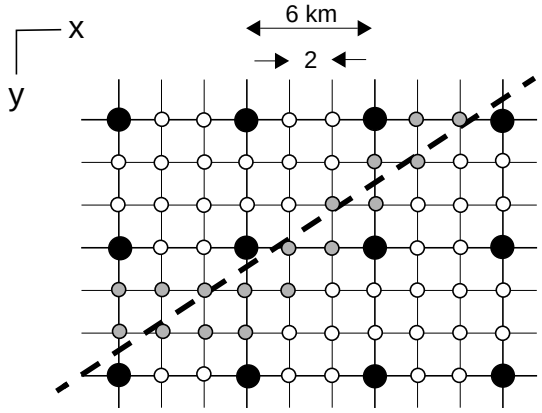


**Figure 3.25** Resampling of the 6 x 6 km gridded Moho interface derived in Section 3.2 (black grid points) to a 2 x 2 km grid (black and white grid points). Gray grid nodes near interface edges (dashed line) are caused by the coarser resolution of the original interface grid. Values for these grid nodes are derived by linearly interpolating between the depths of the adjoining interfaces.

*Control of model consistency: the compensation velocity.*

A 3D computer model, consisting of millions of grid nodes representing structural and velocity information derived by different methods, is hard to check for erroneous model data that may occur due to inconsistency in the original data, inconsistency while merging the data and/or inconsistency in the modeling parameters. As explained in Chapter 2, the task to control construction process and final 3D model is mainly performed by visualization of the model volume and specific seismic parameters. Inconsistencies that appear in the 3D model can be traced back by visualizing individual steps in the construction procedure (i.e., interface modeling, volumetric velocity modeling, etc.). Whereas 3D migration results provide an efficient control of the interface modeling process (Section 2.3.1), the artificial compensation velocity is a good key parameter to detect erroneous data in the 3D crustal velocity distribution (Fig. 3.26). Since this parameter is an expression of the fit between the surface velocity, the lower-crustal velocity and the average crustal velocity, only consistency in the three velocity parameters will result in a reasonable compensation velocity. Reasonable compensation velocities lie within the range of observable top basement velocities such as between about 5 km/s and 6.5 km/s. Such a reasonable value can be strongly exceeded, when, for example,

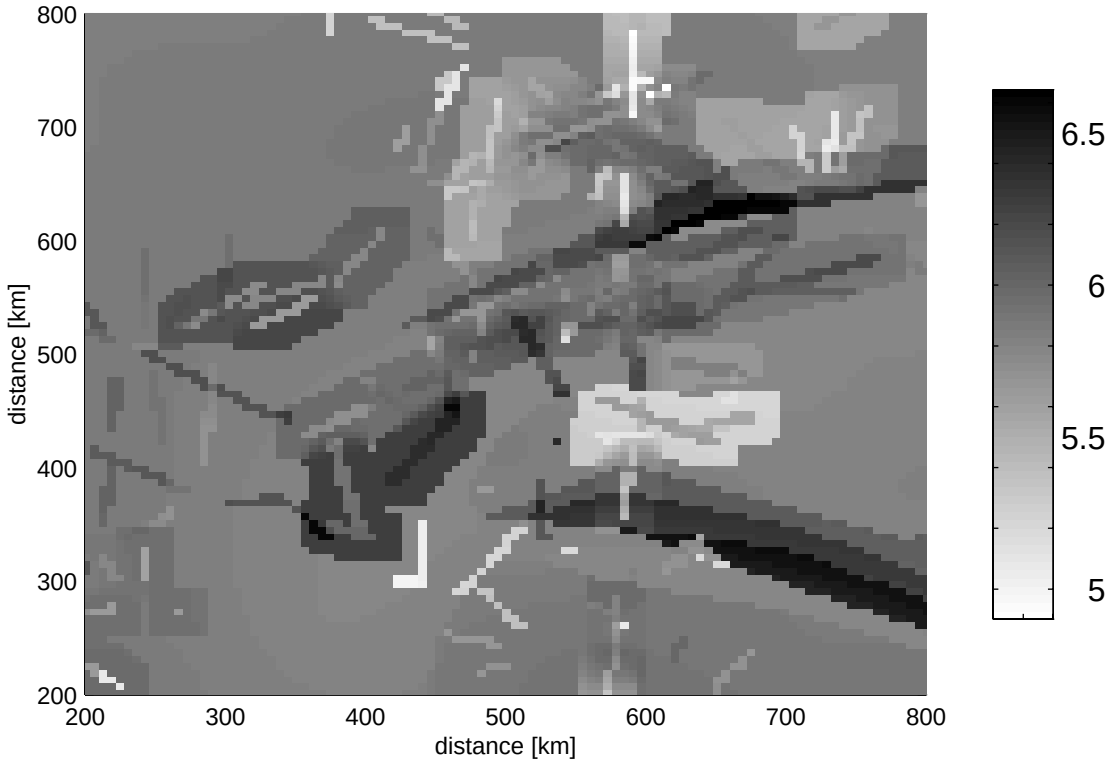


**Figure 3.26** Compensation velocity extracted from the final 3D velocity model. Velocities in km/s. See text for explanation.

accounting for sediment basins while modeling average velocities that have been already corrected for these low velocities (e.g. fan observations in the western Alps, Nadir, 1988). In other cases, inconsistent velocity data has been detected that originated from CSS data that were strongly affected by 3D effects (e.g. Apennine longitudinal profile LW-LC, seeFig. 3.11). In those cases, the corresponding data has been replaced by their reference values. Figure 3.26 maps the compensation velocity that was extracted from the final 3D velocity model. The values range between 4.9 km/s and 6.6 km/s (reference value is 5.85 km/s). As expected, high values for compensation velocities appear below sediment basins where they are deeper located (2 to 6 km) than the reference depth for compensation velocity (2 km). Higher compensation velocities appear also where low lower-crustal-velocities are imaged by CSS methods and combined with reference average velocities (western Alps, Fig. 3.26). Vice versa, high lower-crustal velocity combined with reference average velocity result in low compensation velocities (southern Alps, Fig. 3.26).

*Investigating the 3D Alpine model: cross-sections and tracked sections*

Information about seismic velocity distribution using controlled-source seismic methods is obtained for a vertical plane below the profile. Velocity-depth sections between seismic profiles are usually obtained by projecting structural information provided by the nearby seismic profiles onto the section of interest (e.g., Swiss Geotraverse by Mueller et al., 1980, Fig. 3.27a). Such a procedure assumes continuity between the seismic information and the section on which the information has been projected on.

Using 3D models allow to directly slice velocity-depth sections out of the volume of interest. Figure 3.27b shows a velocity-depth section derived from the 3D Alpine model along the Swiss Geotraverse. Different from the projection method used by Mueller et al. (1980), structures in the 3D model section are derived by interpolation between the nearby seismic information. Such a modeling procedure allows to quantify structures outside the cross-section and to account for their effects on the structures along the cross-section (3D-migration of seismic structures).

Tracking model parameters that lie within a certain threshold allows to map the relief defined by this specific parameter value (tracked section). Such tracked sections in seismic models may be, f.e., velocity contrasts across seismic interfaces. A combined representation of cross-sections and tracked sections allows to visualize the lateral continuity of structures appearing in cross-sections and to control their reliability by mapping the weighting factor (not shown in Fig. 3.27c, see Section 3.2) along the seismic interfaces. Figure 3.27c visualizes the 3D Alpine velocity model by showing the same velocity-depth section along the Swiss Geotraverse as shown in Figure 3.27b and in addition the 3D relief of the crust-mantle interface. It can be seen that the cross-section runs perpendicular to the strike of the European Moho and slices at its southern end the north-western tip of the Adriatic Moho in an oblique fashion.

The main difference in terms of structure between the model by Mueller et al. (1980) (Fig. 3.27a) and the model derived in this study (Fig. 3.27b), is the quantified offset be-

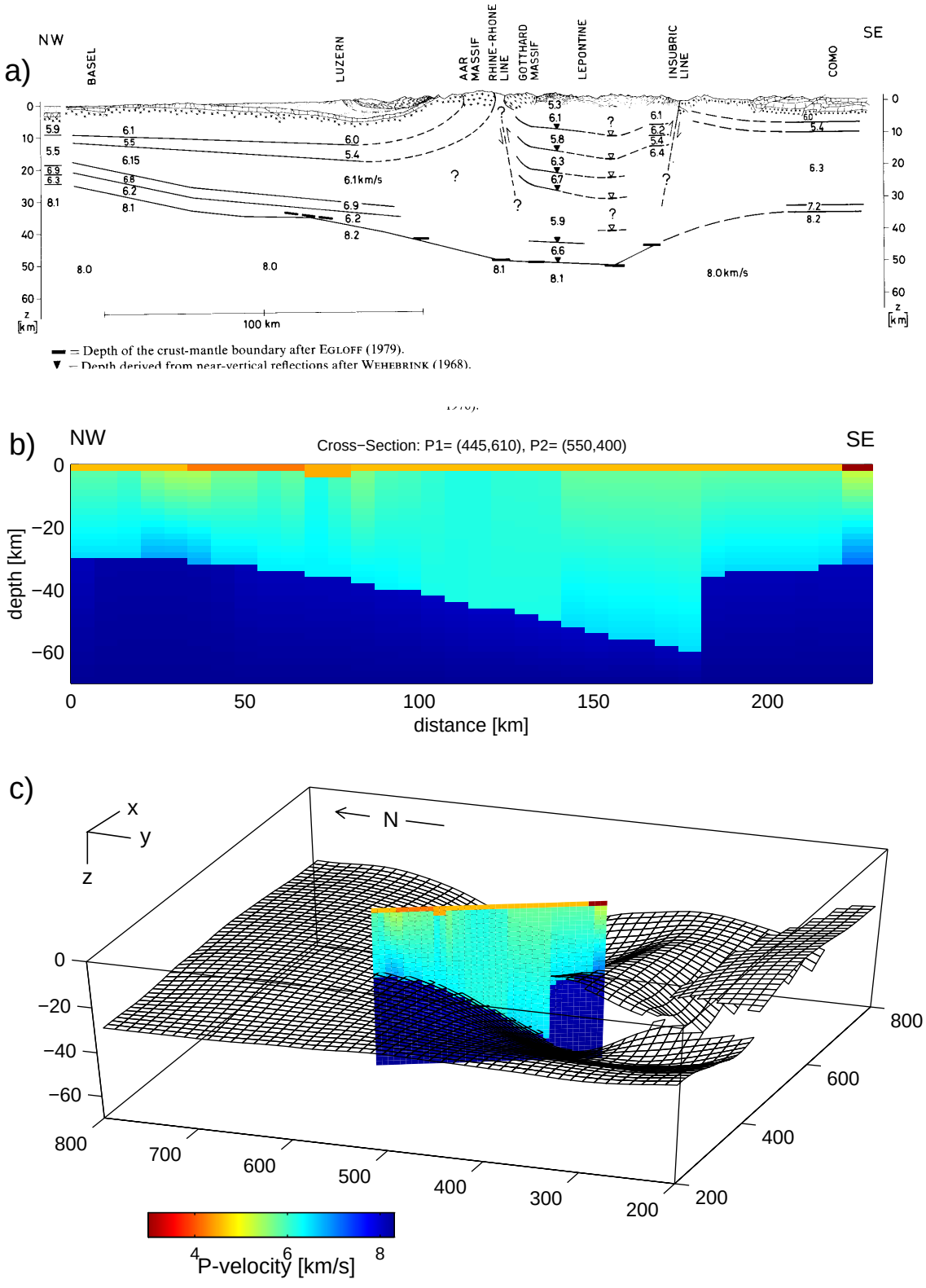


**Figure 3.27** 2D cross-sections along the Swiss Geotraverse (SG): a) Proposed cross-section according to geological and geophysical data derived by projection of nearby information on the SG (after Mueller et al., 1980) b) Velocity cross-section extracted from the 3D velocity model along the SG, derived by interpolation of nearby seismic information. c) Spatial location of the SG in the 3D velocity model with respect to the lateral extension of the three Alpine Mohos.

tween the European and the Adriatic Moho at 180 km model distance in the later model. Mueller et al. (1980) presented, due to lack of seismic data and as consequence, to projection, a rather unreliable smooth transition between these interfaces (dashed line in Fig. 3.27a). 2D interpretations of new CSS data, mainly derived along and perpendicular to the EGT (e.g. Ye et al. 1995; see Section 3.1), and the new method for three-dimensionally modeling these data in space, lead to the quantified Moho offset along the Swiss Geotraverse as shown in Fig. 3.27b. Not only is this most dominant crustal feature quantitatively obtained along the Swiss Geotraverse, but modeled as lateral continuous interface within greater Alpine region (see Fig. 3.27c). Such 3D structural features with quantified reliability are of great importance for tectonic interpretations and hypothesis on lithospheric evolution.

## 3.4 Implications of the 3D Seismic Model

The 3D seismic model reflects the present large-scale Alpine crustal structure resulting from the collision of the African with the European plate. The new seismic model, in particular, depicts three crustal blocks defined by the tectonic regions associated with the European, the Adriatic and the Ligurian Moho interfaces.

As demonstrated in Section 3.2 (see Figs. 3.17 and 3.18), strong evidence from seismic data exist for vertical offsets between the European and Adriatic Moho below the Insubric Line, and between the Adriatic and the Ligurian Moho below the northern Apennines. The former offset indicates a southward subduction of the European Moho under the shallower, north-dipping Adriatic Moho. The latter shows southward subduction of the Adriatic Moho beneath the Ligurian Moho. Both offsets are dominantly ENE-WSW oriented merging into south-ward trending arcs. The Adriatic Moho, while sandwiched between the European Moho in the north and the Ligurian Moho in the south, is up-doming below the Po-plain (see Figs. 3.17 and 3.18), most likely as a result of the compressional forces due to the NNW drifting and anti-clockwise rotating African plate.

No presently available seismic data provide conclusive and direct evidence that the European and the Adriatic lithosphere penetrate deep into upper mantle beneath the Southern Alps, and the Ligurian Sea, respectively. Crustal balancing considerations (Pfiffner et al., 1990, 1991), however, suggest a continuation of the lower European crust in the Adriatic upper-mantle material south of the Insubric Line (see Fig. 3.28 after Schmid et al., 1996). Such a ‘double Moho’ is also likely below the Apennines, where the Adriatic Moho possibly underthrusts the Ligurian Moho. Resolving of such crustal-slab structures beneath a shallower Moho of the overriding plate for geometrical reasons demands deep-seated seismic sources as are employed by local earthquake seismic tomography (Kissling, 1993). The model does not intend to propose possible deep lithospheric structures on the base of tectonic considerations, but relies on available seismic data from robust structural features. Subducting European and Adriatic Moho may be followed into the upper mantle using the parametrization scheme when corresponding

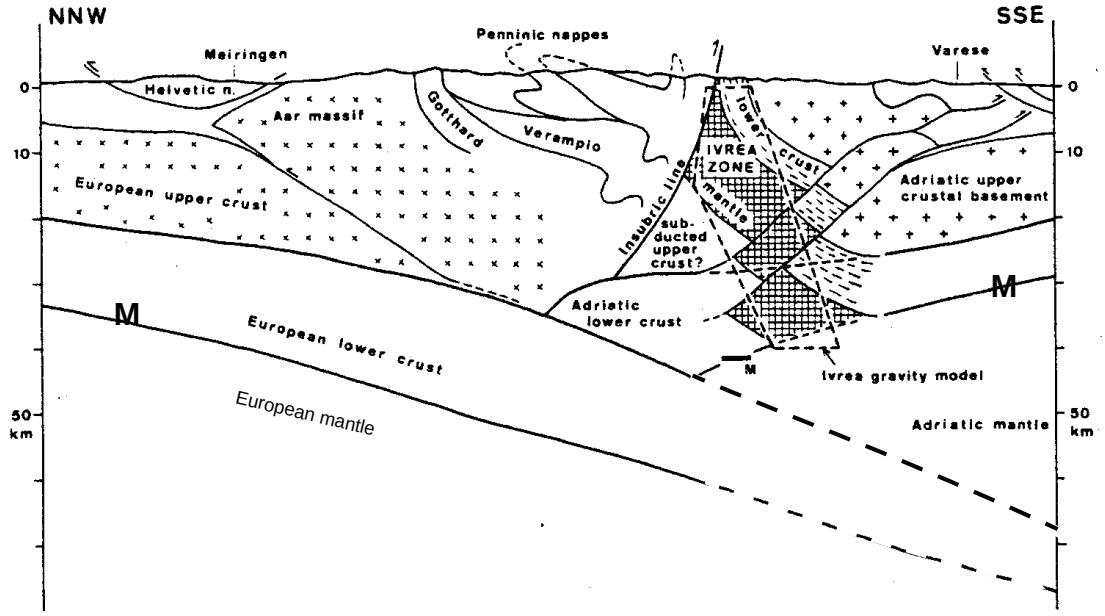


**Figure 3.28** 2D tectonic model (after Schmid et al., 1996) representing approximately the same cross-section as the Swiss Geotraverse does (compare with Figure 3.27). M = Moho interface. Dashed structures: not imaged by controlled-source seismic methods (zone of possible double Moho).

seismic data becomes available.

This concept of model construction leads to the somewhat unlikely velocity discontinuities across the vertical Moho offsets in the 3D model (see e.g. Fig. 3.27b), simulating the change from lower-crustal to upper-mantle velocities at the transition of adjoining crustal blocks. Such zones of artificial velocity structures must be kept in mind when using the model for further studies.

The difference between seismic data gaps and offsets is significant when it comes to tectonic interpretations of the present lithospheric system. Seismic data gaps may be interpreted as zones of absent Moho interface (Pfiffner, 1990), so-called ‘Verschluckungs’-geometry (Laubscher, 1970), showing symmetric subduction of lithosphere. Moho offsets are interpreted as regions of underthrusting lithosphere (Pfiffner, 1992) producing asymmetric subduction geometry. Thus, quantification of vertical Moho offsets is of great importance for tectonic interpretation of the Alpine lithosphere system. Data gaps along 2D profiles must be verified by crossing profiles (see Fig. 1.3).

The smoothness of the Moho interface is in accordance with the resolution capability of the applied method, the data quality and the density of the data distribution. The intra-crustal velocity structure of the 3D model, based on reference and CSS-derived velocity data for average crust and lower crust, does not resolve small-scale velocity inhomogeneities, also they may have been imaged along the 2D profiles. Structures that are of smaller scale than the smallest volume possible to resolve are not shown in the model. Smaller-scale tectonic processes during the Alpine mountain building, however, may also have left traces on the topography of the Moho, but they remain either unre-

solved or occur in regions of seismic data gaps. Thus, the fact of non-existence of second order structures (e.g. crocodile structures) in the model may not be used as an argument for tectonic interpretations.

The Ivrea body (Fig. 3.28), is not integrated in the 3D model because CSS-derived information about this high-velocity anomaly does not allow its adequate parametrization within the 3D model. A good way to include the Ivrea velocities in the 3D model is by integration of local earthquake tomography results (see Chap. 5). The integration of the Ivrea body is of great importance for the further use of the 3D model for teleseismic travel time studies. Calculated teleseismic travel times deviate from the expected travel times in the Ivrea region by greater values (see Chap. 4).

# CHAPTER 4

# 3D TELESEISMIC WAVEFRONT SCATTERING

Due to the low frequencies and the near-vertical angle of incidence of incoming waves, teleseismic travel time tomography only poorly resolves crustal-scale structure. Nevertheless, complex crustal structures such as those in the Alpine region influence teleseismic travel times. Effects in the order of 0.5 s to 1 s are expected in the central and western Alps (Baer, 1979; Guyoton, 1991). Neglecting these effects during inversion will result in tomographic models of lesser reliability, and in artifacts in the images of deeper structures. Hence, in order to use teleseismic data to study in detail upper-mantle structures below the Alpine orogen, the 3D crustal model derived in Chapter 3 must be integrated in the tomographic process. For such an inversion of teleseismic data, a forward problem solver, properly accounting for strongly heterogeneous velocity structures, is necessary.

In this chapter, a numerical solution to accurately solve the forward problem in strongly heterogeneous velocity structures is described and the determination of the spherical time field of an incoming teleseismic wavefront at the base of the model is discussed. Synthetic tests have been performed on crustal-scale velocity heterogeneities and on the 3D Alpine velocity model. Teleseismic wavefronts from various azimuths are computed through the 3D Alpine crustal structure and the scattering effects are investigated. Finally, travel time residuals from selected events, computed for the 3D model, are compared along profiles with measured teleseismic travel time residuals from the literature.

## 4.1 Method and Synthetic Tests

### 4.1.1 The Forward Problem in Teleseismic Tomography

The earthquake location procedure and the determination of the three-dimensional velocity structure require the calculation of seismic rays in a heterogeneous medium between two given endpoints. Such ray tracing procedures are responsible to determine these nodes that influence the rays (ray geometry) and how much time the rays spend near each node (ray travel time). The ‘two-point’ boundary value problem for true 3D cases can not be solved, in general, directly. The minimum time path can be found by iteratively refining approximate solutions using a number of distinct strageties. The two

strategies most commonly employed are sometimes called ‘shooting’ or ‘bending’ of rays (Julian and Gubbins, 1977; Thurber, 1987).

The shooting method reformulates the problem in terms of an initial value problem in which ray slowness at one point is specified. The ray is propagated forward until a termination condition is met, at which time the error between the ray endpoint and the desired coordinates are compared. This shooting error is used to refine the initial conditions and the process is repeated until satisfactory agreement between the desired and actual endpoints are obtained. The bending method, introduced in seismology by Wesson (1970, 1971) connects the desired endpoints of the ray by a line path which is iteratively deformed until Fermat’s principle of stationary time is satisfied. The bending method is successfully used in local earthquake studies where it rapidly traces the ray from source to receiver through the 3D velocity field (e.g. Thurber, 1986). Thurber (1987) discusses shooting and bending methods in more detail.

Since the true entry point of a teleseismic ray into the base of the model is unknown, the two-point boundary problem can not be solved. What is known in the teleseismic forward problem is the slowness vector along the bottom boundary - which is given by the ray parameter and azimuth from standard seismological tables - and the position at the surface (usually the receiver site). These conditions lead to the adaption of the shooting technique for the solution of this mixed-boundary problem (e.g. Steck and Prothero, 1991). The main limitations of raytracing for the teleseismic problem are: the difficulty in finding the minimum travel time path in strongly varying velocity fields, the time consuming process to find minimum travel time paths, and the problem to find correct rays in shadow zones. In both bending and shooting methods, it is possible that the result denotes only a local travel time minimum, while the global minimum and its corresponding ray path remain unknown. With single ray methods, travel times are obtained at specific points on the Earth’s surface only (receiver sites). The whole time field of an incoming teleseismic wavefront on the Earth’s surface can not be displayed. Being able to calculate the whole travel time field of teleseismic waves, however, allows to check the velocity model for accuracy of the chosen parametrization and for erroneous model parameters. This is an important task when including ‘a priori’ information in the initial model for seismic tomography, since this information may be held fixed during the inversion process. Fixed erroneous features will project artifacts into the neighboring structure. The main advantage of knowing the whole time field at the surface, however, is the possibility to correlate phases across a larger area.

The above considerations led seek a method able to trace first-arrival times along wavefronts through 3D heterogeneous media. Finite differencing of the 3D eikonal equation provides an efficient method to do so (for an overview see Nowack, 1992).

### 4.1.2 Numerical Solution for the Forward Problem: Finite Differencing of the 3D Eikonal Equation

The rapid travel time calculations required for three-dimensional forward modeling of the teleseismic wavefronts are provided by the finite difference algorithm described by

Vidale (1988, 1990). The algorithm has been modified by Hole and Zelt (1995) to handle strong and sharp velocity contrasts properly. It calculates first arrival travel times by propagating wavefronts through a grid of velocity nodes sampled uniformly in three dimensions. The iterative extrapolation of travel times is based on the 3D eikonal equation of ray tracing

$$\left(\frac{\partial t}{\partial x}\right)^2 + \left(\frac{\partial t}{\partial y}\right)^2 + \left(\frac{\partial t}{\partial z}\right)^2 = s^2(x, y, z) \qquad (4\text{-}1)$$

that relates the gradient of the travel time to the velocity structure. *t* is the travel time, the cartesian coordinate axes are x, y, and z, and s is the slowness. In the finite difference solution of Equation 4-1 local plane wavefronts or local spherical wavefronts are used within cells of the spatial grid (see Vidale, 1990 and Hole and Zelt, 1995).

The problem of the generally multi-valued nature of time fields is avoided by tracing only minimum arrival times. The algorithm is much faster than three-dimensional ray-tracing (see above) and determines travel times from a given point-source and velocity structure to all points within the 3D grid, eliminating the need to find the correct ray connecting the two points. Head waves and diffractions filling shadow zones, are properly computed if they are the first arrivals. Travel times of sufficient accuracy can be obtained by using a sufficiently dense velocity grid spacing. Simulating plane and curved wavefronts as sources at model faces (e.g. the base of a 3D model) is performed by Hole et al. (1992). They used a re-gridding technique for basin modeling that required a starting wave field at model faces next to incoming wavefronts to proceed with travel time calculation.

### 4.1.3 Incoming Teleseismic Wavefronts

*Plane and spherical wavefronts*

Studies on teleseismic data require the definition of the incoming wavefront at the base of a pre-assumed velocity model below the receiver array (local model). Inadequate description of ray path segments outside the modeled volume are a potential source of systematic errors in travel time residuals. Due to the great distances of teleseismic sources from a receiver array (between 25° and 103°, see Fig. 2.2), incoming teleseismic wavefronts are in general approximated by a plane wave, i.e. they are assumed to exhibit the same horizontal slowness at the base and the top of a local model. In reality, these wavefronts are curved and differ for the base and the top of a local 3D model. Deviations of curved wavefronts from a plane wavefront below the receiver array at the base of the local model are caused by: the radial symmetry of earthquake generated waves, the radial increasing P-velocity in the Earth's crust and mantle, and the local velocity inhomogeneities along the wave path between source and receiver array.

A plane wavefront approximation for teleseismic travel times at a certain depth below the receiver array is normally performed by using a mean of the ray parameters from

some standard seismological tables for the area of interest. In this case, none of the above-mentioned causes for plane wavefront deviations are considered.

Another method is fitting observed travel times ($t_i$) by a plane surface. Plane surfaces can be described by linear equations with $m$ as the coefficient vector and with ($x_i$,$y_i$) as the horizontal coordinates of the observed travel time $t_i$ in a particular location:

$$t_i = m_1 + m_2 x_i + m_3 y_i . \qquad (4\text{-}2)$$

Equation (4-2) can be written as

$$G \cdot m = t \qquad (4\text{-}3)$$

and solved for the coefficients $m$ by least-square methods (e.g. Menke, 1984):

$$m = [G^T G]^{-1} G^T t. \qquad (4\text{-}4)$$

A plane time field determined at the surface by this procedure may be back-projected using a reference model to the base of the local 3D model from where the forward problem is solved again, now using the local 3D velocity structure.

Approximation of the time field of an incoming teleseismic wave by planes is justified only for arrays with small apertures of about 1° or 2°. Then this source of model error may be unimportant for some arrays (Ellsworth, 1977). The effect of plane wavefront approximations on teleseismic travel times becomes, however, significant for larger areas. In regions of investigation with an aperture of about 8°, as treated in Section 4.2, the curvature of incoming teleseismic wavefronts need to be considered.

*Procedure to derive spherical wavefronts*

Figure 4.1 depicts the procedure used in the following to derive spherical wavefronts at the base $z_m$ of an 'a priori' 3D local model. Travel time $t_k$ and slowness $s_k$ of a ray $k$ for any source depth $z_s$ and epicentral distance $\Delta$ is computed on the Earth's surface (i.e. model surface) for the grid nodes ($x_i$,$y_j$) of the local 3D model using the 1D standard whole-earth model IASP91 (Kennett and Engdahl, 1991; Kennett, 1991). The travel times are corrected for ellipticity using the formulation of Dziewonski and Gilbert (1976) with ellipticity coefficient as listed by Kennett (1991). The derived values for travel time and slowness are appropriate for a point on the surface, but not below this point at depth (e.g. at the base of the local model). To find position ($x$,$y$) and travel time ($t'$) of the ray at the point where it enters the local model at depth $z_m$, the ray is traced back from the surface to the base of the local model through the IASP91 1D velocity structure. A simple 1D ray tracer following Snell's law is used with slowness $s_k$ at the surface as starting condition.

Performing the above procedure for all grid points of the local model at the surface, uneven distributed entry points at the base of the local model with corresponding entry times $t'_k(x,y,z_m)$ and slowness $s'_k(x,y,z_m)$ values are obtained. These travel times are in-

terpolated on an even horizontal grid equal to the model grid ($t'_k(x_i,y_j)$). Different from the plane-wave approximations, taking into account the curvature of the teleseismic wavefronts specify the correct slowness at every point at the base of the local model. With these values, a forward calculation of travel times is then performed through the 3D local model to the surface ($t''_k(x_i,y_j,z=0)$).

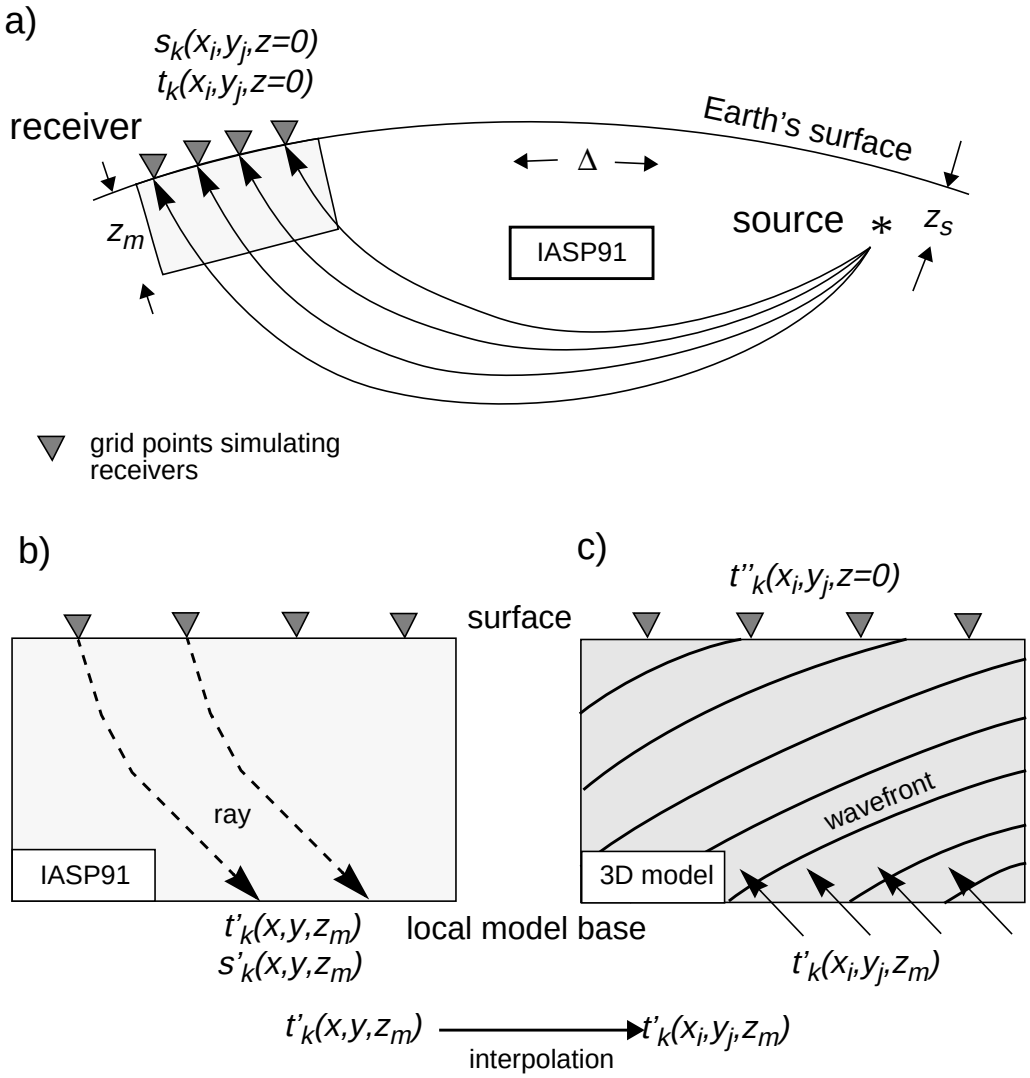


**Figure 4.1** Procedure to determine time fields of incoming teleseismic wavefronts at depth *zm* below a receiver array at the base of a local 3D model (shaded). a) Obtain slowness *s* and travel times *t* for all model grid points at the surface for a specific source depth *zs* and epicentral distance Δ. A 1D standard whole-earth model (e.g. IASP91, Kennett, 1991) is used. b) Trace rays back through the 1D IASP91 model, using the slowness at the surface from (a) and Snell's law. c) Calculate wavefronts through the local 3D model using the time field t' obtained by interpolation in at the the base of the model.

### 4.1.4 Tests on Synthetic Velocity Structures

The following synthetic tests are performed to check the algorithm described above for 3D travel time calculation in the presence of crustal-scale velocity heterogeneities as parametrized in the 3D Alpine velocity model established in Chapter 3. This allows to test the model parametrization for teleseismic wavefront calculations. A grid spacing of 2 km in all spatial direction is used for all tests. Although shown by 2D sections, travel times are obtained for 3D models. All wavefronts are calculated using a vertically propagating plane wave starting at the base of the synthetic models at time $t_0$= 1 second.

TEST 1: In Figure 4.2, wavefronts are calculated for a velocity structure showing a mean velocity of 6 km/s to a depth of 100 km. The model includes a low velocity (4 km/s) cube at depths between 20 km and 40 km and a high velocity cube (8 km/s) at depths between 60 km and 80 km (Fig. 4.2a). Both cubes extend 40 km in either horizontal directions. The upper cube with a velocity of 4 km/s simulates a contrast to the surrounding mean velocity as observed between sedimentary basins and basement. The lower cube with a velocity 8 km/s simulates a contrast to the surrounding mean velocity as observed across the crust-mantle transition. The finite difference scheme properly calculates head waves along the sides of the cubes (Fig. 4.2b). Wavefronts travelling through the centers of the cubes are not distorted.

TEST 2: Figure 4.3a shows a velocity model that simulates an offset of 30 km for the crust-mantle interface. Near-surface-, lower-crustal-, and upper-mantle velocities are held constant for the whole model. *Compensation-velocity* is calculated using an average crustal velocity of 6.1 km/s for both sides of the Moho offset. The calculated wavefronts (Fig. 4.3b) clearly show the head waves (indicated by dashed lines on two wavefronts in Fig. 4.3b) generated from the vertical contrast between crust and mantle at the offset location. The small travel time peaks on the right side of the head waves at about 51 km distance (indicated by arrows for three wavefronts in Fig. 4.3b) are most likely numerical artifacts produced by the strongly heterogeneous velocity structure. The strong vertical velocity contrast above the edge of the lower black interface (at distance 50 km and between depths of 50 km and 60 km, see white dashed box in Fig. 4.3a) is a result of the model parametrization and most likely too strong compared to what would be observed in the real world (see Section 3.3.3). However, the strong contrast for the area indicated (Fig. 4.3a) generates significant head waves and affects wavefronts even at the corresponding surface position. Attention must be paid to wavefronts arriving with larger incident angles. They may be reflected at those vertical velocity contrasts.

TEST 3: Figure 4.4 shows a velocity structure with horizontal interface simulating the crust-mantle transition at a depth of 40 km. Near-surface and vertical average velocity are held constant along the model and the *compensation velocity* and intra-crustal velocity distribution are calculated with different lower-crustal velocities for each side of the model. The lower-crustal velocities are 6 km/s for the left side (distance 0 - 50 km in Fig. 4.4a) and 7 km/s for the right side (distance 50 km - 100 km in Fig. 4.4a) of the

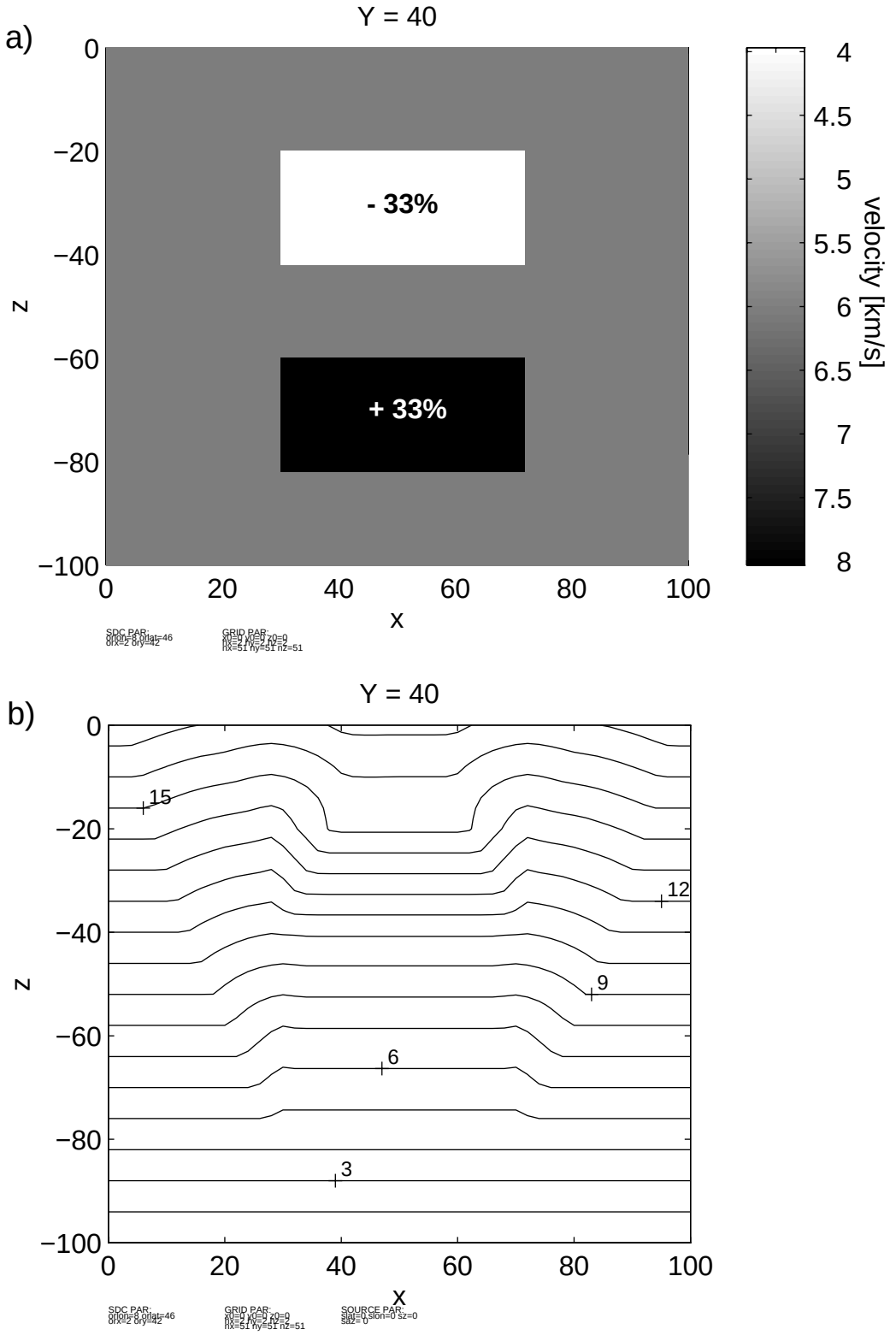


**Figure 4.2** TEST 1: Synthetic test on travel times calculated for a model with 3D crustal-scale velocity heterogeneities. 2D vertical sections are depicted. a) Velocity model. b) Travel times (contoured at 1s intervals) of a zero slowness plane wave which started at time $t_0$=1 second from the base (-100 km) of the model shown in a. See text for discussion.

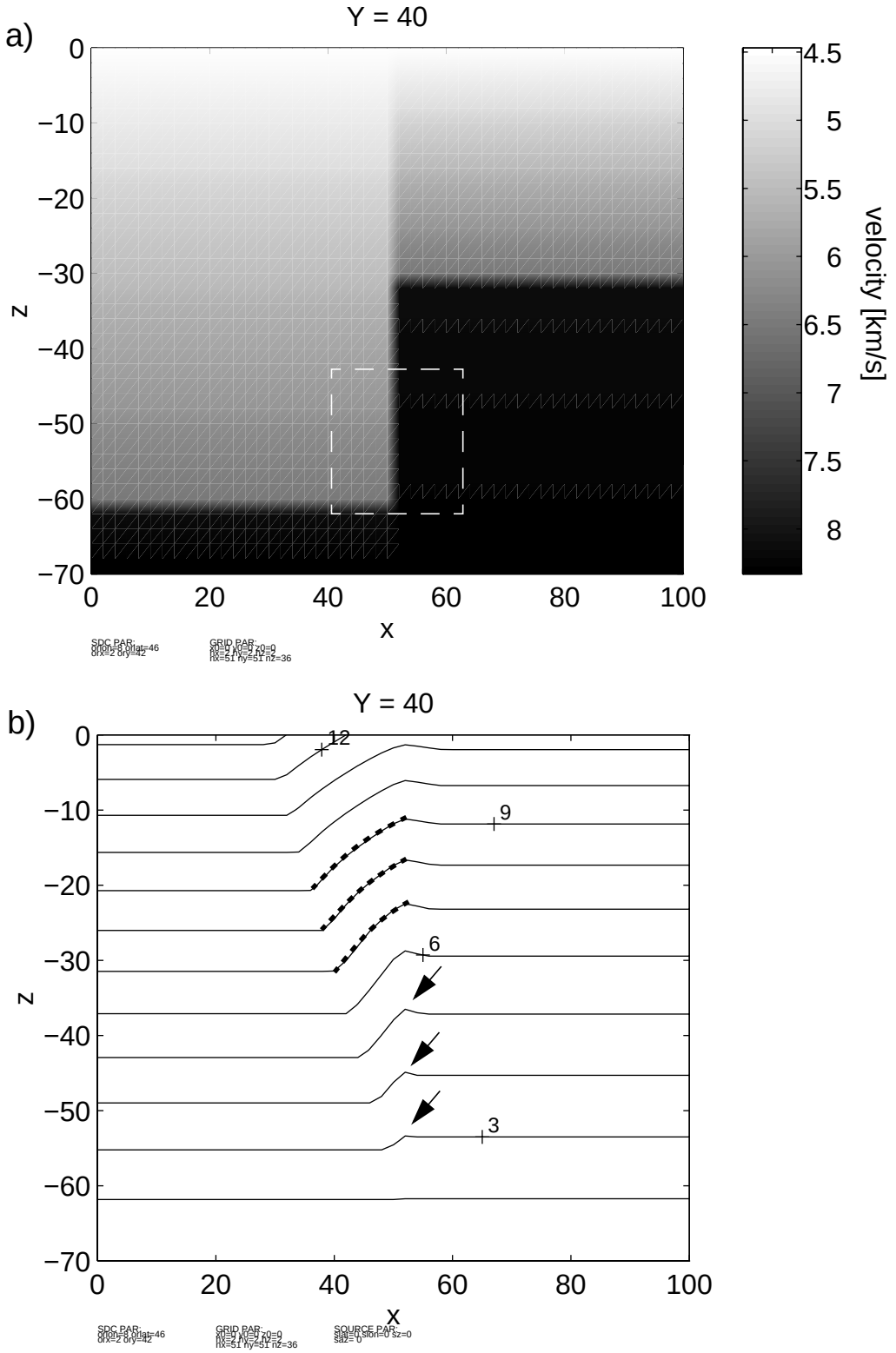


**Figure 4.3** TEST 2: Synthetic test on travel times calculated for a model with 3D crustal-scale velocity heterogeneities. 2D vertical sections are depicted. a) Velocity model. b) Travel times (contoured at 1s intervals) of a zero slowness plane wave which started at time $t_0$=1 second from the base (-70 km) of the model shown in a. See text for discussion, dashed lines and arrows.

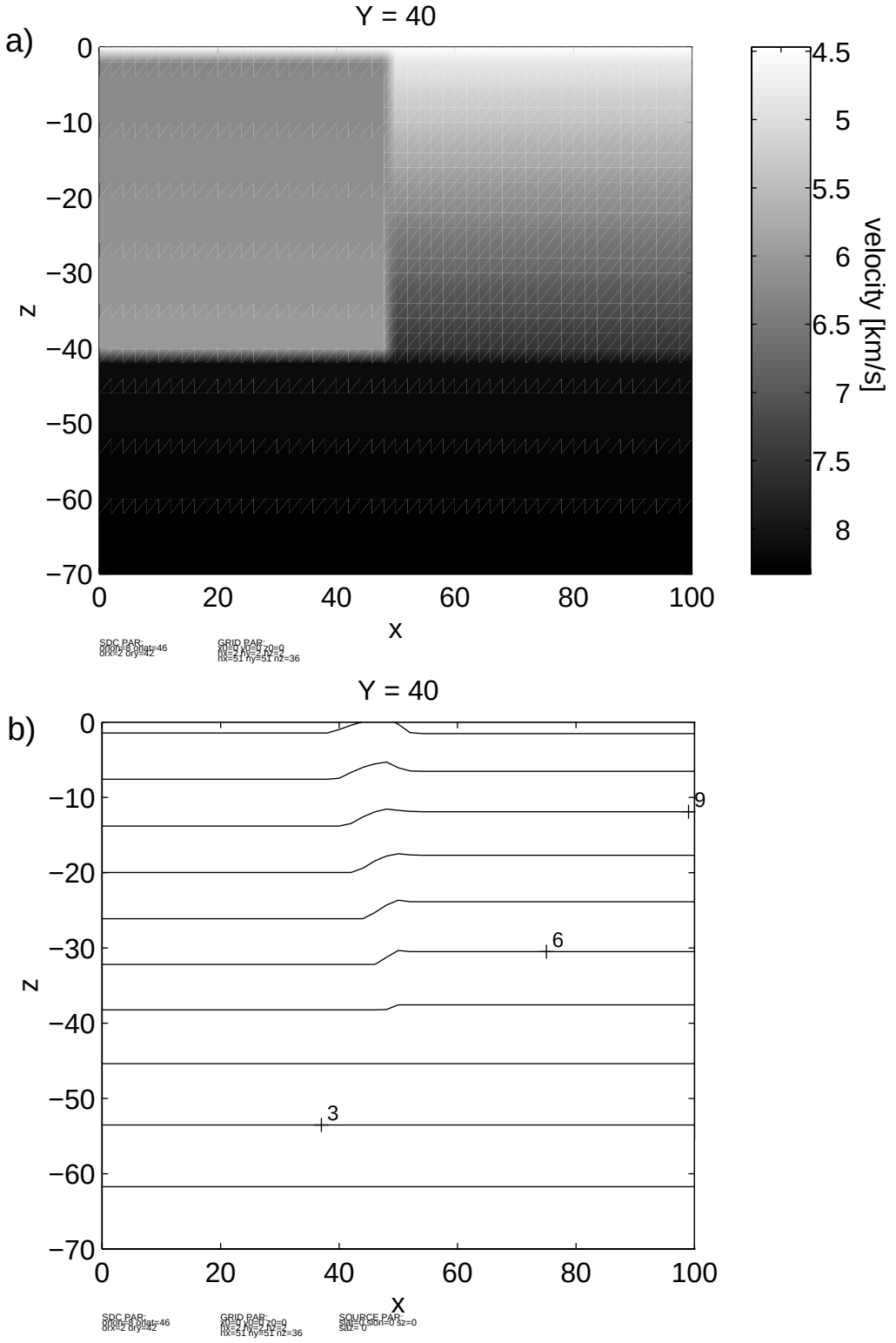


**Figure 4.4** TEST 3: Synthetic test on travel times calculated for a model with 3D crustal-scale velocity heterogeneities. 2D vertical sections are depicted. a) Velocity model. b) Travel times (contoured at 1s intervals) of a zero slowness plane wave started at time $t_0$=1 second from the base (-70 km) of the model shown in a. See text for discussion.

model. The velocity changes across one grid spacing (2 km). Calculated wavefronts show (Fig. 4.4b) that head waves on the left side (0 - 50 km) for the lower part of the crust and on the right side (50 - 100 km) for the upper part of the crust are generated. Outside the vertical contrast (0 - 35 km and 60 - 100 km model distance in Fig. 4.4b) wavefronts properly arrive horizontally at the surface. The earlier arrivals of about 0.2 s for head waves along such a vertical contrast is most certainly not a realistic feature. It results from the way, CSS velocities are integrated in, e.g., reference models without smoothing across the arising contrasts.

The tests show how sensitive wavefronts react near velocity heterogeneities caused by the model parametrization. These results have to be kept in mind when in the following teleseismic travel times are calculated through the 3D Alpine model.

## 4.2 Teleseismic Travel Time Residuals in the Alps

In this section, the 3D Alpine velocity model established in Chapter 3 is used to calculate the crustal effects on teleseismic first arrival travel times. Before scattering of wavefronts from teleseismic distances by the parameterized structures is simulated, the parameterization and data consistency of the 3D model is tested.

### 4.2.1 Tests on 3D Alpine Model

As explained before, computation of entire seismic wave fields within 3D velocity models allow to control consistency of model parametrization and may uncover artifacts and erroneous data compiled. In the following, the parametrization of the 3D Alpine model is tested by wavefront calculations.

In a first step, the parametrization of the crust-mantle interface and sedimentary basins is tested using the model shown in Figure 3.24c (see Section 3.3). This model is based on average Alpine crustal reference velocities. A vertically incident plane wave is generated with zero time at the base of the model (z= 70 km) and travel time of wavefronts are calculated through that model to the surface. Figure 4.5a shows the absolute travel times at the model surface. As expected, this figure mainly represents crustal thickness in terms of travel times. Smallest travel times are observed in the Ligurian area caused by the shallow Ligurian Moho. A typical large increase of travel times is observed above the sedimentary Po basin. No significant numerical oscillations occur at the surface above the Moho interface offsets. The chosen parametrization of seismic structures seems, therefore, to be adequately designed for the purpose of such travel time calculations.

In a next step, the parameterization and integration of CSS velocities are tested on the more detailed 3D Alpine model shown in Figure 3.24d. In addition to sedimentary basins and crust-mantle interface, this model includes volumetrically modeled CSS velocities where available. As in the foregoing, a zero slowness plane wave is generated with zero time at the base of the model (z= 70 km) and travel times of wavefronts are calcu-

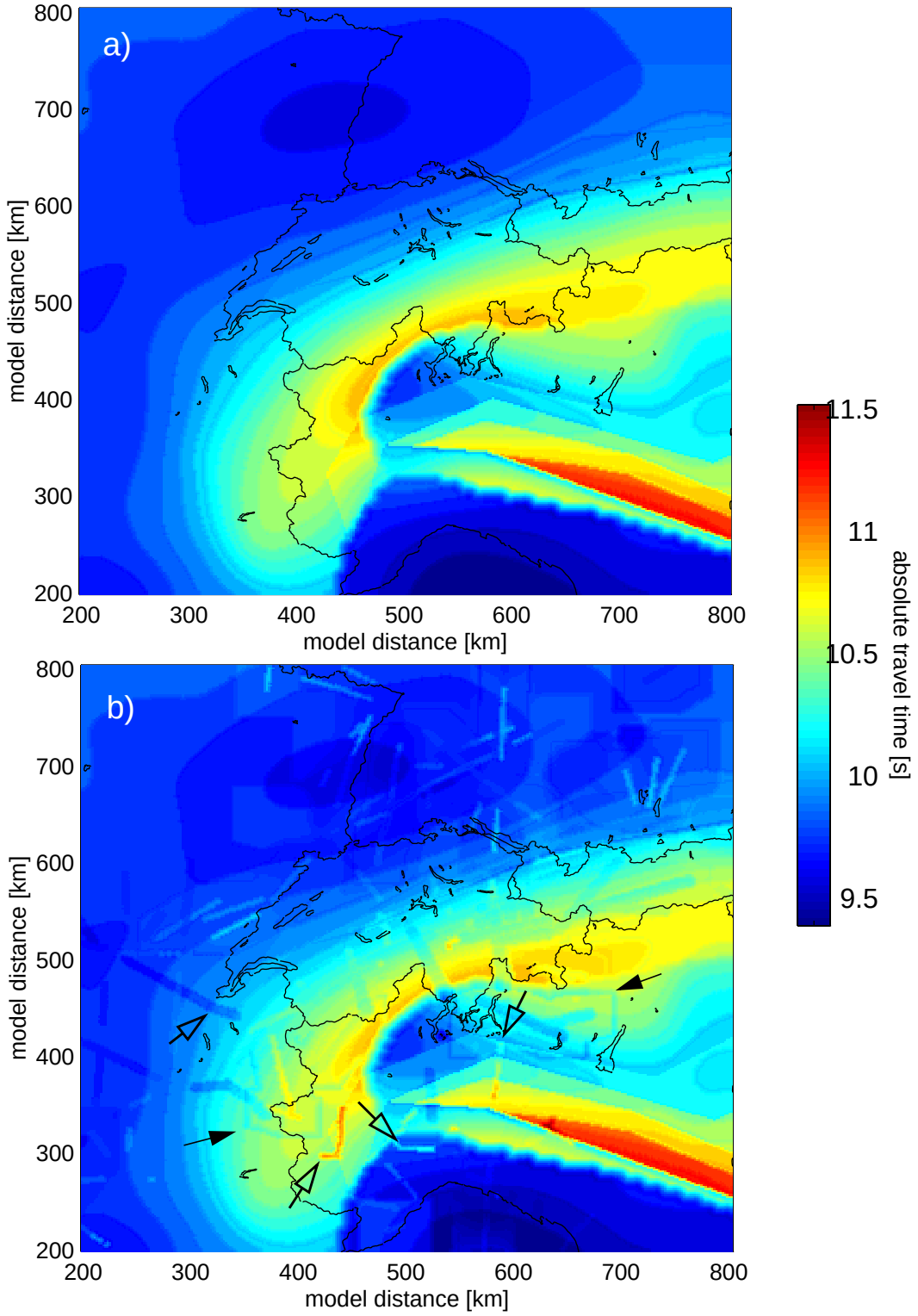


**Figure 4.5** Absolute travel times at the surface of two different versions of the Alpine 3D model for a vertically incoming plane wavefront at depth = 70km. a) 3D Alpine model based on reference average crustal velocities. Sedimentary basins and crust-mantle interface are included (see model shown in Fig. 3.24c). b) 3D Alpine model as in a), but additionally updated with lower-crustal, upper-mantle and average crustal velocities from CSS methods (see model shown in Fig. 3.24d). See text for discussion and arrows.

lated through that model to the surface. Figure 4.5b shows the absolute travel times at the model surface. It can be seen, that effects as observed in the synthetic test # 3 in Section 4.1.4 (see Fig. 4.4) clearly appear also in the 3D Alpine model. Vertical velocity contrasts, that result from abrupt lateral changes in lower-crustal velocity - i.e. transition from CSS to reference values - by retaining average crustal velocity, affect the time field at the surface of the model by narrow bands of earlier travel times (solid arrows in Fig. 4.5b). Thus, these artifacts are not related to structure but to the way lateral changes in lower-crustal velocities are parametrized.

Different from those artifacts caused by parametrization, structural inconsistencies can be seen in cases where CSS average velocities strongly contrast with the nearby reference average velocity (see open arrows in Fig. 4.5b). The reason for such inconsistencies may lie in the chosen reference average velocity for that area or in the approximations used for the ‘box representation’ (see Section 2.3.2) of CSS average velocities. The approximative method of volumetric modeling of CSS average velocities does not represent average velocities within the volume actually sampled by the ray tube, and does not properly 3D-migrate the ‘boxes’ (see Section 2.3.2). This may be a reason why the strongest inconsistencies are observed in strongly 3D-variable structures (open arrows in Fig. 4.5b).

The discussion of this topic with possible solutions to the problem is taken up in Chapter 5, and for subsequent steps we rely on the 3D Alpine model (see Fig. 3.24c in Section 3.3, and Fig. 4.5a) that features sedimentary basins, the crust-mantle boundary, and Alpine reference values for lower-crustal, upper-mantle and average crustal velocity. However, as can be seen from Figure 4.5b, travel time delays are mainly a result of major 3D structures such as crust-mantle boundary and sedimentary basins and less than 5 % are caused by the CSS updated velocities.

### 4.2.2 Wavefronts from Selected Azimuths of Teleseismic Source Locations

To investigate the azimuthal dependence of teleseismic wavefront diffraction by 3D Alpine crustal structure, distant source regions with strong seismic activity are selected. Case studies are carried out using a mean location of the observed hypocenters in these regions. Table 4.1 lists the source locations used (latitude, longitude, and depth) and approximative azimuths and inclination of the incoming wavefronts (see Fig. 4.6 for geographical location).

For each source location, the corresponding spherical travel time field of the incoming teleseismic wavefront (see Section 4.1.3) is calculated at the base of the 3D Alpine model at 70 km depth. Proceeding from these initial travel times at the model base, wavefronts are computed through the 3D Alpine velocity structure and models of travel time fields are obtained for each source location. The wavefront computations are based on the 3D Alpine velocity model with reference values for lower-crustal, uppermost-mantle and average crustal velocities is used (see previous section).

**Table 4.1** Source locations and wavefront parameters (azimuth, distance, slowness) at the surface of the 3D model area derived from the IASP91 tables.

| latitude | longitude | depth [km] | azimuth [deg] | distance [deg] | slowness [s/deg] | Region |
|---|---|---|---|---|---|---|
| 10˚S | 75˚E | 10 | 118˚ | 81.7˚ | 5.26 | Indian Ocean |
| 7˚N | 75˚W | 100 | 270˚ | 80.3˚ | 5.35 | Northern Columbia |
| 45˚N | 121˚W | 70 | 322˚ | 78.5˚ | 5.5 | Oregon |
| 55˚N | 160˚E | 80 | 15˚ | 76˚ | 5.18 | Kamtchatka |
| 22˚N | 93˚E | 100 | 75˚ | 70.8˚ | 6.06 | India-Bangladesh |
| 5˚S | 13˚W | 10 | 210˚ | 54.7˚ | 7.26 | Ascension Islands |

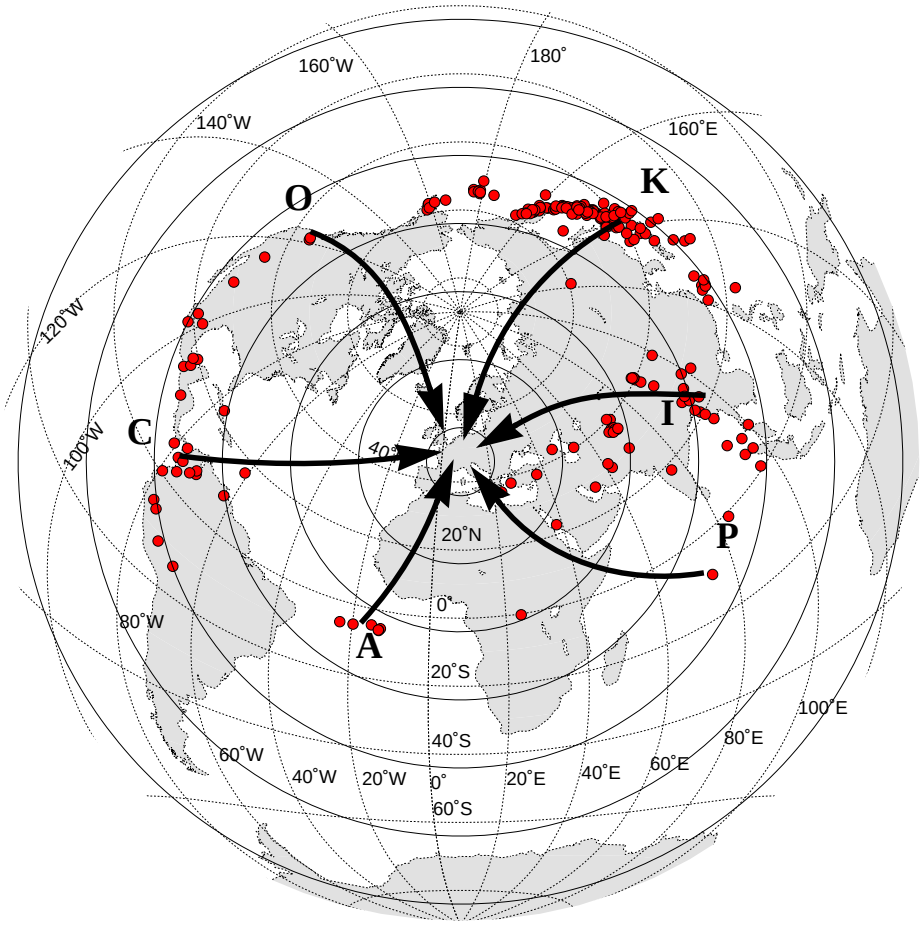


**Figure 4.6** World epicenter map (dots) showing events with magnitudes larger than 6.0 $m_b$ which occured between 1992-1996 (recorded at the Swiss Seismological Service). Arrows indicate epicentral distances and azimuths of high seismicity regions which are selected for the case studies in this work. K = Kamchatka, I = East-India (and Bangladesh), P= Indian Ocean, A= Ascension Island, C= Northern Columbia, O= Oregon. Solid circles indicate distances from model region at 20˚-intervals starting with 10˚.

Figure 4.7 maps absolute travel times (contoured at 1s intervals) of teleseismic waves at the surface of the 3D model for each of the six source locations. In Figure 4.7a absolute travel times for a source in the region of Kamchatka (see K in Fig. 4.6) are displayed. The wavefront, coming from north-north east and oblique to the Alpine strike, remains almost undistorted for most of the European crust. Wavefront distortion can be observed in the southern Alps, the Apennines, and the Po plain, caused by the deepening European Moho, the updoming Adriatic Moho, the shallow Ligurian Moho, and the Po sediments. Similar observations can be made for wavefronts coming from south-south west (Ascension Island, Fig. 4.7b), from the east (East-India, Fig. 4.7c), from west-south west (Northern-Columbia, Fig. 4.7d), from south-east (Indian Ocean, Fig. 4.7e), and from north-west (Oregon, Fig. 4.7f). In all cases, wavefronts are almost undistorted or only slightly delayed for most of the European crust and severely distorted for the Adriatic and the northern part of the Ligurian crust.

Absolute first arrival travel times at the Earth's surface, especially if calculated across the surveyed area, are perfect for correlation of teleseismic phases observed in that area. For structural studies with teleseismic travel time data, however, travel time residuals relative to a fixed station are required. Before proceeding into this problem with real data from the literature, it is tried to quantify expected teleseismic travel time delays for the above chosen azimuths.

What is of real interest when studying teleseismic data, are travel time delays caused by specific structures. Such travel time delays (or advances) can be obtained from residuals between travel times calculated through an 'a priori' known 3D structure and the corresponding travel times calculated through a 1D reference structure. Figure 4.8 maps calculated travel time residuals of teleseismic waves from the same source locations as discussed above (see Fig. 4.6). The residuals are obtained by subtracting the calculated absolute travel times for the 3D Alpine model (compare with Fig. 4.7) from the calculated absolute travel times for the 1D Alpine reference model described in Chapter 3 and displayed in Figure 3.24a. The spherical time field of the incoming teleseismic wave at the base of the model is kept constant for both models. Since reference average velocity is used, travel time residuals are a result of varying crustal thickness, low-velocity sedimentary basins, and effects from wave scattering by these structures. Figure 4.8a displays the travel time residuals calculated for a teleseismic wave from the Kamchatka region (see K in Fig. 4.6). Negative residuals (dark blue in Fig. 4.8a) indicate faster travel times with respect to travel times calculated for the 1D Alpine reference model. Such travel time advances occur in the Rhinegraben area (about -0.3 seconds),

**Figure 4.7** (next page) Absolute travel times at model surface (contoured at 1s intervals) calculated for teleseismic waves with source locations in the following regions (see Fig. 4.6): a) Kamtchatka (55°N, 160°E, depth=80 km), b) Ascension Island (5°S, 13°W, depth=10 km), c) East-India (22°N, 93°E, depth=100 km), d) Northern-Columbia (7°N, 75°W, depth=100 km), e) Indian Ocean (10°S, 75°E, depth=10 km), and f) Oregon (45°N, 121°E, depth=70 km). Travel times are calculated through the 3D Alpine velocity model from its base at 70 km depth to the surface. Travel times between source and base of the model are calculated with the 1D standard whole-earth model IASP91. Labeled dashed lines indicate location of the vertical velocity and time sections shown in Figure 4.9 and the approximative azimuth of incoming wavefront.

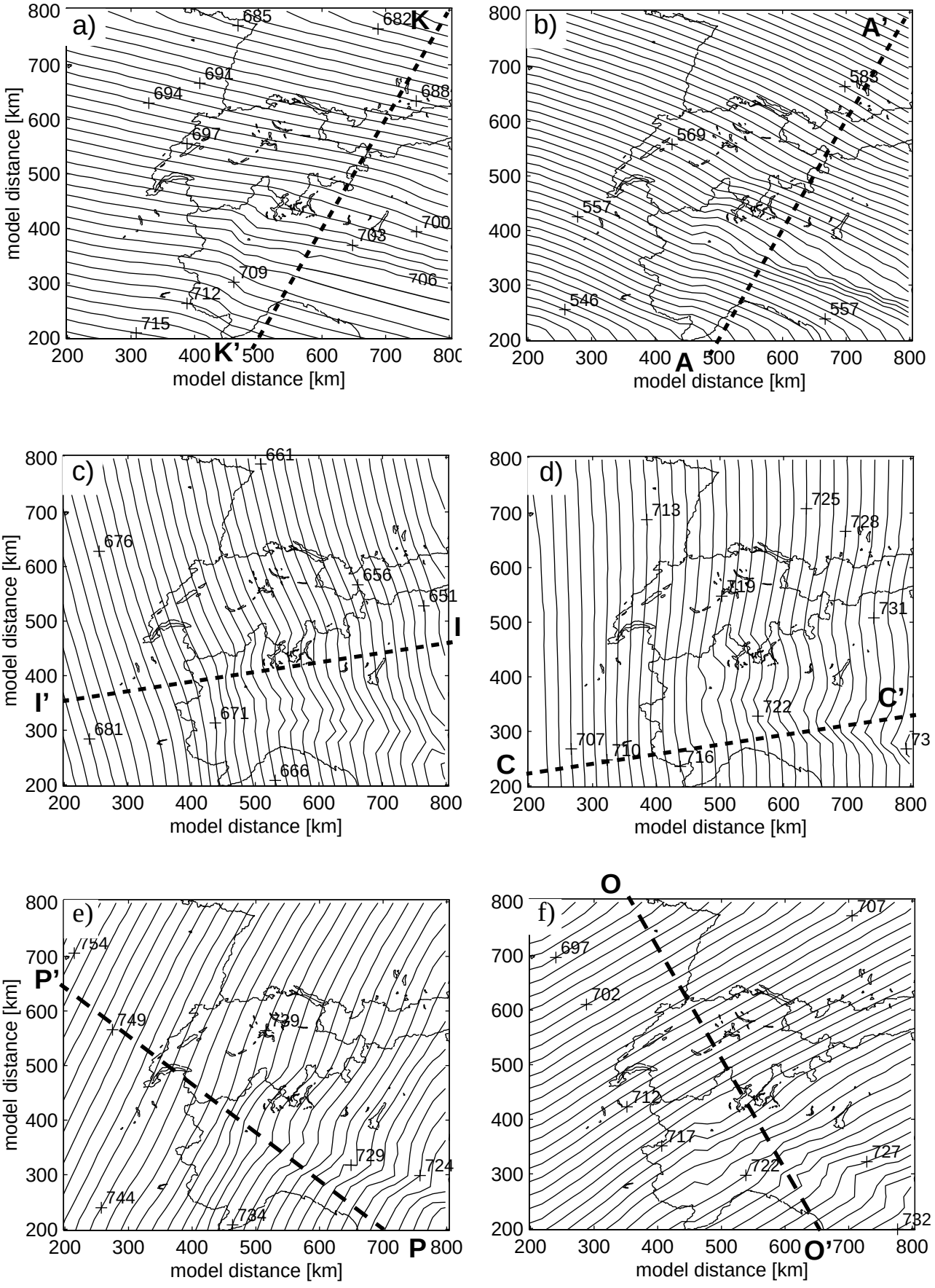
a)
b)
c)
d)
e)
f)
model distance [km]
model distance [km]
K
K'
A
A'
I
I'
C
C'
P
P'
O
O'
685
682
691
694
688
697
700
703
709
706
712
715
585
569
557
546
557
661
676
656
651
671
681
666
713
725
728
719
731
722
707
710
716
73
754
749
739
729
724
744
734
707
697
702
712
717
722
727
732

above the shallow Ligurian Moho (about -0.4 s) and above the western part of the Adriatic Moho (about -0.1 to -0.2 s). Note, that these latest negative travel time residuals are a result of the shallow Adriatic Moho in that region only, and not caused by the high intra-crustal velocities (Ivrea zone) observed in CSS and earthquake data. Integrating such high crustal velocities in that region would shift the residuals to even more negative values. Positive travel time residuals (light blue to red in Fig. 4.8a) indicate travel time delays with respect to travel times calculated for the 1D Alpine reference model. Travel time delays follow along the strike of the European crust with increasing values towards the inner, deep arc of the European Moho structure, reaching a maximum delay of about 1.1 seconds in the western Alps. Travel time delays of about 1.4 seconds are obtained for the southern margin of the sedimentary Po basin. In general, travel time residuals range between -0.4 to 1.4 seconds for a source located in the Kamchatka region.

A similar range of calculated teleseismic travel time residuals is obtained for sources located on the Ascension Islands (Fig. 4.8b), in East-India (Fig. 4.8c), in Northern Columbia (Fig. 4.8d), in the Indian Ocean (Fig. 4.7e), and in Oregon (Fig. 4.7f). Travel time residuals between -0.6 and 1.8 seconds are obtained for these azimuths of incoming teleseismic wavefronts. As expected, travel time anomalies of waves coming from different azimuths do not significantly change their location at the surface if they are caused by near-surface structures such as the sedimentary basins (Fig. 4.8a-f). Travel time anomalies observed at the surface caused by deep structures such as the ‘root’ of the European crust (see red residuals along the deep European crust in Fig. 4.8a-f) slightly migrate to the south for teleseismic waves coming from the north-north west (Kamchatka region, Fig. 4.8a) and to the north for seismic waves from south-south west (Ascension Islands, Fig. 4.8b). The migration distance of these travel time anomalies caused by the deeply dipping European crust is about 20 km (Fig. 4.8a,b). Accordingly, such deep structures cause travel time anomalies at the surface to migrate to the west for waves coming from the east (e.g. eastern India, Fig. 4.8c) and vice versa, to the east for waves coming from the west (e.g. northern Columbia, Fig. 4.8d).

To provide an impression on how the teleseismic wavefronts from the different azimuths travel through the 3D velocity structure, vertical sections through the 3D velocity model and the corresponding time models are presented in Figure 4.9. Sections are given along profiles (indicated by labeled dashed lines in Figure 4.7 and Figure 4.8) for

**Figure 4.8** (next page) Calculated travel time residuals (in seconds) at the model surface calculated for teleseismic waves with source locations in the following regions (see Fig. 4.6): a) Kamtchatka (55°N, 160°E, depth=80 km), b) Ascension Island (5°S, 13°W, depth=10 km), c) East-India (22°N, 93°E, depth=100 km), d) Northern-Columbia (7°N, 75°W, depth=100 km), e) Indian Ocean (10°S, 75°E, depth=10 km), and f) Oregon (45°N, 121°E, depth=70 km). The residuals are obtained by subtracting absolute travel times calculated through the 3D Alpine velocity model (see Fig. 4.7) from absolute travel times calculated through the 1D Alpine reference model (see text). Labeled dashed lines indicate location of the vertical velocity and time sections shown in Figure 4.9.

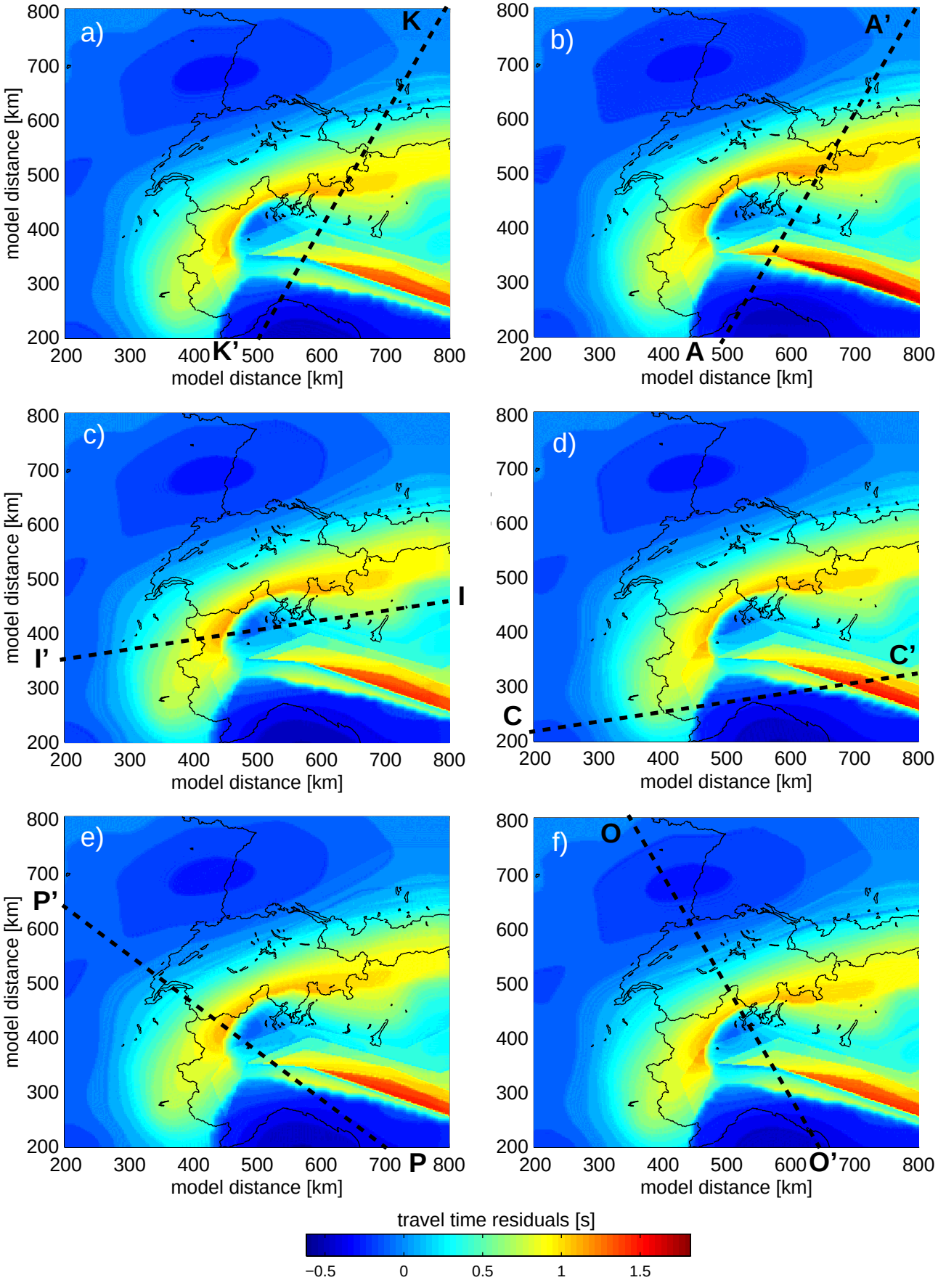
a)
K
K'
b)
A'
A
c)
I
I'
d)
C'
C
e)
P'
P
f)
O
O'
model distance [km]
travel time residuals [s]
−0.5
0
0.5
1
1.5

waves from Kamtchatka (Fig. 4.9a), the Ascension Islands (Fig. 4.9b), India (Fig. 4.9c), Columbia (Fig. 4.9d), the Indian Ocean (Fig. 4.9e), and Oregon (Fig. 4.9f). On all wavefront models, effects of scattering by the strong velocity contrast across the crust-mantle boundary and the low-velocity sedimentary basins in the corresponding velocity models are clearly seen.

The results obtained in this section show that incoming teleseismic wavefronts are significantly diffracted by the Alpine crust-mantle boundary and the low-velocity sedimentary basins and produce residuals at the surface in the range of -0.6 and 1.8 seconds. Azimuthal variations of incoming teleseismic wavefronts, however, do only slightly influence travel times and locations of travel time anomalies at the surface.

### 4.2.3 Comparison with 2D Profile Data

Studies on teleseismic travel time data along profiles were carried out by Baer (1979, 1980) for the central Alps and by Guyoton (1991) for the western Alps. The results of these studies are in the following compared with calculations for the 3D Alpine model established in Chapter 3.

In contrast to the expected large delays of teleseismic travel times in the central Alps due to a thickened crust, Baer (1980) observed no significant residuals between stations in the northern Alpine foreland and in the central Alps. This observation in conjunction with information from Panza and Mueller (1979) on lower-lithospheric and asthenospheric structure led him to propose a P-wave travel time model (Fig. 4.10) for the lithosphere-asthenosphere system below the Alpine foreland and the central Alps between 0 km and 220 km as suggested earlier from seismic surface-wave studies by Panza and Mueller (1979) (Fig. 4.10). Along the NW-SE oriented profile, one-way travel times within individual layers (i.e. crust, lower lithosphere, and asthenosphere) were calculated in order to obtain absolute travel times with residuals close to zero for a depth of 220 km. Teleseismic rays are assumed to propagate vertically for a depth of 220 km to the surface. For a trough-like crustal structure with an average P-wave velocity of 6.05 km/s, one-way travel times of 5.0 s for the crust below the northern Alpine foreland and 9.1 s for the thickened crust below the central Alps are obtained (Fig. 4.10). No low-velocity sedimentary basins were considered by Baer (1980) in this travel time estimation.

**Figure 4.9** (next two pages) Vertical sections through 3D Alpine velocity and travel time models along profiles indicated in Fig. 4.7 and Fig. 4.8. Absolute travel times (contoured at 1-s intervals) are shown for teleseismic wave from source locations in the following regions (see Fig. 4.6): a) Kamtchatka (55°N, 160°E, depth=80 km), b) Ascension Island (5°S, 13°W, depth=10 km), c) East-India (22°N, 93°E, depth=100 km), d) Northern-Columbia (7°N, 75°W, depth=100 km), e) Indian Ocean (10°S, 75°E, depth=10 km), and f) Oregon (45°N, 121°E, depth=70 km). Travel times between source and base of the model at 70 km are calculated with the 1D standard whole-earth model IASP91. Note that vertical exaceration of about 2:1 of the travel time models lead to steeper incidence of the wavefronts.

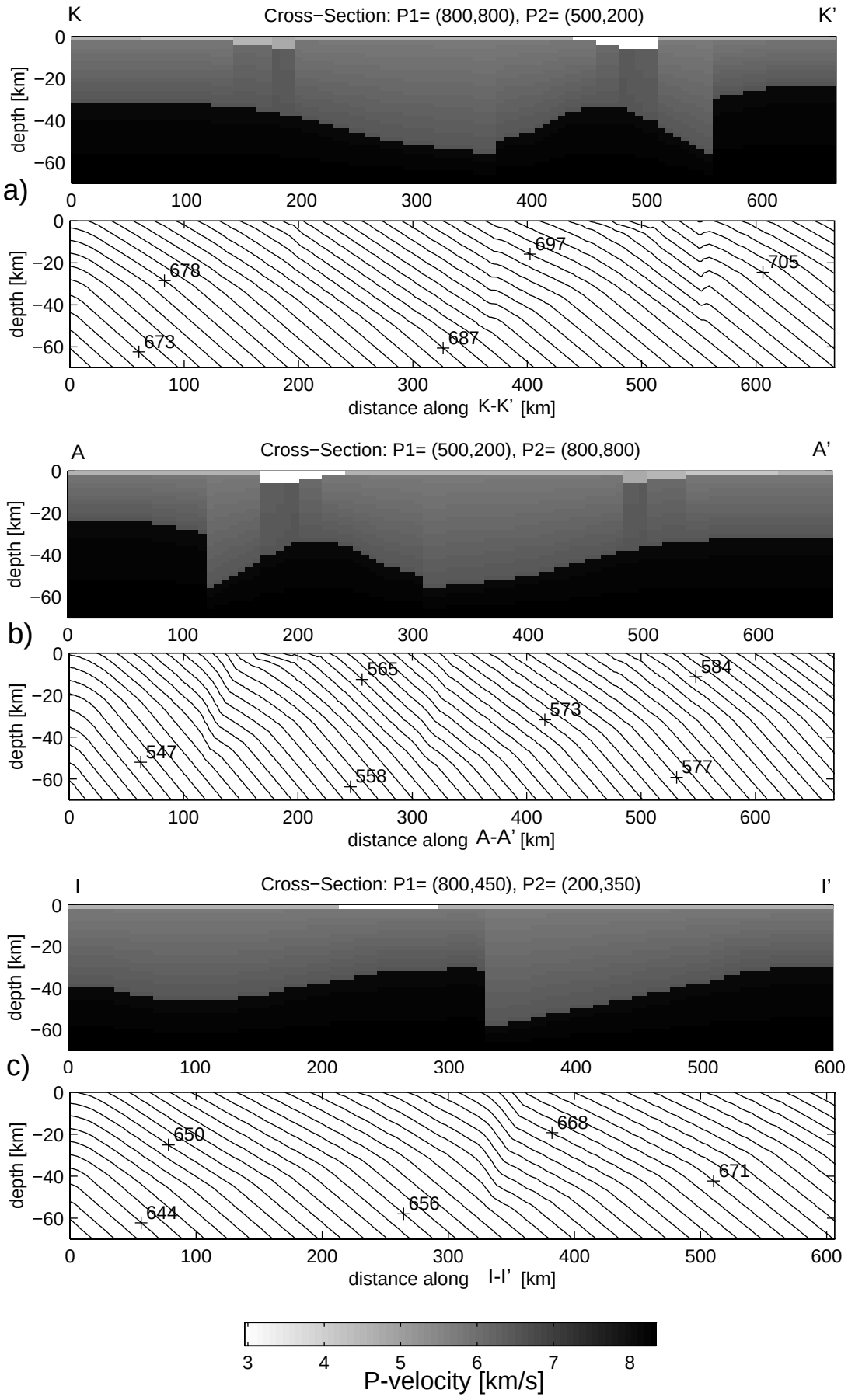
K
Cross−Section: P1= (800,800), P2= (500,200)
K'
depth [km]
a)
678
697
705
673
687
distance along K-K' [km]
A
Cross−Section: P1= (500,200), P2= (800,800)
A'
b)
565
584
573
547
558
577
distance along A-A' [km]
I
Cross−Section: P1= (800,450), P2= (200,350)
I'
c)
650
668
671
644
656
distance along I-I' [km]
P-velocity [km/s]

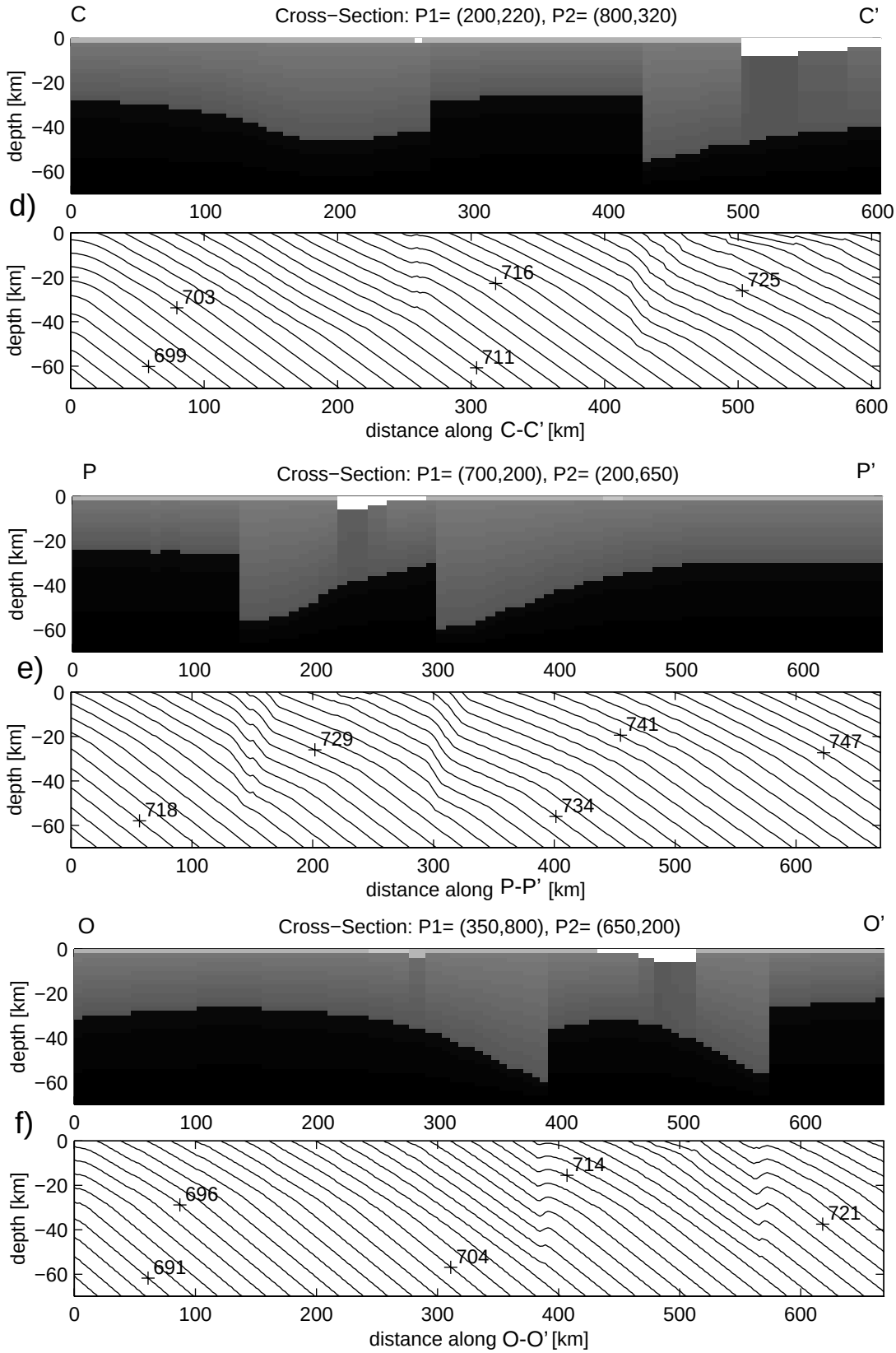
C
Cross−Section: P1= (200,220), P2= (800,320)
C'
depth [km]
d)
703
716
725
699
711
distance along C-C' [km]
P
Cross−Section: P1= (700,200), P2= (200,650)
P'
e)
729
741
747
718
734
distance along P-P' [km]
O
Cross−Section: P1= (350,800), P2= (650,200)
O'
f)
696
714
721
691
704
distance along O-O' [km]

In order to compare the lithospheric travel times by Baer (1980) with results in this study, a zero slowness plane wavefront is propagated through the 3D Alpine model with zero time at the base of the model at 70 km depth. A vertical cross-section through the 3D model is derived across the central Alps in NW-SE direction (see dashed box in Fig. 4.10). Figure 4.11a shows the velocity structure along this section and super-imposed the propagating wavefronts contoured at 1s intervals. The south-dipping European Moho, the shallow Adriatic Moho, and the low-velocity sedimentary basins are the dominant features depicted in this section. An average crustal velocity of 6.1 km/s is used (for parametrization see Section 2.2).

Absolute travel times calculated for the 3D Alpine model from a depth of 70 km are shown along the NW-SE profile in Figure 4.11b (thick line). Travel times range from 9.6 s for waves in the Alpine foreland to a maximum of about 10.8 s for waves travelling through the deepest part of the European crust. Travel times of about 10 s are

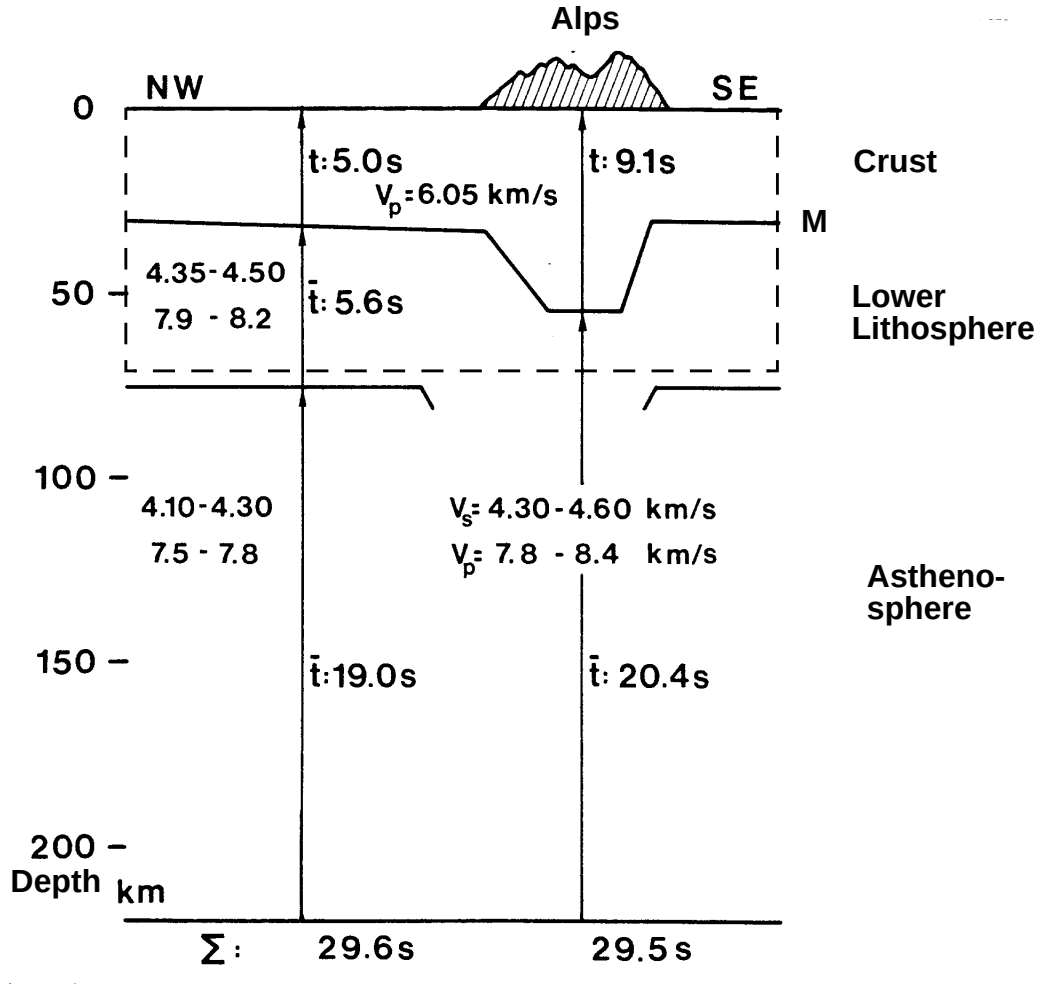


**Figure 4.10** Schematic NW-SE section of the lithosphere-asthenosphere system below the Central Alps with one-way travel times indicated (after Baer, 1980). Structure after Panza and Mueller (1979), $v_p/v_s$= 1.82 after Sprecher (1976). Dashed box indicates 3D model section shown in Figure 4.11.

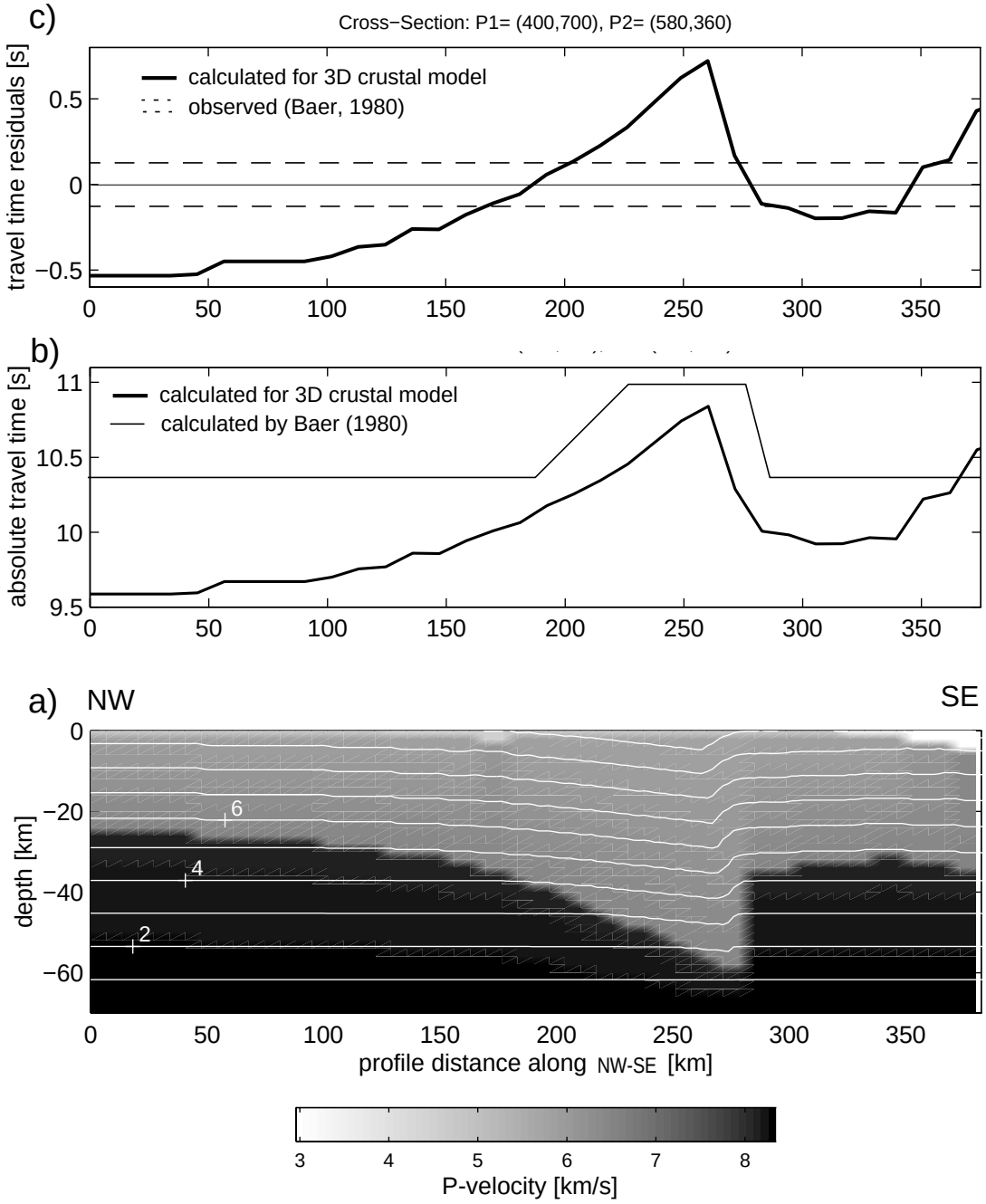


**Figure 4.11** Travel time residuals for the 3D Alpine model along a profile from NW to SE crossing the Central Alps (see dashed box in Fig. 4.10). a) Vertical section through the 3D velocity (gray scale) and travel time (contoured at 1-s intervals) model. Intra-crustal velocity variation is only poorly resolved by the used gray scale. A vertically incident plane wavefront is generated with zero time at the base of the model at 70 km depth. b) Calculated absolute travel times for the 3D Alpine model shown along the profile to a depth of 70 km (thick line). Calculated absolute travel times derived by Baer (1980) (thin line). c) Travel time residuals (solid thick line), calculated for the 3D Alpine model and depicted along the profile. Reference location (zero residual) is at 190 km profile distance, which corresponds to the reference station used by Baer (1980). Observed teleseismic travel time residuals (thin solid line) with uncertainty estimation (dashed lines) across the Central Alps.

calculated for waves travelling through the Adriatic crust, rapidly increasing to 10.6 s towards the south when the Po basin is encountered. Baer (1980) in his estimate obtained absolute travel times to a depth of 70 km (see thin line in Fig. 4.11b) of about 10.3 s outside the Alps and of about 11.0 s for the central Alps. Travel times for the crust only in Fig. 4.11a are of about 4.8 s in the European foreland (compared to 5.0 s by Baer (1980)) and of about 9.5 s for the thickest part of European crust (compared to 9.1 s by Baer (1980)). Differences between the two travel time models along the profile result from the different relief of the crust-mantle boundary (see Fig. 4.10 and Fig. 4.11a), from different velocities for the crust and uppermost mantle, and from considering the low-velocity sedimentary basins in this work.

In Figure 4.11c, residuals of the calculated travel times for the 3D model are derived relative to a reference station at profile distance 190 km (thick solid line in Fig. 4.11c). The reference station matches approximatively the one used by Baer (1980) relative to which he observed insignificant small teleseismic travel time residuals (thinly dashed lines in Fig. 4.11c). The contribution to the residuals by the 3D model range from -0.5 s to +0.7 s relative to the reference station. Negative residuals are obtained for the European foreland (-0.5 s) and the southern Alps (-1 s), positive residuals are derived for the central Alps (+0.7 s) and the Po basin (+0.5 s). These travel time residuals for the 3D model, subtracted from the observed residuals, may be used for further studies on structures of lower-lithosphere and asthenosphere (for a discussion on this topic see Chap. 5). However, the observed residuals close to zero (Baer, 1980) together with the asymmetric distribution of calculated travel time residuals for the crust (Fig. 4.11c) are direct evidence for the asymmetric geometry of lithospheric structure below 70 km.

Although Baer (1980) has shown the 1D gross distribution of teleseismic travel times in the Alpine lithosphere-asthenosphere system on a quantitative basis, the method followed in this work has obviously significant advantages. First, it uses a quantified velocity model, consistently parametrized and with reliability estimation for the model parameters. This allows to determine the confidence of the calculated teleseismic travel times, and to improve the velocity model according to new findings. Second, accurate calculation of teleseismic travel times through strongly heterogeneous 3D-velocity structures is possible, considering spherical time fields of incoming wavefronts from any azimuth at the base of the model. Third, the 2D velocity section shown in Figure 4.11a is only a cut out from the 3D Alpine velocity model. Studies on teleseismic data using the 3D Alpine model and the wave propagator can be easily performed along any profile within the model area (i.e. central and western Alps, and northern Apennines) to a depth of 70 km. Fourth, 2D teleseismic data modeling can account for effects from strongly heterogeneous structure outside the profile only approximatively by projecting these structures onto the profile. Heterogeneous velocity structures in 3D models influence seismic waves at the proper location in space.

Guyoton (1991) used teleseismic travel time residuals to derive a 2D lithospheric model by 2D ray tracing method along a profile across the western Alps (see Fig. 4.12a). Travel time residuals are derived by projection of stations near the profile onto that profile.

For an event located in San Francisco, California, in the approximative direction of the profile (about 326°), incoming wavefronts are calculated for our 3D Alpine model (Chap. 3), and travel time residuals along the profile are derived with respect to station OG17 (Fig. 4.12b). The calculated residuals fit well the observed travel time residuals (Guyoton, 1991) between 0 and 220 km model distance, where the south-east thickening crust causes positive travel time residuals. For distances between 220 km and the southern end of the profile, however, they are significantly larger than the observed residuals. The observed negative residuals in this region are mainly due to the high-velocity Ivrea body, which is located to the north of the profile and is not integrated in our 3D Alpine model (see Section 3.4).

By 2D ray-tracing for a teleseismic wavefront arriving from a slightly different azimuth (349°), Guyoton (1991) derived a simple 2D lithospheric model, and calculated travel time residuals (Fig. 4.12c) that are similar to the calculated residuals for our 3D Alpine model (Fig. 4.12b). By refining his 2D model and by projection of the high-velocity Ivrea zone onto the cross-section, Guyoton (1991) obtained better fits with the observed residuals for model distances larger than 220 km (Figs. 4.12d and 4.12e). Although the two refined models shown in Figures 4.12d and 4.12e are significantly different in their lithospheric structure, they both produce similar travel time residuals. The simpler model featuring average crustal structure (Figs. 4.12c) is a good first order approximation for the regionally observed teleseismic travel time residuals. The great advantage of the model derived in this work (Fig. 4.12b) is its spatial extension across the western and central Alps (see inset in Fig. 4.12a), which allows 3D modeling of travel time residuals without projection of observed residuals and/or inhomogeneous structure onto 2D profiles. Strong velocity inhomogeneities such as the Ivrea zone, however, need to be integrated in the 3D model for a better fit of locally observed arrival time anomalies. A further advantage of the new approach in this work is the method of tracing wavefronts (Fig. 4.12b) instead of rays (see Figs. 4.12c - 4.12e), that eliminates the problems of shadow zones generated by ray-tracing near caustics (see Figs. 4.12d and 4.12e) and leads to complete wavefields at the surface of the 3D model.

**Figure 4.12** (next two pages) a) Profile location (solid line) and stations (within dashed lines) used for teleseismic travel time residual studies by projection onto the profile (adapted from Guyoton, 1991). Inset: Location of the profile in the 3D Alpine model area.
b) Lower part: Cross-section through the 3D Alpine velocity model along profile shown in (a) with wavefronts superimposed. Intra-crustal velocity variation is only poorly resolved by the used gray scale. Wavefronts are indicated by contour lines in 1-s intervals for a spherical wave arriving from an azimuth of about 326° and a distance of about 85° (source location in San Francisco). Slowness at surface derived from the IASP91 model is about 5 s/deg. Upper part: Travel time residuals calculated with the 3D model along the profile (solid line) and travel time residuals ('+') observed by Guyoton (1991) with respect to station OG17.

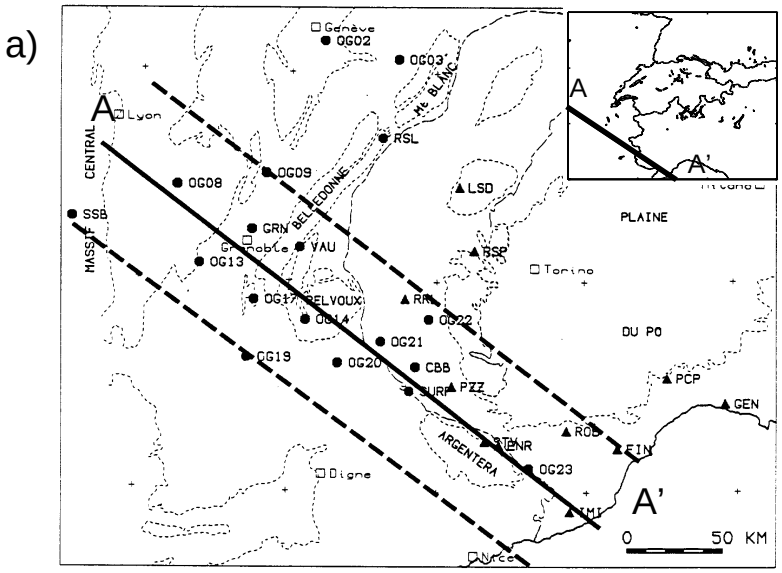
a)
Genève
OG02
OG03
Mt. BLANC
A
Lyon
RSL
CENTRAL
OG08
OG09
BELLEDONNE
LSD
PLAINE
SSB
MASSIF
GRN
VAU
Grenoble
OG13
BSP
Torino
OG17
BELVOUX
RR
OG14
OG22
DU PO
OG21
OG19
OG20
CBB
PCP
SURF
PZZ
GEN
ROE
TENR
FIN
ARGENTERA
OG23
Digne
TMT
A'
0 50 KM
Nice

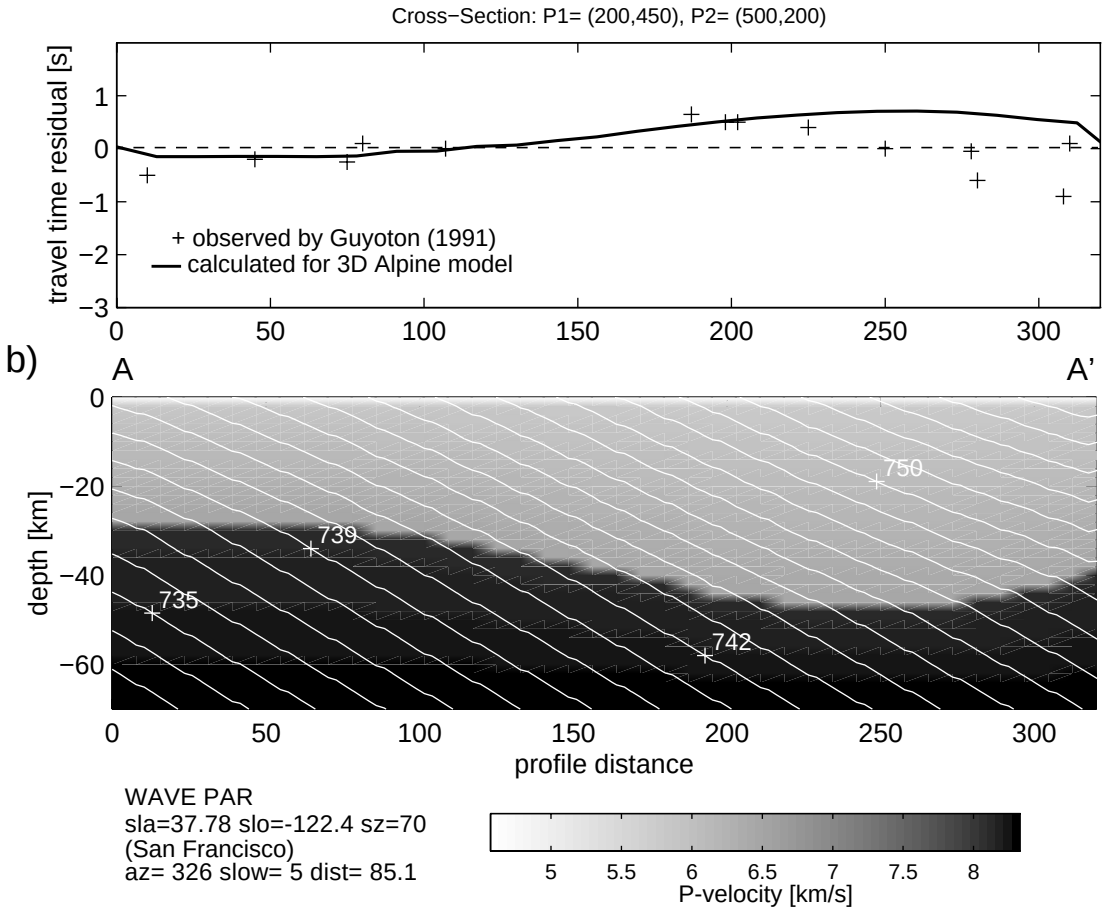
Cross−Section: P1= (200,450), P2= (500,200)
travel time residual [s]
+ observed by Guyoton (1991)
calculated for 3D Alpine model
b)
A
A'
depth [km]
750
739
735
742
profile distance
WAVE PAR
sla=37.78 slo=-122.4 sz=70
(San Francisco)
az= 326 slow= 5 dist= 85.1
P-velocity [km/s]

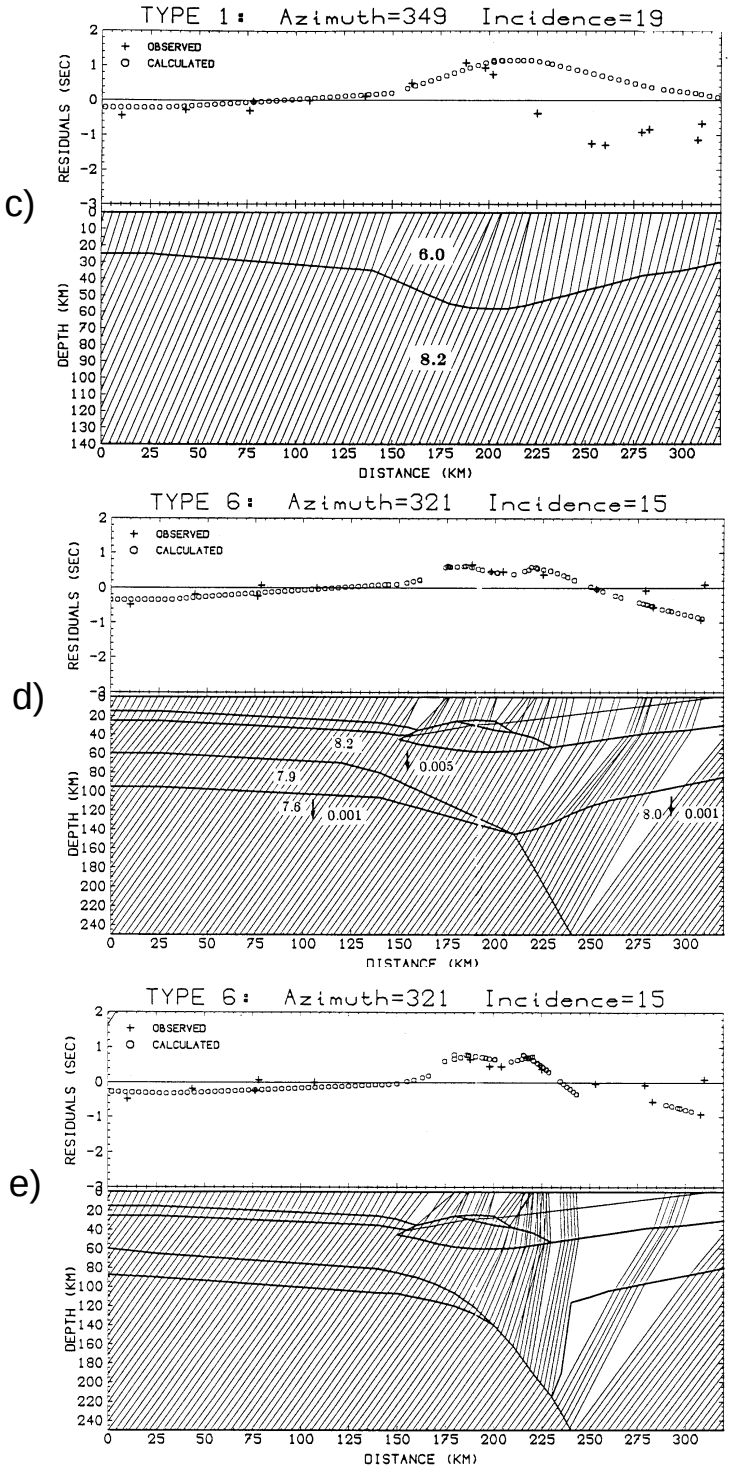


Figure 4.12 (continued) c) After Guyoton, 1991. Simple 2D lithospheric structure with rays being traced for a plane wave with azimuth=349° and inclination=19°. Calculated travel time residuals (open circles) and observed travel time residuals ('+') with respect to station OG17 are displayed.
d) and e) After Guyoton, 1991. Complex lithospheric structures with rays being traced for a plane wave with azimuth=321° and inclination=15°. Calculated travel time residuals (open circles) and observed travel time residuals ('+') with respect to station OG17 are displayed.

# CHAPTER 5

# DISCUSSION AND CONCLUSION

Throughout this study, it has been shown, that the control of ‘a priori’ 3D models for erroneous input data, for inconsistencies in data compilation, and for sufficient accuracy of parametrization is of great importance. Interactive modeling of seismic interfaces may be successfully controlled by the display of 3D migration paths (see Section 3.2). The display of key-parameters such as compensation velocity (see Section 3.3.3) or travel times of zero slowness waves (see Section 4.2.1) has been proven an efficient tool to control 3D models. These key-parameters represent mean values for the vertical velocity distribution and can be homogeneously mapped for the entire model area. Since mean values for geophysical parameters vary only within narrow limits, erroneous data compilation may be detected when mean values exceed these limits. Such data errors, detected in an early stage of model construction by mapping the compensation velocity of the 3D model, are shown Figure 5.1. Spots with unrealistically high compensation velocities of about 8 km/s (see solid arrow in Fig. 5.1) are shown, causeded by errors in limits for sedimentary basins. Unrealistically low compensation velocities (see open arrows in Fig. 5.1) may result when average velocities are derived from 2D CSS models with strong heterogeneous velocity structures that have not been 3D migrated.

Mapping of zero slowness wave travel times to control data consistency and the accuracy of model parametrization for travel time calculation has been performed in Section 4.2.1 (see Fig. 4.5). There, it has been shown that parametrization of lateral changes in lower-crustal velocities without smoothing effects waves travelling along this contrast by generating unrealistic head waves (see Fig. 4.5b). Smoothing across the edges of boxes (see Fig. 2.23) would possibly remove such artifacts. However, smoothing velocity values beyond Fresnel volumes is not in accordance with the present 3D model concept. Travel time field calculation for 3D model controlling revealed also the inadequate approximations in modeling CSS average crustal velocities (Fig. 4.5b). As described in Section 2.3.2, average crustal velocities from 2D CSS profiles are derived by averaging layer velocities and representing the volume of influence by a vertical and rectangular box above the migrated structural element. Such an approximation does not represent the velocity values at locations where they are actually sampled, i.e. they are not properly 3D migrated but horizontally shifted for the amount of the horizontal migration distance. Accurate modeling of CSS average velocities include tracking the velocity values that are sampled within the 3D migrated ray tube. This may be performed by 3D ray tracing and accounting for Fresnel volumes along the ray path, an improvement suggested for future studies. Following such improvements, adequate ways need-

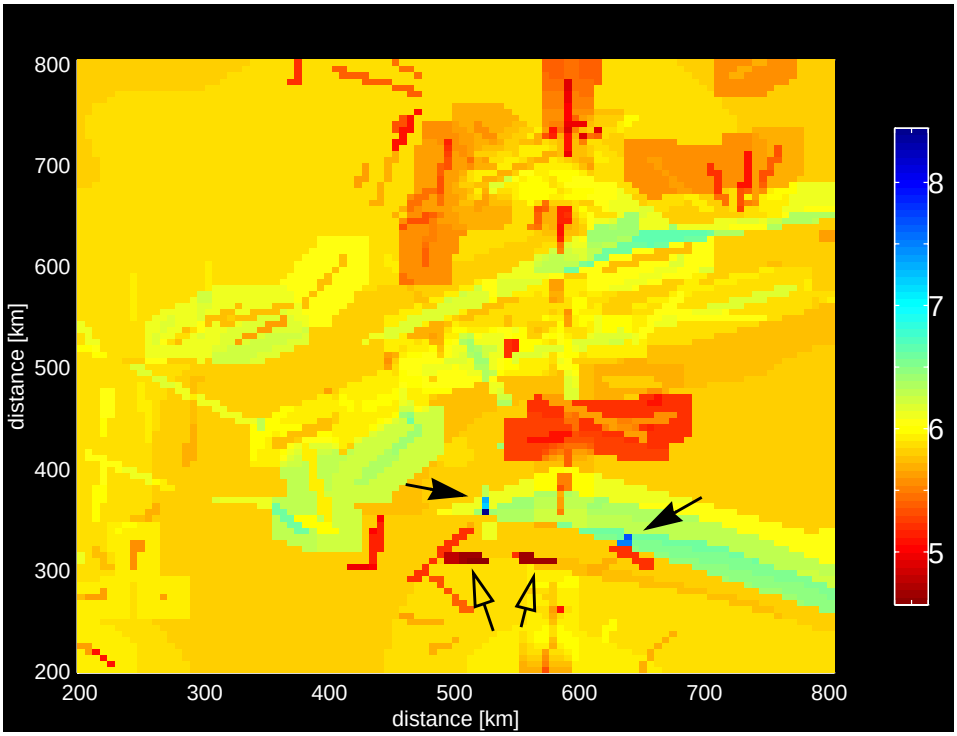


**Figure 5.1** Compensation velocity [km/s] of 3D model with erroneous data. Erroneous data cause unrealistic high (solid arrow) and low (open arrows) compensation velocities. See text.

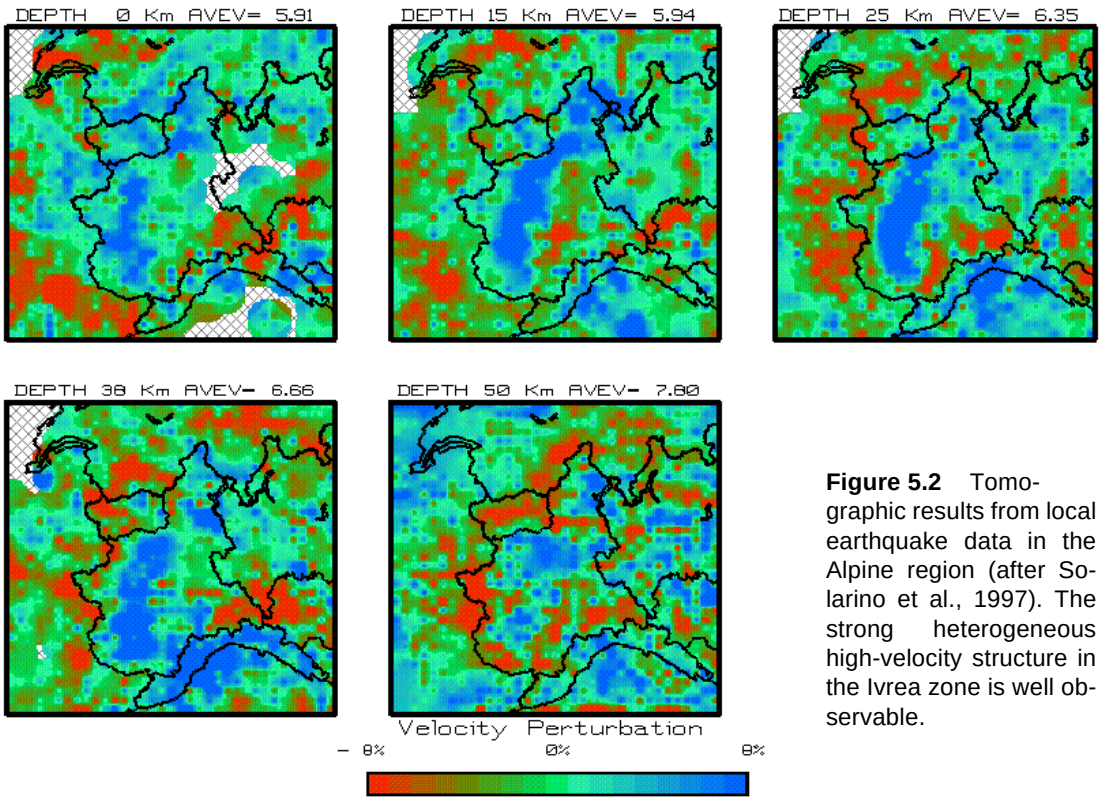


**Figure 5.2** Tomographic results from local earthquake data in the Alpine region (after Solarino et al., 1997). The strong heterogeneous high-velocity structure in the Ivrea zone is well observable.

ed to be developed for interpolation between the CSS velocity volumes. Such a proceeding promises success when CSS velocities are consistently observed in regions with simple structure and a dense network of 2D profile data (e.g. northern Alpine foreland, Ligurian crust, western Alps, see Fig. 4.5b).

A more efficient method to image average velocities over certain volumes is provided by local earthquake tomography. Such studies have recently been carried out in the Alpine region (Fig. 5.2, Solarino et al., 1997). These results cover about 60 % of the 3D model volume. The strength of the tomographic velocity information for 3D model update, in addition, is not only the amount and density of information, but also the way the information is sampled. Whereas CSS methods are 2D methods applied to 3D velocity fields, and 3D ray tracing must rely on 'a priori' information from structures outside the profile (3D-migration, see Section 2.3.1), local earthquake tomography is a 3D method - for direct and refracted rays - sampling the 3D velocity field more or less at the correct location in space. On the other hand, many tomographic methods only poorly resolve interfaces with high-velocity contrasts such as the crust-mantle boundary, whereas CSS methods are most sensitive to these structures and produce highly reliable information about their geometry (see Section 3.2). Therefore, due to the comparative character of CSS and tomographic methods, updating the established structural 3D model with velocity information from studies on local earthquake data is most efficient. Nevertheless, the enormous and painstaking work of 3D ray tracing for at least some of the CSS profile data to obtain average crustal velocities at the correct location in space is highly recommended since it provides control on the tomographically-derived velocity structure by independent data. Furthermore, the effect of possible anisotropy may be studied, which is of great importance when using the crustal velocity model for studies with teleseismic data.

As elaborated above, the studies on teleseismic wavefront scattering in Section 4.2 have been carried out by using reference values for the Alpine average crustal velocity. It has been shown by Baer (1980) and in Section 4.2 that strong effects on teleseismic travel times are caused by major crustal structures such as the crust-mantle interface and the sedimentary basins. However, these studies did not account for strong heterogeneous intra-crustal velocity structures, such as the Ivrea body. Although the high crustal velocities in the Ivrea zone are observed by CSS data, this data could not be used for proper 3D parametrization. By integration of the tomographic results from local earthquake data (Solarino et al., 1997; see Fig. 5.2) in the established 3D Alpine model, however, strong heterogeneous velocity structures such as the Ivrea body can be accounted for. Teleseismic waves would then be affected by the Ivrea body at the correct location in space, and the effect on teleseismic travel time residuals can be mapped at the corresponding correct location at surface. Thus, studies on teleseismic data by projecting the Ivrea body on a profile located according to available seismic stations (Guyoton, 1991), may be replaced by calculation of wave fields through the 3D model thus accounting for scattering effects of the Ivrea body (see Fig. 4.12).

The presently available information about lithospheric structure suggests a lithospheric slab beneath the Po plain and the northern Apennines connected with the European

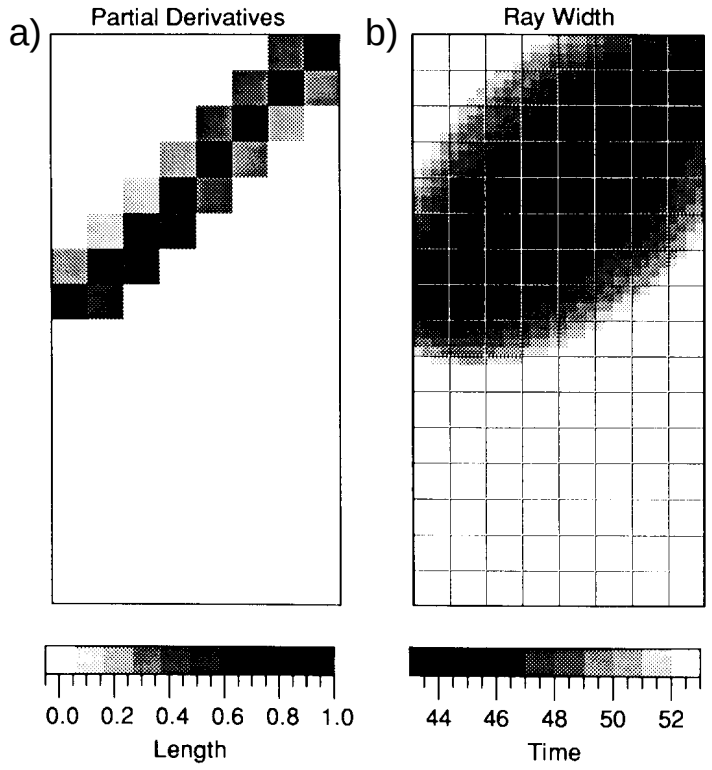


**Figure 5.3** Partial derivatives (left) and ray width (right) calculated through a smooth velocity model (after Ammon and Vidale, 1993).

lithosphere in the central Alps and overlain by an Adriatic lithosphere of normal thickness for continental plates (Kissling and Spakman, 1996). The thickness and the internal structure of the slab remain unknown due to inadequate resolution. The three Alpine crustal blocks derived in Chapter 3 represent the upper part of the Alpine lithospheric plate system. On lithospheric as well as on crustal scale, the asymmetric subduction of European lithosphere, resulting from the convergence of the Adriatic promontory of the African plate and the European lithospheric plate, is well observed. On crustal-scale, as shown in the 3D model by the Adriatic crust-mantle boundary, the Adriatic promontory, sandwiched between the European and the African plate, is up-doming and underthrusting the African plate. To follow these structures into the lower lithosphere down to the lithosphere-asthenosphere boundary, high-quality teleseismic data must be inverted for lithospheric structures accounting for the derived complex 3D crustal structure. The crucial part when using such strong 3D heterogeneous ‘a priori’ information in tomographic process is the proper solution to the teleseismic forward problem (Section 4.1.1). In Chapter 4, existing methods for computing first-arrival wavefields through 3D heterogeneous velocity structures have been tested for the teleseismic problem by propagating wavefronts through the 3D Alpine model to calculate absolute teleseismic travel times and relative travel time residuals. In the tomographic process, ray paths through the 3D velocity structure are also needed to calculate partial derivatives $\partial T / \partial m$ along the rays. Ammon and Vidale (1993), by using the finite-difference travel time calculation scheme by Vidale (1990) (see Chapter 4), presented a simple approach to identify those grid nodes that influence a specific travel time observation. They summed up travel times from the source to each point in a travel time grid and the travel

time from receiver to each point in the slowness image, and identified the region surrounding the wave's travel path between two specific points (see Fig. 5.3). The area with nonzero partial derivatives is directly related to the Fresnel zone ('fat-rays', Woodward, 1989), which allows to invert for actually resolved structures. Adapting this method to the teleseismic ray problem, travel time tables for the incoming spherical teleseismic wavefield and for a wavefield that is derived by propagating travel times from the receiver back to the bottom of the 3D model (back-shooting) have to be summed up. The resulting ray-tubes differ from that shown in Figure 5.3 by a smaller width at the surface and increasing width towards the bottom of the 3D model. During the tomographic process, travel times within the ray tubes may be inverted for floating structures only whereas reliable 'a priori' known structures are held fixed. For highly reliable 3D crustal models, calculated travel time residuals for the local 3D model - as performed in Chapter 4 - may be subtracted from observed teleseismic travel time residuals. The remaining residuals may then be inverted for sub-crustal structures by stripping off the crust from the lithosphere. Thus, models of higher reliability for the lithosphere-asthenosphere system may be obtained.

In this work, a method has been developed for 3D modeling of seismic information obtained by CSS profiling considering quantified data uncertainty. It has been successfully applied to the crust-mantle boundary in the greater Alpine region and a highly reliable 3D model of that significant seismic interface has been obtained. A concept for 3D lithospheric model construction by comparative use of different seismic data and information has been outlined. According to this concept, an Alpine P-wave velocity model has been constructed with the derived crust-mantle boundary as the main structural element, sedimentary basins and velocities obtained by CSS methods. The 3D model has been used for teleseismic travel time calculations and for studying effects of wave scattering by the parameterized structures. Results have been compared with earlier studies by Baer (1980) and Guyoton (1991) along 2D profiles. Compared with this studies on teleseismic data, the method followed in this work has some significant advantages. First, it uses a quantified velocity model, consistently parametrized and with reliability estimation for the model parameters. This allows to determine the confidence of the calculated teleseismic travel times, and to improve the velocity model according to new findings. Second, accurate calculation of teleseismic travel times through strong heterogeneous 3D-velocity structures is possible, considering spherical time fields of incoming wavefronts from any azimuth at the base of the model. Third, the above mentioned earlier studies have been carried out along 2D profiles. With the 3D Alpine model and the wavefront scatterer, studies on teleseismic data can be easily performed along any profile within the model area (i.e. central and western Alps, and northern Apennines) to a depth of 70 km. Fourth, 2D teleseismic data modeling can account for effects from strong heterogeneous structures outside the profile only approximatively by projecting these structures on the profile. Heterogeneous velocity structures in 3D models influence seismic waves at the proper location in space.

# REFERENCES


Aichroth, B., Prodehl, C. and Thybo, H., 1992. Crustal structure along the Central Segment of the EGT from seismic-refraction studies. Tectonophysics, 207, 43-64.

Aki, K., 1977. Three-dimensional seismic velocity inhomogeneities in the lithosphere. J. Geophys., 43, 235-242.

Aki, K., Christoffersson, A. and Husebye, E.S., 1977. Determination of three-dimensional seismic structure of the lithosphere. Bull. J. Geophys. Res., 82, 277-296.

Ammon, Ch.J. and Vidale, J.E., 1993. Tomography without rays. Bull. Seismol. Soc. Am., 83/2, 509-528.

Ansorge, J., 1968. Die Struktur der Erdkruste an der Westflanke der Zone von Ivrea. Schw. Min. Petrol. Mitt., 48, 247-254.

Ansorge, J., Kissling, E., Deichmann, N., Schwendener, H., Klingelé, E., and Mueller, St., 1987. Krustenmächtigkeit in der Schweiz aus Refraktionsseismik und Gravimetrie. Abstract. Nat. Forschungsprogramm 20 (NFP20) 'Geologische Tiefenstructur der Schweiz', Bull. 4,12.

Ansorge, J. and Baumann, M., 1997. Acquisition of seismic refraction data within NFP20 (Switzerland). In: *Deep structure of the Swiss Alps*. P. Heitzmann, P. Lehner, St. Mueller, A. Pfiffner, A. Steck (eds.), Birkhäuser, Basel, *in press.*

Babuska, V., Plomerova, J. and Granet, M., 1990. The deep lithosphere in the Alps: a model inferred from P residuals. Tectonophysics, 176, 137-165.

Baer, M., 1979. Kalibrierung des neuen Stationsnetzes des Schweizerischen Erdbebendienstes im Hinblick auf die Verbesserung der Lokalisierung seismischer Ereignisse mit Epizentralentfernungen bis 100 Grad. Ph.D. thesis, ETH Zürich, Nr. 6401, 146pp.

Baer, M., 1980. Relative travel-time residuals for teleseismic events at the new Swiss seismic station network. Ann. Géophys. 36, 119-126.

Banda, E. and Mooney, W.D., 1982. Present and future trends in controlled source seismology: a partial view. Terra Cognita, Vol. 2, No. 4, 355-362.

Baumann, M., 1994. Three-dimensional modeling of the crust-mantle boundary in the Alpine region. Ph.D. thesis Nr. 10772, ETH-Zürich, 147pp.

Berckhemer, H., 1968. Topographie des "Ivrea-Körpers abgeleitet aus seismischen und gravimetrischen Daten. German Research Group for Explosion Seismology. Schweiz. Mineral. Petrogr. Mitt., 48, 235-246.

Berthelsen, A., Burollet, P., Dal Piaz, G.V., Franke, W., and Trümpy, R., 1992. Tectonics. In: *A Continent Revealed: The European Geotraverse* (D. Blundell, R. Freeman and St. Mueller (eds.) with Atlas of Compiled Data (R. Freeman and St. Mueller, eds.), Cambridge University Press, Cambridge (UK), 3-5.

Blundell, D., Freeman, R. and Mueller, St. (Eds), 1992. *A continent revealed, the European Geotraverse*. Cambridge University Press, 275pp.

Bott, M.H.P., 1990. Stress distribution and plate boundary force associated with collision mountain ranges. Tectonophysics, 182, 193-209.

Braile, L.W. and Chiang, C.S., 1986. The continental Mohorovicic discontinuity: results from near-vertical and wide-angle seismic reflection studies. In: *Reflection Seismology; A Global Perspective.* M. Barazangi and L. Brown (eds), Geodynamics Series, AGU.

Braile, L.W., Keller, G.R., Mueller, S., and Prodehl, C. 1995. Seismic techniques. In: *Continental Rifts: Evolution, structure, tectonics.* K.H. Olson (Ed). Elesevier, Amsterdam, 61-92.

Buness, H., 1992. Krustale Kollisionsstrukturen an den Rändern der nordwestlichen Adriaplatte. Dissertation, FU Berlin, 221pp.

Butler, R. W. H., 1986. Thrust tectonics, deep structure and crustal subduction in the Alps and Himalayas. J. Geol. Soc. Lond., 143, 857-873.

Cassano, E., Aneli,L., Fichera, R. and Cappelli, V., 1986. Pianura Padana, interpretazione integrata di dati geofisici e geologici. 73 Congr. Soc. Geol. Ital., Roma, 36pp.

Cattaneo, M. and Eva, C., 1990. Propagation anomalies in Northwestern Italy by inversion of teleseismic residuals. Terra Nova, 2, 577-584.

Cerveny, V., Molotkov, I.A. and Psencík, I., 1977. Ray methods in seismology. Prague, Charles University Press.

Cerveny, V. and Soares, E.P., 1992. Fresnel volume ray tracing. Geophysics, Vol. 57, No. 7, 902-915.

Channell, J.E.T., J'Argenio, B. and Horvath, F., 1979. Adria, the African promotory. In: *Mesozoic Mediterranean paleogeography*. Earth Sci. Rev., 15, 213-292.

Cline, A.K., 1974. Scalar and planar curve fitting using spline under tension. Comm. of ACM, 17, 4, 218-223.

Closs, H. and Labrouste, Y., 1963. Recherches sismologiques dans les Alpes occidentales au moyen de grandes explosions en 1956. Mém. collectif, Année géophys. int., C.N.R.S. Sér. III/2.

Colombi, B., Guerra, I. and Scarascia, S., 1977. Crustal structure along two seismic refraction lines in the Northern Apennines (lines 1b and 2). Boll. Geof. Teor. Appl., 75-76, 214-224.

Deichmann, N. and Ansorge, J., 1983. Evidence for lamination in the lower continental

crust beneath the Black Forest (Southwestern Germany). J. Geophys., 52, 109-118.

Deichmann, N, Ansorge, J. and Mueller, St., 1986. Crustal structure of the Southern Alps beneath the intersection with the European Geotraverse. Tectonophysics, 126, 57-83.

Dziewonski, A.M. and Gilbert, F., 1976. The effect of small, aspherical perturbations on travel times and re-examination of the correction for ellipticity. Geophys. J. R. astr. Soc, 44, 7-17.

Egger, A., 1992. Lithospheric structure along a transect from the Northern Apennines to Tunesia derived from seismic refraction data. Ph.D. thesis, ETH-Zürich, Nr. 9675, 207pp.

Egloff, R., 1979. Sprengseismische Untersuchungen der Erdkruste in der Schweiz. Ph.D. thesis, ETH Zürich, Nr. 6502, 167pp.

Ellsworth, W.L., 1977. Three-dimensional structure of the crust and mantle beneath the island of Hawaii. Ph.D. thesis, Mass. Inst. of Technol., Cambridge, 327pp.

Fleitout, D.M. and Froidevaux, C., 1982. Tectonics and topography for a lithosphere containing density anomalies. Tectonics, 1, 21-56.

Freeman, R. and Mueller, St., 1992. Atlas of Compiled Data to *A Continent Revealed: The European Geotraverse* (D. Blundell, R. Freeman and St. Mueller (eds.)). Cambridge University Press, Cambridge (UK).

Frei, W., Heitzmann, P. and Lehner, P., 1990. Swiss NFP-20 research program of the deep structure of the Alps. In: *Deep structure of the Alps,* F. Roure, P. Heitzmann and R. Polino (Eds.) Mém. Soc. géol. Fr., Paris, 156; Mém. Soc. géol. Suisse, Zürich, 1; Vol. Soc. Geol. It., Roma, 1, 29-46pp.

Giese, P., 1976. General remarks on travel time data and principles of correlation. In: *Explosion Seismology in Central Europe,* P. Giese, C. Prodehl and A. Stein (Eds.), Springer-Verlag, Berlin, Heidelberg, New York, 130-136.

Giese, P., Prodehl, C. and Stein, A. (eds), 1976. *Explosion Seismology in Central Europe*. Springer Verlag, Berlin, Heidelberg, New York, 430pp.

Giese, P. and Prodehl, C., 1976. Main features of crustal structure in the Alps. In: *Explosion Seismology in Central Europe.* P. Giese, C. Prodehl and A. Stein (Eds.) Springer Verlag, Berlin, Heidelberg, New York. 347-375.

Giese, P., Nicolich, R. and Reutter, K.-J., 1982. Explosion Crustal Seismic Studies in the Alpine-Mediterranean Region and their Implications to Tectonic Processes. In: *Alpine-Mediterranean Geodynamics*. H. Berckhemer and K.J. Hsü, AGU Geodynamics series Vol.7, 39-74.

Giese, P. and Buness, H., 1992. Moho depth. In: *A Continent Revealed: The European Geotraverse* (D. Blundell, R. Freeman and St. Mueller (eds.) with Atlas of Compiled Data (R. Freeman and St. Mueller, eds.), Cambridge University Press, Cambridge (UK), 11-13.

Giese, P., Roeder, D., and Scandone, P., 1992. The fragmented Adriatic microplate: evolution of the Southern Alps, the Po basin and the northern Apennines. In: *A Continent Revealed: The European Geotraverse*, D. Blundell, R. Freeman and St. Mueller (Eds), Cambridge Univ. Press, Cambridge, UK, 190-199.

Guyoton, F., 1991. Sismicité et structure lithospherique des Alpes occidentales. Ph.D. thesis, Observatoire de Grenoble et Institut de Recherches Interdisciplinaires de Géologie et de Méchanique, Univ. Joseph Fourier de Grenoble, 290pp.

Heitzmann, P., Lehner, P., Mueller, St., Pfiffner, A., Steck, A., 1997. Deep structure of the Swiss Alps. NFP 20 Final Report (ATLAS). Birkhäuser, Basel.

Herglotz, G., 1907. Über das Benndorfsche Problem der Fortpflanzungsgeschwindigkeit der Erdbebenstrahlen. Phys. Z., 8, 145-147.

Hinz, E., Kaminski, W. and Stein, A., 1976. Results from a seismic refraction profile from the Hoher Meissner to the North German Plain. In: *Explosion Seismology in Central Europe.* P. Giese, C. Prodehl and A. Stein (Eds.), Springer Verlag, Heidelberg 257-267.

Hitz, L., 1995. The 3D crustal structure of the Alps of eastern Switzerland and western Austria interpreted from a network of deep-seismic profiles. Tectonophysics, 248, 71-96.

Hole, J.A., Clowes, R.M., and Ellis, R.M., 1992. Interface Inversion Using Broadside Seismic Refraction Data and Three-Dimensional Travel Time Calculations. J. Geophys. Res., 97/B3, 3417-3429.

Hole, J.A. and Zelt, B.C., 1995. 3D finite-difference reflection traveltimes. Geophys. J. Int., 121, 427-434.

Holliger, K., 1991. Ray-based image reconstruction in controlled-source seismology with an application to seismic reflection and refraction data in the Central Swiss Alps. Ph.D. thesis Nr. 9335, ETH-Zürich, 156pp.

Holliger, K. and Kissling, E., 1991. Ray-theoretical depth migration: methodology and application to deep seismic reflection data across the eastern and southern Swiss Alps. Eclogae Geol. Helveticae, 84/2,369-402.

Holliger, K. and Kissling, E., 1992. Gravity interpretation of a unified 2D acoustic image of the central Alpine collision zone. Geophys. J. Int., 111, 213-225.

Hubbard, M. and Mancktelow, N.S., 1992. Lateral displacement during Neogene convergence in the western and central Alps. Geology, 20, 943-946.

Julian, B.R. and Gubbins, D., 1977. Three-dimensional seismic ray tracing. J. Geophys. Res. 43, 95-114.

Kennett, B.L.N., 1991. IASPEI 1991, Seismological Tables. Research School of Earth Sciences, Australian National University, 167pp.

Kennett, B.L.N. and Engdahl, E.R., 1991. Travel times for global earthquake location and phase association. Geophys. J. Int.

Kissling, E., 1980. Krustenaufbau und Isostasie in der Schweiz. Ph.D. thesis Nr. 6655, ETH-Zürich, 165pp.

Kissling, E., 1988. Geotomography with local earthquake data. Rev. Geophys., 26, 659-698.

Kissling, E., 1993. Deep structure of the Alps - what do we really know? Phys. Earth and Planet. Int., 79, 87-112.

Kissling, E., Ellsworth, W.,L., Eberhart-Phillips, D., and Kradolfer, U., 1994. Initial reference models in local earthquake tomography. J. Geophys. Res., 99, 19635-19646.

Kissling, E. and Spakman, W., 1996. Interpretation of tomographic images of uppermost mantle structure: examples from the western and central Alps. J. Geodynamics, 21 (1), 97-111.

Kissling E., Ansorge, J., and Baumann, M., 1997. Methodological considerations of 3-D crustal structure modeling by 2-D seismic methods. In: *Deep structure of the Swiss Alps*. P. Heitzmann, P. Lehner, St. Mueller, A. Pfiffner, A. Steck (eds), Birkhäuser, Basel, *in press.*

Klingelé, E., 1972. Contribution à l'étude gravimétrique de la Suisse Romande et des régions avoisinantes. Matériaux pour la Géologie de la Suisse, Série Géophysique, 15, Kümmerly & Frey, Geographischer Verlag, Bern, 94pp.

Kradolfer, U., 1989. Seismische Tomographie in der Schweiz mittels lokaler Erdbeben. Ph.D. thesis, No. 8807, ETH-Zürich, 109pp.

Lancaster, P. and Salkauskas, K., 1990. *Curve and surface fitting.* Academic Press, New York. 280pp.

Laubscher, H., 1988. Material balancing in Alpine orogeny. Geol. Soc. Am. Bull., 100, 1313-1328.

Laubscher, H.P., 1994. Deep structure of the Central Alps in the light of recent seismic data. Geol. Rundschau, 83, 237-248.

Lees, J.M. and Crosson, R.S., 1989. Tomographic inversion for three-dimensional velocity structure at Mount St. Helens using earthquake data. J. Geophys. Res., 94, 5716-5728.

Lemoine, M. and Trümpy, R., 1987. Pre-oceanic rifting in the Alps. Teconophysics, 133, 305-320.

Lindsey, J.P., 1989. The Fresnel zone and its interpretative significance. The Leading Edge of Exploration, 33-39.

Luetgert, J.H., 1988. Users manual for RAY84/R83PLT — Interactive two-dimensional raytracing/synthetic seismogram package. U.S. Geological Survey, Menlo Park, California, Open-file report 88-238, 52pp.

Lyon-Caen, H. and Molnar, P., 1989. Constraints on the deep structure and dynamic

processes beneath the Alps and adjacent regions from an analysis of gravity anomalies. Geophys. J. Int., 99, 19-32.

Maurer, H. and Ansorge, J., 1992. Crustal structure beneath the northern margin of the Swiss Alps. Tectonophysics, 207, 165-181.

Mayrand, L.J., Green, A.G., and Milkereit, B., 1987. Aquantitative approach to bedrock velocity resolution and precision: The LITHOPROBE Vancouver Island Experiment. J. Geophys. Res., 92, 4837-4845.

Meissner, R., 1973. The Moho as a transition zone. Geophysical surveys, 1, 195-216.

Meissner, R., and Bortfeld, 1990. *Dekorp-Atlas*. Springer-Verlag Berlin, Heidelberg.

Meissner, R., Brown, L., Dürbaum, H.J., Franke, W., Fuchs, K., and Seifert, F. (eds), 1991. Continental Lithosphere: Deep Seismic Reflections. American Geophysical Union, Washington, DC, USA, Geodynamics Series 22, 69-76, 1991.

Ménard, G., 1988. Structure et cinematique d'une chaine de collision, les Alpes occidentales et centrales. Ph.D. Thesis, University of Grenoble, 268pp.

Ménard, G. and Thouvenot, F., 1987. Coupes équilibrées crustales: méthodologie et application aux Alpes occidentales. Geodinamica Acta (Paris), 1, 35-45.

Ménard, G., Molnar, P. and Platt, J.P., 1991. Budget of crustal shortening and subduction of continental crust in the Alps. Tectonics, 10/2, 231-244.

Menke, W., 1984. Geophysical Data Analysis: Discrete Inverse Theory. Academic Press, Orlando, Florida, USA, 260pp.

Mohorovicic, A., 1910. Das Beben vom 8.X.1909. Jahrbuch des Meteorol. Obs., Zagreb, 9, Teil 4, Abschn. 1-63.

Montrasio, A. and Sciesa, E., 1994. Proceedings of Symposium «CROP - Alpi Centrali », Sondrio, 20-22October 1993. Quaderni di Geodynamica Alpina e Quaternaria, Milano, 296pp.

Mooney, W.D., 1989. Seismic methods for determining earthquake source parameters and lithospheric structure. In: *Geophysical framework of the continental United States,* L.C. Parkiser and W.D. Mooney (Eds.), Geological Society of America, Memoir 172, Boulder, Colorado.

Mooney, W.D. and Brocher, T.M., 1987. Coincident seismic reflection / refraction studies of the continental lithosphere: A global review. Reviews of Geophysics, 25, 723-742.

Mueller, St., 1977. A new model of the continental crust. In: the Earth's crust. Geophysical Monograph 20, AGU, Washington D.C., 289-317.

Mueller, St., 1989. Deep-reaching geodynamic processes in the Alps. In: *Alpine Tectonics*. M.P. Coward, D. Dietrich and R.G. Park (eds.), Special Publication of the Geological Society of London, 45, 303-328.

Mueller, St., 1996. The Lithosphere-Asthenosphere System of the Alps. In: *Deep*

*structure of the Swiss Alps*. P. Heitzmann, P. Lehner, St. Mueller, A. Pfiffner, A. Steck (eds), Birkhäuser, Basel, *in press.*

Mueller, St., Ansorge, J., Egloff, R. and Kissling, E., 1980. A crustal cross section along the Swiss Geotraverse from the Rhinegraben to the Po Plain. Eclogae geol. Helv., 73/2, 463-483.

Müller, G., 1973. Theoretical body wave seismograms for media with spherical symmetry — Discussion and comparison of approximate methods. Zeitschrift für Geophysik, 39, 229-246.

Musacchio, G., De Franco, R., Cassinis, R. and Grosso, G., 1993. Reinterpretation of a wide-angle reflection 'fan' across the Central Alps. J. Appl. Geophys., 30, 43-53.

Nadir, S., 1988. Structure de la croûte continentale entre les Alpes Occidentales et les Alpes Ligures et ondes S dans la croûte continental à l'ouest du Bassin de Paris. Ph.D. thesis, University of Paris VII.

Nolet, G. (ed), 1987. Seismic Tomography. D. Reidel, Dordrecht, 386pp.

Nowack, R.L., 1992. Wavefronts and solutions of the eikonal equation. Geophys. J. Int., 110, 55-62.

Ogilvy, J.A., 1991. Theory of Wave Scattering from Random Rough Surfaces. Adam Hilger, Bristol.

Panza, G.F. and Mueller, St., 1979. The plate boundary between Eurasia and Africa in the Alpine Area. Memorie di Scienze Geologiche, Vol. XXXIII, 43-50, Padova.

Panza, G.F., Mueller, St. and Calcagnile, G., 1980. The gross features of the lithosphere-asthenosphere system in Europe from seismic surface waves and body waves. Pure and Appl. Geophys., 118, 1209-1213.

Parsons, T., McCarthy, J., Kohler, W.M., Ammon, C.J., Benz, H.M., Hole, J.A., and Criley, E.E., 1996. Crustal structure of the Colorado Plateau, Arizona: Application of new long-offset seismic data analysis techniques. J. Geophys. Res., 101 (B5), 11,173-11,194.

Pfiffner, A., 1986. Evolution of the north Alpine foreland basin in the Central Alps. In: *Foreland Basins*, P.A. Allen and P. Homewood (eds), Int. Ass. Sediment. Spec. Publ., 8, 219-228

Pfiffner, A., Frei, W., Valasek, P., Stäuble, M., Levato, L., DuBois, L., Schmid, S.M., and Smithson, S.B., 1990. Crustal shortening in the Alpine orogen: results from deep seismic reflection profiling in the eastern Swiss Alps, line NFP20-east. Tectonics, 9/6, 1327-1355.

Pfiffner, A., 1992. Alpine orogeny. In: *A Continent Revealed: The European Geotraverse*, D. Blundell, R. Freeman and St. Mueller (eds), Cambridge Univ. Press, Cambridge, UK, 180-190.

Pieri, M., 1983. Three seismic profiles through the Po Plain. In: *Seismic Expression of Structural Style. A Picture and Work Atlas.* Am. Assoz. Petrol. Geol. Geol. Studies

in Geology Series No. 15, vol.3.

Pieri, M. and Croppi, G., 1981. Subsurface geological structure of the Po plain, Italy. CNR Progretto Finalizzato Geodinamico, Sottoprogretto 'Modello Structurale', Pub. 414, 1-13.

Prodehl, C., Mueller, St., and Haak, V., 1995. The European Cenozoic rift system. In: *Continental Rifts: Evolution, structure, tectonics.* K.H. Olson (Ed). Elesevier, Amsterdam, 133-212.

Roure, F., Heitzmann, P. and Polino, R., (eds), 1990. *Deep structure of the Alps.* M. Geol. It., Roma, 1, 350pp.

Schmid, St., 1992. Geodynamic evolution of the Alps along the European Geotraverse. Part 1: Pennine units and deep structure. Abstract to oral presentation, 4th Symposium Nat. Forschungsprogramm 20 (NFP20) "Geologische Tiefenstruktur der Schweiz", 4.-7. November 1992, Interlaken, Switzerland, Bull. 11, 69pp.

Schmid, S.M., Froitzheim, N., Pfiffner, O.A., Schönborn, G., and Kissling, E., 1996. Geophysical-geological transect and tectonic evolution of the Swiss-Italian Alps. Tectonics, 15/5, 1036-1064.

Schwendener, H., 1984. Ein gravimetrisches Krusten-Mantel-Modell fur ein Profil vom nördlichen Alpenvorland bis an die Ligurische Kruste, Geodätisch-Geophysikalische Arbeiten in der Schweiz, Schweizerische Geodätische Kommision, 36, 160pp.

Sénéchal, G. and Thouvenot, F., 1991. Geometrical migration of line-drawings: a simplified method applied to ECORS data. In: *Continental Lithosphere: Deep Seismic Reflections,* R. Meissner, L. Brown, H.J. Dürbaum, W. Franke, K. Fuchs and F. Seifert (Eds.), American Geophysical Union, Geodynamic Series, 22, 401-407.

Sheriff, R.E. and Geldart, L.P., 1995. *Exploration Seismology*. 2nd edition, Cambridge University Press, 592pp.

Sleijko, D. and 11 others, 1987. Modello sismotettonico dell'Italia Nord-Orientale. Consiglio Nazionale delle Ricerche, Gruppo Nazionale per la Difesa dai Terremoti, Rendiconto no 1, Trieste, Italy, 82pp.

Snieder, R., 1988a. Large-scale waveform inversions of surface waves for lateral heterogeneity 1. Theory and numerical examples. J. Geophys. Res., 93/B10, 12,055-12,065.

Snieder, R., 1988b. Large-scale waveform inversions of surface waves for lateral heterogeneity 2. Application to surface waves in Europe and the Mediterranean. J. Geophys. Res., 93/B10, 12,067-12,080.

Solarino, S., Kissling, E., Sellami, S., Smriglio, G., Thouvenot, F., Granet, M., Bonjer, K.P., and Sleijko, D., 1997. Compilation of recent seismicity data base of greater Alpine region from several seismological networks and preliminary 3D tomographic results. Annali di Geofisica, *in review.*

Spakman, W., 1991. Delay-time tomography of the upper mantle below Europe, the Mediterranean, and Asia Minor. Geophys. J. Int., 107, 309-332.

Spakman, W., Van der Lee, S., and Van der Hilst, R., 1993. Travel-time tomography of the European-Mediterranean mantle down to 1400 km. Phys. Earth. Planet. Int., 79, 3-74.

Stampfli, G.M., 1993. Le Briançonnais terrain exotique dans les Alpes. Eclogae Geol. Helv., 86/1, 1-46.

Stäuble, M. and Pfiffner, O.A. 1991a. Evaluation of the seismic response of basement thrust and fold geometry in the Central Alps based on 2D raytracing. Ann. Teconicae, 5, 3-17.

Steck, L.K., and Prothero Jr., W. A., 1991. A 3-D raytracer for teleseismic body-wave arrival times. Bull. Seismol. Soc. Am., 81, 1332-1339.

Tardy, M., Deville, E., Fudral S., Guellec, St., Ménard, G., Thouvenot, F. and Vialon, P., 1990. Interprétation des données du profil de séismique réflexion profonde ECORS-CROP Alpes entre le front Pennique et la ligne du Canavese (Alpes occidentales). In: *Deep structure of the Alps*. F. Roure, P. Heitzmann, R. Polino, (eds), Zürich, 1; Vol. Soc. Geol. It., Roma, 1, 217-226.

Thouvenot, F., Paul, A., Sénéchal, G., Hirn, A., Nicolich, R., 1990. ECORS-CROP wide-angle reflection seismics: constraints on deep interfaces beneath the Alps. Mém. Soc. géol. France, N.S, 156, 97-106.

Thurber, C.H., 1981. Earth structure and earthquake locations in the Coyote lake area, central California. Ph.D. thesis, Mass. Inst. of Technol., Cambridge.

Thurber, C.H., 1986. A fast algorithm for three-dimensional seismic raytracing (Abstract), Eos Trans. AGU, 67(16), 304.

Thurber, C.H, 1987. Analysis methods of kinematic data from local earthquakes. Rev. Geofis. 24, 793-805.

Valasek, P., 1992. The tectonic structure of the Swiss Alpine crust interpreted from a 2D network of deep crustal seismic profiles and an evaluation of 3D effects. Ph.D. thesis Nr. 9637, ETH-Zürich, 195pp.

Valasek, P., Mueller, St., Frei, W. and Holliger, K., 1991. Results of NFP 20 seismic reflection profiling along the Alpine section of the European Geotraverse (EGT), Geophys. J. Int., 105, 85-102.

Valasek, P. and Mueller, St., 1996. A 3D tectonic model of the central Alps based on a synoptic (integrated) interpretation of seismic refraction and NFP20 reflection data. In: *Deep structure of the Swiss Alps*. P. Heitzmann, P. Lehner, St. Mueller, A. Pfiffner, A. Steck (eds), Birkhäuser, Basel, *in press.*

Vidale, J.E., 1988. Finite-difference calculation of traveltimes. Bull. Seism. Soc. Am., 78, 2062-2076.

Vidale, J.E., 1990. Finite-difference calculation of traveltimes in three dimensions.

Geophysics, 55, 521-526.

Waldhauser, F., 1992. Geschwindigkeitsverteilung von Scherwellen in der Erdkruste aus Messungen auf der Europäischen Geotraverse (EGT). Diploma Thesis, ETH-Zürich, pp. 182.

Waldhauser, F., Ansorge, J. and Kissling, E., 1995. The effect of crustal structure on teleseismic tomography of Alpine lithosphere (Abstract). European Geophysical Society, XX General Assembly, Hamburg, Annales Geophysicae, 13, Supplt I, C56.

Weiland, C.M, Steck, L.K., Dawson, P.B., and Korneev, V.A., 1995. Nonlinear teleseismic tomography at Long Valley caldera, using three-dimensional minimum travel times ray tracing. J. Geophys. Res. 100, B10, 20.379-20.390.

Werner, D. and Gundmundsson, H., 1992. Geodynamic profiles crossing the Swiss Alps. Abstract to poster, 4th Symposium Nat. Forschungsprogramm 20 (NFP20) "Geologische Tiefenstruktur der Schweiz", 4.-7. November 1992, Interlaken, Switzerland, Bull. 11, 90pp.

Wesson, R.L., 1970. Seismic ray computations in laterally inhomogeneous crustal models, Ph.D. thesis, Stanford Univ.

Wesson, R.L., 1971. Travel time inversion for laterally inhomogeneous crustal velocity models. Bull. Seis. Soc. Am., 61, 729-746.

Wiechert, E., 1910. Bestimmung des Weges der Erdbebenwellen im Erdinnern, 1. Theoretisches. Phys. Z., 11, 294-304.

Woodward, M.J., 1989. Wave-equation tomography. Ph.D. thesis, Stanford University, Palo Alto, California, USA, 73pp.

Ye, S., 1992. Crustal structure beneath the central Swiss Alps derived from seismic refraction data. Ph.D. thesis, Swiss Fed. Inst. Technology Zürich, 126pp.

Ye, S., Ansorge, J., Kissling, E., and Mueller, St., 1995. Crustal structure beneath the eastern Swiss Alps derived from seismic refraction data. Tectonophysics, 242, 199-221.

Zeis, St., Gajewski, D. and Prodehl, 1990. Crustal structure of southern Germany from seismic refraction data. Tectonophysics, 176, 59-86.

Zelt, C.A. and Smith, R.B., 1992. Seismic traveltime inversion for 2-D crustal velocity structure. Geophys. J. Int, 108, 16-34.

# ACKNOWLEDGMENTS

Professor Stephan Mueller's deep insight into geophysics and his genuine leadership strongly influenced two generations of scientists. He supervised nearly thirty Ph.D. theses - and kindly agreed to do so one last time. I am very thankful to Stephan Mueller for his continued interest in this study and his many suggestions and advices during the past four years. Especially his continuous support of my thesis after his retirement in fall 1995 has been greatly appreciated. I am very sorry that Stephan Mueller died shortly after the completion of this work.

Prof. Jörg Ansorge and Prof. Edi Kissling have been my closest advisors and supported and substantially influenced this thesis with their engaged and constant reading, criticism and suggestions on first drafts to final versions. Thanks go to Edi for the time he spent on my hare-brained writing which he managed to put into a logical order. I greatly benefited from his straight approach to many geophysical problems. Discussions with Jörg were always based on his vast experience in geophysics and were of great help in finding the way out of the scientific maze. I am very grateful to Jörg for giving me the opportunity of recording the Earth's rumor during many geophysical field trips, which I will always remember as thrilling road movies.

I am very thankful to Dr. Bill Ellsworth (U.S. Geological Survey, Menlo Park, California) for his readiness to act as an external referee. His advices on many teleseismic questions, the valuable comments on my work, and of course, showing me Rodin at Stanford have been greatly appreciated.

Many people at the Institute of Geophysics have been helpful in solving (and accepting) day-to-day happenings. I owe thanks to Eric Rüttener for his support on a broad range of problems with his innate minimum-input/maximum-output approach; to Patrick Smit for his patience on sharing an office with cluttered desks, dead printers and me; to Florian Haslinger for taking over a lot of system managing work when it came to the end of the thesis and helping me make a highly heterogeneous network to seem homogeneous; to Souad Sellami for the mystery of managing a poster to be re-designed in Zürich, printed in Lausanne, and exhibited in Hamburg (all within a day, of course); to Prof. Emile Klingelé for the highly required adrenaline-breaks on the rope; to Walter Rasa for not bothering me at all with talk session problems; to Stefano Solarino (University of Genova, Italy) for being Italian when he physically was in Zürich (although he splashed blood all over the bytes when virtually working on *tomo*); to the staff at the Swiss Seismological Service next door and Stefano Parolai (University of Genova, Italy) for providing the teleseismic data used in Chapter 4; and to the staff of the Institute - Claire Goldmann and André Blanchard - for their help on administrative matters.

Lonesome after-dusk hours at Satellite Hönggerberg have been shortened by Tho-

mas Mégel and Roy Freeman, who shared the somewhat strange (although efficient) working times in the last thesis year. I couldn’t wish for a better collaborator than Thomas Mégel to finish the thesis (and not only for that), always pushing it to the limits and ending with late night beers at Rosi’s or Don’s.

Over a thousand e-mails from her popped up at my screen during the last three years. I wish to thank Patty Seifert for these windows of recreation and humanity in a strongly digital environment - and for much more. Manfred Ladinig was the address to drop in for spontaneous outbreaks from scientific work, which I greatly appreciated. Nicola Chow is thanked for her patience going through these pages.

My parents made it all happen (but I don’t hold that against them). I thank them not only for their financial support, but also for giving me all the freedom I ever could have wished for.

This study was financially supported by the Kanton Basel-Land and the ETH Zürich.

# CURRICULUM VITAE

WALDHAUSER FELIX

| | |
|---|---|
| Day of Birth: | August 31, 1966, as son of Willi and Pia Waldhauser-Weinmann |
| Place of Birth: | Basel-Stadt, Switzerland |
| Citizenship: | Switzerland |

| | |
|---|---|
| 1993 - 1996 | Ph.D. student and teaching assistant at the Institute of Geophysics, Swiss Federal Institute of Technology (ETH) in Zürich, Switzerland |
| Feb. 1993 to Apr. 1993 | Courses at the International Center of Photography, New York, USA |
| Mai 1992 to Jan. 1993 | Research assistant at the Institute of Geophysics, ETH-Zürich |
| 1992 (April) | Diploma in Earth Sciences (Geophysics) at ETH-Zürich with a thesis entitled: “Geschwindigkeitsverteilung von Scherwellen in der Erdkruste aus Messungen auf der Europäischen Geotraverse (EGT)” |
| 1990 - 1992 | Student in Earth Sciences (Geophysics), ETH-Zürich |
| 1986 - 1990 | Student in Earth Sciences (Geology), University of Basel, Switzerland |
| 1986 | Military Service |
| 1985 | Maturity exam type C (mathematics/physics direction) |
| 1973 - 1985 | Primary, Secondary, Grammar school in Münchenstein, Switzerland |

# APPENDIX A

# CONTROLLED-SOURCE SEISMIC DATA COMPILATION

The controlled-source seismic (CSS) model data compilation consists of four ASCII files storing the seismic profile data and at present two ASCI files with parameters from CSS model data (see Tab. A.1). All files can be viewed and controlled graphically with the Fortran77/MATLAB program package *SeisMap* (Section A.2).

## A.1 CSS Data Base

The profile compilation consists of two files for each of the two seismic method, i.e. wide angle (*rfrprof.dat*, *rfrprof.plt*) and near-vertical reflection method (*rflprof.dat*, *rflprof.plt*). One file (**.dat*) stores the geographic position of individual profile endpoints whereas the second file (**.plt*) defines the profiles by connecting their endpoints.

The interface and velocity parameters from the crust-mantle boundary are compiled in file *moho.dat* which is the input file for 3-D model construction (see Chap. 3 and Appendix B). *reference.dat* contains an indexed list of publications used for the interface data compilation.

**Table A.1** File organization of the CSS data compilation. [2)] Possible extension. Not existing yet.

| CSS Data Compilation | | | | |
|---|---|---|---|---|
| Profile Data | | Interface / Velocity Data | | |
| Refraction Profiles Fans | Reflection Profiles | Moho Interface | Conrad Interface | References |
| **rfrprof.dat rfrprof.plt** | **rflprof.dat rflprof.plt** | **moho.dat** | ***conrad.dat*[2]** | **reference.dat** |

### A.1.1 Profile Compilation

Refraction profiles are defined by their shot points and profile end points. Shot and end points are labeled with unique character strings consisting of one to four characters. Each label holds a pair of geographical coordinates (latitude/longitude). Shot point la-

bels (SL) describe abbreviation of the geographical place of the explosion (e.g. J = Jaunpass) or refer to the shot point identifier of the particular experiment (e.g. D = shot point D of the EGT project). Profile end point labels (PL) usually contain the shot point label and the azimuth of the profile (e.g. DSW = shot point D in south west direction).

Fan labels (FL) consist of shot point and average recording direction (e.g. DW = shot point D recorderd in west direction). Each fan label holds a fan identifier (FI), fan radius (r) and opening angle ($\phi 1$, $\phi 2$).

Geographical coordinates of shot and profile end points are stored in the file *rfrprof.dat* (Tab. A.2). The file *rfrprof.plt* (Tab. A.3) contains the information used to define the profiles by indicating corresponding profile labels. Up to 10 labels can be connected per line. The same procedure was followed to compile near-vertical reflection profiles. The corresponding files are named *rflprof.dat* and *rflprof.plt*.

**Table A.2** Parameter format in *rfrprof.dat* and *rflprof.dat*.

```
Profiles
[ A4,F7.4,A1,TR2,F7.4,A1,TR1,A1 ]
    [ A4,F7.4,A1,TR2,F7.4,A1 ]
      SL/PL        lat          lon     SI
      J          46.6019N    7.3373E +
      D          47.2415N    9.3003E +
      DSW        46.4617N    6.9488E
      JNE        47.2890N    9.4798E
      *
      FAN    DW     110.0   189    287
      FAN    JE     110.0    23    115
      *
        FI     FL       r      ϕ1     ϕ2
Fan [ 2(A4),TR1,F5.1,TR1,I3,TR1,I3 ] (no such format in rflprof.dat)
```

*Parameter Description (see Tabs. A.2 and A.3):*

| | | |
|---|---|---|
| **PN** | *# [A6] | Project name. Refer to list in the header of *moho.dat*. |
| **SL** | [A4] | Shot point label. Any 4-character string except ‘FAN’. |
| **PL** | [A4] | Profile label |
| **FL** | [A4] | Fan label |
| **SI** | [A4] | Shot identifier. ‘+’ for shot point; ‘ ‘ for profile end point. |
| **FI** | [A4] | Fan identifier. Begin line with ‘FAN ’. |
| **lat** | [F7.4] | Latitude. Followed by ‘N’ (for North). |
| **lon** | [F7.4] | Longitude. Followed by ‘E’ (for East). |
| **r** | [F5.1] | Fan radius [km] |
| $\phi 1$, $\phi 2$ | [I3] | Opening angle, clockwise |

**Table A.3** Parameter format in *rfrprof.plt* and *rflprof.plt*.

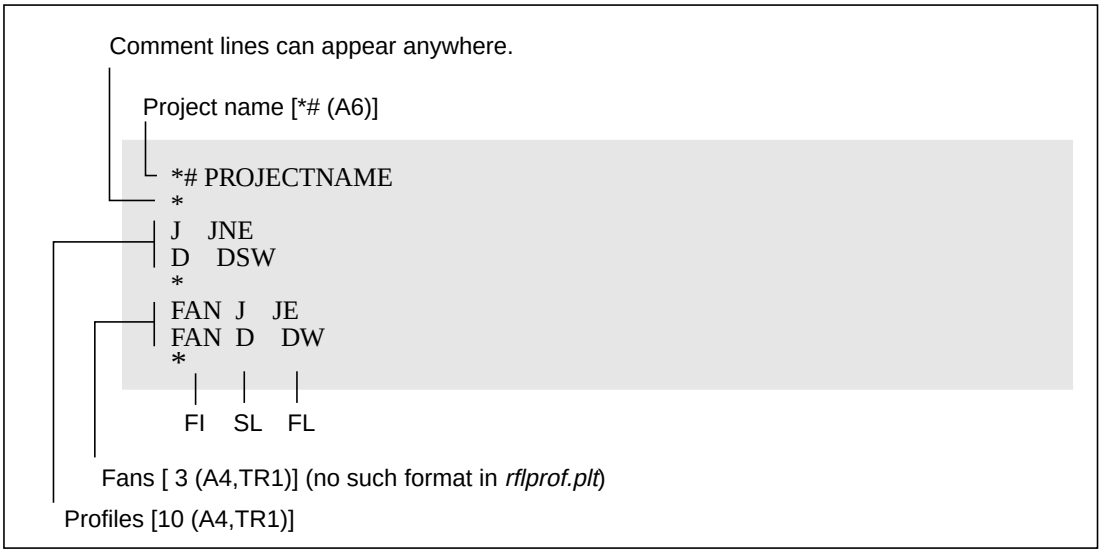


## A.1.2 Compilation of Interface and Velocity Data

File *moho.dat* stores the seismic parameters of the crust-mantle boundary and is described in the follwing as an example to store interface and corresponding velocity data from CSS methods. It is used as input file for the plot program *SeisMap* (see below) and for the 3D modeling program *SeisMod3D* (Appendix B) for computation of 3D velocity models as described in Chapter 3. Basically the file stores reflector point parameters per line. Reflector points are grouped to reflectors. Along a reflector, reflector points are connected (see Fig. A.1). For a detailed description of reflector parametrization see Chapter 3.1. Reflectors are organized in terms of seimic projects (e.g. EGT) or regional aspects (e.g. western Alps).

Reflector point parameters describe spatial reflector position, data weighting, corresponding velocity information and information about the experimental and interpretational characteristics. Table A.4 shows the parameter format for one reflector. Any line in the file beginning with a '*' is treated as comment line and is ignored during file processing, except the project label line. The project label line starts with '*#' which is used as project separator in program *SeisMap* (see below). The '#' sign in the second column must not appear in other lines than the project label line. Comment lines may appear at any position within the file.

*Parameter description of moho.dat (see Tab. A.4):*

**project name** **# [a]*
Label for project/experiment name (see header of *moho.dat* for project labels). The # sign in the 2nd column is used as identifier for individual project plotting (program *SeisMap*). A project normally consists of a cluster of profiles and thus of several reflectors.

**Table A.4** Format and parameter description of seismic parameters stored in the Moho data base (*moho.dat*). The shaded area is an extract from the file *moho.dat*. Parameter values are derived from the wide-angle reflection profile ALP87 interpreted by Maurer and Ansorge (1992). RFR: reflectors derived from refraction and wide-angle reflection profiles; 1) Set to 0.00 for FAN and RFL reflector elements. 2) for RFL: NMO velocity. 3) Linked to file: *reference.dat*. 4) Linked to file: *shot.dat* (see App. A.1). 5) Linked to file *RFRprof.dat* and *RFLprof.plt.* 6) Total point weight. Not used in the modeling procedure. 7) Possible link to file *itp.dat.*

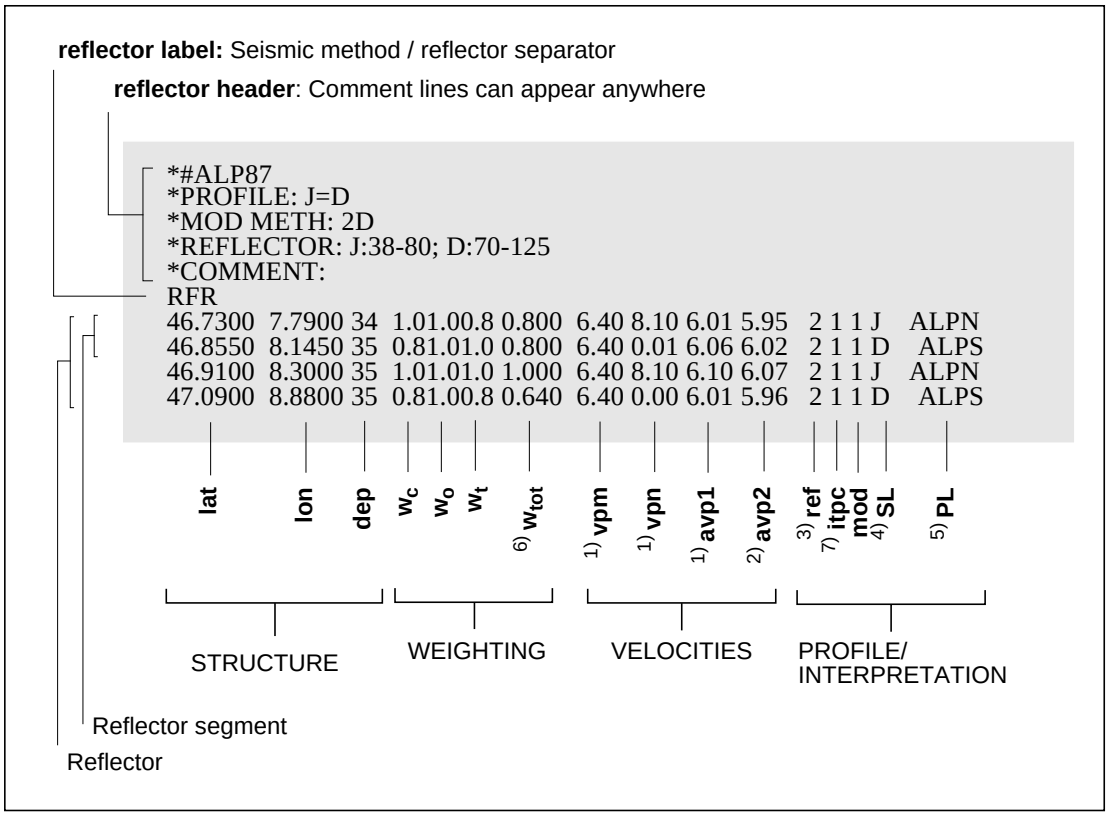


**reflector header** *[a]
Comment lines describing the following reflector (reflector points).
PROFILE: shotpoint (x) recording direction/reversed shotpoint. x: = reversed; - unreversed. Shotpoint: see **'SL'** in section A.1.1. Recording direction: Shotpoint label plus azimuth, see **'P'** in section A.1.1. Azimuth: N,S,W,E,NW,NE,SW,SE. Reversed shotpoint if identical with profile end.
MOD METH: Method used for interpretation of the CSS data.
REFLECTOR: Parts of interface sampled by rays. Distance in model units. Shotpoint at 0 km.

Reflector parameter:

**reflector label** [A3]
Label indicating the method of seismic investigation applied to get the following reflection points. Used as separator for individual reflectors.

*RFR*: Wide angle reflection and refraction experiment.
*FAN*: Fan observation.
*RFL*: Near-vertical reflection.

Reflector point parameters:

| | | |
|---|---|---|
| **lat** | [F7.4] | Latitude |
| **lon** | [F8.4] | Longitude |
| **dep** | [I3] | Depth [km] |
| **$w_c$** | [F3.1] | Weighting for phase confidence (RFR,FAN) / reflectivity signature (RFL). |
| **$w_o$** | [F3.1] | Weighting for profile orientation (RFR,FAN) / migration criteria (RFL). |
| **$w_t$** | [F3.1] | Weighting for profile type (RFR,FAN) / projection criteria (RFL). |
| **$w_{tot}$** | [F5.3] | Total point weight $w_{tot} = w_c \cdot w_o \cdot w_t$. Recomputed for reflector segments (see below). |
| **vpm** | [F5.2] | P-velocity of lower crust. Only for RFR reflector points. Set 0.00 for FAN and RFL reflector points. |
| **vpn** | [F5.2] | P-velocity of upper-mantle. Only for RFR reflector points. Set 0.00 for FAN and RFL reflector points. Set 0.00 when $p_n$ phase in RFR data is not observed. |
| **avp1** | [F5.2] | Geometrically averaged crustal P-velocity. Set to 0.00 for FAN and RFL reflectors. |

$$avp1 = \frac{\sum_i (v_i \cdot z_i)}{\sum_i z_i}$$

| | | |
|---|---|---|
| **avp2** | [F5.2] | Travel time based average crustal P-velocity. Corresponds to NMO velocity in RFL experiments. |

$$avp2 = \frac{\sum_i z_i}{\sum_i (z_i / v_i)}$$

| | | |
|---|---|---|
| **ref** | [I4] | Reference index. Linked to file *reference.dat*. |
| **itpc** | [I1] | Data selection code. Used for the interface interpolation process. |
| **mod** | [I1] | Interpretation method. 1 = 1D; 2 = 2D. Used for CSS data interpretation and modeling. |
| **SL** | [A4] | Shot point. 4 character label. Linked to file *rfrprof.dat*. |
| **PL** | [A4] | Profile end point. 4 character label. Linked to file *rfrprof.dat* (RFR, FAN) and *rflprof.dat* (RFL). |

*Determination of reflector segment weights from point weights*

The parameter $w_{tot}$ is recomputed for each reflector segment separately using the individual weights $w_c$, $w_o$, and $w_t$ of reflector points. Thus, changing weights due to overlying or reversed reflector segments can be considered. Following scheme is used to derive the weighting factor of reflector segments (rw) out of the three reflector point weights (pw) compiled from CSS data and model information (see Fig. A.1):

| | | |
|---|---|---|
| $r1w_c = p1w_c$ | $r1w_o = p1w_o$ | $r1w_t = p1w_t = 0.8$ |
| $r2w_c = \max( p2w_c , p3w_c )$ | $r2w_o = p2w_o$ | $r2w_t = p2w_t = p3w_t = 1.0$ |
| $r3w_c = p4w_c$ | $r3w_o = p3w_o$ | $r3w_t = p4w_t = 0.8$ |
| $r1w_{tot} = r1w_c + r1w_o + r1w_t$ | $r2w_{tot} = r2w_c + r2w_o + r2w_t$ | $r3w_{tot} = r3w_c + r3w_o + r3w_t$ |

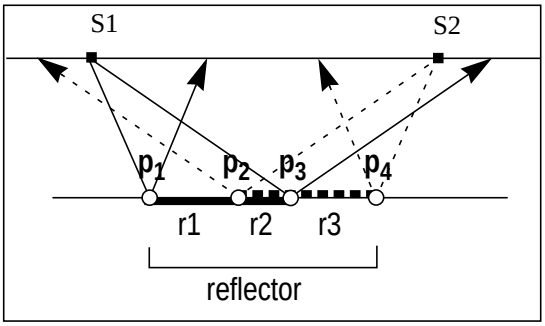


**Figure A.1** Reflector segment weight determination. S = shot points; P = compiled reflector points (moho.dat); r = reflector segment;

## A.2 Program *SeisMap*

*SeisMap* is a Fortran77/MATLAB4.2c program package to display and analyse the CSS data compilation described above.

### A.2.1 Program Flow and Structure

*SeisMap* consists of the two source code parts *seismap.f* and *seismap.m* (Fig. A.2). *seismap.f* processes the CSS data base according to the control parameters defined in *seismap.inp* and outputs plot files subsequently used as input files for the MATLAB interface modules called by *seismap.m* (see Fig. A.3).

*MATLAB interface modules*

| | |
|---|---|
| seismap.m | Controls the process flow. |
| profile.m | Plots profile lines. |
| plotlab.m | Plots shot and profile end point labels. |
| plotsymb.m | Plots various symbols. |
| CSSdata.m | Controls plot option for CSS data. |
| reflector.m | Plots interface reflectors. |
| wghtdisp1,2,3.m | Performs different kind of reflector weight display. |

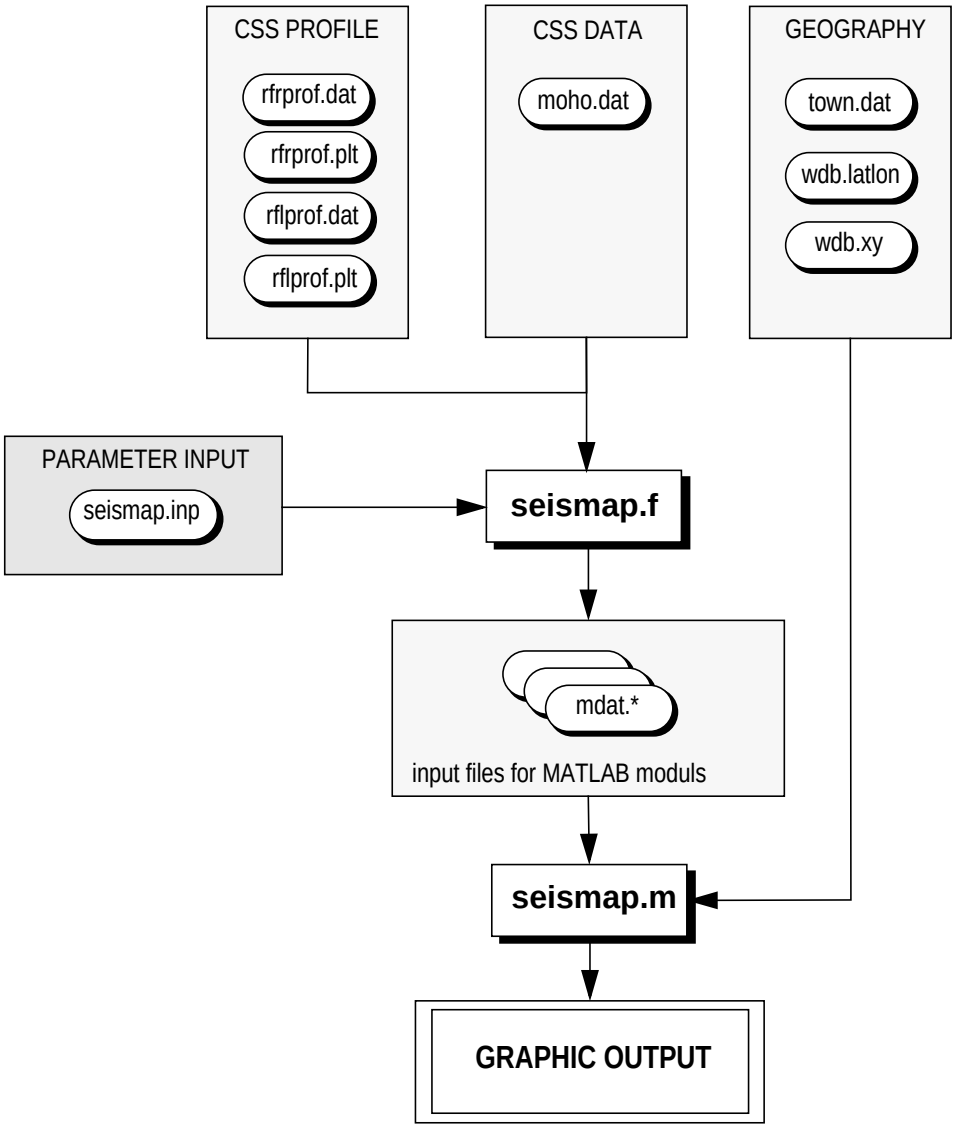


**Figure A.2** Process flow of *SeisMap*.

| | |
|---|---|
| border1.m | Plots geography of central Europe. |
| plotweight.m | Plots interface reflector weight. |
| zerrdisp.m | Plots reflector depth error limits. |
| wghthist.m | Plots reflector weight histogram. |
| itpcode.m | Plots interpolation code along reflector. |

### A.2.2 Input / output

Input for *seismap.f* are the CSS data base described previously and a parameter file (*seismap.inp*) to control the data display (see Fig. A.2). Input for the MATLAB modules are the output of *seismap.f* (*mdat.**) and files that store the geography data base. In the following, format and parameters of *seismap.inp* are described.

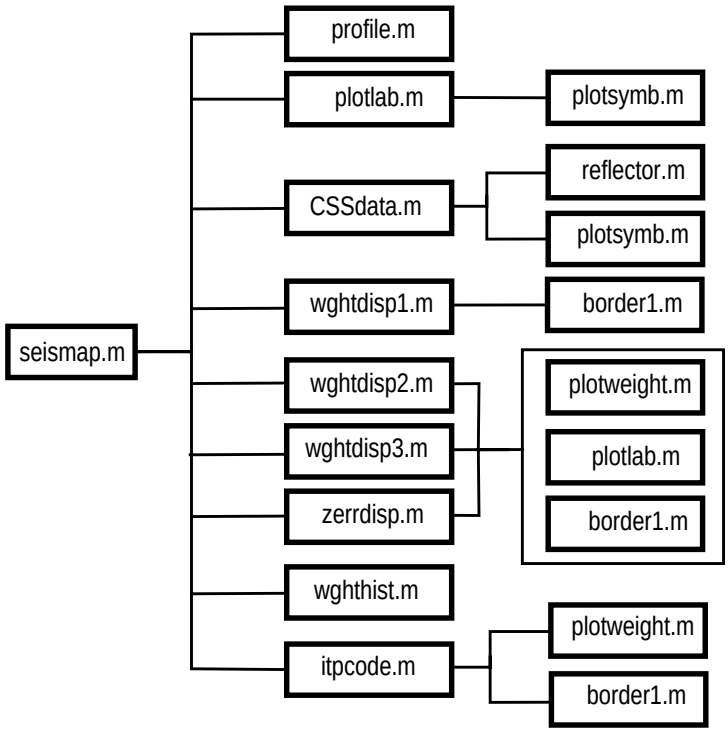


**Figure A.3** Structure of the MATLAB interface moduls.

Any line in the file *seismap.inp* beginning with a '*' is treated as comment line and is ignored during file processing. Input is in free format and colors are indicated by one-string characters (e.g. 'w', 'r' etc.). The first column in the following parameter list represents line number, second column parameter identifier and third column parameter description.

*Parameter description of seismap.inp*

INPUT FILENAMES:

| | | |
|---|---|---|
| 1. | **mfile** | Input file name for CSS data [*moho.dat*] |
| 2. | **rfrfile1** | Input file name for refraction profile data [*rfrprof.dat*] |
| 3. | **rfrfile2** | Input file name for refraction profiles to plot [*rfrprof.plt*] |
| 4. | **rflfile1** | Input file name for reflection profile data [*rflprof.dat*] |
| 5. | **rflfile2** | Input file name for reflection profiles to plot [*rflprof.plt*] |

MODEL PARAMETERS:

| | | |
|---|---|---|
| 6. | **titl** | Plot title (use '_' for spaces) |
| 7. | **itrans** | Input coordinates. 0 = lat/lon; 1 = cartesian |
| 8. | **orlon**, **orlat** | Origin of short-distance conversion (SDC) |
| | **orx**, **ory** | Orgin of cartesian coordinate (lower, left corner) in lat/lon |

SEISMIC PROFILE PARAMETERS:

| | | |
|---|---|---|
| 9. | **explab1** | Label to select profiles from a single project / experiment.<br>See *project name (PN)* in *rfrprof.plt*, resp. *rflprof.plt*.<br>Use 'ALL' to select all projects / experiments. |

10. **ilab** Plot profile labels. 0 = no; 1 = yes.
**sizlab**, **clab** Size and color of profile labels
11. **irfr**, **crfr** Plot refraction profiles. 0 = no; 1 = yes. Use color *crfr.*
**ifan**, **cfan** Plot fan profiles. 0 = no; 1 = receiver position;
2 = reflector postion (half of the receiver position);
3 = receiver and reflector position. Use color *cfan*.
**irfl**, **crfl** Plot reflection profiles: 0 = no; 1 = yes. Use color *crfr.*
*crfr* = 'd': dashed black line.
12. **ishot** Plot shot label. 0 = no; 1 = shots for selected profiles
(**irfr**, **ifan**, **irfl**); 2 = all shots. Set **ishot** = 0 when **ilab** = 1
**sizshot**, **cshot** Size and color of shot label

CSS DATA PARAMETERS:

13. **explab2** Label to select CSS data from a single project / experiment.
See *project name (PN)* in *rfrprof.plt*, resp. *rflprof.plt*.
Use 'ALL' to select all projects / experiments.
14. **irfrdat** Plot data from refraction profiles
**ifandat** Plot data from fan profiles
**irfldat** Plot data from reflection profiles
15. **imrflctr** Plot reflector. 0 = no; 1 = yes.
**cmrflctr** Color of reflector
**irsymb** Plot symbol at reflector endpoints to identify shot point. 0 = no;
1 = yes. Set irsymb = 0 when ilab = 1!
**sizsymb**,**csymb** Size and color of symbol.
16. **idat** Plot data value from input data file (e.g. *moho.dat*).
0 = no data plot;
1 = values in columns or lines (use **rot**). Selection with **iwc, ...**
2 = weights as 3 x 3 subplot auto select (rfr, fan, rfl, wc, wo, wt)
3 = weights as 2 x 2 subplot auto select (wc, wo, wt, wght)
4 = weight histogram. Selection with **irfrdat**, **ifandat**, **irfldat**
5 = interpolation code. Selection with **irfrdat**, **ifandat**, **irfldat**.
Set **imrflctr** = 0.
6 = not used
7 = plot weight. Select with **irfrdat**, **ifandat**, **ifrldat, iwc,**
**iwo, owt, iwght, igeo, ishot** (= 2, no profiles).
Set **irfr**, **ifan**, **irfl** = 0; **imrflctr** = 0!
8 = depth error. Selection with **irfrdat**, **ifandat**, **irfldat.**
**sizdat, cdat** Size and color of data values (**idat** = 1)
**rot** Values in columns (90) or lines (0) (**idat** = 1)
17. **iwc,iwo,iwt,iwght** Confidence, orientation, type and total weight. 0 = no;
1 = display in values (see **idat** = 1);
2 = display in colors; combination of 1 & 2 possible.
18. **idep** Depth of structural data. 0 = no; 1 = yes
**ivpm, ivpn** Vel. contrast at interface, e.g. lower-crustal/upper-mantle (0,1)
**iavp1, iavp2** Average crustal velocity. geometry, travel time based (0,1)
**iref, imod** Literature reference and modeling method (0,1)

GEOGRAPHY INFORMATION:

19. **igeo, cgeo** Plot geography (0,1) with color cgeo.
**itown, siztown, ctown** Plot town labels (0,1) with size siztown and color ctown.

LAYOUT PARAMETERS:

20. **xmin,xmax,ymin,ymax**Axis limits
21. **xlabel, ylabel** Axis labels
22. **igrid, iorient** Plot grid (0,1). paper orientation: 0 = portrait, 1 = landscape
23. **xleg, yleg** Coordinates of legend block. xleg = -9: lower, left corner of map
    xleg = -99: no legend

# APPENDIX B

# DESCRIPTION OF *SEISMOD3D*

## B.1 Program Purpose and Description

*SeisMod3D* is a modular FORTRAN 77 program developed to model 2D seismic data in three dimensions to produce horizontally continuous seismic interfaces and spatially continuous 3D velocity models. The method and its theoretical justification are outlined in Chapter 2 and the program is tested and applied in Chapter 3. *SeisMod3D* has been coded and used on a SUN Sparc20 running under Solaris 2.4 with 96MB core memory, which is necessary to handle 3D models such as computed in Chapter 3 (about 3'000'000 grid nodes). It must be noted at this point that *SeisMod3D* is not a 'plug and play' program. A great effort must be undertaken in the CSS data compilation (see Appendix A) in order to run *SeisMod3D* sucessfully. Adaption of certain parameters in the code may be necessary when applying the program to interfaces other than the crust-mantle boundary or to other tectonic structures as modeled in this work. The current version of *SeisMod3D* allows one interface (that may consist of several sub-interfaces) in the 3D model construction process.

*SeisMod3D* has three major modules (see Fig. B.1 and B.2): *main*, *interface*, and *cvolume*. *main* organizes the lare scale process flow; *interface* performs the interface modeling process; *cvolume* performs the volumetrical velocity modeling process. The graphic display of individual modeling steps and resulting models is handeled by *VISTA3D*, a program package based on MATLAB modules (see Appendix D).

### B.1.1 Modules

The structure of the program at a modular level and the flow of control is illustrated in Figure B.2.

| | |
|---|---|
| main | Opens and closes I/O files and directs the process flow. |
| getinp | Reads in the parameter file. |
| setorg | Sets up the coordinate system. |
| SDC | Transforms geographical coordinates to cartesian coordinates (dist) and vice versa (redist) by short distance conversion. |
| modCSS | Directs the process flow for CSS data modeling. |
| filecheck | Checks the CSS data file for its consistency. |
| convdat | Converts the CSS data from lat/lon to cartesian coordinates (SDC). |

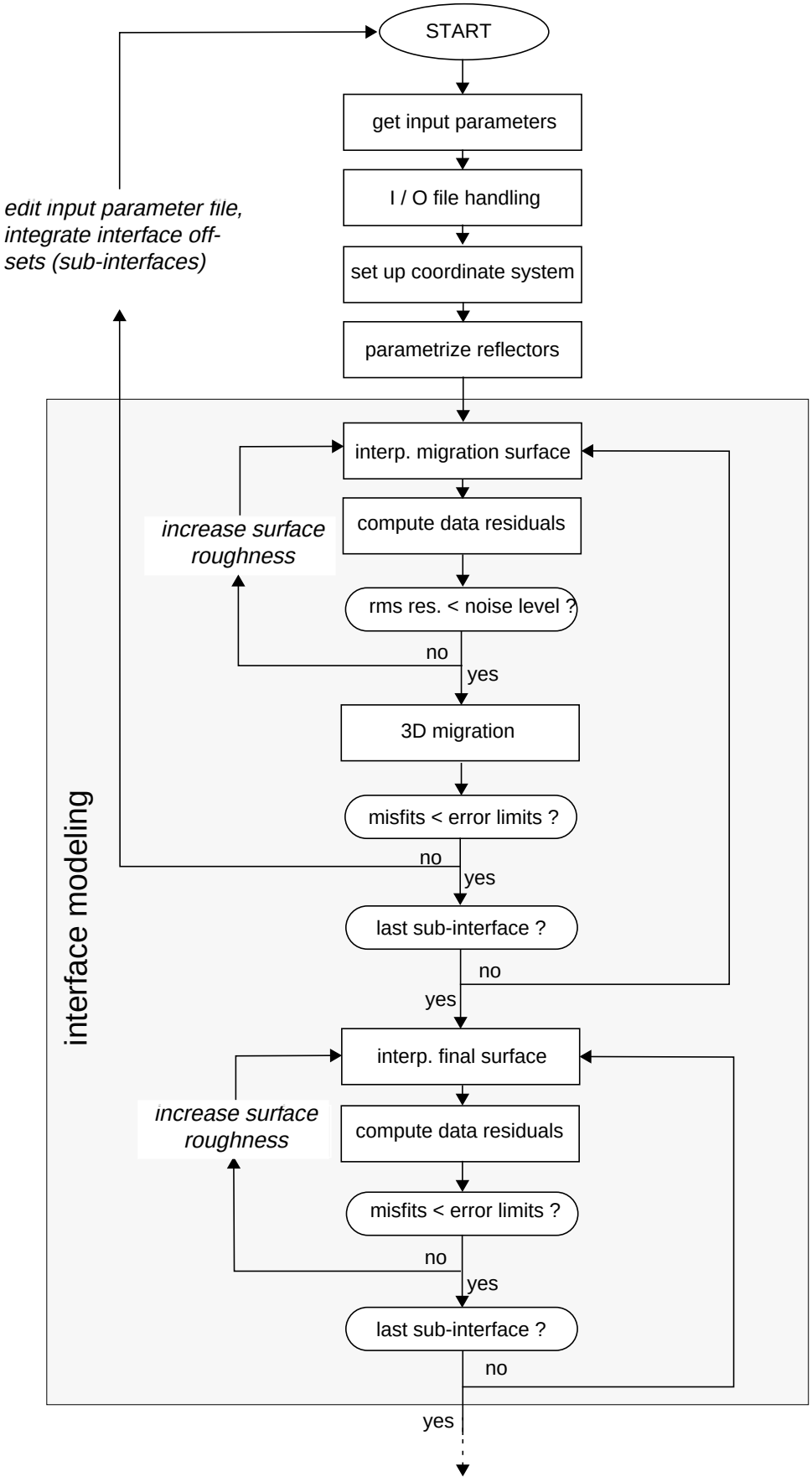
START
get input parameters
I / O file handling
set up coordinate system
parametrize reflectors
edit input parameter file, integrate interface off-sets (sub-interfaces)
interface modeling
interp. migration surface
compute data residuals
increase surface roughness
rms res. < noise level ?
no
yes
3D migration
misfits < error limits ?
no
yes
last sub-interface ?
no
yes
interp. final surface
compute data residuals
increase surface roughness
misfits < error limits ?
no
yes
last sub-interface ?
no
yes

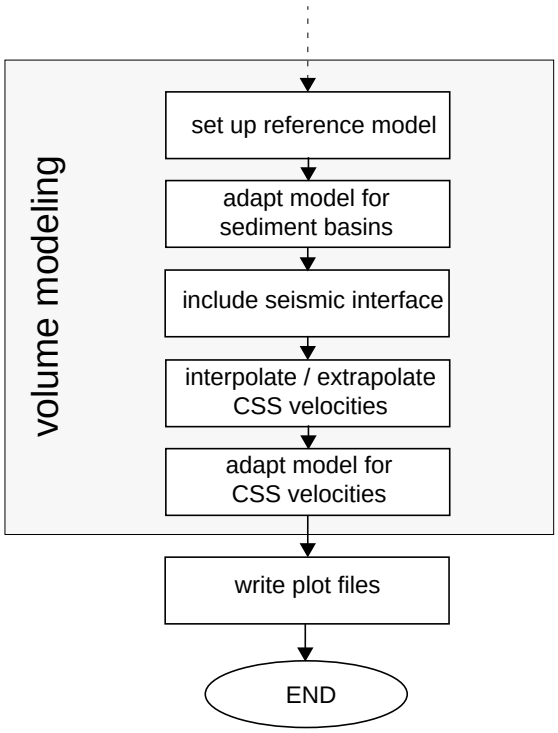


**Figure B.1** (above and previous page) Flow of the interface and volume modeling process in program *SeisMod3D*.

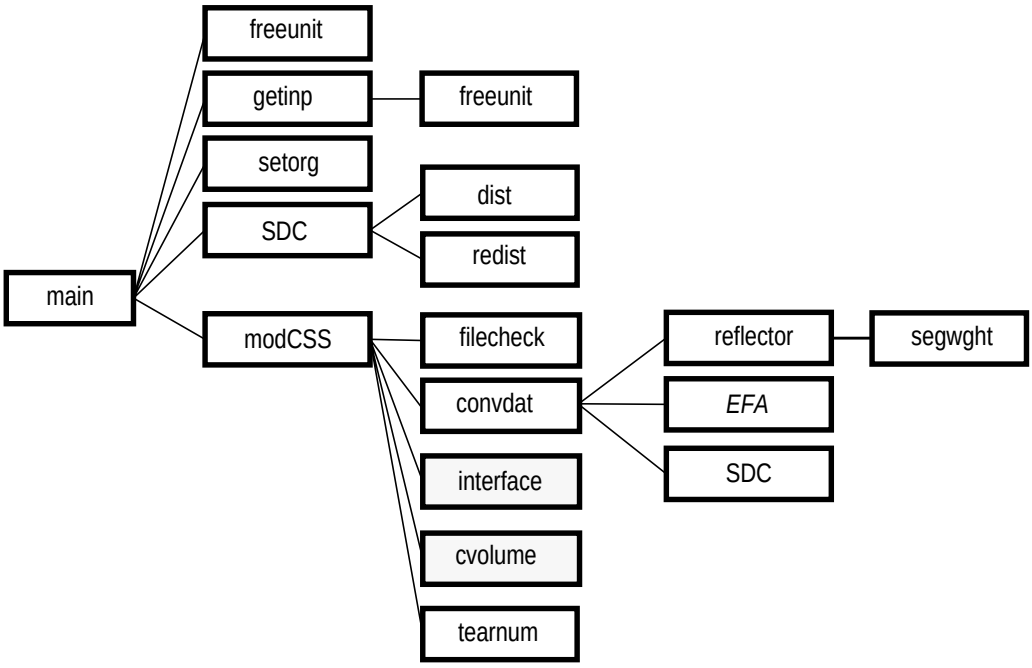


**Figure B.2** (this and next page) Structure of the three major modules main, interface and cvolume of the program *SeisMod3D*.

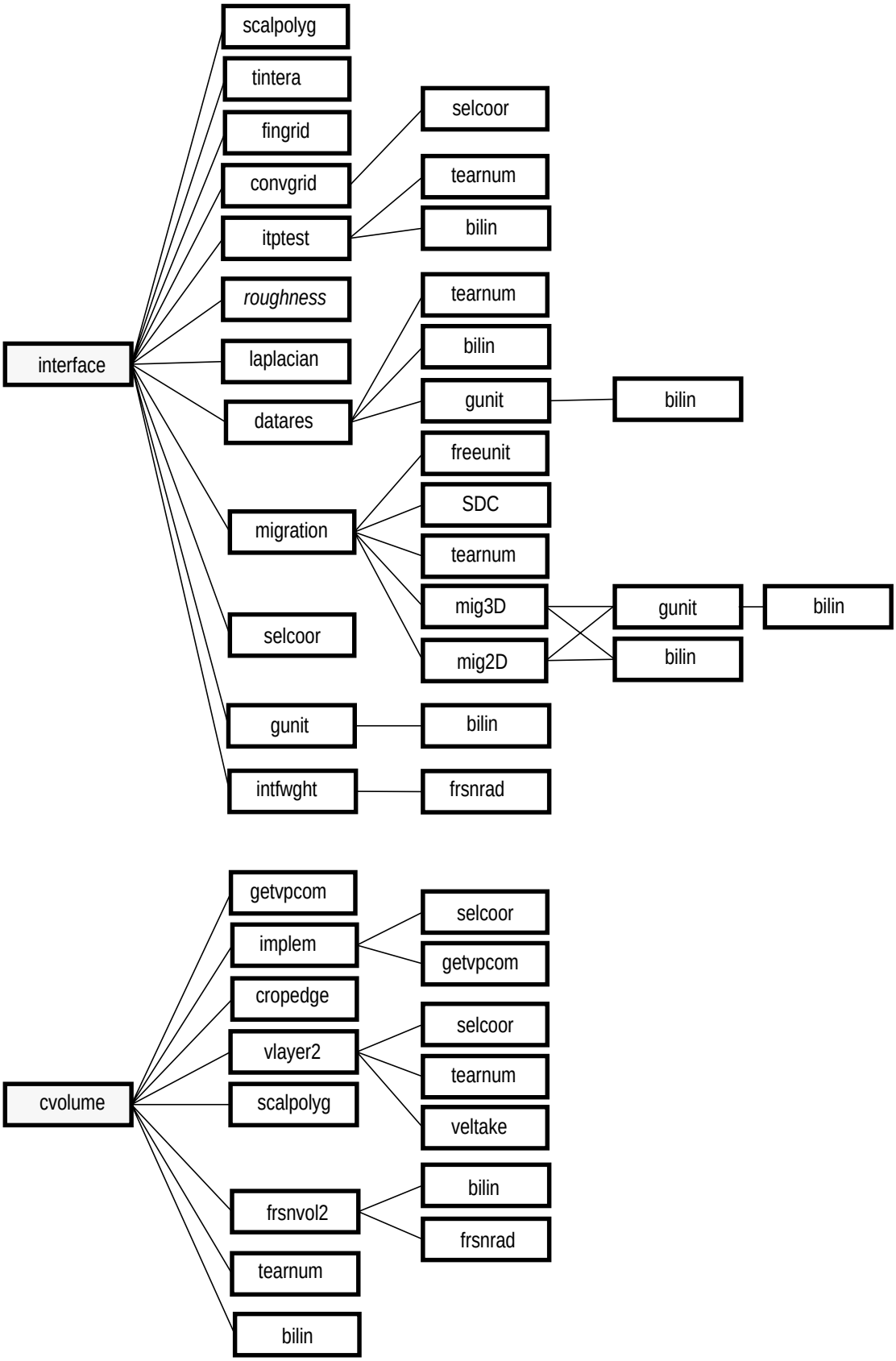
interface
scalpolyg
tintera
fingrid
convgrid
itptest
roughness
laplacian
datares
migration
selcoor
gunit
intfwght
selcoor
tearnum
bilin
tearnum
bilin
gunit
bilin
freeunit
SDC
tearnum
mig3D
mig2D
gunit
bilin
bilin
bilin
frsnrad
cvolume
getvpcom
implem
cropedge
vlayer2
scalpolyg
frsnvol2
tearnum
bilin
selcoor
getvpcom
selcoor
tearnum
veltake
bilin
frsnrad

| | |
|---|---|
| EFA | Computes Earth flattening approximation. |
| reflector | Parametrizes the reflectors defined by the CSS input data. |
| segwght | Determines the reflector segment weights. |
| interface | Directs the process flow for interface modeling. Handles sub-interface modeling. |
| scalpolyg | Scales polygone. |
| tintera | Interpolates uneven sampled data. Routine by E. Klingele (1972). |
| fingrid | Refines grid derived in *tintera*. Routine by E. Klingele (1972). |
| convgrid | Reads and converts *fingrid* output into sub-interface array. |
| selcoor | Selects coordinates lying inside a polygone. |
| itptest | Seeks for interpolated data lying outside data errors. |
| tearnum | Reads a character string into an integer array. |
| bilin | Performs bilinear interpolation. |
| laplacian | Determines the Laplacian roughness criteria of a surface. |
| datares | Calculates individual and root mean square data residuals. |
| gunit | Calculates nearest grid points and dip of a grid unit. |
| migration | Directs the process flow for migration. |
| mig3D | Migrates 1D-interpreted CSS data. |
| mig2D | Migrates 2D-interpreted CSS data. |
| intfwght | Determines the weighting factor along a surface. |
| frsnrad | Calculates the Fresnel radii at a certain depth. |
| cvolume | Directs the process flow for volume modeling. Sets up reference model and adapts it subsequentely with ‘a priori’ and CSS information. |
| getvpcom | Calculates the compensation velocity. |
| implem | Computes velocity-depth distribution and updates the volume array. |
| cropedge | Crops a refined surface grid along its edge according to the coarser grid. |
| vlayer2 | Interpolates the individual velocity parameters from the CSS input data. |
| veltake | Selects for velocity data to be interpolated. |
| frsnvol2 | Determines the approximated Fresnel volume of the average velocity. |

### B.1.2 Common blocks

No common blocks have been used in *SeisMod3D* except in routine *tintera* and *fingrid* (both by E. Klingele, 1972). A description of the major arrays and their maximal sizes are given in the header of the code.

## B.2 Input / Output

Figure B.3 shows the file handling of *SeisMod3D*. File formats for the controlled-source seismic data (*moho.dat, rfrprof.dat*) are described in Appendix A. *seismap.inp* stores the parameters to control the 3D model construction procedure (see below). The output of *SeisMod3D* is written on binary files (*mdat.**) ready to be displayed by VISTA3D (see Appendix D). *SeisMod3D* produces scratch files for intermediate term storage of results from individual modeling steps in order to save computer memory. However, these files are in ASCII format and are usefull for back tracing inconsistencies in the

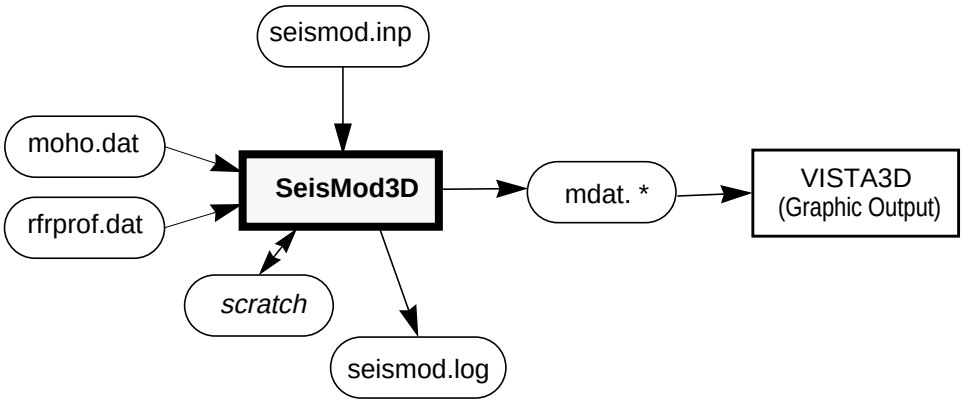


**Figure B.3** Input /output files of *SeisMod3D*.

model construction process. A run-time documentation is written to *seismod.log*.

### B.2.1 Input parameter file (*seismod.inp*)

*seismod.inp* stores the control and modeling parameters for the 3D model construction process such as input file names, grid parameters, values for reference model and surface information, interpolation and migration parameters, and velocity modeling parameters. Any line in the file beginning with a '*' is treated as comment line and is ignored during file processing. Comment lines may appear at any position within the file. Input format is free format.

The parameters must appear in the following order:

* seismod.inp:
* execution control for interface and volume modeling:
**IINTF, IVOL1, IVOL2, IVOL3, IVOL4, IVOL5, IVOL6**
* input specification:
**ISDC**
**FN**
* grid and model definition:
**HX, HY, HZ, NX, NY, NZ, LLCLON, LLCLAT**
**ZCOM, ORLON, ORLAT**
* reference values for 1D reference model:
**ZMR, VPSRFR, VPMR, VPNR, VPBR, VPAV1R, VPAV2R, IAV**
* sediment basin definition:
**NSPOL**
**VPSED, ZSED**
**(SPOLLON, SPOLLAT), ...**
* interface parameters (see Chap. 2.3.1 for mathematical parameter description)
**NTOPO**
**SELCO, SR0, SMF0, SR1, SMF1, PSCD**
**(POLX, POLY), ...**
**(PTSX, PTSY, PTSZ), ...**

* velocity parameters (this parameter block is NOT ACTIVE in the code version used for the 3D model derived in this work. Velocity parameters are defined in the code and held fixed as described in Chapter 2.3.2!). Set dummy values.
**DUM, V1SR0, V1SMF0, DUM,DUM, V1PSCD**
**(V1POLX, V1POLY), ...**
**(V1PTSX, V1PTSY, V1PTSV), ...**
**DUM, V2SR0, V2SMF0, DUM,DUM, V2PSCD**
**(V2POLX, V2POLY), ...**
**(V2PTSX, V2PTSY, V2PTSV), ...**
**DUM, V3SR0, V3SMF0, DUM,DUM, V3PSCD**
**(V3POLX, V3POLY), ...**
**(V3PTSX, V3PTSY, V3PTSV), ...**
**DUM, V4SR0, V4SMF0, DUM,DUM, V4PSCD**
**(V4POLX, V4POLY), ...**
**(V4PTSX, V4PTSY, V4PTSV), ...**

**IINTF** [I] Interface modeling switch. 0 = no interface modeling; 1 = migration surface interpolation only; 2 = 3D migration and final interface interpolation
**IVOL1** [I] Volume modeling switch: 0 = no velocity modeling; 1 = consider IVOL2 -IVOL6.
**IVOL2** [I] Adaption of reference model for sediment basins. 0 = no adaption; 1 = include sediments, no output; 2 = include sediments, output: reference model (*mdat.v3d_ref0*); 3 = include sediments, output: adapted reference model (*mdat.v3d_ref*); 4 = include sediments, output: *mdat.v3d_ref0* & *mdat.v3d_ref*.
**IVOL3** [I] Adaption for CSS information. 0 = no adaption. 1 = include crust-mantle boundary; no output. 2 = include CMB; output: *mdat.v3d_a0*; 3 = include CMB and velocities; output: *mdat.v3d_a*; 4 = include CMB and velocities; output: *mdat.v3d_a0* & *mdat.v3d_a*.
**IVOL4** [I] Interpolation/extrapolation of the velocity contrast across Moho only.
**IVOL5** [I] Not used in this version. Set dummy value.
**ISDC** [I] Coordinates of input data. 0 = cartesian input; 1 = lat/lon input.
**FN** [A] Name of the CSS data file.
**HX, HY, HZ** [3F] Grid spacing in each spatial direction. Set HX=HY for interface interpolation.
**NX, NY, NZ** [3I] Number of grid nodes in each spatial direction.
**LLCLON, LLCLAT** [2F]Geographical origin in lat/lon of the coordinate system with positive x-axis towards E and positive y-axis towards N. .
**ZCOM** [F] Depth to compute compensation velocity.
**ORLON, ORLAT** [2F] Origin of short distance conversion (lat/lon).
**ZMR** [F] Reference value for Moho depth.
**VPSRFR** [F] Reference value for surface velocity.
**VPMR** [F] Reference value for lower crustal velocity.
**VPNR** [F] Reference value for sub-Moho velocity.
**VPBR** [F] Reference value for upper mantle velocity at model base.
**VPAV1R** [F] Reference value for geometrical average crustal velocity.
**VPAV2R** [F] Reference value for travel time based average crustal velocity.
**IAV** [I] Selection of average crustal velocity. 1 =VPAV1R ; 2 = VPAV2R

**NSPOL** [I] Number of sedimentary basin definitions following (NSPOL sediment parameter blocks). Max. 10 sediment parameter blocks.
**VPSED** [F] Sediment velocity.
**ZSED** [F] Basin depth.
**SPOLLON, SPOLLAT** [F] Horizontal dimension of the basin defined by the corners (in geographical coordinates lat/lon) of a polygone. 7 coordinate pairs per line, max. 50 pairs per polygone. End input with -999.0.
**NTOPO** [I] Number of sub-interfaces following (NTOPO sub-interface parameters blocks). Max. 6 sub-interfaces.
**SELCO** [I] Codes to select depth points for interpolation (see parameter in CSS data file). E.g. SELCO = 513 uses points with codes 5, 1, and 3. First code (5) defines reference sub-interface, on which surface analysis computation is performed (roughness comp., migration etc.). Max. 6 point codes possible (i.e. [I6]).
**SR0** [F] Search radius for interpolation of migration surface.
**SMF0** [F] Smoothing factor for interpolation of migration surface.
**SR1** [F] Search radius for interpolation of final surface.
**SMF1** [F] Smoothing factor for interpolation of final surface.
**PSCD** [F] Scaling distance for the polygone defined below.
**POLX, POLY** [2F] Horizontal dimension of the sub-interfaces defined by the corners (in model coordinates x,y) of a polygone. 7 coordinate pairs per line, max. 50 pairs per polygone. End input with -999.0.
**PTSX, PTSY, PTSZ** [3F] Supporting points (in model coordinates x,y,z) to prevent numerical instabilities. 4 coordinate triples per line, max. 60 triples per sub-interface. End input with -999.0.

### B.2.2 Scratch files

moho2r.dat Parametrized structural data in *moho.dat* format.
moho2mr.dat Parametrized migrated structural data in *moho.dat* format.

### B.2.3 Output files (*mdat.**)

The *mdat.** files store the *SeisMod3D*-output and can be directly viewed with *VISTA3D* (see Appendix D). In the following list, SMF indicate surface file format, and VMF volume file format (see Appendix D for format description).

mdat.sedpolyg Sediment polygones.
mdat.m2r Parametrized unmigrated structural data.
mdat.m2mr Parametrized migrated structural data.
mdat.mtest Interpolation test results from unmigrated interface.
mdat.mtestm Interpolation test results from migrated interface.
mdat.itffit Results from interface fit criteria (data residuals).
mdat.migout Migration results.
mdat.mgrid2 Unmigrated interface and sub-interfaces (SMF).
mdat.mgrid2m Migrated interface and sub-interfaces (SMF).
mdat.mgrid2wght Weighting factor along unmigrated interface (SMF).
mdat.mgrid2mwght Weighting factor along migrated interface (SMF).

| | |
|---|---|
| mdat.mgrid2dz | Vertical (depth) migration amount (SMF). |
| mdat.mgrid2sl | Slope of unmigrated interface (SMF). |
| mdat.mgrid2slm | Slope of migrated interface (SMF). |
| mdat.mgrid2dsl | Slope difference between migrated and unmigrated interface (SMF). |
| mdat.mgrid3m | Refined migrated interface grid (used for 3D model) (SMF). |
| mdat.mgrid3mwght | Weighing factor along refined migrated interface grid (SMF). |
| mdat.vel_c | Parametrized migrated velocity data. |
| mdat.vgrid2 | Layers of surface, lower crustal, sub-Moho and average crustal velocity (SMF). |
| mdat.vtest | Velocity interpolation test results. |
| mdat.v3di_ref0 | Reference velocity model (VMF). |
| mdat.v3di_ref | Reference velocity model adapted for sediment basins (VMF). |
| mdat.v3di_a0 | Velocity model with reference velocities, sediment basins and Moho interface included (VMF). |
| mdat.c3di_a0 | Data origin model for mdat.v3di_a0 (VMF).<br>1-7: reference velocities<br>11-17: ‘a priori’ information (e.g. sediment velocites).<br>21-27: CSS information.<br>1,11,21: surface velocity.<br>2,12,22: compensation velocity.<br>3,13,23: intra crustal velocity.<br>4,14,24: lower crustal velocity.<br>5,15,25: sub-Moho velocity.<br>6,16,26: upper mantle velocity.<br>7,17,27: upper mantle velocity at model base. |
| mdat.v3di_a | Velocity model with reference velocities, sediment basins, Moho and CSS velocities included (VMF). |
| mdat.c3di_a | Data origin model for mdat.v3di_a (VMF). See above. |

# APPENDIX C

# WAVEFRONT COMPUTATION PROGRAMS

## C.1 Description

A program package is put together to calculate plane and curved teleseismic wavefronts through a 1D mantle model and subsequently through a 3D heterogeneous crustal velocity model. The main program is *punch.c* (Fig. C.1), a finite-difference travel time calculation code written in C by Vidale (1990) and modified by Hole et al. (1992) and Hole and Zelt (1995). The modifications include the handling of large velocity contrasts and the possibility to input source time fields at the model walls. No change of the original code of *punch.c* has been performed within this work except some minor input/output modifications. *punch.c* is called by *conv1.f*, a Fortran77 code that mainly converts the *SeisMod*/*VISTA*-format of the velocity and source time files to *punch.c*-format and the output of *punch.c* to *VISTA*-format for visualization.

The source time field at the base of the local 3D model is calculated by the Fortran77 program *sphere.f*. It uses the IASP91 program package to determine IASP91 travel times and slowness (Kennett and Engdahl, 1990) from a given hypocenter at the surface of the local 3D model, including the correction for ellipticity. Given slowness and travel time at each grid point at the surface of the local 3D model, the rays are traced back through the 1D IASP91 velocity structure to the base of the local model (routine *traceback* in *sphere*). The derived spherical wavefield of the incoming teleseismic wavefront at model base is the input to *conv1.f*.

## C.2 Input / Output

### *C.2.1 sphere.f*

*sphere.f* uses an input file storing the geographical coordinates of the surface grid points of the local model. The default file name is *latlon.grid2D*. The file contains nx*ny lines with each line storing the following parameters:

xi, yi Grid point location in model distance.
lon, lat Grid point location in geographical coordinates (lat/lon degrees).

Running *sphere.f* will ask interactively for source location (geographical coordinates

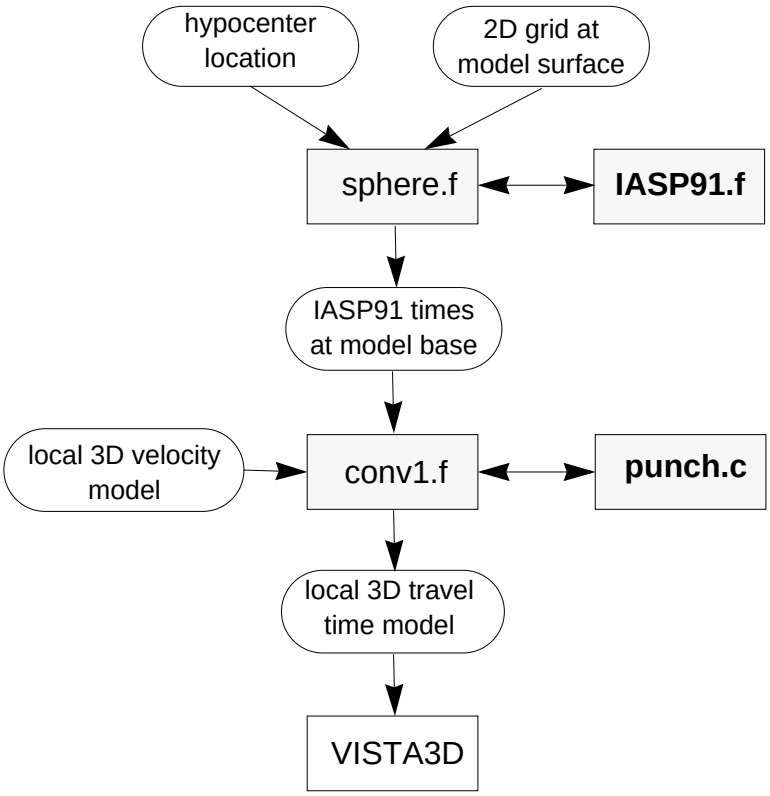


**Figure C.1** Flow of the teleseismic wavefront computation process using a 3D local model. *IASP91* is programed by Buland (), *punch.c* by Vidale (1990) and Hole and Zelt (1995). *VISTA3D* is described in Appendix D.

and source depth), the depth of the local model, and the phase codes for the desired branches.

*sphere.f* outputs two files in SMF-format (see Appendix D) storing the gridded time values from the surface (*mdat.t2d_IASPz0*) and the base (*mdat.t2d_IASPz*) of the local 3D model. Both files are used as input files for *conv1.f* and can be viewed by VISTA3D.

### C.2.2 conv1.f

*conv1.f* uses as input a 3D velocity model file (default file name *mdat.v3d*) in VMF-format (see Appendix D), a source time file at model base (*mdat.t2d_IASPz*) and a surface time file (*mdat.t2d_IASPz0*) at model surface, both in SMF format.

*conv1.f* outputs the calculated 3D travel time model in VMF-format (*mdat.t3d*), the calculated travel time field at model surface (*mdat.t2d_z0*) and the residuals between IASP91 and local 3D model travel times at the surface (*mdat.t2d_resz0*). All output files can be displayed by VISTA3D (see Appendix D).

# APPENDIX D

# DESCRIPTION OF *VISTA3D*

## D.1 Program Purpose and Description

*VISTA3D* is developed to visualize 1D, 2D, and 3D data as produced by the programs *SeisMod3D* (Appendix B) and *conv1* (Appendix C). It rapidely computes cross-sections and displays gridded interface and velocity models by line contouring, color contouring, and artificial illumination combined with the overlay of vector information. *VISTA3D* consists of MATLAB routines based on MATLAB 4.2c modules. The three major routines are (Fig. D.1): *interface.m*, *vellay.m*, and *volume.m*. *interface.m* displays the interface output of *SeisMod3D*, from results of individual modeling steps to final interface models. *vellay.m* displays the results from the velocity parameter modeling as performed by *SeisMod3D*. *volume.m* visualizes 3D models such as velocity models produced by *SeisMod3D* or travel time models calculated by *conv1*.

### D.1.1 Modules (Fig. D.1)

| | |
|---|---|
| VISTA.m | Stores all parameters and defines the look of the final display. |
| interface.m | Directs the process flow of the interface visualization. |
| datapoint.m | Plots data points by marks or values. |
| topo.m | Plots the 3D relief of interfaces. |
| selgrid2D.m | Resamples 2D grid lines. |
| gridpoint.m | Plots grid points by marks or values. |
| intfwght.m | Plots the weighting factor along interfaces. |
| migration.m | Plots migration results. |
| arrowtop.m | Plots an arrow with its size depending on the length of the line. |
| itptest.m | Plots interpolation test results. |
| border1.m | Plots geographical borders. |
| vellay.m | Plots the individual velocity layers. |
| vellab.m | Plots velocity values as labels. |
| sedpolyg.m | Plots sediment polygones. |
| volume.m | Directs the process flow of volume visualization. |
| section.m | Plots section through a 3D model along axis direction. |
| array3D.m | Builds up x, y, z, and v arrays from the input data. |
| fsection.m | Plots fence sections through a 3D model along axis direction. |
| csection.m | Plots a vertical cross-section through a 3D model in 2D display. |
| slicer.m | Slices a 3D model in axis directions. |

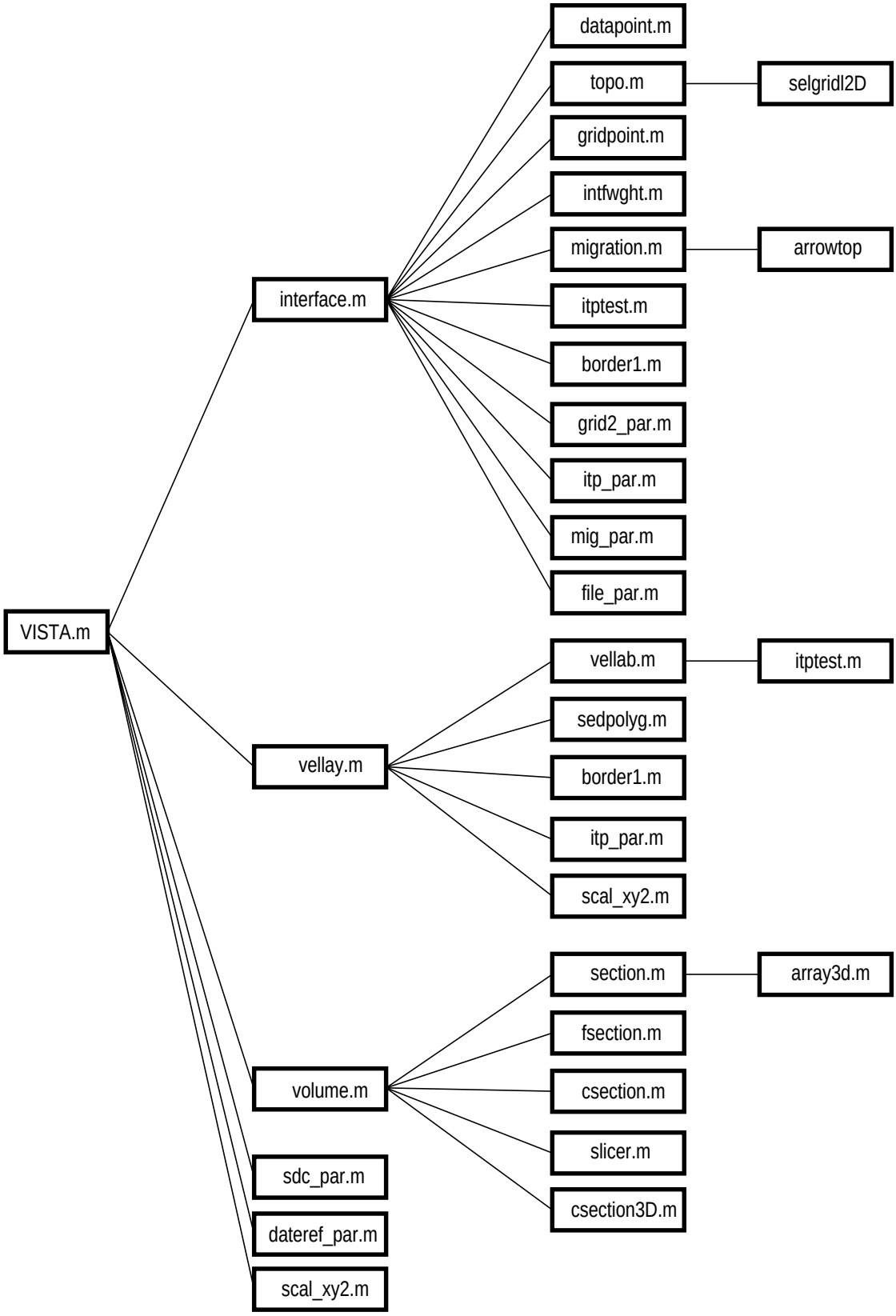


**Figure D.1** Structure of the *VISTA3D* Matlab modules.

| | |
|---|---|
| csection3D.m | Plots a vertical cross-section through a 3D model in 3D display. |
| scal_xy2.m | Performs plot scaling. |
| grid2_par.m | Writes grid parameter legend. |
| itp_par.m | Writes interpolation parameter legend. |
| mig_par.m | Writes migration parameter legend. |
| file_par.m | Writes file parameter legend. |
| sdc_par.m | Writes short-distance parameter legend. |
| dateref_par.m | Writes date and reference on plot. |

*Additional modules*

| | |
|---|---|
| datares.m | Plots data residuals. |
| datarms.m | Computes root mean square values. |
| rghcrit.m | Computes and displays surface roughness criteria. |
| extract3D.m | Extracts velocity values from 3D model according to defined data origin code. |
| selgrid3D.m | Resamples 3D grid lines. |
| vz1D.m | Plots velocity-depth function at a given location at model surface. |
| intfwght3D.m | Plots 3D interface grid and weighting factor superimposed. |

## D.2 Input / Output

*VISTA3D* can be started using *VISTA.m* which defines all parameters and has a switch at the beginning of the file to chose one of the three modules (*interface.m*, *vellay.m*, or *volume.m*). The chosen *VISTA3D* modules then read the input files in the fomat as produced by *SeisMod3D* or *conv1* (*mdat.** files). The graphical output can be viewed and written on postscript files or any other format provided by MATLAB (see MATLAB manual).

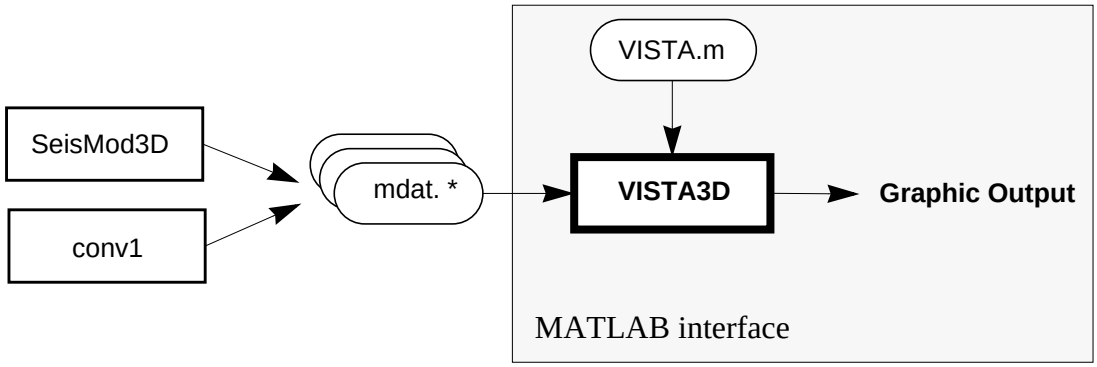


**Figure D.2** I/O file handling of *VISTA3D* module package.

## D.2.1 Input Parameter Description

If not otherwise indicated, the following switches take 0 for *no plot* and 1 for *do plot*! Input is in free format and colors are indicated by one-string characters (e.g. ‘w’, ‘r’ etc.; see MATLAB manual for color definition).

**interface**(file0,file1,file2,file3,file4,file5,imohotopo,imitp,itopo,imohogrid,cmohogrid,irflpts,crflpts,ierrb,iintfwght,imval,cmval,isuppts,csuppts,itestpts,ctestpts,tsmf,ipolyg,cpolyg,ipolygsc,cpolygsc,imig,cmig,imgeo,cmgeo,orlon,orlat,orx,ory,xmin,xmax,ymin,ymax,zmin,zmax,xlab,ylab,zlab,xview,zview,lightdir,lightsrc,ibox,igrid,szpar)

**file0** [A] Input parameter file used for the *SeisMod3D* run (e.g. *seismod3d.inp*).
**file1** [A] File with gridded surface model (e.g. *mdat.mgrid2m*; SMF format, see below).
**file2** [A] File with parametrized structural CSS data (e.g. *mdat.m2mr*).
**file3** [A] File with interpolation test results (e.g. *mdat.mtestm*).
**file4** [A] File with migration results (*mdat.migout*).
**file5** [A] File with surface weight values (*mdat.mgrid2mwght*).
**imohotopo** [I] Plot surface model.
**imitp** Look of surface plot. ‘**s**’ [A1] = surface interpolation; ‘**m**#’ [A1,I1] = mesh interpolation with grid lines displayed every # line of the original grid; ‘**c**#$’ [A1,F3.1,A1] = contour plot at # interval and with color $ (e.g. imitp= ‘c1.0w’).
**itopo** [I] Array with a 0 or a 1 for each sub-interface (e.g. [1,1,0] = plot first two of three sub-interfaces).
**imohogrid** [I] Plot grid points with color **cmohogrid** [A1]. 1 = grid points; 2 = values at grid points.
**irflpts** [I] Plot data points with color **crflpts** [A]. 1 = at depth -abs(z); 2 = at zero depth; 3 = at depth abs(z).
**ierrb** [I] Plot error bars
**iintfwght** [I] Plot weight factors along interface.
**imval** [I] Plot data value with color **cmval** [A1]. Depths values (1,2), error values (3,4), interpolation codes (5,6) of reflector endpoints (1,3,5) or of all sampled points along reflector (2,4,6).
**isuppts** [I] Plot supporting points with color **csuppts** [A1]. 1 = depth value; 2 = ‘+’.
**itestpts** [I] Plot interpolated points (color **ctestpts** [A1]) lying outside the error bar. Choose smoothing factor with **tsmf** [F] when file contains a series of tested surfaces.
**ipolyg** [I] Plot sub-interface polygones with color **cpolyg** [A].
**ipolygsc** [I] Plot scaled sub-interface polygones with color **cpolygsc** [A].
**imig** [I] Plot migration vector information. 1 = horizontal migration path; 2 = depth migration value; 3 = scattered migration reflectors; 4 = 3D migration ray paths. Color **cmig** [A] is used.
**imgeo** [I] Plot geography with color **cmgeo** [A1].
**orlon, orlat** [F] Origin of short distance conversion (see *SeisMod3D* input file parameters). Used to select geograhy file.
**orx, ory** [F] Origin of coordinate system with positive x-axis towards E and positive y-axis towards N (see SeisMod3D input file parameters).
**xmin, xmax, ymin, ymax, zmin,zmax** [F] Axis dimension.
**xlab,ylab,zlab** [A] Axis labels.

**xview,zview** [F] Perspective view direction of 3D plot (see MATLAB manual).
**lightdir,lightsrc** [F] Light direction (see MATLAB manual).
**ibox,igrid** [I] Plot box and/or grid.
**szpar** [F] Font size of parameter legend.

**vellay**(file11,file12,file13,ivpsrf,ivpm,ivpmlb,ivpn,ivpnlb,ivpavgm,ivpavgmlb,ivpavtt,ivpavttlb,ivplot,itestpts,cvlab,ipolyg,cpolyg,ivgeo,itrans,orlon,orlat,orx,ory,cvgeo,xmin,xmax,ymin,ymax,szpar)

**file11** [A] File with gridded surface model (e.g. *mdat. vgrid2*; SMF format, see below).
**file12** [A] File with parametrized CSS velocity data (e.g. *mdat. vel_c*).
**file13** [A] File with interpolation test results (*mdat.vtest*).
**ivpsrf** [I] Plot interpolated surface velocities. 1 = image plot; 2 = values.
**ivpm** [I] Plot interpolated lower crustal velocities. 1 = image plot; 2 = values.
**ivpmlb** [I] Plot values of sampled lower crustal velocities.
**ivpn** [I] Plot interpolated sub-Moho velocities. 1 = surface plot; 2 = values.
**ivpnlb** [I] Plot values of sampled sub-Moho velocities.
**ivpavgm** [I] Plot interpolated geometrically-derived average velocities. 1 = surface plot; 2 = values.
**ivpavgmlb** [I] Plot values of sampled geometrically-derived average velocities.
**ivpavtt** [I] Plot interpolated travel times based average velocities. 1 = surface plot; 2 = values.
**ivpavtlb** [I] Plot values of sampled travel times based average velocities.
**ivplot** [I] Single figures (1) or sub-plots (2).
**itestpts** [I] Plot interplation test results (NOT used with the current version of *SeisMod3D*).
**cvlab** [A] Color of the value labels.
**ipolyg** [I] Plot interpolation polygones with color **cpolyg** [A]. (Not used with the current version of *SeisMod3D*).
**ivgeo** [I] Plot geography with color **cvgeo** [A].
**itrans** [I] Input is in cartesian coordinates (1).
**orlon,orlat,orx,ory,xmin,xmax,ymin,ymax,szpar** See above.

**volume**(file0,file21,isec,c,cd,cdx,cdy,cdz,cvol,idisp,prof,rang,xmin,xmax,ymin,ymax,zmin,zmax,szpar)

**file0** [A] Input parameter file used for the *SeisMod3D* run (e.g. *seismod3d.inp*).
**file21** [A] File with gridded volume model (e.g. *mdat.v3D*; VMF format, see below).
**isec** [I] Switch for section. 1 = cube section (single & fence) along coordinate axis, use only when the model array is to large for isec=3; 2 = cross-section, 2D displayed; 3 = cube slicer (see also isec = 1); 4 = cross-section, 3D displayed.
**c** [A] Cut axis('x', 'y', 'z'). Use when isec=1.
**cd** [F] Cut distance on **c**. Use when isec=1.
**cdx**, **cdy, cdz** [F] Cut distances ([cdx1 cdx2 ...]) on x-, y-, and z-axis. Use when isec=3.
**cvol** [6F] Defines volume ([amin amax bmin ...]) which will be cut away in the plot.
**idisp** [A] 'p' for pcolor plot; 'n' for numbers (only single section mode).

**prof** [F] Cross-section coordinates. Start and end point ([x1 y1 x2 y2]).
**rang** [3F] Defines view angle (see MATLAB manual).
**xmin,xmax,ymin,ymax,zmin,zmax,szpar** See above.

*Surface and volume model file formats:*

SMF (surface model format): 2D gridded surface models.
**ntopo, nx, ny, x0, y0, hx, hy**, followed by **nx*ny values**.

| | |
|---|---|
| ntopo | Number of interfaces following (only for interface models). |
| nx, ny | Number of grid nodes in x-, y-direction. |
| x0, y0 | Distances at model origin (lower, left corner). |
| hx, hy | Grid spacing in x-, y-direction. |

VMF (volume model format): 3D gridded volume models
**nx, ny, nz, x0, y0, z0, hx, hy, hz,** followed by **nx*ny*nz values**.

| | |
|---|---|
| nx, ny, nz | Number of grid nodes in x-, y-, and z-direction. |
| x0, y0, z0 | Distances at model origin (lower, left corner at surface). |
| hx, hy, hz | Grid spacing in x-, y-, and z-direction. |